EUSKAL HERRIKO UNIBERTSITATEA
THE UNIVERSITY OF THE BASQUE COUNTRY

Department of Electricity and Electronics

CAMPUS OF INTERNATIONAL EXCELLENCE

Theoretical description of light emission in the presence of nanoscale resonators: from classical scattering to photon states entanglement and statistics

Thesis by

Álvaro Nodar Villa

Supervised by

Prof. Javier Aizpurua Iriazabal

and

Dr. Rubén Esteban Llorente

Donostia-San Sebastián, February 2023

ACKNOWLEDGMENTS

Quisiera dar las gracias / I would like to express my gratitude:

A Javier y a Rubén, por haberme dado la oportunidad de realizar esta tesis y por haberme dirigido durante todos estos años. Ha sido un viaje largo y ha habido etapas duras, pero posiblemente sin esos retos no estaría tan seguro ni tan orgulloso como lo estoy ahora de cada una de las páginas que siguen en esta tesis. Gracias por ofrecerme vuestro apoyo y vuestra paciencia. He crecido mucho bajo vuestra tutela.

A Gabriel, quien también me ha supervisado durante una larga etapa de esta tesis. Gracias, Gabriel, por remangarte y echarte las cuentas conmigo. Gracias por tu dedicación, me alegra mucho haber podido contar contigo durante esta etapa.

To Mike and Mikołaj, for welcoming me with open arms in Sydney. The project on the correlations really motivated me through the last stages of my thesis. I want to especially thank Mikołaj for showing me a different way of doing science. Thank you for being so humble and supportive. The last time we went to a pub, you invited me. I hope to have many chances of repaying this debt.

A mi gente del segundo piso (en orden alfabético, evitemos favoritismos): Adrián, Alberto, Antton, Bruno, Carlitos, Iker, Jon, Jonathan, Mario, Martín, Mikel, Miriam, Roberto, Txemikel. ¿Qué decir? Hemos compartido el día a día durante años, ya sabéis que os considero muy buenos amigos y que sois una parte importante de mi vida. Un cachito de esta tesis es de cada uno de vosotros. Ya me invitaréis a un café en el Etna, ¿no?

I would like to thank the support I received from all the friends I have made along the way in the Donosti scientific community. To the old gang: Andrea, Berni, Borinaga, Donaldi, Fede, Moritz, Thomas, Tomáš... thank you for showing me the ropes! To the new gang: Alex, Auguste, Carmela, Cris (Sanz), Edurne, Fer, Gabriele, Jorge (JOT), Jorge (Melillo), Josa, Joseba, Josu, Maria, Marina, Mathias, Matteo, Miguel Angel, Mikel, Paul, Raulillo, Stefan, Unai, Xabi... esta tesis no habría sido posible sin vuestro apoyo y amistad, gracias por estar a mi lado en esta etapa.

A mis padres y a toda mi familia por todo el apoyo incondicional que me habéis brindado durante mi larga etapa de estudiante. Sé que estaréis tan orgullosos de esta tesis como lo estoy yo hoy.

A Cris, durante estos años he sido (y sigo siendo) muy feliz a tu lado. Estoy muy agradecido por haber compartido cada día de esta etapa contigo. Gracias por apoyarme en los momentos duros y celebrar conmigo cuando las cosas salían bien. Te quiero mucho.

Por último, y mucho más importante que el resto, quiero agradecer el apoyo económico brindado por el proyecto PID 2019-107432GB-I00 del Ministerio de Ciencia e Innovación y de la Agencia Estatal de Investigación, así como por el proyecto IT 1526-22 del Gobierno Vasco. Ha sido una inversión muy acertada, os los aseguro.

RESUMEN

Al pasar un dedo por el borde de una copa, su cuerpo vibra creando un sonido. Esto ocurre porque la copa soporta una resonancia mecánica, que se excita al pasar el dedo con una velocidad y presión específicas. Algo similar ocurre con la luz y las nanoestructuras fotónicas. Al iluminar algunas nanoestructuras con una longitud de onda o frecuencia (color) específicas, podemos aumentar la intensidad del campo dispersado por la nanoestructura. Por ejemplo, las nanoestructuras metálicas soportan resonancias plasmónicas que consisten en una oscilación colectiva de su densidad de carga electrónica y que pueden ser excitadas con luz a frecuencias ópticas. La excitación resonante de las corrientes de polarización en el interior de nanoestructuras dieléctricas, es otro ejemplo de cómo la luz puede excitar resonancias ópticas en otros materiales. Cada tipo de nanoestructura ofrece ciertas ventajas para controlar la luz en la nanoescala. Por ejemplo, las nanoestructuras metálicas pueden confinar la luz en volúmenes mucho más pequeños, mientras que las nanoestructuras dieléctricas tienen pérdidas por absorción mucho menores.

Gran parte de este tipo de fenómenos se pueden explicar dentro del marco de la teoría de electromagnetismo clásico propuesta por James Clerk Maxwell en 1865 [1]. Desde entonces, se han desarrollado modelos analíticos (y semianalíticos) así cómo métodos numéricos que permiten analizar la respuesta de nanoestructuras fotónicas en condiciones muy generales. Por ejemplo, en esta tesis empleamos la llamada teoría de Mie para obtener una solución semianalítica a las ecuaciones de Maxwell de los campos dispersados por nanopartículas esféricas bajo diversas iluminaciones [2]. Las predicciones que se obtienen resolviendo la respuesta electromagnética clásica de nanoestructuras han sido de gran utilidad para el desarrollo de diversas aplicaciones fotónicas basadas en el aumento y la localización del campo electromagnético. Dentro de estas aplicaciones, cabe destacar las técnicas de espectroscopía aumentada por superficies [3–5], las técnicas de microscopía con resolución submolecular [6–8], los tratamientos de cáncer [9, 10], ó las mejoras en la captación y almacenamiento de energía solar [11, 12].

Por otra parte, los avances recientes en la fabricación y caracterización de nanoestructuras fotónicas han permitido alcanzar un nivel de precisión lo suficientemente alto como para demostrar diversos efectos cuánticos, lo cual ha generado un creciente interés en el campo de la nanofotónica cuántica durante las últimas décadas [13, 14].

La nanofotónica cuántica permite describir fenómenos muy variados. Por

ejemplo, el campo electromagnético aumentado que genera una nanoestructura fotónica puede dar lugar a una fuerte interacción óptica con un emisor cuántico (por ejemplo, un punto cuántico o una molécula) situado en su entorno. Si esta interacción es muy fuerte se pueden dar fenómenos no lineales en la respuesta del sistema emisor-nanoestructura que solo pueden ser descritos con un formalismo cuántico. Al mismo tiempo, la interacción de nanoestructuras con estados de luz cuánticos es particularmente interesante por su potencial aplicación en diversas tecnologías de información cuántica. Los estados cuánticos de luz son muy resistentes a perder la información codificada en ellos al mantener su propagación, constituyéndose en excelentes candidatos para la transmisión de información cuántica. Sin embargo, las posibilidades de modificar la información codificada en estados de luz cuánticos se ven limitadas debido a la débil interacción de la luz con la materia. Una solución prometedora a este reto es aprovechar la interacción amplificada entre la luz y materia que se da al excitar las resonancias ópticas de las nanoestructuras.

Esta tesis está dedicada a estudiar la interacción entre estados de luz clásicos y cuánticos con nanoestructuras fotónicas aisladas o interaccionando con emisores cuánticos. A continuación se presenta una discusión resumida de los contenidos principales de cada capítulo:

En el **capítulo 1** revisamos algunos aspectos de los fundamentos del electromagnetismo clásico que emplearemos en esta tesis. En concreto mostramos el tratamiento teórico para entender la respuesta a la luz de una nanopartícula esférica, una nanoestructura canónica en el campo de la nanofotónica que nos permite ilustrar diversos fenómenos de la interacción de la luz con nanoestructuras fotónicas resonantes. Para el estudio de este sistema consideramos varias descripciones. Primero introducimos la aproximación cuasiestática, válida para describir la respuesta de nanopartículas con un diámetro mucho más pequeño que la longitud de onda de la luz incidente. La aproximación cuasiestática nos permite explicar de una manera intuitiva los aspectos principales de la física de estos sistemas. Por ejemplo, describimos cómo la luz puede excitar las resonancias plasmónicas. También discutimos cómo se puede mejorar este modelo aproximado para incluir la corrección radiativa que tiene en cuenta las pérdidas de la nanoestructura al dispersar la luz incidente. Estos modelos aproximados son utilizados en el capítulo 3 para analizar los diferentes mecanismos físicos que intervienen en la interacción entre una nanoestructura y un emisor cuántico.

Junto con estas descripciones aproximadas, en el capítulo 1 también introducimos formalmente la teoría semianalitica de Mie. En concreto, la solución de Mie permite expresar los campos dispersados por una nanopartícula esférica como una suma de distintas contribuciones, cada una de ellas correspondiendose con la excitación de diferentes modos resonantes de la nanopartícula. A lo largo de esta tesis utilizamos el modelo de Mie para analizar la interacción de la luz con nanopartículas esféricas.

Finalmente, en el capítulo 1 describimos las propiedades del momento angular de la luz (espín, helicidad, momento angular orbital y momento angular total), y revisamos la interacción entre haces de luz con propiedades de momento angular bien

definidas y nanopartículas esféricas. Para ello extendemos la solución semianalitica de la teoría de Mie para describir la dispersión de este tipo de haces. Este tipo de problemas de dispersión son muy interesantes en el campo de la nanofotónica, ya que el momento angular de la luz introduce nuevos grados de libertad que pueden ser controlados con nanoestructuras y que presentan un gran potencial en diversas aplicaciones tecnológicas, por ejemplo, para aumentar la información codificada en un haz de luz [15–18] ó para detectar propiedades de substancias químicas (como la quiralidad de las moléculas) [19, 20].

En el **capítulo 2** revisamos algunos de los fundamentos de la nanofotónica cuántica que emplearemos en el resto de esta tesis. En particular, nos centramos en dos problemas canónicos. Primero estudiamos cómo se puede tratar la transformación de la luz incidente con un divisor de haz. Esta transformación es la base formal de nuestro estudio presentado en el capitulo 5. De manera más general, el divisor de haz es el elemento principal en muchos interferómetros, por ejemplo, el interferómetro Hanbury-Brown-Twiss (HBT) que empleamos en el capítulo 4. El interferómetro HBT permite la caracterización de la estadística del número de fotones emitidos por una fuente, y en el capitulo 2 discutimos detalladamente cuál es la base de su funcionamiento y cómo dicha caracterización nos permite clasificar diferentes tipos de luz dependiendo de si los fotones tienden a llegar individualmente o en grupos.

El segundo problema estudiado en este capítulo es la descripción cuántica de la interacción entre una cavidad óptica (tal cómo una nanoestructura resonante) y un emisor cuántico basada en el formalismo de electrodinámica cuántica de cavidades (*cavity-quantum electrodynamics*, en inglés). En concreto presentamos la formulación del Hamiltoniano que describe esta interacción según el modelo cuántico de Rabi (QRM, *quantum Rabi model* en inglés), el cuál es válido para cualquier valor de la energía de interacción entre la cavidad y el emisor. También introducimos el formalismo de la ecuación maestra (*master equation* en inglés) que describe la dinámica de un sistema cuántico interaccionando con su entorno, y que nos permite introducir las pérdidas de la cavidad y la iluminación incoherente del emisor. El Hamiltoniano del QRM y la ecuación maestra son las principales herramientas que utilizamos en el capítulo 4 para describir la emisión de sistemas formados por un emisor cuántico interaccionando con una nanoestructura.

El **capítulo 3** está dedicado al estudio de la asimetría en las resonancias Fano que emergen en el espectro de extinción de sistemas formados por una nanoestructura metálica interaccionando débilmente con un emisor cuántico. Este tipo de sistemas emisor-nanoestructura han sido estudiados extensivamente en el contexto de las técnicas de espectroscopía de campo aumentado (*surface-enhanced spectroscopy* en inglés), dónde el campo aumentado generado al excitar las resonancias plasmónicas de la nanoestructura metálica se usa para mejorar la señal espectral de una molécula en la cercanía de la nanoestructura, lo que permite detectar y caracterizar cantidades muy pequeñas de moléculas.

Cuándo la fuerza de acoplamiento entre el emisor y la nanoestructura es débil, el espectro del sistema emisor-nanoestructura se caracteriza por la aparición de una resonancia tipo Fano, la cual es originada por la interferencia entre una resonancia

espectralmente estrecha correspondiente al emisor y otra mucho más ancha (que se comporta como un continuo de modos) correspondiente a la nanoestructura metálica.

Las resonancias de tipo Fano se identifican por la aparición de un cambio de la señal abrupto en una región espectral estrecha, dando lugar a lo que se denomina un perfil Fano. La forma de este perfil varía con la naturaleza de la interacción emisor-nanoestructura, y puede presentar varios grados de asimetría, pero un modelo sencillo predice que la resonancia Fano es perfectamente simétrica si el sistema es resonante, es decir, cuándo la resonancia del excitón del emisor y de la resonancia óptica de la nanoestructura tienen la misma frecuencia central. Sin embargo, trabajos experimentales recientes han demostrado que la resonancia Fano puede ser asimétrica incluso en sistemas resonantes [8].

Para entender mejor esta observación experimental, analizamos en detalle el origen de la asimetría en las resonancias de tipo Fano en sistemas emisor-nanoestructura resonantes. Para ello empleamos simulaciones numéricas de la respuesta óptica del sistema híbrido en tres tipos de nanoestructuras diferentes (una nanopartícula esférica de plata, una nanopartícula esférica de oro, y un dímero compuesto por dos nanopartículas esféricas de oro, todas ellas iluminadas por una onda plana), así como una serie de modelos analíticos basados en sistemas de dos osciladores armónicos acoplados. De esta manera podemos identificar cinco efectos que producen la asimetría en la señal Fano: (i) la fase que adquieren los campos inducidos por la nanoestructura al propagarse hasta el emisor cuántico (y viceversa), (ii) la excitación directa del emisor cuántico por la luz incidente sobre el sistema, así como la emisión directa del emisor cuántico al detector, (iii) las pérdidas radiativas de la nanoestructura, (iv) la contribución de los electrones de valencia a la constante dieléctrica de la nanoestructura metálica, y (v) la contribución de las resonancias de orden alto que soporta la nanoestructura.

Los dos primeros efectos (la fase de propagación y la excitación y emisión directa) son claves para explicar el origen de la asimetría en todos los sistemas considerados. El impacto de la contribución de los electrones de valencia depende del material considerado. Por ejemplo, encontramos que esta contribución afecta fuertemente a la asimetría en las nanoestructuras de oro, mientras que en las nanoestructuras de plata es mucho menor. Por otra parte, la contribución de las resonancias de orden alto es pequeña en los sistemas considerados, pero puede adquirir más importancia en otro tipo de sistemas e iluminaciones, cómo la iluminación por la corriente túnel de un microscopio de efecto túnel (*scanning tunneling microscope*, en inglés). Por último, es necesario considerar las pérdidas radiativas de la nanoestructura para obtener una correcta descripción de la interacción emisor-nanoestructura, y por tanto para capturar correctamente la influencia de todos los otros efectos en la asimetría.

En el **capítulo 4** seguimos considerando un sistema formado por un emisor cuántico interaccionando con una nanoestructura metálica en condiciones resonantes. Sin embargo, a diferencia del capítulo anterior, en el capítulo 4 consideramos un amplio rango de energías de acoplamiento entre la nanoestructura y el emisor, pasando del régimen de acoplamiento débil (dónde el intercambio de excitaciones

entre la nanoestructura y el emisor es más lento que la disipación de la energía incidente por el sistema híbrido), al régimen de acoplamiento fuerte (dónde el intercambio de excitaciones es más rápido que la disipación, de forma que aparecen nuevos estados híbridos), y por último al régimen de acoplamiento ultrafuerte (caracterizado por la aparición de fenómenos no lineales asociados con términos que no conservan el número de excitaciones). Además, en este capítulo consideramos situaciones donde la iluminación es muy intensa, y para describir correctamente la respuesta del emisor consideramos que este actúa como un sistema de dos niveles (*two level system*, en inglés), lo cual puede introducir fenómenos no lineales adicionales (por ejemplo, el denominado bloqueo de fotones, *photon blockade*, en inglés).

En este capítulo estudiamos las correlaciones de intensidad de la luz emitida por este sistema híbrido bajo una excitación incoherente del emisor, lo cual requiere ir más allá de la descripción clásica. Para ello utilizamos dos modelos cuánticos diferentes. Primero introducimos una formulación del QRM desarrollada recientemente que es válida para cualquier régimen de acoplamiento. En segundo lugar consideramos el modelo Jaynes-Cummings (JCM, *Jaynes-Cummings model*, en inglés), el cual puede derivarse a partir del QRM trás aplicar la aproximación de onda rotante (RWA, *rotating wave approximation*, en inglés) que desprecia los términos que no conservan el número de excitaciones en el Hamiltoniano del QRM. Esta aproximación no es válida para describir el régimen de acoplamiento ultrafuerte, donde los términos que no conservan el número de excitaciones se vuelven más importantes, sin embargo ha sido utilizada con éxito para simplificar el análisis de sistemas acoplados débilmente [21, 22].

Al comparar las correlaciones de intensidad calculadas con el QRM y con el JCM observamos que, en el régimen de acoplamiento ultrafuerte, el QRM predice una emisión amontonada (*bunched*, en inglés), mientras que el JCM predice una emisión anti-amontonada (*antibunched*, en inglés). Sorprendentemente, bajo iluminaciones débiles, esta diferencia no solo se da en el régimen de acoplamiento ultrafuerte, sino que también ocurre en el régimen fuerte y débil, dónde se esperaría que el QRM y el JCM coincidieran.

A continuación, analizamos en detalle la influencia de cada autoestado del sistema en la emisión, y encontramos que la emisión amontonada en el QRM se puede atribuir al decaimiento de un sólo autoestado, el polariton $|3-\rangle_{\mathrm{R}}$ (correspondiente al quinto estado excitado del sistema bajo energías de acoplamiento pequeñas). Debido a la presencia de términos que no conservan el número de excitaciones en el Hamiltoniano del QRM, el estado $|3-\rangle_{\mathrm{R}}$ puede ser excitado de manera directa desde el estado base (*ground state*, en inglés), así cómo decaer emitiendo múltiples fotones de manera simultánea, lo que produce la emisión amontonada del sistema. Por el contrario, en el marco del JCM el estado análogo $|3-\rangle$ sólo puede excitarse de manera secuencial, mediante tres procesos de absorción, un mecanismo mucho menos eficiente para intensidades y fuerzas de acoplamiento suficientemente bajas. Recalcamos que esta diferencia entre el JCM y el QRM se puede extender al régimen de acoplamiento débil, donde normalmente se espera que los resultados del JCM y el QRM coincidan, lo que indica que los términos que no conservan el número

de excitaciones pueden ser importantes más allá del régimen de acoplamiento ultrafuerte. La influencia de estos términos es mucho más difícil de apreciar en otras magnitudes típicamente accesibles en fotónica tales como el espectro óptico del sistema. Por ello nuestros resultados indican que la caracterización de las correlaciones de intensidad se presentan como una posibilidad muy atractiva para identificar fenómenos característicos de sistemas acoplados ultrafuertemente así como para revelar las limitaciones de la RWA.

En los capítulos 3 y 4 nos centramos en la respuesta de sistemas nanoestructurados iluminados con haces clásicos. En cambio, en el **capítulo 5** consideramos una iluminación por estados cuánticos de luz. En concreto estudiamos la respuesta óptica de nanoestructuras rotacionalmente simétricas iluminadas por estados cuánticos de luz compuestos por dos fotones entrelazados que tienen información codificada en sus propiedades de momento angular. Por un lado, este tipo de estados son particularmente interesantes por su potencial en aplicaciones de tratamiento de información cuántica, ya que el momento angular de la luz es una propiedad que no está limitada a dos valores cómo el espín de un cúbit (*qubit*, en inglés) de un ion atrapado, sino que el momento angular orbital de la luz abre un espacio de Hilbert (en principio) infinito para codificar información. Por otro lado, las nanopartículas rotacionalmente simétricas conservan el momento angular total del estado en un proceso de dispersión, por lo que ofrecen la posibilidad de manipular el estado cuántico de la luz de una manera controlada. Este control en la manipulación del estado cuántico de la luz es muy interesante para procesar la información cuántica del estado, pero a su vez exige que se respete la pureza cuántica del estado incidente en un alto grado.

En nuestro estudio desarrollamos un formalismo teórico para modelar el proceso de dispersión en estos sistemas basado en la transformación de un estado cuántico de la luz al pasar por un divisor de haz con pérdidas. Esta transformación es general y se puede extender a otros escenarios en los que la luz es dispersada por una nanoestructura mientras que la interacción esté definida en base a dos posibles modos de entrada y dos posibles modos de salida.

Empleando este formalismo encontramos que la pureza del estado incidente se puede perder por la interacción con la nanoestructura. Para identificar el mecanismo físico por el cual se origina la pérdida de pureza, desarrollamos un modelo semi-analítico basado en el tratamiento de los modos de entrada y salida cuasi-monocromáticos. Este modelo describe al estado total de salida cómo una superposición de dos estados pulsados, e indica que estas dos contribuciones pueden emerger a distintos tiempos y a distintas frecuencias. Cuando esto ocurre se da una pérdida de pureza. Este análisis se puede ampliar a distintas nanoestructuras e iluminaciones y aporta una explicación intuitiva sobre los mecanismos físicos que pueden generar pérdida de pureza en la interacción de estados cuánticos de luz con nanoestructuras.

En resumen, la investigación presentada en esta tésis supone un avance en la comprensión de aspectos físicos fundamentales de la interacción tanto de luz clásica como de estados cuánticos de luz con nanoestructuras.

LIST OF ABBREVIATIONS

cavity-QED	Cavity-Quantum electrodynamics
CTS	Cavity-two-level-system
GKSL	Gorinski-Kossakowski-Sudarshan-Lindblad
HBT	Hanbury Brown and Twiss
JCM	Jaynes Cummings model
QE	Quantum emitter
QRM	Quantum Rabi model
RRWA	Reservoir rotating wave approximation
RWA	Rotating wave approximation
SC	Strong coupling
SPDC	Spontaneous parametric down conversion
TLS	Two level system
USC	Ultrastrong coupling
WC	Weak coupling

CONTENTS

Acknowledgments **iii**

Resumen **v**

List of abbreviations **xi**

Introduction **1**

1 Classical description of the interaction between light and matter at the nanoscale **7**
1.1 Maxwell's equations 8
1.2 Electromagnetic response of very small objects 10
1.2.1 Response of a very small spherical nanoparticle within the quasistatic approximation 10
1.2.2 Radiative-corrected model 16
1.2.3 Optical cross-sections of a small particle 19
1.2.4 Response of a quantum emitter 22
1.3 Full electromagnetic response of spherical nanoparticles 23
1.3.1 Mie theory formulation 24
1.3.2 Fields scattered by a spherical nanoparticle under plane wave illumination 27
1.4 Angular momentum of light 34
1.4.1 Paraxial beams with non-zero orbital angular momentum and spin 35
1.4.2 Beyond the paraxial approximation 38
1.4.3 Scattering of a beam with well-defined angular momentum by a spherical nanoparticle 40

2 Fundamentals of the quantum description of the interaction of light and optical resonators **45**
2.1 States of light and observables 46
2.2 Quantization of light 47
2.3 Quantum transformations by a lossless and a lossy beam splitter . 49
2.4 The Hanbury-Brown and Twiss interferometer 52

2.4.1 General description of the Hanbury-Brown and Twiss interferometer . . . 52
2.4.2 Statistics of light emitted by a coherent source . . . 54
2.4.3 Statistics of light emitted by a thermal source . . . 56
2.4.4 Statistics of light emitted by a single photon source . . . 58
2.4.5 Statistics of light emitted by a realistic two-photon source . 60
2.5 The Hamiltonian of cavity-QED systems . . . 62
2.5.1 From the classical Lagrangian to the first quantization of the Coulomb gauge quantum Rabi Hamiltonian . . . 63
2.5.2 Truncation of the Hilbert space of the emitter, loss of locality, and quantum Rabi Hamiltonian in the dipole gauge . . . 67
2.5.3 From the dipole gauge to the Coulomb gauge . . . 70
2.5.4 Jaynes-Cummings model Hamiltonian . . . 71
2.6 Quantum dynamics in open quantum systems: the quantum master equation . . . 71
2.6.1 From the Von Neumann equation to the Markovian master equation . . . 72
2.6.2 From the Markovian master equation to the Lindbladian master equation . . . 75

3 Fano asymmetry in zero–detuned exciton–plasmon systems 79
3.1 Introduction . . . 79
3.2 Fano asymmetry under resonant conditions . . . 80
3.3 Fano lineshape . . . 84
3.3.1 Analytical derivation of the Fano lineshape in the extinction cross-section . . . 84
3.3.2 Evaluation of the Fano lineshape . . . 89
3.4 Dissection of the asymmetry . . . 92
3.4.1 Analytical expression of the total asymmetry factor . . . 92
3.4.2 Effect of different optical response approximations on the asymmetry . . . 94
3.4.3 The Fano asymmetry factor in additional scenarios . . . 102
3.5 Fano resonance in dimers . . . 106
3.6 Conclusions . . . 108

4 Unbound strong bunching and breakdown of the Rotating Wave Approximation in the quantum Rabi model 111
4.1 Introduction . . . 111
4.2 Cavity-two-level-system Hamiltonian models . . . 113
4.2.1 Quantum Rabi model . . . 114
4.2.2 Jaynes-Cummings model . . . 117
4.3 Origin of the bunching in ultrastrongly coupled systems . . . 122
4.4 Probing the breakdown of the RWA . . . 125
4.4.1 Qualitative dependence of the bunching on the pumping . . 125
4.4.2 Breakdown of the JCM Hamiltonian in the WC regime . . 126

4.4.3 Emission spectra 128
4.5 Conclusions 130

5 Preservation and destruction of the purity of two-photon states in the interaction with a nanoscatterer 131
5.1 Introduction 131
5.2 Input and output states 132
5.3 Quantum transformation 134
5.3.1 Helicity-splitting coefficients 135
5.3.2 Output $|\Psi_+^o\rangle$ state 135
5.3.3 Other excitation states 140
5.4 Loss of purity due to the scattering by a silicon spherical nanoparticle 141
5.4.1 Classical response: helicity-splitting coefficients 141
5.4.2 Quantum response: Analysis of the purity of the scattered state 145
5.5 Conclusions 148

Conclusions and Outlook 149

Appendices

A Derivation of the two contributions to the Fano asymmetry 155
A.1 Derivation of q_{R} 155
A.2 Derivation of q_{E} 156

B Relationship between the field enhancement and the Purcell Factor 159

C Details of the classical electromagnetic calculations of the optical response of a dimer nanostructure under different illuminations 161

List of publications 163

Bibliography 165

INTRODUCTION

By running our finger along the rim of a cup, we cause its body to vibrate, creating a sound. This happens because the body of the cup supports a mechanical resonance, which we can excite by running our finger with a specific speed and pressure. Something similar happens with light and photonic nanostructures. By illuminating some nanostructures with a specific wavelength or frequency (color), we can increase the intensity of the electromagnetic field scattered by them. For example, metallic nanoparticles support plasmonic resonances at optical frequencies that consist of a collective oscillation of the electronic charge density of the nanostructure. As another example, exciting the polarization currents of dielectric nanostructures (of a few hundred nanometers in size) can also gives rise to the excitation of optical resonances. Each type of nanostructure offers certain advantages for controlling light at the nanoscale. For example, metallic nanostructures can confine light in smaller volumes, while dielectric nanostructures have lower absorption losses.

Much of this type of phenomena can be explained within the framework of the classical theory of electromagnetism proposed by James Clerk Maxwell in 1865 [1]. Since then, analytical (and semi-analytical) models and numerical methods have been developed to analyze the response of photonic nanostructures under very general conditions. For example, in this thesis, we use the so-called Mie theory [2] to obtain a semi-analytical solution to Maxwell's equations of the fields scattered by spherical nanoparticles under various illuminations. The predictions obtained by solving the classical electromagnetic response of nanostructures have been very useful for the development of several applications based on the enhancement and localization of the electromagnetic field. Among these applications, one can cite surface-enhanced spectroscopy techniques [3–5], microscopy techniques with submolecular resolution [6–8], cancer treatment [9, 10], or improvements in solar energy harvesting [11, 12].

On the other hand, recent advances in the fabrication and characterization of photonic nanostructures have made it possible to achieve a level of precision high enough to demonstrate various quantum effects in the optical response of such nanostructures. Consequently, the interest in the field of quantum nanophotonics has grown in recent decades [13, 14].

Quantum nanophotonics makes it possible to describe a wide variety of phenomena. For example, the enhanced electromagnetic field generated by a photonic nanostructure can lead to a strong optical interaction with a quantum

emitter (QE, *e.g.* a quantum dot or a molecule) located in the proximity of the nanoparticle. If this interaction is very strong, a variety of nonlinear phenomena can occur in the response of the QE-nanostructure system that can be better described through a quantum framework. At the same time, the interaction of nanostructures with quantum states of light is particularly interesting for various quantum information technologies. Quantum states of light are very resilient to the loss of their information through propagation, establishing themselves as excellent candidates for the transmission of quantum information. However, the possibilities of controlling the information encoded in quantum light states are limited by the weak interaction of light with matter. A promising solution to this challenge is to exploit the amplified interaction between light and matter that occurs upon the excitation of optical resonances in nanostructures.

This thesis is devoted to studying the interaction between classical and quantum states of light with photonic nanostructures and QE-nanostructure systems. In the following, we introduce a summary of the main contents of each chapter.

In **chapter 1** we summarize some of the fundamentals of classical electromagnetism that we use in this thesis. In particular, we review the response to light of a spherical nanoparticle, a canonical nanostructure in the field of nanophotonics that allows us to illustrate various phenomena of the interaction of light with resonant photonic nanostructures. We use different approaches to describe the optical response. First, we introduce the quasi-static approximation, valid for describing the response of nanoparticles with a size much smaller than the incident wavelength of light. The quasi-static approximation allows for explaining, in an intuitive way, the main aspects of light-matter interaction. For example, we describe how light can excite the plasmonic resonances in metallic nanoparticles. We also discuss how this approximated model can be improved to include the radiative correction that takes into account the increase in the losses of the nanostructure due to the scattering of light. We use these approximated models in chapter 3 to analyze the different aspects of the interaction between a QE and a metallic nanostructure.

Along with these approximate descriptions, in chapter 1 we formally introduce the semianalytical Mie theory that describes the exact solution of Maxwell's equations to the field scattered by a spherical nanoparticle. Specifically, Mie's solution allows for expressing the field scattered by a nanoparticle as a sum of different contributions, each corresponding to the excitation of different resonant modes of the nanoparticle. Throughout this thesis, we use Mie theory to analyze the interaction of light with spherical nanoparticles.

Finally, in chapter 1 we describe the angular momentum properties of light (spin, helicity, orbital angular momentum, and total angular momentum), and review the interaction between light beams with well-defined angular momentum properties and nanoparticles. For this purpose, we extend the semi-analytic solution of Mie theory to describe the scattering of such beams by a spherical nanoparticle. Such scattering problem is very interesting in the field of nanophotonics, since the angular momentum of light introduces new degrees of freedom that can be controlled with nanostructures and have great potential in a variety of applications, for example,

to increase the information encoded in a light beam [15–18] or to detect additional properties of chemical substances (such as the chirality of molecules) [19, 20].

In **chapter 2** we review the fundamentals of quantum nanophotonics that we use in this thesis. In particular, we focus on two canonical problems. First, we describe the transformation of a state of light by a beam splitter. This transformation is the formal basis of the study presented in chapter 5. Moreover, the beam splitter is the main element in many interferometers, for example, in the Hanbury-Brown-Twiss (HBT) interferometer that we use in chapter 4. The HBT interferometer enables the characterization of the statistics of the number of photons emitted by a light source. In chapter 2, we discuss in detail what is the basis of the HBT operation and how it allows us to characterize different types of light depending on whether the photons are emitted mostly separately (antibunched) or in groups (bunched).

The second problem studied in this chapter is the quantum description within cavity Quantum Electrodynamics (cavity-QED) of the interaction between an optical cavity (such as a resonant nanostructure) and a QE. In particular, we present the formulation of the Hamiltonian that describes this interaction according to the quantum Rabi model (QRM), which is valid for any value of the interaction strength between the cavity and the QE. We also introduce the master equation formalism that describes the dynamics of a quantum system interacting with its environment and allows us to describe the losses and the incoherent illumination of the system. The QRM Hamiltonian and the master equation are the two pillars we use in chapter 4 to describe the light emission from systems consisting of a QE interacting with a nanostructure.

Chapter 3 is devoted to the study of the asymmetry in the Fano resonances that emerges in the extinction spectrum of systems formed by a metallic nanostructure interacting weakly with a QE. Such QE-nanostructure systems have been extensively studied in the context of enhanced field spectroscopy techniques, where the enhanced field generated by exciting the plasmon resonances of the metallic nanostructure is used to increase the spectral signal of the molecule. These techniques allows for the detection and characterization of very small quantities of molecules.

When the coupling strength between the QE and the nanostructure is weak, the extinction spectrum of the hybrid QE-nanostructure system is characterized by the appearance of a Fano-type resonance, caused by the interference between a spectrally narrow resonance corresponding to the QE and a much wider one (which behaves as a continuum of modes) corresponding to the metallic nanostructure.

Fano resonances are identified by the appearance of a sharp spectral feature, which is the so-called Fano lineshapes. These lineshapes depend on the nature of the QE-nanostructure interaction and can exhibit different degrees of asymmetry. In particular, a simple model indicates that a Fano resonance is perfectly symmetric if the system is resonant, *i.e.* when the central frequency of the (excitonic) resonance of the QE is tuned to the central frequency of the optical resonance of the nanostructure. However, recent experimental work has shown that the Fano resonance can be asymmetric even in resonant systems.

To better understand this experimental observation, we analyze in detail the origin of the asymmetry in the Fano resonances of zero-detuned QE-nanostructure

systems. For this purpose, we analyze the optical response in three different types of nanostructures (a spherical silver nanoparticle, a spherical gold nanoparticle, and a dimer composed of two spherical gold nanoparticles, all illuminated by a plane wave) using numerical simulations and a series of analytical models based on coupled harmonic oscillators. In this way, we identify the different physical mechanisms that originate the Fano asymmetry in zero-detuned QE-nanostructure systems.

In **chapter 4** we also consider a QE interacting with a nanostructure under resonant conditions. However, unlike the previous chapter, in chapter 4 we consider a wide range of coupling strengths between the nanostructure and the QE, ranging from the weak coupling regime (where the exchange of excitations between the nanostructure and the QE is slower than the dissipation of the incident energy by the system), to the strong coupling regime (where the exchange of excitations is faster than the dissipation so that new hybrid states appear), and finally to the ultra-strong coupling regime (the coupling strength becomes so large that nonlinear phenomena associated with terms that do not conserve the number of excitations becomes possible). Furthermore, in this chapter, we take into account that an (excitonic) transition of a QE acts as a two-level-system, which introduces additional nonlinear phenomena under strong illumination (for example, the so-called photon blockade).

We study the intensity correlations of the light emitted by this hybrid QE-nanostructure system under incoherent excitation of the QE. This study requires going beyond the classical description. In particular, we use two different quantum models. First, we introduce a recently-developed formulation of the QRM that is valid for any coupling regime. Second, we consider the Jaynes-Cummings model (JCM), which can be derived from the QRM after applying the rotating wave approximation (RWA) that neglects the terms that do not preserve the number of excitations in the Hamiltonian of the QRM. This approximation is known to fail in the ultra-strong coupling regime, where the role of the terms that do not conserve the number of excitations becomes more important, but it has been successfully used to simplify the analysis of many systems in the weak and strong coupling regime [21, 22].

We compare the intensity correlations calculated with the QRM and the JCM, and observe that, in the ultra-strong coupling regime, the QRM predicts a bunched emission while the JCM predicts an antibunched emission. Surprisingly, under weak illuminations, this difference does not only occurs in the ultra-strong coupling regime but also in the strong and weak regimes, where the QRM and JCM are expected to agree. In this chapter, we analyze in detail the origin of the bunched emission in the QRM and the deviation between the QRM and the JCM, *i.e.* the breakdown of the RWA.

In chapters 3 and 4 we focus on the response of nanostructures illuminated with classical beams. In contrast, in **chapter 5** we consider a nanostructure illuminated by a quantum state of light. Specifically, we study the response of rotationally symmetric nanostructures illuminated by a quantum state composed of two entangled photons with information encoded in their angular momentum

properties. On the one hand, such states are particularly interesting for quantum information processing applications, since the angular momentum of light is a property that is not limited to two values like the spin of a trapped ion qubit. The orbital angular momentum of light opens an (in principle) infinite Hilbert space to encode information. On the other hand, rotationally symmetric nanoparticles preserve the total angular momentum of the state after scattering, thus offering the possibility of manipulating the quantum state in a controlled manner. This control in the manipulation of a quantum state of light is very interesting for processing its quantum information, but requires that the quantum purity of the incident state is respected to a high degree.

We develop a general theoretical formalism to model the scattering process in these systems, which is based on the transformation of a quantum state by a lossy beam splitter. Using this formalism we calculate the output state scattered by the nanostructure and find that the purity of the incident state can be lost in the interaction with the nanostructure. We then develop a semi-analytical model based on treating the quasi-monochromatic input and output modes that allows us to identify the physical mechanism that causes the loss of purity.

In summary, the research presented in this thesis advances our understanding of fundamental physical aspects of the interaction of both classical light and quantum states of light with nanostructures.

CHAPTER 1

CLASSICAL DESCRIPTION OF THE INTERACTION BETWEEN LIGHT AND MATTER AT THE NANOSCALE

The main topic of this thesis is the interaction between light and matter at the nanoscale. In this chapter, we introduce the theoretical framework that we use to study the interaction between classical states of light and a nanostructure.

Nanostructures can be used to control light at the nanoscale, allowing for concentrating incident electromagnetic fields in very small regions [3, 23–26], change the polarization properties of incident light [27–29], or generate light of a frequency different than that of the illumination [30–32]. Most of these effects can be described within the theory of classical electromagnetism, where light-matter interaction can be captured Maxwell's equations, a set of differential equations that describe how electromagnetic fields evolve in time and space in a particular dielectric configuration. By applying the appropriate boundary conditions, Maxwell's equations can be solved to obtain the response of an arbitrary nanostructure under specific illumination.

In section 1.1 of this chapter, we review the formulation of Maxwell's equations. In sections 1.2 and 1.3 we review the analytical and semi-analytical solutions of Maxwell's equations for a canonical nanostructure: a spherical nanoparticle. The analytical or semi-analytical solutions allow us to discuss the general properties of the optical response. Specifically, in section 1.2 we treat the nanoparticle as a polarizable object that behaves as an electric point-like dipole, a commonly used approximation in nanophotonics. We also discuss how a similar approach can be used to describe the optical response of molecules and other quantum emitters (QEs). On the other hand, in section 1.3 we introduce a semi-analytical solution to Maxwell's equations (obtained without any approximation) for the

fields scattered by a spherical nanoparticle. We evaluate these frameworks in a canonical configuration, the scattering of linearly polarized light by a metallic spherical nanoparticle. Finally, in section 1.4 we expand the formalism introduced in section 1.3 to describe the scattering of a spherical nanoparticle illuminated by complex beams of light, in particular, beams of light with well-defined angular momentum properties, as those used in chapter 5.

1.1 Maxwell's equations

In 1865 the Scottish mathematician James Clerk Maxwell published "A Dynamical Theory of the Electromagnetic Field" [1], a paper containing the original formulation of his famous equations showing the interrelationship between electric fields $\boldsymbol{E}(\boldsymbol{r},t)$ and magnetic fields $\boldsymbol{B}(\boldsymbol{r},t)$ in a dielectric medium ($\boldsymbol{E}(\boldsymbol{r},t)$ and $\boldsymbol{B}(\boldsymbol{r},t)$ are evaluated at a position $\boldsymbol{r}$ and time t). Nineteen years later, in 1884, the English mathematician Oliver Heaviside used his developments in vectorial and complex number calculus to reformulate Maxwell's equations into the form that has been known ever since [33],

$$\begin{aligned}
\nabla \times \boldsymbol{E}(\boldsymbol{r},t) &= -\frac{\partial \boldsymbol{B}(\boldsymbol{r},t)}{\partial t}, \\
\nabla \times \boldsymbol{H}(\boldsymbol{r},t) &= \frac{\partial \boldsymbol{D}(\boldsymbol{r},t)}{\partial t} + \boldsymbol{J}_{\text{ext}}(\boldsymbol{r},t), \\
\nabla \cdot \boldsymbol{D}(\boldsymbol{r},t) &= \rho_{\text{ext}}(\boldsymbol{r},t), \\
\nabla \cdot \boldsymbol{B}(\boldsymbol{r},t) &= 0,
\end{aligned} \tag{1.1}$$

where $\boldsymbol{J}_{\text{ext}}$ is the external current density, and ρ_{ext} is the external charge density. The electric field displacement is $\boldsymbol{D}(\boldsymbol{r},t) = \varepsilon_0 \boldsymbol{E}(\boldsymbol{r},t) + \boldsymbol{P}_{\boldsymbol{D}}(\boldsymbol{r},t)$, where $\boldsymbol{P}_{\boldsymbol{D}}$ is the polarization field of the medium and ε_0 is the electric permittivity in a vacuum. Similarly, the magnetizing field is $\boldsymbol{H}(\boldsymbol{r},t) = \boldsymbol{B}(\boldsymbol{r},t)/\mu_0 - \boldsymbol{M}_{\boldsymbol{B}}(\boldsymbol{r},t)$, with $\boldsymbol{M}_{\boldsymbol{B}}$ the magnetization field of the medium and μ_0 the magnetic permeability in a vacuum. In this thesis, we assume linear light-matter interaction, with $\boldsymbol{P}_{\boldsymbol{D}}(\boldsymbol{r},t) \propto \boldsymbol{E}(\boldsymbol{r},t)$ and $\boldsymbol{M}_{\boldsymbol{B}}(\boldsymbol{r},t) \propto \boldsymbol{B}(\boldsymbol{r},t)$ and we assume that the materials we are treating are isotropic. Thus, we introduce the constitutive relationship [34–36] of electric field displacement and the magnetizing field,

$$\boldsymbol{D}(\boldsymbol{r},t) = \varepsilon_0 \varepsilon \boldsymbol{E}(\boldsymbol{r},t), \tag{1.2}$$

and

$$\boldsymbol{B}(\boldsymbol{r},t) = \mu_0 \mu \boldsymbol{H}(\boldsymbol{r},t), \tag{1.3}$$

where ε and μ are the relative dielectric and relative magnetic permittivity of the medium, respectively.

For convenience, in this thesis, we treat the fields in the frequency domain, with $\boldsymbol{E}(\boldsymbol{r},\omega) = \int dt \boldsymbol{E}(\boldsymbol{r},t) e^{i\omega t}/(2\pi)$ and $\boldsymbol{B}(\boldsymbol{r},\omega) = \int dt \boldsymbol{B}(\boldsymbol{r},t) e^{i\omega t}/(2\pi)$, respectively, where ω is the (angular) frequency of light. Maxwell's equations (1.1) can then be

written as:

$$\begin{aligned}
&\nabla \times \boldsymbol{E}(\boldsymbol{r},\omega) = i\omega \boldsymbol{B}(\boldsymbol{r},\omega),\\
&\nabla \times \boldsymbol{H}(\boldsymbol{r},\omega) = \boldsymbol{J}_{\text{ext}}(\boldsymbol{r},\omega) + i\omega \boldsymbol{D}(\boldsymbol{r},\omega),\\
&\nabla \cdot \boldsymbol{D}(\boldsymbol{r},\omega) = \rho_{\text{ext}}(\boldsymbol{r},\omega),\\
&\nabla \cdot \boldsymbol{B}(\boldsymbol{r},\omega) = 0.
\end{aligned} \tag{1.4}$$

Furthermore, for all the systems studied in this thesis, we consider the case where there are no external currents or charges [37], *i.e.*, $\boldsymbol{J}_{\text{ext}} = 0$ and $\rho_{\text{ext}} = 0$, so that Eq. (1.4) simplifies to,

$$\begin{aligned}
&\nabla \times \boldsymbol{E}(\boldsymbol{r},\omega) = i\omega \boldsymbol{B}(\boldsymbol{r},\omega),\\
&\nabla \times \boldsymbol{B}(\boldsymbol{r},\omega) = i\omega \frac{\varepsilon_0 \varepsilon}{\mu_0 \mu} \boldsymbol{E}(\boldsymbol{r},\omega),\\
&\nabla \cdot \boldsymbol{D}(\boldsymbol{r},\omega) = 0,\\
&\nabla \cdot \boldsymbol{B}(\boldsymbol{r},\omega) = 0,
\end{aligned} \tag{1.5}$$

where we have also accounted for the constitutive relationship in Eqs. (1.2) and (1.3).

In 1901 the German mathematician Heinrich Weber reformulated Eq. (1.5) in vacuum ($\varepsilon = 1$ and $\mu = 1$) as [37]

$$\begin{aligned}
&i\frac{\partial \boldsymbol{F}_{\pm}(\boldsymbol{r},t)}{\partial t} = c_0 \nabla \times \boldsymbol{F}_{\pm}(\boldsymbol{r},t),\\
&\nabla \cdot \boldsymbol{F}_{\pm}(\boldsymbol{r},t) = 0,
\end{aligned} \tag{1.6}$$

where $c_0 = 1/\sqrt{\varepsilon_0 \mu_0}$ is the speed of light in vacuum and

$$\boldsymbol{F}_{\pm}(\boldsymbol{r},t) = \boldsymbol{E}(\boldsymbol{r},t) \pm i c_0 \boldsymbol{B}(\boldsymbol{r},t), \tag{1.7}$$

are the Riemann–Silberstein vectors named after the German mathematician Bernhard Riemann, who inspired Heinrich Weber to publish Eq. (1.6), and after the Polish-American physicist Ludwik Silberstein, who also published this equation independently of Weber's work in 1907 [38, 39].

Equation (1.6) can be easily written in the frequency domain,

$$\frac{\nabla \times}{k} \boldsymbol{F}_{\pm}(\boldsymbol{r},\omega) = \pm \boldsymbol{F}_{\pm}(\boldsymbol{r},\omega), \tag{1.8}$$

where

$$\boldsymbol{F}_{\pm}(\boldsymbol{r},\omega) = \boldsymbol{E}(\boldsymbol{r},\omega) \pm i c_0 \boldsymbol{B}(\boldsymbol{r},\omega), \tag{1.9}$$

and $k = \omega/c_0$ is the wavevector of light.

In this thesis, we mostly use the standard formulation in Eq. (1.5) that considers the electric and magnetic fields $\boldsymbol{E}$ and $\boldsymbol{B}$. However, we also discuss the advantages of the Riemann–Silberstein formalism (Eq. (1.8)) when treating light

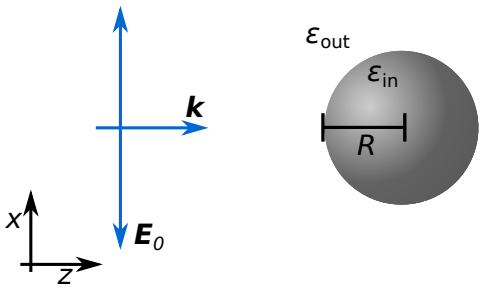

Figure 1.1: Scheme of the problem studied in subsections 1.2 and 1.3. A x-polarized plane wave that propagates along the z-axis interacts with a spherical nanoparticle of radius R. We have explicitly indicated the relative dielectric permittivity inside and outside the nanoparticle, ε_{in} and ε_{out}, respectively.

with well-defined angular momentum in section 1.4.

1.2 Electromagnetic response of very small objects

Throughout this thesis, we often calculate the electromagnetic response of very small objects, such as a small nanoparticle or a quantum emitter (QE, *e.g.*, a molecule, a quantum dot, or a nitrogen-vacancy center in diamond). This section discusses a very common approach to solving this problem: considering that the small object is excited (or polarized) by the illumination and behaves as a point-like electric dipole [35]. During this section we focus on describing the separate response of a nanoparticle and a QE. In chapter 3, we use the same framework introduced here to describe the response of a nanoparticle interacting with a QE.

This section is structured as follows: we first introduce, in subsection 1.2.1, the fields induced (or scattered) by a spherical nanoparticle under plane-wave illumination treated within the quasistatic approximation. Next, in subsection 1.2.2, we briefly formulate the response beyond this quasistatic approximation. In subsection 1.2.3, we use the framework developed in the previous subsections to illustrate the far-field spectral response of the nanoparticle. Finally, in subsection 1.2.4 we use a similar formalism to treat the response of a QE.

1.2.1 Response of a very small spherical nanoparticle within the quasistatic approximation

Near-field response

We first review the solution of the near fields induced (scattered) by a very small spherical nanoparticle of radius R much smaller than the wavelength of light λ. The material of the nanoparticle has a relative dielectric permittivity ε_{in} and the

medium outside the nanoparticle has a relative dielectric permittivity ε_{out}. We consider the particle to be illuminated by an incident plane wave of amplitude E_0, polarized along the x-axis, and propagating along the z-axis (Fig. 1.1). First, we consider that the particle is very small compared to the wavelength, and thus we can assume the electric field to be constant along the space. This is the so-called electrostatic approximation, within which the electromagnetic fields fulfill

$$\begin{aligned}
\nabla \times \boldsymbol{E}(\boldsymbol{r},\omega) &= 0,\\
\nabla \times \boldsymbol{H}(\boldsymbol{r},\omega) &= 0,\\
\nabla \cdot \boldsymbol{D}(\boldsymbol{r},\omega) &= 0,\\
\nabla \cdot \boldsymbol{B}(\boldsymbol{r},\omega) &= 0.
\end{aligned} \tag{1.10}$$

in the frequency domain, where we have already accounted for the absence of external currents or charges, *i.e.*, $\boldsymbol{J}_{\text{ext}} = 0$ and $\rho_{\text{ext}} = 0$.

To solve $\boldsymbol{E}$ in Eq. (1.10), we notice first that the rotational of the electric field is zero. Thus, we can write $\boldsymbol{E}$ as the gradient of a scalar function [35, 36, 40],

$$\boldsymbol{E}(\boldsymbol{r},\omega) = -\nabla V_E(\boldsymbol{r},\omega) \tag{1.11}$$

where the scalar function, V_E, is the electric or electrostatic potential. Using the standard constitutive relations [34–36] of the displacement vector ($\boldsymbol{D}(\boldsymbol{r},\omega) \propto \boldsymbol{E}(\boldsymbol{r},\omega)$) in Eq. (1.2), and $\nabla \cdot \boldsymbol{D}(\boldsymbol{r},\omega) = 0$ (in Eq. (1.10)) we find that V_E must satisfy Laplace equation,

$$\nabla^2 V_E(\boldsymbol{r},\omega) = 0. \tag{1.12}$$

The fields outside the nanoparticle include the incident plane wave and the fields scattered by the nanoparticle. However, we consider that the fields induced by the nanoparticle decay with the distance, and thus, far from the particle $\boldsymbol{E}_{\text{out}}$ reduces to the incident plane wave,

$$\lim_{\boldsymbol{r}\to\infty} \boldsymbol{E}_{\text{out}}(\boldsymbol{r},\omega) = E_0 \boldsymbol{u}_x, \tag{1.13}$$

with $E_0\boldsymbol{u}_x$ the electric field of the incident plane wave ($\boldsymbol{u}_x$ is the unity vector along the x-axis). The boundary conditions at the surface of the spherical nanoparticle, $\boldsymbol{R}$, are given by [35, 36],

$$\boldsymbol{n} \times [\boldsymbol{E}_{\text{out}}(\boldsymbol{R},\omega) - \boldsymbol{E}_{\text{in}}(\boldsymbol{R},\omega)] = 0, \tag{1.14}$$

and

$$\boldsymbol{n} \cdot [\boldsymbol{D}_{\text{out}}(\boldsymbol{R},\omega) - \boldsymbol{D}_{\text{in}}(\boldsymbol{R},\omega)] = 0. \tag{1.15}$$

The solution of Eqs. (1.12)-(1.15) is [36],

$$\boldsymbol{E}_{\text{in}}(\boldsymbol{r},\omega) = 4\pi\varepsilon_0 \frac{3\varepsilon_{\text{out}}(\omega)}{\varepsilon_{\text{out}}(\omega) + 2\varepsilon_{\text{in}}(\omega)} E_0 \boldsymbol{u}_z, \tag{1.16}$$

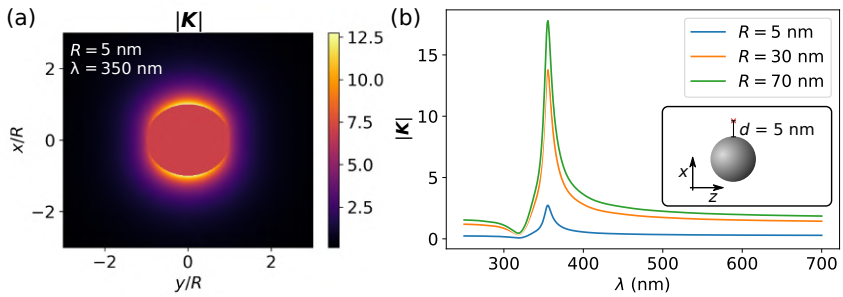

Figure 1.2: (a) Near-field distribution of a silver spherical nanoparticle of radius $R = 5$ nm. (b) Near-field enhancement factor $|K|$ as a function of the wavelength of an x-polarized incident plane wave. The enhancement factor is calculated at a distance $d = 5$ nm from the surface of the spherical nanoparticle along the x-axis (see inset). We calculate the enhancement factor for three silver spherical nanoparticles of different radius, $R = 5$ nm, (blue line) 30 nm, (orange line), and 70 nm (green line). The results in (a) and (b) are obtained using the electrostatic approximation introduced in subsection 1.2.1. The dielectric permittivity of silver used for these calculations is obtained from reference [41].

and

$$\boldsymbol{E}_{\text{out}}(\boldsymbol{r},\omega) = E_0\boldsymbol{u}_x + \underbrace{4\pi\varepsilon_0\frac{\varepsilon_{\text{in}}(\omega)-\varepsilon_{\text{out}}(\omega)}{\varepsilon_{\text{in}}(\omega)+2\varepsilon_{\text{out}}(\omega)}E_0\frac{R^3}{r_{\text{s}}^3}[3(\boldsymbol{u}_r\cdot\boldsymbol{u}_x)\boldsymbol{u}_r-\boldsymbol{u}_x]}_{\boldsymbol{E}_{\text{sca}}(\boldsymbol{r},\omega)}, \tag{1.17}$$

where r_{s} is the radial spherical coordinate (considering the center of the particle at $r_{\text{s}} = 0$), and $\boldsymbol{u}_r$ is the unity vector along the radial r_{s}-direction. $\boldsymbol{E}_{\text{sca}}(\boldsymbol{r},\omega)$ in Eq. (1.17) is the field induced (scattered) by the nanoparticle in its proximity. The induced fields thus depend on the ratio r_{s}/R. We discuss below that this equation is only valid for positions not too far from the nanoparticle.

Figure 1.2a shows the near-field distribution of the amplitude of the electric field enhancement factor, $|\boldsymbol{K}|$, in the surroundings of a silver nanoparticle of radius $R = 5$ nm illuminated at $\lambda = 350$ nm (we use the experimental values of the silver permittivity from reference [41]). The enhancement factor is defined as

$$|\boldsymbol{K}(\boldsymbol{r},\omega)| = \frac{|\boldsymbol{E}_{\text{sca}}(\boldsymbol{r},\omega)|}{E_0}, \tag{1.18}$$

for fields outside the particle ($|\boldsymbol{r}| > R$) or $|\boldsymbol{K}(\boldsymbol{r},\omega)| = |\boldsymbol{E}_{\text{in}}(\boldsymbol{r},\omega)|/E_0$ for fields inside the particle ($|\boldsymbol{r}| < R$). We can observe that the enhancement factor is of the order of ~ 10 in the immediate surroundings of the nanoparticle. In other words, there is a strong amplification of the fields illuminating the nanoparticle concentrated on the top and the bottom of the nanoparticle, following the polarization of the incident light.

Figure 1.2b shows the changes of $|\boldsymbol{K}|$ with the wavelength of the incident field,

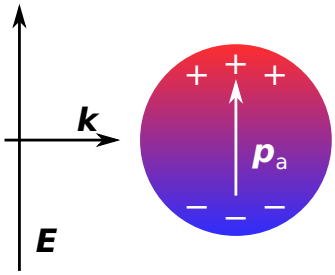

Figure 1.3: Snapshot of the response of plasmonic resonance. An incident field induces a charge polarization at a metallic nanoparticle by displacing the electron gas of the metal along the axis of polarization of the incident electric field $\boldsymbol{E}$. The electrons are displaced to one region at a given time, causing a negative charge distribution in that region. On the opposite side of the nanoparticle, the absence of electrons causes a positive charge distribution. The difference in charge between these two regions induces an electric dipole moment $\boldsymbol{p}_a$. The charges and the corresponding dipole moment oscillate at the frequency of the incident field.

λ. Specifically, we evaluate $|\boldsymbol{K}|$ at a distance $d = 5$ nm (along the x-axis, see inset in the pannel) from the surface of silver spherical nanoparticles of different radius $R = 5$ nm, 30 nm, and 70 nm (blue, orange, and green lines, respectively). The spectra for these three values of R show a peak at approximately $\lambda \approx 350$ nm. The strength of the peak diminishes with decreasing radius because, within the quasistatic approximation, $|\boldsymbol{K}|$ outside of the nanoparticle is proportional to $R^3/(R+d)^3$ (Eq. (1.17)). As we discuss in sections 1.2.2 and 1.3, these quasistatic results for $R = 30$ nm, and especially for $R = 70$ nm, are significantly modified when considering more accurate descriptions or the exact solution. Thus, the quasistatic approximation is very useful to gain insights into the plasmonic response, but it is only really accurate for the smallest nanoparticle ($R = 5$ nm) considered in Fig. 1.2b.

Plasmonic resonances

The peak in the enhancement factor at $\lambda \approx 350$ nm shown in Fig. 1.2b corresponds to the excitation of an optical resonance of the nanoparticle. Optical resonances show different characters depending on the material. We consider here a metallic nanoparticle that supports localized surface plasmon resonances (or just plasmonic resonances in the following); hence, metallic nanoparticles are often called plasmonic nanoparticles.

The plasmonic resonance sustains a collective oscillation of the free-electron gas of the metal. In this particular situation, the illuminating plane wave displaces the electrons to one single side of the nanoparticle so that, at a given time, a negative charge accumulates in this region and a positive charge distribution (or absence of negative charges) accumulates in the opposite region. Thus, the nanoparticle experiences an induced electric dipole moment $\boldsymbol{p}_a$, as sketched in Fig. 1.3. Due to the oscillatory behavior of the electromagnetic waves, the electric field causes a

back-and-forth displacement of the electron gas of the metal, which is maximized for a resonant frequency given by the electron density and the geometrical boundary conditions of the nanoparticle.

Within the quasistatic approximation, we can obtain the frequency of the plasmonic resonance of a small spherical particle from the minimization of $\varepsilon_{\rm in}(\omega)+2\varepsilon_{\rm out}(\omega)$, the denominator of $\boldsymbol{E}_{\rm sca}$. In this section we use the experimental values of the silver permittivity [41] to obtain $\varepsilon_{\rm in}$. However, it is instructive to analytically obtain $\varepsilon_{\rm in}(\omega)$ by using a modified Drude expression to describe the material of the particle,

$$\varepsilon_{\rm in}^{\rm MD}(\omega)=\varepsilon_\infty-\frac{\omega_p^2}{\omega(\omega+i\kappa)}, \tag{1.19}$$

where ε_∞ is a constant that accounts for the influence of the d-electrons to the permittivity (in the original Drude model $\varepsilon_\infty=1$), ω_p is the plasma frequency of the metal, and κ is the plasmon damping rate. Using Eq. (1.19) we find that for a spherical nanoparticle in a vacuum, the plasmonic resonant frequency is $\omega_0=\omega_p/\sqrt{\varepsilon_\infty+2}$. For example, if we use the Drude values for silver [41], $\varepsilon_\infty=6$ and $\hbar\omega_p=9.17$ eV (with $\hbar$ the reduced Plank constant) we obtain $\hbar\omega_0\approx 3.24$ eV, equivalent to a resonant wavelength $\lambda_0\approx 388.67$ nm, in good agreement with the resonant frequency obtained in Fig. 1.2a (for the experimental values of the permittivity).

Beyond the near-field contribution

Next, we improve our description by accounting for the fields scattered by the nanoparticle. With this purpose, we calculate the fields induced at the nanoparticle with Eq. (1.16), which allows for obtaining the induced dipole moment $\boldsymbol{p}_{\rm a}$. However, once we calculate the value of $\boldsymbol{p}_{\rm a}$, we take into account that this dipole is oscillating and calculate the fields emitted by such a source (the fields outside the nanoparticle) from the exact solution to Maxwell's equations. The fields emitted by the oscillating point-like electric dipole can be obtained using the Green's function formalism (see chapters 2 and 8 in reference [35]). Within this description, the external field generated by the dipolar excitation induced at the nanoparticle is

$$\boldsymbol{E}_{\rm sca}(\boldsymbol{r},\omega)=\overleftrightarrow{\boldsymbol{G}}(\boldsymbol{r},\boldsymbol{r}_0,\omega)\boldsymbol{p}_{\rm a}(\omega) \tag{1.20}$$

where

$$\overleftrightarrow{\boldsymbol{G}}(\boldsymbol{r},\boldsymbol{r}_0,\omega)=\overleftrightarrow{\boldsymbol{G}}^{\rm NF}(\boldsymbol{r},\boldsymbol{r}_0,\omega)+\overleftrightarrow{\boldsymbol{G}}^{\rm IF}(\boldsymbol{r},\boldsymbol{r}_0,\omega)+\overleftrightarrow{\boldsymbol{G}}^{\rm FF}(\boldsymbol{r},\boldsymbol{r}_0,\omega) \tag{1.21}$$

with

$$\overleftrightarrow{\boldsymbol{G}}^{\rm NF}(\boldsymbol{r},\boldsymbol{r}_0,\omega)=-\omega^2\mu_0\frac{e^{ik|\boldsymbol{v}_r|}}{4\pi k^2|\boldsymbol{v}_r|^3}\left[\overleftrightarrow{\mathbb{1}}-3\frac{\boldsymbol{v}_r\otimes\boldsymbol{v}_r}{|\boldsymbol{v}_r|^2}\right], \tag{1.22}$$

$$\overleftrightarrow{\boldsymbol{G}}^{\rm IF}(\boldsymbol{r},\boldsymbol{r}_0,\omega)=i\omega^2\mu_0\frac{e^{ik|\boldsymbol{v}_r|}}{4\pi k^2|\boldsymbol{v}_r|^2}\left[\overleftrightarrow{\mathbb{1}}-3\frac{\boldsymbol{v}_r\otimes\boldsymbol{v}_r}{|\boldsymbol{v}_r|^2}\right], \tag{1.23}$$

and

$$\overleftrightarrow{\boldsymbol{G}}^{\mathrm{FF}}(\boldsymbol{r},\boldsymbol{r}_0,\omega)=\omega^2\mu_0\frac{e^{ik|\boldsymbol{v}_r|}}{4\pi k^2|\boldsymbol{v}_r|}\left[\overleftrightarrow{\mathbb{1}}-\frac{\boldsymbol{v}_r\otimes\boldsymbol{v}_r}{|\boldsymbol{v}_r|^2}\right]. \tag{1.24}$$

In Eqs. (1.22)-(1.24) $\overleftrightarrow{\mathbb{1}}$ is the tensorial identity matrix, $\boldsymbol{v}_r=\boldsymbol{r}-\boldsymbol{r}_0$, and $\otimes$ denotes the outer product. $\overleftrightarrow{\boldsymbol{G}}$ in Eq. (1.21) is decomposed into three contributions, $\overleftrightarrow{\boldsymbol{G}}^{\mathrm{NF}}$, $\overleftrightarrow{\boldsymbol{G}}^{\mathrm{IF}}$, and $\overleftrightarrow{\boldsymbol{G}}^{\mathrm{FF}}$, which describe the field generated by the dipole in the near-field region ($r\lesssim\lambda$), intermediate-field region, and far-field region ($r\gg\lambda$), respectively.

Further, using Eq. (1.20), Maxwell's equations Eq. (1.5), and the constitutive relation in Eq. (1.3), we can obtain the expression of the magnetizing field generated by an oscillating point-like electric dipole in terms of $\overleftrightarrow{\boldsymbol{G}}$ [35, 36],

$$\boldsymbol{H}_{\mathrm{sca}}(\boldsymbol{r},\omega)=\frac{-i}{\omega\mu_{\mathrm{out}}\mu_0}[\nabla\times\overleftrightarrow{\boldsymbol{G}}(\boldsymbol{r},\boldsymbol{r}_0,\omega)]\boldsymbol{p}_{\mathrm{a}}(\omega). \tag{1.25}$$

Induced dipole moment of a small spherical nanoparticle

We next discuss how to obtain the values of $\boldsymbol{p}_{\mathrm{a}}$ by comparing the expression of the field scattered by the nanoparticle, $\boldsymbol{E}_{\mathrm{sca}}$, as given in Eq. (1.17) with those obtained with the Green's function formalism (Eq. (1.20)). For the latter, we only consider the near-field contribution to the Green's function (Eq. (1.22)) and neglect the oscillation in the propagation of the fields (*i.e.,* we make $e^{ikz}=1$ in Eq. (1.22)). Equation (1.20) then becomes,

$$\boldsymbol{E}_{\mathrm{sca}}(\boldsymbol{r},\omega)=\overleftrightarrow{\boldsymbol{G}}^{\mathrm{qs}}(\boldsymbol{r},\boldsymbol{r}_0=0)\boldsymbol{p}_{\mathrm{a}}(\omega), \tag{1.26}$$

where $\overleftrightarrow{\boldsymbol{G}}^{\mathrm{qs}}$ is the quasistatic Green's function,

$$\overleftrightarrow{\boldsymbol{G}}^{\mathrm{qs}}(\boldsymbol{r},\boldsymbol{r}_0=0)=-\frac{1}{4\pi\varepsilon_0|\boldsymbol{r}|^3}\left[\overleftrightarrow{\mathbb{1}}-3(\boldsymbol{u}_r\otimes\boldsymbol{u}_r)\right], \tag{1.27}$$

and we have set the center of the spherical coordinates to the center of coordinates ($\boldsymbol{r}_0=0$). Comparing Eq. (1.26) with Eq. (1.17) indicate that the induced electric dipole moment $\boldsymbol{p}_{\mathrm{a}}$ is given by,

$$\boldsymbol{p}_{\mathrm{a}}(\omega)=\alpha_{\mathrm{a}}(\omega)E_0\boldsymbol{u}_x, \tag{1.28}$$

with

$$\alpha_{\mathrm{a}}=\frac{\varepsilon_{\mathrm{in}}(\omega)-\varepsilon_{\mathrm{out}}(\omega)}{2\varepsilon_{\mathrm{out}}(\omega)+\varepsilon_{\mathrm{in}}(\omega)}4\pi\varepsilon_0R^3, \tag{1.29}$$

the quasistatic polarizability of the nanoparticle.

Once $\boldsymbol{p}_{\mathrm{a}}$ is known, we obtain the fields outside the spherical nanoparticle by directly applying Eq. (1.20) (with the full Green's function $\overleftrightarrow{\boldsymbol{G}}$). The fields obtained in this way are very similar to those given by Eq. (1.17) near the nanoparticle, but they reproduce better the exact result for large distances. Last, to obtain the fields induced very far from the nanoparticle (scattered far-field $\boldsymbol{E}_{\mathrm{sca}}^{\mathrm{FF}}$), only the

far-field component of the Green's function $\overleftrightarrow{\boldsymbol{G}}^{\mathrm{FF}}$ (which decays more slowly with increasing r_{s}) needs to be considered:

$$\boldsymbol{E}_{\mathrm{sca}}^{\mathrm{FF}}(\boldsymbol{r},\omega)(\boldsymbol{r},\omega) = \overleftrightarrow{\boldsymbol{G}}^{\mathrm{FF}}(\boldsymbol{r},\boldsymbol{r}_0=0,\omega)\boldsymbol{p}_{\mathrm{a}}(\omega). \tag{1.30}$$

1.2.2 Radiative-corrected model

The quasistatic model presented so far can reproduce the optical response of very small metallic nanoparticles (much smaller than the wavelength of the incident light). However, beyond the quasistatic approximation, one needs to include further effects related to the oscillatory evolution of the electric and magnetic fields (and thus, of the induced dipole moment of the nanoparticle, $\boldsymbol{p}_{\mathrm{a}}(t) \propto e^{-i\omega t}$. Next, we explore how this oscillatory behavior directly affects the polarizability and response of the nanoparticle. Specifically, we consider in this section the effect that the electromagnetic field created by the moving (oscillating) charges of the $\boldsymbol{p}_{\mathrm{a}}$ dipole exerts on itself. This correction is usually called as radiative correction, radiation reaction, or radiation damping because the main effect of this correction is to introduce an increase in the losses (or broadening) of the plasmonic resonance. This correction is based on the radiation reaction force $\boldsymbol{F}_{\mathrm{AL}}$ (also called Abraham-Lorentz force) that describes the force on a charged particle at position $\boldsymbol{r}_{\mathrm{a}}$ with acceleration $\partial^2\boldsymbol{r}_{\mathrm{a}}/\partial t^2$ caused by the same charged particle [35,36],

$$\boldsymbol{F}_{\mathrm{AL}}(t) = \frac{q_{\mathrm{a}}}{6\pi\varepsilon_0 c^3}\frac{\partial^3\boldsymbol{p}_{\mathrm{a}}(t)}{\partial t^3}, \tag{1.31}$$

where, we have modeled the electric dipole of the particle as a single charged particle q_{a} placed at $\boldsymbol{r}_{\mathrm{a}}$ and oscillating in time ($\boldsymbol{r}_{\mathrm{a}}(t) \propto e^{-i\omega t}$).

In the frequency domain Eq. (1.31) becomes,

$$\boldsymbol{F}_{\mathrm{AL}}(\omega) = \frac{ik^3}{6\pi\varepsilon_0}\boldsymbol{p}_{\mathrm{a}}(\omega)q_a. \tag{1.32}$$

This equation can also be written as $\boldsymbol{F}_{\mathrm{AL}}\omega) = q_{\mathrm{a}}\boldsymbol{E}_{\mathrm{Self}}(\boldsymbol{r}_{\mathrm{a}},\omega)$, the force experienced by the charge q_{a} under the field $\boldsymbol{E}_{\mathrm{Self}}$ that the nanoparticle exerts on itself. We then obtain,

$$\boldsymbol{E}_{\mathrm{Self}}(\boldsymbol{r}_{\mathrm{a}},\omega) = \frac{ik^3}{6\pi\varepsilon_0}\boldsymbol{p}_{\mathrm{a}}(\omega), \tag{1.33}$$

Thus, the induced dipole moment by both the external field $\boldsymbol{E}_0$ and $\boldsymbol{E}_{\mathrm{Self}}$ can be expressed as

$$\boldsymbol{p}_{\mathrm{a}}(\omega) = \alpha_{\mathrm{a}}(\omega)(\boldsymbol{E}_0(\boldsymbol{r}_{\mathrm{a}},\omega) + \boldsymbol{E}_{\mathrm{Self}}(\boldsymbol{r}_{\mathrm{a}},\omega)). \tag{1.34}$$

We then substitute Eq. (1.33) into Eq. (1.34) and obtain,

$$\left(1 - i\alpha_{\mathrm{a}}(\omega)\frac{k^3}{6\pi\varepsilon_0}\right)\boldsymbol{p}_{\mathrm{a}}(\omega) = \alpha_{\mathrm{a}}(\omega)\boldsymbol{E}_0(\boldsymbol{r}_{\mathrm{a}},\omega) \rightarrow \boldsymbol{p}_{\mathrm{a}}(\omega) = \alpha_{\mathrm{a}}^{\mathrm{RC}}(\omega)\boldsymbol{E}_0(\boldsymbol{r}_{\mathrm{a}},\omega), \tag{1.35}$$

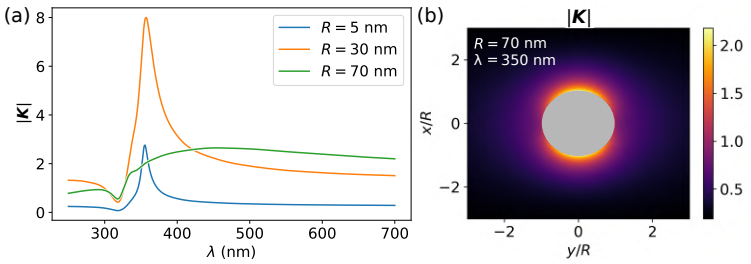

Figure 1.4: (a) Near-field enhancement factor $|K|$ as a function of the wavelength of the z-polarized incident plane wave. The enhancement factor is calculated at a distance $d = 5$ nm from the surface of a spherical nanoparticle. We calculate the enhancement factor for three silver spherical nanoparticles of different radius, $R = 5$ nm, 30 nm, and 70 nm (see labels in the figure). (b) Near-field distribution of a silver spherical nanoparticle with radius $R = 70$ nm. The results in (a) and (b) are obtained using the radiative-corrected model introduced in subsection 1.2.2. The dielectric permittivity of silver used for these calculations is obtained from reference [41].

where we define an effective, radiative-corrected polarizability,

$$\alpha_{\mathrm{a}}^{\mathrm{RC}}(\omega) = \frac{\alpha_{\mathrm{a}}(\omega)}{1 - i\alpha_{\mathrm{a}}(\omega)\frac{k^3}{6\pi\varepsilon_0}}. \tag{1.36}$$

The response of the system can now be evaluated by substituting $\boldsymbol{p}_{\mathrm{a}}(\omega) = \alpha_{\mathrm{a}}(\omega)\boldsymbol{E}_0(\omega)$ by $\boldsymbol{p}_{\mathrm{a}}(\omega) = \alpha_{\mathrm{a}}^{\mathrm{RC}}(\omega)\boldsymbol{E}_0(\omega)$ in Eq. (1.20). We evaluate the radiative-correction by analyzing again the response of silver spherical nanoparticles under the illumination of a z-propagating, x-polarized plane wave. Figure 1.4a shows the amplitude of the near-field enhancement $|\boldsymbol{K}|$ as a function of the wavelength λ of the incident plane wave. We calculate the enhancement at a distance $d = 5$ nm along the x-axis from the surface of a silver spherical nanoparticle of different radius $R = 5$ nm, 30 nm, and 70 nm (see inset in Fig. 1.2b). In this case the enhancement factor is obtained by evaluating $\boldsymbol{E}_{\mathrm{sca}}$ in Eq. (1.20) with $\boldsymbol{p}_{\mathrm{a}}$, the induced dipole moment of the spherical nanoparticle (Eq. (1.34)) and taking into account the radiative correction (Eq. (1.36)). By comparing this figure with the results shown in Fig. 1.2a (calculated in the quasistatic approximation) we can observe that the importance of the radiative correction clearly depends on the radius R. For the smallest radius considered, $R = 5$ nm, (blue line in the figure), the enhancement factor is almost identical to the one in the quasistatic approximation.

On the other hand, comparing the enhancement spectrum for the intermediate situation of $R = 30$ nm radius (orange line) within both approximations, we find a qualitative agreement in the enhancement spectrum, but with some significant quantitative differences. For example, comparing the radiative corrected model (Fig. 1.4) to the quasistatic approximated results (Fig. 1.2), we find that (in the radiative corrected model) the maximum enhancement is reduced by (approximately) half, and the peak in the enhancement spectra is slightly broadened and red-shifted

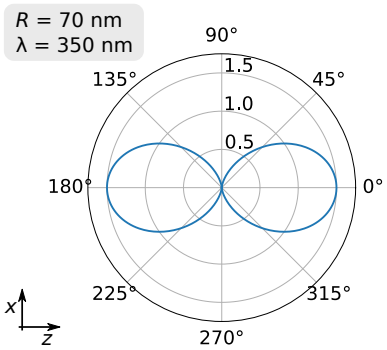

Figure 1.5: Far-field directivity of a $R = 70$ nm radius silver nanoparticle illuminated by a x-polarized plane wave propagating along the z-direction with $\lambda = 350$ nm. The results are obtained within the quasistatic approximation (using Eqs. (1.20), (1.35), and (1.36)). The directivity is shown for different θ_s-angles along the xz-plane.

towards $\lambda \approx 380$ nm.

Last, for the largest radius considered, $R = 70$ nm, the maximum enhancement factor spectra obtained with the quasistatic approximation (Fig. 1.2b) is almost an order of magnitude larger than the result in Fig. 1.4a. The main cause for this effect is the radiative correction, which according to Eqs. (1.29) and (1.36) scales with R^3. Similar to the $R = 30$ nm case, the radiative correction not only causes a decrease in the maximum enhancement, but it broadens the enhancement peak, and induces a red-shift in the response. Without the radiative correction, the peak of the $R = 70$ nm nanoparticle was centered at $\lambda \approx 350$ nm, and with the radiative correction, it is centered at $\lambda \approx 450$ nm. We show in section 1.3 that the radiative-corrected model captures the main changes of the lowest-energy resonance with increasing radius but becomes inaccurate as R increases and does not capture some phenomena as the excitation of higher order resonances.

Figure 1.4b shows the enhancement factor distribution for a silver spherical nanoparticle of radius $R = 70$ nm illuminated at $\lambda = 350$ nm (we only evaluate the scattered fields outside the nanoparticle). The enhancement is significantly reduced within the radiative corrected model, but the region of stronger fields is still localized near the nanoparticle in a very similar way to the quasistatic solution (Fig. 1.2a).

Far-field emission

Next, we evaluate the fields scattered by the nanoparticle in the far-field region ($r \gg \lambda$) within the radiative-corrected model. Figure 1.5 shows the far-field directivity for a $R = 70$ nm silver spherical nanoparticle illuminated at $\lambda = 350$ nm by the same x-polarized, z-propagating plane wave. The directivity is defined

as [42]

$$D_{\mathrm{a}}(\phi_{\mathrm{s}},\theta_{\mathrm{s}}) = \frac{4\pi}{\oiint |\boldsymbol{E}^{FF}_{\mathrm{sca}}(r_{\mathrm{s}},\phi_{\mathrm{s}},\theta_{\mathrm{s}},\omega)|^2 d\Omega} |\boldsymbol{E}^{FF}_{\mathrm{sca}}(r_{\mathrm{s}},\phi_{\mathrm{s}},\theta_{\mathrm{s}},\omega)|^2, \tag{1.37}$$

with $r_{\mathrm{s}} \gg \lambda$ (in the far-field). D_{a} describes the emission of the fields in a $(\theta_{\mathrm{s}},\varphi_{\mathrm{s}})$ direction (in this case, we only show the dependence on θ_{s} because the emission is φ_{s}-symmetric). The directivity pattern in Fig. 1.5 shows two lobes oriented along the z-axis, where the far-field emission of the nanoparticle is maximized. Interestingly, these lobes are oriented along the direction of propagation of the incident plane wave, contrary to the near-fields generated by the nanoparticle, which are concentrated along the x-axis (polarization of the incident plane wave).

1.2.3 Optical cross-sections of a small particle

The radiative corrected model introduced in this section allows us to obtain the far-field response of a spherical nanoparticle excited by a linearly polarized plane wave of amplitude E_0. The far-field spectral response of nanostructures is usually characterized by three different quantities: the absorption cross-section σ_{abs}, the scattering cross-section σ_{sca}, and the extinction cross-section σ_{ext}. The absorption cross-section can be related to the power dissipated by the nanoparticle, P_{abs}, as $P_{\mathrm{abs}}(\omega) = \sigma_{\mathrm{abs}}(\omega) I_0$, where I_0 is the intensity of the incident light. On the other hand, the scattering cross section relates to the power of the light elastically scattered in all directions by the nanoparticle as $P_{\mathrm{sca}}(\omega) = \sigma_{\mathrm{sca}}(\omega) I_0$. Finally, the extinction cross-section corresponds to the sum of the absorption and scattering cross-sections, $\sigma_{\mathrm{ext}}(\omega) = \sigma_{\mathrm{sca}}(\omega) + \sigma_{\mathrm{abs}}(\omega)$, and describes the total power extincted: $P_{\mathrm{ext}}(\omega) = \sigma_{\mathrm{ext}}(\omega) I_0$. In this section we introduce all the optical cross sections for a particle in a vacuum, and the extension to other non-dissipating and linear media is straightforward.

The power scattered by a nanoparticle can be obtained according to Poynting's theorem [35, 36, 43] as,

$$P_{\mathrm{sca}}(\omega) = \iint_{\mathcal{A}} \bar{\boldsymbol{S}}_{\mathrm{sca}}(\boldsymbol{r},\omega) \cdot \boldsymbol{n}_{\mathcal{A}} d\mathcal{A}, \tag{1.38}$$

where $\mathcal{A}$ is an arbitrary closed area surrounding the dipole, $\boldsymbol{n}_{\mathcal{A}}$ is the normal vector to this surface at each surface point, and

$$\bar{\boldsymbol{S}}_{\mathrm{sca}}(\boldsymbol{r},\omega) = \frac{1}{2}\mathrm{Re}\{\boldsymbol{E}_{\mathrm{sca}}(\boldsymbol{r},\omega) \times \boldsymbol{H}_{\mathrm{sca}}(\boldsymbol{r},\omega)^*\} \tag{1.39}$$

is the time-averaged Poynting vector of the scattered electromagnetic fields. Using $\sigma_{\mathrm{sca}}(\omega) = P_{\mathrm{sca}}(\omega)/I_0$, the expressions of $\boldsymbol{E}_{\mathrm{sca}}$ and $\boldsymbol{H}_{\mathrm{sca}}$ in Eqs. (1.20)-(1.25), and $\boldsymbol{p}_{\mathrm{a}}(\omega) = \alpha^{\mathrm{RC}}_{\mathrm{a}}(\omega) E_0$, we obtain

$$\sigma_{\mathrm{sca}}(\omega) = \frac{k^4}{6\pi\varepsilon_0} |\alpha^{\mathrm{RC}}_{\mathrm{a}}(\omega)|^2. \tag{1.40}$$

The extinction cross-section, σ_{ext}, can be directly obtained by using the optical theorem for a system driven by a linearly x-polarized plane wave propagating along z. The optical theorem relates σ_{ext} with the x-component of the field scattered by the nanoparticle at some point $z_{\text{d}} \gg \lambda$ (far-field) along the z-axis [36, 40, 44],

$$\sigma_{\text{ext}}(\omega) = 2\lambda \text{Im}\left\{ z_{\text{d}} \frac{\boldsymbol{E}_{\text{sca}}(z_d, \omega) \cdot \boldsymbol{u}_x}{\boldsymbol{E}_0(z_d, \omega) \cdot \boldsymbol{u}_x} \right\}, \tag{1.41}$$

where $\boldsymbol{u}_x$ is the unity vector along the x-axis. By using Eqs. (1.20), (1.35), (1.36), and (1.41) we obtain,

$$\sigma_{\text{ext}}(\omega) = \frac{k}{\varepsilon_0} \text{Im}\{\alpha_{\text{a}}^{\text{RC}}(\omega)\}. \tag{1.42}$$

Note that we have written σ_{sca} and σ_{ext} in Eqs. (1.40) and (1.42) in terms of the radiative-corrected polarizability, but an equivalent expression can be found for the quasistatic approximated model, by considering the quasistatic polarizability α_{a} given in Eq. (1.29) instead of $\alpha_{\text{a}}^{\text{RC}}$.

Last, the absorption cross-section can be obtained from the extinction cross-section as

$$\sigma_{\text{abs}}(\omega) = \sigma_{\text{ext}}(\omega) - \sigma_{\text{sca}}(\omega). \tag{1.43}$$

Figure 1.6 shows the evaluation of the absorption (red lines), extinction (black lines), and scattering (blue lines) cross-sections spectra for silver spherical nanoparticles of different radius. All cross-sections spectra are normalized to πR^2, the area of the geometrical cross-section of the spherical nanoparticle ($\sigma(\omega)/(\pi R^2)$ is also called the efficiency factor. Figures 1.6(a), (c), and (e) are obtained considering the radiative corrected polarizability, and Figs. 1.6 (b), (d), and (f) are obtained using the quasistatic polarizability, *i.e.*, substituting $\alpha_{\text{a}}^{\text{RC}}$ (Eq. (1.36)) by α_{a} (Eq. (1.29)) in Eqs. (1.40) and (1.42).

Similarly to the near-field enhancement spectra in Figs. 1.2b and 1.4a, the extinction cross-section spectrum of the nanoparticles is dominated by a single peak corresponding to the excitation of a dipolar plasmonic resonance of the nanoparticle. This peak redshifts and broadens for increasing radius, similarly to the near-field enhancement spectra (Fig. 1.4a).

For the smallest radius considered, $R = 5$ nm, in Fig. 1.6(a), the total extinction cross-section (black line) is mostly dominated by the absorption (red line), and the scattering cross-section (blue line) is almost negligible. The weak contribution from the scattering can be understood from the quasistatic expressions. In this approximation, the polarizability of the nanoparticle follows Eq. (1.29), and thus, scales as $\propto R^3$. As a consequence, σ_{sca} in Eq. (1.40) scales as $\propto R^6$ and σ_{ext} in Eq. (1.42) as $\propto R^3$. For small values of R, σ_{ext} is thus much larger than σ_{sca} ($R^3 \gg R^6$). On the other hand, σ_{sca} grows much faster than σ_{abs} with increasing R (even if the R^6 scaling is not valid once the radiative correction becomes large). In fact, for the intermediate $R = 30$ nm radius (Fig. 1.6c), the values of the scattering (blue line) become comparable to the absorption (red line) cross-section. Further, the extinction cross-section spectrum for the $R = 70$ nm case in Fig. 1.6e is dominated

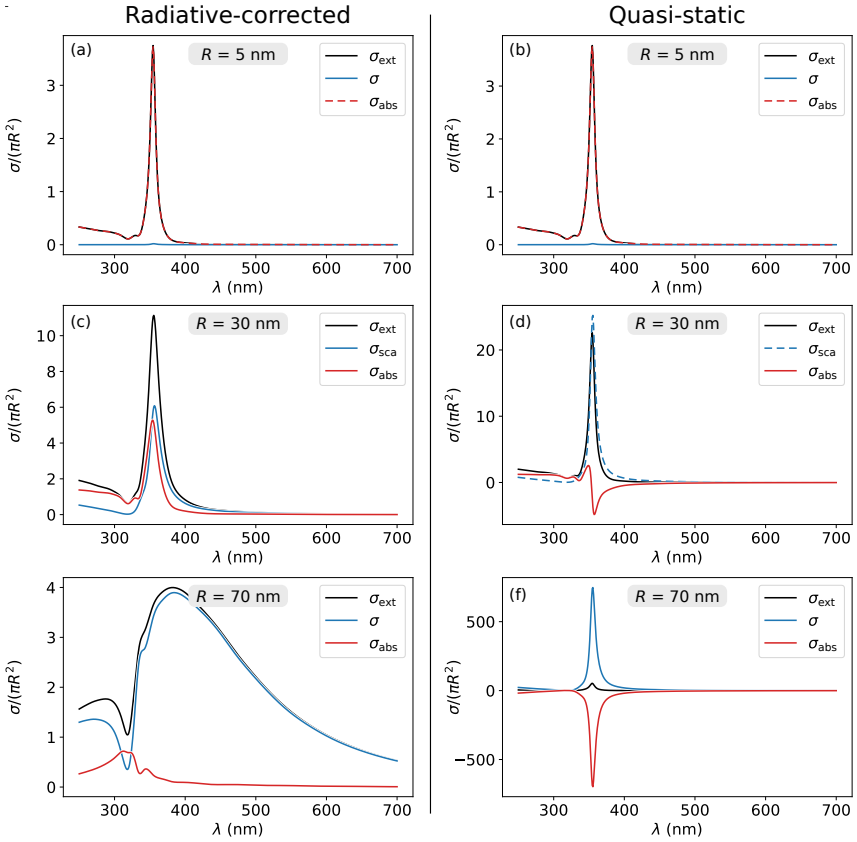

Figure 1.6: Absorption (red lines), extinction (black lines), and scattering (blue lines) cross section spectra for silver spherical nanoparticles with different radius. The cross-section spectra are calculated using the model presented in section 1.2. Figures (a), (c), and (e) are obtained considering the radiative correction of the polarizability of the nanoparticle, and figures (b), (d), and (f) ignore this radiative correction. Figures (a)-(b), (c)-(d), and (e)-(f) show the cross-section spectra for a silver spherical nanoparticle of radius $R = 5$, 30, and 70 nm, respectively. The cross-sections are normalized to πR^2, the area of a circle with the same radius of the spherical nanoparticle. The dielectric permittivity of silver used for these calculations is obtained from reference [41].

by the scattering contribution.

By comparing these results with the ones obtained with the quasistatic approximation, we find that there is a very good agreement for the $R = 5$ nm nanoparticle (compare Figs. 1.6 a and b). However, for the larger $R = 30$ nm and $R = 70$ nm the quasistatic approximation breaks, similar to the results for the enhancement spectra in Figs. 1.2b and 1.4a. Most notably, the quasitatic results for $R = 30$ nm and $R = 70$ nm (in Figs. 1.6 d and f, respectively) show unphysical negative values of the absorption cross-section spectra, which violates

the conservation of energy.

1.2.4 Response of a quantum emitter

In the previous sections we have discussed the response of a very small spherical nanoparticle, but a similar approach can also be valid to describe the electromagnetic response of a quantum emitter (QE), such as a molecule, a quantum dot, or a nitrogen-vacancy center in a diamond. The electromagnetic response of the QE can also be described as an oscillating electric point-like dipole, $\boldsymbol{p}_{\mathrm{e}}$. In this situation, $\boldsymbol{p}_{\mathrm{e}}$ represents the effect of exciting the transition between the two lowest energetic level systems of the QE (the ground state, and the first excited state), energetically separated by $\hbar\omega_\sigma$[i]. If an external field $\boldsymbol{E}_{\mathrm{ext}}$ drives the QE with a frequency close to ω_σ, the first excited state becomes populated (or excited). Then, after an average relaxation time τ_{r}, the excitation stored in the excited state decays to the ground state by emitting a photon with average frequency ω_σ. Thus, the response of the QE can be modeled by treating its electric dipole moment as a damped harmonic oscillator with damping rate γ,

$$\frac{\partial^2}{\partial t^2}\boldsymbol{p}_{\mathrm{e}}(t)+\gamma\frac{\partial}{\partial t}\boldsymbol{p}_{\mathrm{e}}(t)+\omega_\sigma^2\boldsymbol{p}_{\mathrm{e}}(t)=A_{\mathrm{e}}\boldsymbol{E}_{\mathrm{ext}}(t), \tag{1.44}$$

where $A_{\mathrm{e}}=2\omega_\sigma f_0^2/\hbar$, and f_0 is the oscillator strength [35].

Equation (1.44) can be rewritten in the frequency domain (considering that $\boldsymbol{p}_{\mathrm{e}}(t)\propto e^{-i\omega t}$, see discussion of Eq. (1.4)) as

$$\boldsymbol{p}_{\mathrm{e}}(\omega)=\alpha_{\mathrm{e}}(\omega)\boldsymbol{E}_{\mathrm{ext}}(\omega) \tag{1.45}$$

with

$$\alpha_{\mathrm{e}}(\omega)=\frac{A_{\mathrm{e}}}{\omega_\sigma^2-\omega^2-i\gamma\omega}, \tag{1.46}$$

the polarizability of the QE.

The decay rate γ of the QE in this equation can be decomposed as $\gamma=\gamma_0+\gamma_{\mathrm{intr}}$, which account for the radiative or spontaneous decay rate of the QE, γ_0, (due to the emission of photons) and for intrinsic non-radiative losses, γ_{intr} (due to the decay of the QE without emitting photons). γ_0 can be obtained from a quantum electrodynamic description of the coupling of the QE with the vacuum fields [35], resulting in

$$\gamma_0=\frac{\omega_\sigma^3 f_0^2}{3\hbar\pi c_0^3} \tag{1.47}$$

[i] To approximate the response of the QE as the response of an electric point-like dipole we are also considering four additional conditions satisfied in common set-ups: (i) The energy difference between the higher-energetic states (beyond the first excited state) and the ground state is much larger than the energy difference between the ground state and the first excited state. (ii) Light driving the QE has a similar frequency or the two-level transition ω_σ, and thus, it does not drive higher-energetic states. (iii) Light driving the QE is not confined in effective volumes smaller than the size of the QE. (iv) The intensity of the field driving the QE is small enough to avoid non-linear effects.

Interestingly, this value can also be obtained by considering a QE without losses and applying the radiative correction discussed in subsection 1.2.2. The polarizability of a lossless QE corresponds to considering $\gamma = 0$ in Eq. (1.46),

$$\alpha_{\mathrm{e}}^{0}(\omega) = \frac{A_{\mathrm{e}}}{\omega_\sigma^2 - \omega^2}. \tag{1.48}$$

Using the radiative-correction formula (Eq. (1.36)) we obtain,

$$\begin{aligned}&\alpha_{\mathrm{e}}^{0-\mathrm{RC}}(\omega) = \\ &= \alpha_{\mathrm{e}}^{0}(\omega)\frac{1}{1 - i\frac{\omega^3}{6\pi\varepsilon_0 c_0^3}\alpha_{\mathrm{e}}^{0}(\omega)} = \frac{A_{\mathrm{e}}}{\omega_\sigma^2 - \omega^2 - i\frac{\omega^3}{6\pi\varepsilon_0 c_0^3}A_{\mathrm{e}}} \approx \frac{A_{\mathrm{e}}}{\omega_\sigma^2 - \omega^2 - i\omega\frac{\omega_\sigma^3 f_0^2}{3\hbar\pi c_0^3}},\end{aligned} \tag{1.49}$$

where in the last step we have approximated $\omega^3 \approx \omega\omega_\sigma^2$, valid when the response of the QE is negligible far from resonance. From Eq. (1.46) and the last identity in Eq. (1.49) we can identify $\gamma_0 = \omega_\sigma^3 f_0^2/(3\hbar\pi c_0^3)$, which is the same value as in Eq. (1.47).

The equations describing the cross-section spectra of the small spherical nanoparticle can also be extended to the QE, where Eqs. (1.40), (1.42), and (1.43) are evaluated with the use of α_{e} instead of $\alpha_{\mathrm{a}}^{\mathrm{RC}}$.

1.3 Full electromagnetic response of spherical nanoparticles

In the previous section we have introduced a description of the response of small nanoparticles by treating them as electric dipoles. Next, we describe Mie's or Lorenz-Mie theory, a semi-analytical solution of Maxwell's equations of the electromagnetic field scattered by an arbitrarily large spherical particle, which is used in chapters 3 and 5. As we discuss in this section, this complete solution of Maxwell's equations reveals that, although nanoparticles can indeed be treated as electric dipoles, larger nanoparticles cannot. In particular, we show that large nanoparticles have a complex behavior that can be expressed as the sum of different electric and magnetic multipoles, where each multipole corresponds to a different field distribution. In subsection 1.3.1, we first review the Mie's formalism. Then, in subsection 1.3.2 we use this formalism to calculate the optical response in a canonical scenario as studied in this thesis: the fields scattered by a spherical nanoparticle when illuminated by a linearly polarized plane wave. Further, Mie's formalism is the starting point to describe the optical response of nanoparticles under the excitation by more complex beams in the last section of this chapter.

1.3.1 Mie theory formulation

In this subsection, we review the formulation of Mie theory as given by chapter 4 of reference [40], which is very similar to the one followed by Gustav Mie in his original paper written in 1908 [2]. This formulation depart from Helmholtz equations (or electromagnetic wave equation). The Helmholtz equations are a reformulation of Maxwell's equations in the absence of external currents and charges ($\boldsymbol{J}_{\text{ext}} = 0$ and $\rho_{\text{ext}} = 0$ in Eq. (1.1)). By using the constitutive relations in Eqs. (1.2) and (1.3) in Maxwell's equations (1.1), after some algebraic manipulation, we obtain [35, 36, 40]

$$\begin{aligned}\frac{1}{c_0^2}\frac{\partial^2 \boldsymbol{E}(\boldsymbol{r},t)}{\partial t^2} &= \nabla^2 \boldsymbol{E}(\boldsymbol{r},t),\\ \frac{1}{c_0^2}\frac{\partial^2 \boldsymbol{B}(\boldsymbol{r},t)}{\partial t^2} &= \nabla^2 \boldsymbol{B}(\boldsymbol{r},t).\end{aligned} \tag{1.50}$$

In the linear regime, we can write these equations in the frequency domain using $\boldsymbol{E}(\boldsymbol{r},\omega) = \int dt \boldsymbol{E}(\boldsymbol{r},t)e^{i\omega t}/(2\pi)$ and $\boldsymbol{B}(\boldsymbol{r},\omega) = \int dt \boldsymbol{B}(\boldsymbol{r},t)e^{i\omega t}/(2\pi)$, which leads to,

$$\begin{aligned}\frac{-i\omega^2\varepsilon\mu}{c_0^2}\boldsymbol{E}(\boldsymbol{r},\omega) &= \nabla^2 \boldsymbol{E}(\boldsymbol{r},\omega),\\ \frac{-i\omega^2\varepsilon\mu}{c_0^2}\boldsymbol{B}(\boldsymbol{r},\omega) &= \nabla^2 \boldsymbol{B}(\boldsymbol{r},\omega),\end{aligned} \tag{1.51}$$

where ε and μ are the relative dielectric and magnetic permittivity of the medium, respectively.

Equation (1.51) is satisfied by the following family of equations, so-called *multipoles*:

$$\begin{aligned}\boldsymbol{M}_{b,n,m,e}(\boldsymbol{r},\omega) = \frac{m}{\sin(\theta_{\text{s}})}&\sin(-m\varphi_{\text{s}})P_n^m(\cos(\theta_{\text{s}}))B_n^{(b)}(\zeta)\boldsymbol{u}_{\theta_{\text{s}}} -\\ &-\cos(m\varphi_{\text{s}})\frac{dP_n^m(\cos(\theta_{\text{s}}))}{d\theta_{\text{s}}}B_n^{(b)}(\zeta)\boldsymbol{u}_{\varphi_{\text{s}}},\\ \boldsymbol{M}_{b,n,m,o}(\boldsymbol{r},\omega) = \frac{m}{\sin(\theta_{\text{s}})}&\cos(-m\varphi_{\text{s}})P_n^m(\cos(\theta_{\text{s}}))B_n^{(b)}(\zeta)\boldsymbol{u}_{\theta_{\text{s}}} -\\ &-\sin(m\varphi_{\text{s}})\frac{dP_n^m(\cos(\theta_{\text{s}}))}{d\theta_{\text{s}}}B_n^{(b)}(\zeta)\boldsymbol{u}_{\varphi_{\text{s}}},\end{aligned} \tag{1.52a}$$

$$\begin{aligned}
\boldsymbol{N}_{b,n,m,e}(\boldsymbol{r},\omega) = \frac{B_n^{(b)}(\zeta)}{\zeta}\cos(m\varphi_\mathrm{s})n(n+1)P_n^m(\cos(\theta_\mathrm{s}))\boldsymbol{u}_{r_\mathrm{s}}+ \\
+\cos(m\varphi_\mathrm{s})\frac{dP_n^m(\cos(\theta_\mathrm{s}))}{d\theta_\mathrm{s}}\frac{1}{\zeta}\frac{d[\zeta B_n^{(b)}(\zeta)]}{d\zeta}\boldsymbol{u}_{\theta_\mathrm{s}}+ \\
+m\sin(-m\varphi_\mathrm{s})\frac{P_n^m(\cos(\theta_\mathrm{s}))}{\sin(\theta_\mathrm{s})}\frac{1}{\zeta}\frac{d[\zeta B_n^{(b)}(\zeta)]}{d\zeta}\boldsymbol{u}_{\varphi_\mathrm{s}}, \\
\boldsymbol{N}_{b,n,m,o}(\boldsymbol{r},\omega) = \frac{B_n^{(b)}(\zeta)}{\zeta}\sin(m\varphi_\mathrm{s})n(n+1)P_n^m(\cos(\theta_\mathrm{s}))\boldsymbol{u}_{r_\mathrm{s}}+ \\
+\sin(m\varphi_\mathrm{s})\frac{dP_n^m(\cos(\theta_\mathrm{s}))}{d\theta_\mathrm{s}}\frac{1}{\zeta}\frac{d[\zeta B_n^{(b)}(\zeta)]}{d\zeta}\boldsymbol{u}_{\theta_\mathrm{s}}+ \\
+m\cos(-m\varphi_\mathrm{s})\frac{P_n^m(\cos(\theta_\mathrm{s}))}{\sin(\theta_\mathrm{s})}\frac{1}{\zeta}\frac{d[\zeta B_n^{(b)}(\zeta)]}{d\zeta}\boldsymbol{u}_{\varphi_\mathrm{s}},
\end{aligned} \tag{1.52b}$$

where P_n^m are the associated Legendre functions of the (m,n)-order, $\zeta = \sqrt{\varepsilon\mu}k_0 r_\mathrm{s}$ is the optical distance (with k_0 the wave number in vacuum and r_s the radial spherical coordinate), φ_s and θ_s are the azimuthal and polar spherical coordinates[ii], respectively. $\boldsymbol{u}_{r_\mathrm{s}}$, $\boldsymbol{u}_{\varphi_\mathrm{s}}$, and $\boldsymbol{u}_{\theta_\mathrm{s}}$ are the unity vectors in spherical coordinates (corresponding to the radial, azimuthal, and polar directions, respectively).

The subindex n indicates the order of the multipole, and the subindex m satisfies $m \in [-n, n]$. The e and o labels indicate that the functions are even or odd with respect to φ_s, respectively. For convenience, we substitute the e and o labels of Eqs. (1.52a) and (1.52b) with a generic $\sigma \in \{o, e\}$, so, for the rest of this thesis, we refer to $\boldsymbol{M}_{b,n,m,e}$ and $\boldsymbol{M}_{b,n,m,o}$ as $\boldsymbol{M}_{b,n,m,\sigma}$, and to $\boldsymbol{N}_{b,n,m,e}$, and, $\boldsymbol{N}_{b,n,m,o}$ as $\boldsymbol{N}_{b,n,m,\sigma}$.

Last, the label subindex b in Eqs. (1.52a) and (1.52b) indicates that the multipoles depend on the spherical Bessel function of the b-kind (and n-order), $B_n^{(b)}(\zeta)$, where we only need to consider $b = 1, 3$ (for the scenarios studied in this thesis). On the one hand, we use the $b = 1$, first kind functions, to describe incident beams and the field inside a nanoparticle because only the first kind functions, $B_n^{(1)}(\zeta) \equiv j_n(\zeta)$, are finite at the origin. On the other hand, only the $b = 3$ third kind functions (equivalent to the first order Hankel functions, $B_n^{(3)}(\zeta) \equiv h_n^{(I)}(\zeta)$), behave asymptotically as an outgoing spherical wave,

$$\lim_{\zeta\to\infty} B_n^{(3)}(\zeta) = (-i)^{n+1}\frac{e^{i\zeta}}{\zeta}. \tag{1.53}$$

Thus, they are the only appropriate functions to describe the expected behavior of light scattered by a nanoparticle (in contrast with the asymptotical behavior of $b = 1, 2$, and 4 functions, which become non-physical for large distances [40, 45]).

[ii] As in standard notation, θ_s is the angle with respect to the z-axis of the Cartesian coordinates.

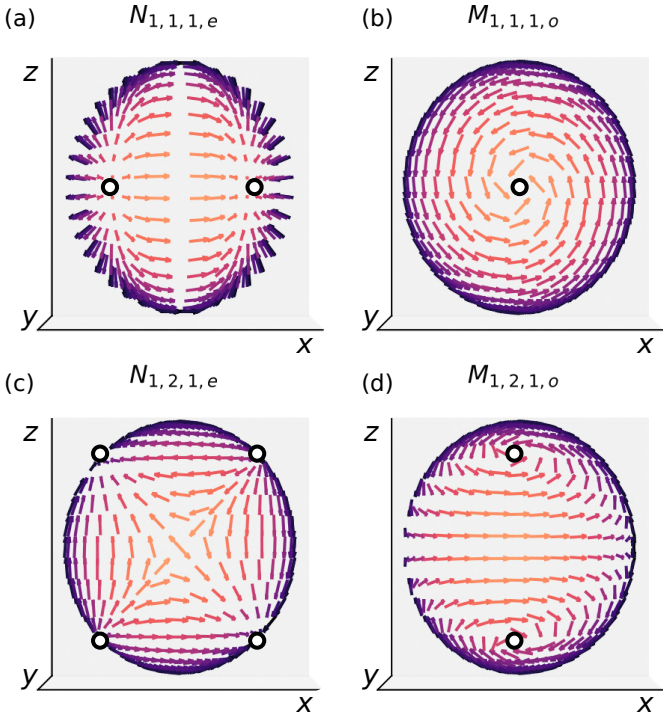

Figure 1.7: Direction of the tangential components of $\boldsymbol{M}_{1,n,1,o}$ and $\boldsymbol{N}_{1,n,1,e}$ (in Eqs. (1.52a) and (1.52b)) with $n = 1, 2$ over a 3D spherical cap with $kr = 10$, $\varphi_s \in [0, \pi]$, and $\theta_s \in [0, \pi]$, following the plotting convention in reference [2] (the perspective of the figure shows the xz-plane in the background, see axis labels for reference). All the arrows have the same length in the 3D space, and they are colored only to help the 3D visualization. The dots represent the position at which the functions become zero.

Electric and magnetic multipoles

Figure 1.7a-d reproduces some of the original results from Mie [2] by evaluating the tangential components of $\boldsymbol{M}_{1,n,1,o}$ and $\boldsymbol{N}_{1,n,1,e}$ with $n = 1, 2$ over a 3D spherical cap with $\zeta = 10$, $\varphi_s \in [0, \pi]$, and $\theta_s \in [0, \pi]$ (the perspective of the figure shows the xz-plane). We can indeed observe how the $\boldsymbol{N}_{1,1,1,e}$ and $\boldsymbol{N}_{1,2,1,e}$ functions in Figs. 1.7a and 1.7c, respectively, show a vectorial pattern of fields going from one or two points ("divergent" poles) to the same number of "convergent" poles (indicated with grey spots in the figure). These vectorial patterns are analogous to those obtained if we placed positive charges in the divergent and negative charges in the convergent points, forming an electric dipole in the case of $\boldsymbol{N}_{1,1,1,e}$ (Fig. 1.7a) and an electric quadrupole for $\boldsymbol{N}_{1,2,1,e}$ (Fig. 1.7c). As a consequence, the $\boldsymbol{N}$-functions are often called electric or electric-type multipoles, as already pointed out by Mie in 1908 [2]. Similarly, the $\boldsymbol{M}_{1,1,1,o}$ and $\boldsymbol{M}_{1,2,1,o}$ functions in Figs. 1.7b and 1.7d, respectively, show a vectorial pattern of fields that surround the poles (grey spots

in the figure), which resembles the electric field produced by a magnetic dipole and a magnetic quadrupole, respectively. Hence, the $\boldsymbol{M}$-functions are often called magnetic or magnetic-type multipoles.

Although the fields generated by a single $\boldsymbol{N}$-function do indeed correspond to the fields generated by an electric multipole, it is convenient to point out that the representation of the $\boldsymbol{N}$-functions followed by Mie and reproduced in Figs. 1.7a and 1.7c can be misleading [40]. In Figs. 1.7b and 1.7d, it might seem that there are charges placed at the poles, but there are not; the indicated poles (grey spots in the figure) correspond to a zero of the transverse component of the $\boldsymbol{N}$-functions, not to a charge existing at the pole. In these positions the vectorial fields become purely radial, which cannot be shown in this representation. Despite this caveat, the identification of the vectorial patterns of the $\boldsymbol{N}$-functions with the fields generated by different electric multiples (*e.g.,* an electric dipole or an electric quadrupole) is quite useful to analyze the response of a nanoparticle.

Expansion of fields in the electric and magnetic multipoles

The multipolar functions in Eqs. (1.52a) and (1.52b), $\boldsymbol{M}_{b,n,m,\sigma}$ and $\boldsymbol{N}_{b,n,m,\sigma}$ (with $\sigma \in \{e,o\}$) form an orthogonal basis themselves, *i.e.*, $\int d\Omega \boldsymbol{X}_{b,n,m,\sigma} \cdot \boldsymbol{X}'_{n',m',\sigma'} \propto \delta^K_{\boldsymbol{X},\boldsymbol{X}'}\delta^K_{b,b'}\delta^K_{n,n'}\delta^K_{m,m'}\delta^K_{\sigma,\sigma'}$ with $d\Omega$ the solid angle differential, δ^K the Kronecker delta, and $\boldsymbol{X} \in \{\boldsymbol{M},\boldsymbol{N}\}$ (we direct the reader to the full orthogonality relations of the multipoles in chapter 7 of reference [46]). Thus, any arbitrary electric (or magnetic) field $\boldsymbol{E}_{\text{arb}}$ can be expanded onto the functions in Eqs. (1.52a) and (1.52b) as:

$$\boldsymbol{E}_{\text{arb}}(\boldsymbol{r},\omega) = \sum_{m=-n}^{n}\sum_{n=0}^{\infty}\sum_{\sigma=e,o}\left[C^M_{b,n,m,\sigma}\boldsymbol{M}_{b,n,m,\sigma}(\boldsymbol{r},\omega) + C^N_{n,m,\sigma}\boldsymbol{N}_{b,n,m,\sigma}(\boldsymbol{r},\omega)\right] \tag{1.54}$$

where $C^M_{b,n,m,\sigma}$ and $C^N_{b,n,m,\sigma}$ are the normalized projections of $\boldsymbol{E}_{\text{arb}}$ onto the basis $\{\boldsymbol{M}_{b,n,m,\sigma},\boldsymbol{N}_{b,n,m,\sigma}\}$:

$$\begin{aligned} C^M_{b,n,m,\sigma} &= \frac{\int d\Omega \boldsymbol{E}_{\text{arb}}(\boldsymbol{r},\omega)\cdot\boldsymbol{M}_{b,n,m,\sigma}(\boldsymbol{r},\omega)}{\int d\Omega |\boldsymbol{M}_{b,n,m,\sigma}(\boldsymbol{r},\omega)|^2}, \\ C^N_{n,m,\sigma} &= \frac{\int d\Omega \boldsymbol{E}_{\text{arb}}(\boldsymbol{r},\omega)\cdot\boldsymbol{N}_{b,n,m,\sigma}(\boldsymbol{r},\omega)}{\int d\Omega |\boldsymbol{N}_{b,n,m,\sigma}(\boldsymbol{r},\omega)|^2}, \end{aligned} \tag{1.55}$$

Similarly, the same method can be applied to decompose the magnetic field on the same basis. Thus, we can use this formalism to describe any arbitrary electric and magnetic field.

1.3.2 Fields scattered by a spherical nanoparticle under plane wave illumination

Expansion of a plane wave in electric and magnetic multipoles

Next we consider a canonical case of study, the electromagnetic response of a spherical nanoparticle with center at the origin of coordinates and illuminated by an x-polarized electric plane wave

$$\boldsymbol{E}_{x\mathrm{PW}}(\boldsymbol{r},\omega) = E_0 e^{ikz}\boldsymbol{u}_x, \tag{1.56}$$

with amplitude E_0 and propagating along the z-axis.

We consider the decomposition of this plane wave on the basis of $\boldsymbol{M}_{b,n,m,\sigma}$– and $\boldsymbol{N}_{b,n,m,\sigma}$–multipoles with $b = 1$, because, the electromagnetic field of a plane wave is finite in the origin of coordinates, and thus, according to the previous discussion, the functions $B_n^{(b)}$ must be evaluated using the spherical Bessel functions of the first kind. We can then find the expressions of the $C^M_{1,n,m,\sigma}$ and $C^N_{1,n,m,\sigma}$ coefficients that decompose $\boldsymbol{E}_{x\mathrm{PW}}$ in the multipolar basis by inserting $\boldsymbol{E}_{x\mathrm{PW}}$ in Eq. (1.55). The solution is [40],

$$\begin{aligned} C^M_{1,n,m,\sigma} &= \delta^K_{b,1}\delta^K_{m,1}\delta^K_{\sigma,o} i^n \frac{2n+1}{n(n+1)} E_0, \\ C^N_{1,n,m,\sigma} &= \delta^K_{b,1}\delta^K_{m,1}\delta^K_{\sigma,e} (-i) i^n \frac{2n+1}{n(n+1)} E_0. \end{aligned} \tag{1.57}$$

Using these coefficients in Eq. (1.54), we obtain,

$$\boldsymbol{E}_{x\mathrm{PW}}(\boldsymbol{r},\omega) = \sum_{n=1}^{\infty} i^n \frac{2n+1}{n(n+1)} E_0 \left[\boldsymbol{M}_{1,n,1,o}(\boldsymbol{r},\omega) - i\boldsymbol{N}_{1,n,1,e}(\boldsymbol{r},\omega)\right]. \tag{1.58}$$

Scattering of a spherical nanoparticle illuminated by a plane wave

The field scattered by a spherical nanoparticle $\boldsymbol{E}_{\mathrm{sca}}$ illuminated by $\boldsymbol{E}_{x\mathrm{PW}}$, can be obtained by applying the boundary conditions at the surface of the spherical nanoparticle [40]:

$$(\boldsymbol{E}_{\mathrm{out}} - \boldsymbol{E}_{\mathrm{in}}) \times \boldsymbol{u}_r = (\boldsymbol{H}_{\mathrm{out}} - \boldsymbol{H}_{\mathrm{in}}) \times \boldsymbol{u}_r = 0, \tag{1.59}$$

where $\boldsymbol{E}_{\mathrm{out}}$ is the electric field outside of the nanoparticle, $\boldsymbol{E}_{\mathrm{out}} = \boldsymbol{E}_{x\mathrm{PW}} + \boldsymbol{E}_{\mathrm{sca}}$, and $\boldsymbol{E}_{\mathrm{in}}$ is the electric field inside of the nanoparticle. $\boldsymbol{H}_{\mathrm{out}}$ and $\boldsymbol{H}_{\mathrm{in}}$ are the corresponding magnetizing fields, which can be related to the magnetic field using the standard constitutive relation (Eq. (1.3)), and to the electric field by using Maxwell's equations (Eq. (1.4)). Due to the orthogonality of the multipoles, Eq. (1.59) imposes that $\boldsymbol{E}_{\mathrm{sca}}$ and $\boldsymbol{E}_{\mathrm{in}}$ only have contributions of $m = 1$ multipoles (same as for the incident plane wave) [40, 45].

Further, $\boldsymbol{E}_{\mathrm{in}}$ is decomposed using only Bessel functions of the first kind (because they are the only Bessel functions that are finite at the origin of coordinates). Thus,

$\boldsymbol{E}_{\text{in}}$ becomes

$$\boldsymbol{E}_{\text{in}}(\boldsymbol{r},\omega) = \sum_{n=1}^{\infty} i^n \frac{2n+1}{n(n+1)} E_0 \left[c_n \boldsymbol{M}_{1,n,1,o}(\boldsymbol{r},\omega) - i d_n \boldsymbol{N}_{1,n,1,e}(\boldsymbol{r},\omega) \right], \tag{1.60}$$

with the c_n and d_n coefficients defined below.

On the other hand, the field scattered by the nanoparticle, $\boldsymbol{E}_{\text{sca}}$, are described with multipoles with $b = 3$, *i.e.*, multipoles with spherical Bessel functions of the third kind (see discussion of Eq. (1.53)), and the general decomposition of $\boldsymbol{E}_{\text{sca}}$ becomes

$$\boldsymbol{E}_{\text{sca}}(\boldsymbol{r},\omega) = \sum_{n=1}^{\infty} i^n \frac{2n+1}{n(n+1)} E_0 \left[-b_n \boldsymbol{M}_{3,n,1,o}(\boldsymbol{r},\omega) + i a_n \boldsymbol{N}_{3,n,1,e}(\boldsymbol{r},\omega) \right]. \tag{1.61}$$

The scattering coefficients a_n, b_n, c_n, and d_n in (1.61) and (1.60) are obtained by solving Eq. (1.59) (term by term) and follow the expressions [40, 45]:

$$a_n = \frac{\mu_{\text{R}} n_{\text{R}}^2 j_n(\zeta_0)\psi'(\zeta_0) - \mu_{\text{in}} j_n(\zeta_0)\psi_n'(n_{\text{R}}\zeta_0)}{\mu_{\text{R}} n_{\text{R}}^2 j_n(n_{\text{R}}\zeta_0)\xi_n'(\zeta_0) - \mu_{\text{in}} h_n^{(I)}(\zeta_0)\psi_n'(n_{\text{R}}\zeta_0)}, \tag{1.62a}$$

$$b_n = \frac{\mu_{\text{in}} j_n(n_{\text{R}}\zeta_0)\psi_n'(\zeta_0) - \mu_{\text{R}} j_n(\zeta_0)\psi_n'(n_{\text{R}}\zeta_0)}{\mu_{\text{in}} j_n(n_{\text{R}}\zeta_0)\xi_n'(\zeta_0) - \mu_{\text{R}} h_n^{(I)}(\zeta_0)\psi_n'(n_{\text{R}}\zeta_0)}, \tag{1.62b}$$

$$c_n = \frac{\mu_{\text{in}} j_n(\zeta_0)\xi_n'(\zeta_0) - \mu_{\text{in}} h_n^{(I)}(\zeta_0)\psi_n'(\zeta_0)}{\mu_{\text{in}} j_n(n_{\text{R}}\zeta_0)\xi_n'(\zeta_0) - \mu_{\text{R}} h_n^{(I)}(\zeta_0)\psi_n'(n_{\text{R}}\zeta_0)}, \tag{1.62c}$$

$$d_n = \frac{\mu_{\text{in}} n_{\text{R}} j_n(\zeta_0)\xi_n'(\zeta_0) - \mu_{\text{in}} h_n^{(I)}(\zeta_0)\psi_n'(\zeta_0)}{\mu_{\text{R}} n_{\text{R}}^2 j_n(n_{\text{R}}\zeta_0)\xi_n'(\zeta_0) - \mu_{\text{in}} h_n^{(I)}(\zeta_0)\psi_n'(n_{\text{R}}\zeta_0)}, \tag{1.62d}$$

with $\zeta_0 = k_0 R$, $n_{\text{R}} = n_{\text{in}}/n_{\text{out}}$, $\mu_{\text{R}} = \mu_{\text{in}}/\mu_{\text{out}}$, n_{in} (n_{out}) the refractive index inside (outside) of the nanoparticle, and μ_{in} (μ_{out}) the relative magnetic permittivity inside (outside) of the nanoparticle, respectively. $\psi_n(\zeta_0) = \zeta_0 j_n(\zeta_0)$ and $\xi_n(\zeta_0) = \zeta_0 h_n^{(I)}(\zeta_0)$ are the Ricatti-Bessel functions of the first and third order, respectively. $\psi_n(\dots)'$ and $\xi_n(\dots)'$ are the derivatives of the Riccatti-Bessel functions.

In this thesis we are interested in obtaining the electric field scattered by the nanoparticle, but Mie theory is also valid to describe the magnetic fields. Using Maxwell's equations (Eq. (1.4)), the rotational properties of the $\boldsymbol{M}$- and $\boldsymbol{N}$-functions [36, 40, 45],

$$\begin{aligned} \boldsymbol{N}_{b,n,m,\sigma}(\boldsymbol{r},\omega) &= \frac{1}{k}(\nabla \times \boldsymbol{M}_{b,n,m,\sigma}(\boldsymbol{r},\omega)), \\ \nabla \times \boldsymbol{N}_{b,n,m,\sigma}(\boldsymbol{r},\omega) &= k \boldsymbol{M}_{b,n,m,\sigma}(\boldsymbol{r},\omega), \end{aligned} \tag{1.63}$$

and the constitutive relations of the $\boldsymbol{H}$ magnetizing field (Eq. (1.3)), we obtain

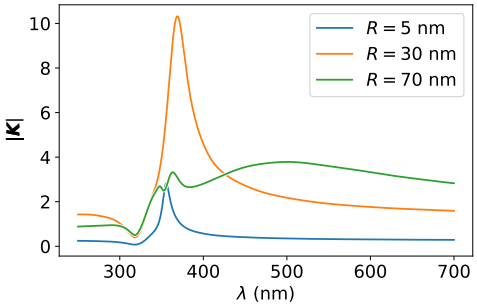

Figure 1.8: Near-field enhancement factor $|\boldsymbol{K}|$ as a function of the wavelength of the x-polarized incident plane wave. The enhancement factor is calculated at a distance $d = 5$ nm for the surface of a spherical nanoparticle. We calculate the enhancement factor for three silver spherical nanoparticles of different radius, $R = 5$ nm (blue line), 30 nm (orange line), and 70 nm (green line). These results are obtained using Mie theory as introduced in section 1.3.2. The dielectric permittivity of silver used for these calculations is obtained from reference [41].

(see also chapter 4 of reference [40]),

$$\boldsymbol{H}_{\text{in}}(\boldsymbol{r},\omega) = \frac{k_{\text{in}}}{\omega\mu_{\text{in}}}\sum_{n=1}^{\infty} i^n \frac{2n+1}{n(n+1)} E_0 \left[-ic_n \boldsymbol{N}_{1,n,1,o}(\boldsymbol{r},\omega) - d_n \boldsymbol{M}_{1,n,1,e}(\boldsymbol{r},\omega)\right], \tag{1.64}$$

and

$$\boldsymbol{H}_{\text{sca}}(\boldsymbol{r},\omega) = \frac{k}{\omega\mu_{\text{out}}}\sum_{n=1}^{\infty} i^n \frac{2n+1}{n(n+1)} E_0 \left[ib_n \boldsymbol{N}_{1,n,1,o}(\boldsymbol{r},\omega) + a_n \boldsymbol{M}_{1,n,1,e}(\boldsymbol{r},\omega)\right], \tag{1.65}$$

where $k_{\text{in}} = n_{\text{R}} k$.

Near-field response of a spherical nanoparticle

Next, we use Mie theory, as given in Eqs. (1.61), (1.62a), and (1.62b), to calculate the field scattered by a silver spherical nanoparticle $\boldsymbol{E}_{\text{sca}}$ of different radius $R = 5$ nm, 30 nm, and 70 nm. Figure 1.8 shows the spectrum of the near-field enhancement factor $|\boldsymbol{K}| = \boldsymbol{E}_{\text{sca}}/E_0$ calculated at a distance $d = 5$ nm from the surface of the nanoparticle along the x-axis, the axis of polarization of the incident plane wave (same incident plane wave as for the calculations in Fig. 1.2b and 1.4a). The enhancement spectra of the $R = 5$ nm (blue line) and $R = 30$ nm (orange line) nanoparticles are dominated by a single peak that can be tracked to the contribution of a single multipole in the equation of the scattered field (Eq. (1.61)). This multipole is the $\boldsymbol{N}_{3,1,1,e}$ electric dipole. The agreement for $R = 5$ nm between the quasistatic (Fig. 1.2b), radiative-corrected (Fig. 1.4a), and exact results obtained within Mie theory (Fig. 1.8) is excellent. On the other hand, comparing Figs.

1.4a and 1.8 for $R = 30$ nm, we can observe some differences: the enhancement obtained within Mie theory is slightly larger and blue-shifted as compared to the radiative-corrected results. We discuss in chapter 3 that these small differences can be reduced with an improved description of the radiative correction [47].

The enhancement spectrum of the $R = 70$ nm nanoparticle in Fig. 1.8 (green line) shows some differences with the radiative-corrected calculations (in Fig. 1.4a, green line). The enhancement spectrum obtained with Mie theory features three main peaks. One main peak at $\lambda \approx 500$ nm, and two additional peaks at $\lambda \approx 360$ nm and $\lambda \approx 350$ nm. The very broad peak at $\lambda \approx 500$ nm is caused by the $\boldsymbol{N}_{3,1,1,e}$ electric dipole contribution in Eq. (1.61), and it is approximately reproduced by the radiative corrected results in the $\lambda \gtrsim 400$ nm region (the peak is again slightly larger and blue-shifted within Mie theory). On the other hand, the two additional peaks at $\lambda \approx 360$ nm and $\lambda \approx 350$ nm are due to the $\boldsymbol{N}_{3,2,1,e}$ electric quadrupole and to the $\boldsymbol{N}_{3,3,1,e}$ electric octopole contributions to the scattered fields. This implies that incident plane waves with smaller wavelengths can drive plasmonic resonances of the nanoparticle with different charge distribution than the electric dipole plasmon resonance introduced in subsection 1.2 (Fig. 1.3).

Optical cross-sections spectra

We next show how to use Mie theory to calculate the different optical cross-sections spectra of a spherical nanoparticle under plane-wave illumination. The scattering cross-section spectra can be calculated by integrating the Poynting vector of the scattered electric and magnetic fields (Eq. (1.38)). Using $\boldsymbol{E}_{\text{sca}}$ and $\boldsymbol{H}_{\text{sca}}$ in Eqs. (1.61) and (1.65), we obtain [40, 45],

$$\sigma_{\text{sca}} = \frac{2\pi}{k^2} \sum_n (2n+1)(|a_n|^2 + |b_n|^2). \tag{1.66}$$

On the other hand, in subsection 1.2.3 we obtained the extinction cross-section of the nanoparticle by using the optical theorem. However, in Mie theory, it is more convenient to use again the Poynting theorem[iii]. In this case, we write P_{ext}, the sum of the absorption and scattered power, as

$$P_{\text{ext}}(\omega) = -\iint_{\mathcal{A}} \bar{\boldsymbol{S}}_{\text{ext}}(\boldsymbol{r}, \omega) \cdot \boldsymbol{n}_{\mathcal{A}} d\mathcal{A}, \tag{1.67}$$

where $\mathcal{A}$ is the area of an arbitrary closed surface surrounding the particle, and $\boldsymbol{n}_{\mathcal{A}}$ is the normal vector to this surface. Here we have introduced a vector $\bar{\boldsymbol{S}}_{\text{ext}}$ that we refer to as the time average of the extinction Poynting vector. To obtain

[iii] Applying the optical theorem presents some technical difficulties in Mie theory for an incident z-propagating beam. It requires to evaluate the $\boldsymbol{M}$-functions at $\theta_{\text{s}} = 0$, where the $\boldsymbol{M}$-functions diverge due to their $1/\sin(\theta_{\text{s}})$ dependence (Eq. (1.52a)). Although this problem can be solved by taking the $\theta_{\text{s}} \to 0$ limit, we use the Poynting theorem to avoid this issue, as developed in references [36, 40, 45].

$\bar{\boldsymbol{S}}_{\text{ext}}$, we first obtain the absorbed power P_{abs} as

$$P_{\text{abs}} = -\iint_{\mathcal{A}} \bar{\boldsymbol{S}}_{\text{tot}}(\boldsymbol{r},\omega)\cdot\boldsymbol{n}_{\mathcal{A}}d\mathcal{A}, \tag{1.68}$$

with $\bar{\boldsymbol{S}}_{\text{tot}}(\boldsymbol{r},\omega) = (1/2)\text{Re}\{\boldsymbol{E}_{\text{tot}}(\boldsymbol{r},\omega)\times\boldsymbol{H}_{\text{tot}}(\boldsymbol{r},\omega)^*\}$ the time average of the total Poynting vector ($\boldsymbol{E}_{\text{tot}}(\boldsymbol{r},\omega) = \boldsymbol{E}_{x\text{PW}}(\boldsymbol{r},\omega) + \boldsymbol{E}_{\text{sca}}(\boldsymbol{r},\omega)$ and $\boldsymbol{H}_{\text{tot}}(\boldsymbol{r},\omega) = \boldsymbol{H}_{x\text{PW}}(\boldsymbol{r},\omega)+\boldsymbol{H}_{\text{sca}}(\boldsymbol{r},\omega)$). Equation (1.68) thus, simply indicates that the absorbed power corresponds to the net energy that enters the $\mathcal{A}$ area. Using $P_{\text{ext}} = P_{\text{abs}}+P_{\text{sca}}$, Eqs. (1.38) and (1.67)-(1.68), we obtain the expression for $\bar{\boldsymbol{S}}_{\text{ext}}$ [36, 40],

$$\bar{\boldsymbol{S}}_{\text{ext}}(\boldsymbol{r},\omega) = \frac{1}{2}\text{Re}\{\boldsymbol{E}_{x\text{PW}}(\boldsymbol{r},\omega)\times\boldsymbol{H}_{\text{sca}}(\boldsymbol{r},\omega)^* + \boldsymbol{E}_{\text{sca}}(\boldsymbol{r},\omega)\times\boldsymbol{H}_{x\text{PW}}(\boldsymbol{r},\omega)^*\}. \tag{1.69}$$

After a lengthy algebraic manipulation [40], we can obtain a simple expression for $\sigma_{\text{ext}}(\omega) = P_{\text{ext}}(\omega)/I_0$,

$$\sigma_{\text{ext}} = \frac{2\pi}{k^2}\sum_n (2n+1)\text{Re}\{a_n + b_n\}. \tag{1.70}$$

Figure 1.9a, shows the extinction (black line), scattering (blue line), and absorption (red line, $\sigma_{\text{abs}} = \sigma_{\text{ext}} - \sigma_{\text{sca}}$) cross-section of the silver spherical nanoparticle of radius $R = 70$ nm under illumination by a x-polarized, z-propagating plane wave, obtained within Mie theory. The extinction and scattering cross-section spectra show two main peaks, one at $\lambda \approx 450$ nm, and another one at $\lambda \approx 350$ nm with similar relative strength. By isolating the contributions of the different terms of the sum in Eqs. (1.66) and (1.70), we find that the total response of these nanoparticles depends mainly on the contributions of the terms proportional to the a_1 and a_2 coefficients. The first one is plotted in Fig. 1.9b (green line), and it corresponds to the contribution of the electric dipole mode to the extinction cross-section. This contribution features a broad main peak centered at $\lambda \approx 450$ nm, very similar to the one calculated with the radiative-corrected model in Fig. 1.6e, although slightly broader and blue-shifted as compared to the results with the radiative-corrected results.

On the other hand, Fig. 1.9b (orange line) shows the contribution of the term proportional to a_2, corresponding to the contribution of the electric quadrupole mode. We find that this quadrupolar mode, not included in the radiative-corrected model, results in an additional narrow peak in Fig. 1.9a at $\lambda \approx 350$ nm.

Last, Figs. 1.9c and d show the far-field directivity of the scattered fields for the $R = 70$ nm silver nanoparticle under illumination at $\lambda = 350$ nm and $\lambda = 500$ nm, respectively. $\lambda = 500$ (approximately) corresponds to the maximum of the electric dipolar extinction cross-section, and in Fig. 1.9d we find a clear dipolar emission (as shown by the quasistatic-approximation results in Fig. 1.5). On the other hand, the scattering of the nanoparticle at $\lambda = 350$ nm illumination is highly influenced by the electric quadrupolar resonance. In this case, the directivity in Fig. 1.9c is no longer dipolar as it clearly shows a suppression of the emission in

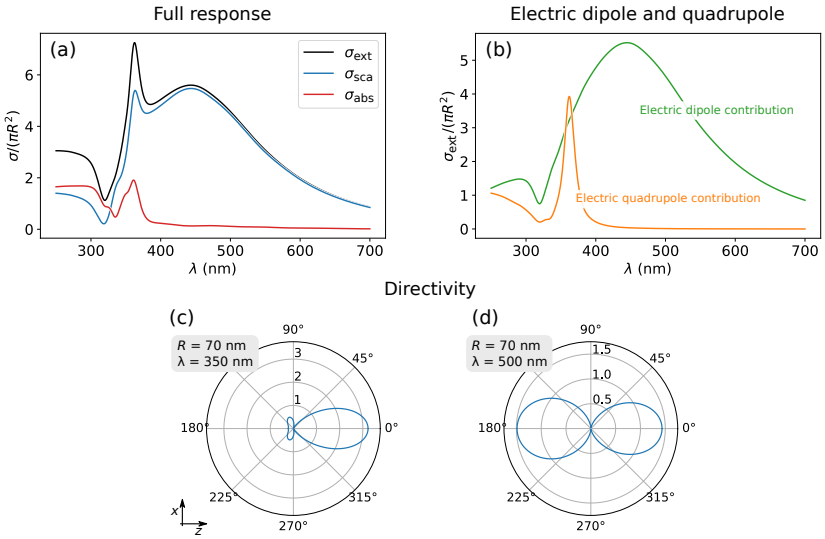

Figure 1.9: Analysis of the far-field response of a $R = 70$ nm silver spherical nanoparticle. (a) Absorption (red line), scattering (blue line), and extinction (black line) cross-section spectra obtained considering the full response (accounting for every multipole contribution). (b) Extinction cross-section of the contributions of the electric dipole (green line) and electric quadrupole (orange line) for the same system as in (a). (c) and (d) far-field directivity of the $R = 70$ nm silver spherical nanoparticle for $\lambda = 350$ nm and $\lambda = 500$ nm, respectively. All calculations are obtained with Mie theory. The dielectric permittivity of silver used in these calculations is obtained from reference [41].

the backward direction (towards $\theta_s = 180°$). We note that this directivity pattern is likely affected by both the quadrupolar and dipolar modes because the latter is very broad, and it is still excited at $\lambda = 350$ nm.

Spectral response of dielectric nanoparticles

Dielectric nanoparticles constitute a good alternative to metallic nanoparticles for controlling light at the nanoscale, presenting some advantages such as supporting optical resonances with very low thermal losses [49–52]. Figure 1.10a shows the extinction cross-section spectrum for a spherical nanoparticle made of silicon with a radius $R = 230$ nm under illumination by a linearly polarized plane wave (the same system is analyzed in detail in reference [53]). The spectrum in Fig. 1.10 displays three peaks, each corresponding to the excitation of an optical resonance of the nanoparticle, as identified from the different contributions to Eq. (1.69). The extinction cross-section spectrum shows a strong influence of a magnetic quadrupole mode at $\lambda \approx 1200$ nm, an electric dipole mode at $\lambda \approx 1300$ nm, and a magnetic dipolar mode at $\lambda \approx 1700$ nm. In contrast to the response of a metallic nanoparticle, both electric and magnetic resonances supported by the dielectric

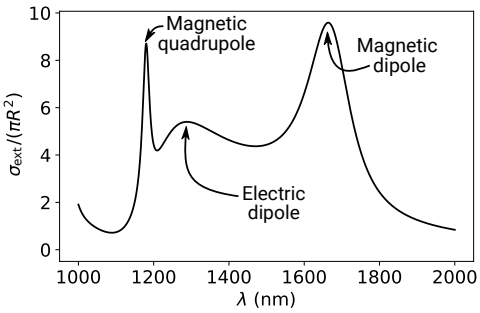

Figure 1.10: Extinction cross section spectrum of a $R = 230$ nm silicon spherical nanoparticle obtained with Mie theory and accounting for the contribution of all multipoles. The dielectric permittivity of silicon used for these calculations is obtained from reference [48].

nanoparticle contribute significantly to the cross-section spectra.

1.4 Angular momentum of light

So far, we have focused on describing the interaction between a linearly polarized plane wave and a spherical nanoparticle. However, it is also interesting to explore the interaction between a spherical nanoparticle with more sophisticated light beams, such as light beams with well-defined angular momentum properties, as these type of beams will be used in chapter 5. The angular momentum properties introduce new degrees of freedom that can be exploited in different applications, such as sensing [19, 28, 54] or information processing [15–18].

There are four properties associated with the angular momentum of light, namely the spin angular momentum, the orbital angular momentum, the helicity, and the total angular momentum. In the simple case of a weakly-focused beam, so-called a paraxial beam, the spin value is directly given by its circular polarization; for example, a plane wave with circularly left polarization has spin $s = +1$. On the other hand, the orbital angular momentum is connected with changes in the spatial distribution of the phase on an individual wavefront (how many times the phase changes from 0 to 2π when moving along a circular trajectory around the axis of propagation). In subsection 1.4.1, we discuss the spin and orbital angular momentum in more detail for weakly focused beams with a wavefront propagating in a single defined direction (paraxial beams).

On the other hand, we also consider in this section the angular momentum properties of non-paraxial beams, for example, with a spherical wavefront. For these type of fields, the spin and orbital angular momentum of light are ill-defined [55]. Thus, in that case, we introduce two auxiliary properties: the total angular momentum and the helicity. The helicity is an intrinsic property of the photons [56], defined as the spin projected in the direction of propagation, and it determines the torque that light can exert on matter [57–59]. On the other hand, in simple paraxial

beams, the total angular momentum is the sum of the spin and the orbital angular momentum. The total angular momentum of light determines the total angular momentum that can be transferred to matter, for example, to drive circular motion of nanoparticles [58–60]. In subsection 1.4.2, we adapt Mie theory formulation in section 1.3.2 to formally describe the helicity and total angular momentum of non-paraxial beams. Finally, in subsection 1.4.3, we derive the expressions for fields scattered by a spherical nanoparticle when illuminated by a beam with well-defined angular momentum focused by a lens, a typical experimental setup that we consider in chapter 5.

1.4.1 Paraxial beams with non-zero orbital angular momentum and spin

Laguerre-Gauss beams

Let us first consider the simplified case of paraxial beams to introduce the angular momentum properties of light. A paraxial light beam is an electromagnetic wave that propagates towards a fixed direction and that has a relatively small divergence or expansion while propagating (for example, the beam emitted by a laser). Formally, the defining characteristic of a paraxial beam is that one component of the wavevector, $\boldsymbol{k} = (k_x, k_y, k_z)$, dominates the rest; for example, a z-propagating paraxial beam satisfies $k_z \gg (k_x + k_y)$. If we consider a paraxial beam propagating in free space along the z-direction with an electric field,

$$\boldsymbol{E}(\boldsymbol{r}, \omega) = E_0(\boldsymbol{r}) e^{i(kz - \omega t)} \boldsymbol{v}_E, \tag{1.71}$$

where $E_0(\boldsymbol{r})$ is the spatial distribution that varies with z only slowly (compared with the wavelength), and $\boldsymbol{v}_E$ is the polarization vector, perpendicular to z [35, 36]. We can approximate the Helmholtz equation (Eq. (1.51)) in the paraxial regime as

$$\nabla_\perp^2 E_0(\boldsymbol{r}) + 2ik \frac{\partial E_0(\boldsymbol{r})}{\partial z} = 0. \tag{1.72}$$

Here, we have approximated $\partial^2 E_0(\boldsymbol{r})/\partial z^2 \approx -k^2 E_0(\boldsymbol{r}) + 2ik \partial E_0(\boldsymbol{r})/\partial z e^{ikz}$ (*i.e.*, we neglect $\partial^2 E_0(\boldsymbol{r})/\partial z^2$ over the rest of the contributions due to the slow spatial variation of the fields along z), where $\nabla_\perp^2$ is the Laplacian in the coordinates perpendicular to the z–axis. The standard solution of $E_0(\boldsymbol{r})$ in Eq. (1.72) obtained in cylindrical coordinates (radial r_c, polar φ_c, and axial z_c coordinates) is [61, 62],

$$\begin{aligned} E_0(\boldsymbol{r}) \equiv LG_q^l(r_c, \varphi_c, z_c) = \sqrt{\frac{2q!}{\pi(q+|l|)!}} \frac{w_0}{w(z_c)} \left(\frac{r_c \sqrt{2}}{w(z_c)} \right)^{|l|} \exp\left(\frac{-r_c^2}{w(z_c)^2} \right) \\ L_q^{|l|}\left(\frac{2r_c^2}{w(z_c)^2} \right) \exp\left(-ik \frac{r_c^2}{2R_C(z_c)} \right) \exp\left(il\varphi_c \right) \exp\left(i\psi_G(z_c) \right), \end{aligned} \tag{1.73}$$

where LG_q^l are the Laguerre-Gauss beams of (l, q)–order, $\psi_G(z_c) = \arctan(z_c/z_R)$ is the Gouy phase, $R_C(z_c) = (z_c^2 + z_E^2)/z_c$ is the position-dependent radius of curvature of the beam, and $z_R = w_0^2 k/2$ is the Rayleigh range. $w(z_c) = w_0\sqrt{1 + (z_c/z_R)^2}$ in Eq. (1.73) is the position-dependent waist of the beam, which shows a minimum waist w_0 at the focal plane $z_c = 0$. In Eq. (1.73), $L_{|l|}^q$ are the generalized Laguerre polynomials of $(|l|, q)$–order.

Orbital angular momentum

The field in Eqs. (1.71) and (1.73) is said to have well-defined orbital angular momentum. This means that LG_q^l is an eigenfunction of a particular projection of the orbital angular momentum operator, $\boldsymbol{L} = -i(\boldsymbol{r} \times \nabla)$. In our case, LG_q^l is an eigenfunction of L_z, the projection along z, the direction of propagation,

$$L_z = \boldsymbol{L} \cdot \boldsymbol{u}_z = -i\frac{\partial}{\partial \varphi_c}. \tag{1.74}$$

The eigenvalue of LG_q^l with respect to L_z is l,

$$L_z LG_q^l(\boldsymbol{r}) = l LG_q^l(\boldsymbol{r}), \tag{1.75}$$

which is determined by the $\exp(il\varphi_c)$ term in Eq. (1.73), *i.e.*, the rotation of the phase around the z axis directly results in the value of the orbital angular momentum carried by the beam. For illustration, we show in Fig. 1.11 the spatial distribution of the amplitude and phase of the LG_0^0, LG_0^1, and LG_0^2 Laguerre-Gauss beams in the $z_c = 0$ plane. The phase of the LG_0^l beams cycles l-times from $-\pi$ to π as φ_c varies over $[-\pi, \pi]$. For example, the phase of LG_0^1 in the figure changes (with φ_c) from $-\pi$ to π one time, while the phase of LG_0^2 goes from $-\pi$ to π twice. On the other hand, the LG_0^0 beam (left column in the figure) has a constant phase, which shows its $l = 0$ orbital angular momentum.

Spin angular momentum

In free space or in a homogeneous medium, Maxwell's equations impose that any electromagnetic wave has a polarization transverse to its propagation [63]. Hence, $\boldsymbol{v}_E$ in Eq. (1.71) must have a form (in Cartesian coordinates) as:

$$\boldsymbol{v}_E = \begin{pmatrix} v_x \\ v_y \\ 0_z \end{pmatrix}, \tag{1.76}$$

i.e., a zero contribution in the direction of propagation, which in this case is z. The x- and y-components, v_x and v_y, respectively can have any arbitrary complex value. However, specific values of v_x and v_y make the $\boldsymbol{v}_E$ vector an eigenvector of the spin operator projected in the direction of propagation, S_z. The spin operator

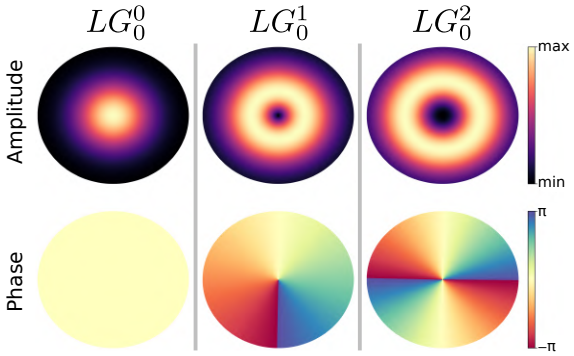

Figure 1.11: Representation of different Laguerre-Gauss fields in the $z_c = 0$ focal plane. The three columns in the figure correspond from left to right to LG_0^0, LG_0^1, and LG_0^2 beams. In the upper row, we plot the amplitude of the fields and in the row below we plot the phase of the fields. These beams are obtained for a z-propagating beam.

in the Cartesian coordinates is [64]

$$\overleftrightarrow{\boldsymbol{S}} = \begin{pmatrix} 0 & 0 & 0 \\ 0 & 0 & -i \\ 0 & i & 0 \end{pmatrix} \boldsymbol{u}_x + \begin{pmatrix} 0 & 0 & i \\ 0 & 0 & 0 \\ -i & 0 & 0 \end{pmatrix} \boldsymbol{u}_y + \begin{pmatrix} 0 & -i & 0 \\ i & 0 & 0 \\ 0 & 0 & 0 \end{pmatrix} \boldsymbol{u}_z. \tag{1.77}$$

The eigenvectors of $S_z = \overleftrightarrow{\boldsymbol{S}} \cdot \boldsymbol{u}_z$ are,

$$\boldsymbol{v}_+ = \frac{1}{\sqrt{2}} \begin{pmatrix} 1_x \\ i_y \\ 0_z \end{pmatrix}, \tag{1.78}$$

and

$$\boldsymbol{v}_- = \frac{1}{\sqrt{2}} \begin{pmatrix} 1_x \\ -i_y \\ 0_z \end{pmatrix}, \tag{1.79}$$

These eigenvectors (normalized in Eqs. (1.78) and (1.79)) correspond to circularly left polarized light and circularly right polarized light, respectively. $\boldsymbol{v}_+$ has a spin $s = +1$ eigenvalue ($S_z\boldsymbol{v}_+ = +\boldsymbol{v}_+$), and $\boldsymbol{v}_-$ has a spin $s = -1$ eigenvalue ($S_z\boldsymbol{v}_- = -\boldsymbol{v}_-$).

As an example of a paraxial beam without a well-defined spin, we can consider a beam in Eq. (1.71) with a linear polarization vector

$$\boldsymbol{v}_x = \begin{pmatrix} 1_x \\ 0_y \\ 0_z \end{pmatrix}. \tag{1.80}$$

The spin associated with this vector is ill-defined because $\boldsymbol{v}_x$ is not an eigenvalue

of S_z. In fact, $\boldsymbol{v}_x$ can be written as the sum of two different contributions with opposite spin, $\boldsymbol{v}_x \propto \boldsymbol{v}_+ + \boldsymbol{v}_-$.

Total angular momentum

From the discussion above, a paraxial beam with field

$$\boldsymbol{E}_{LG}(\boldsymbol{r},\omega) = LG_l^q(\boldsymbol{r})e^{i(kz-\omega t)}\boldsymbol{v}_\pm \tag{1.81}$$

has a well-defined spin and orbital angular momentum. Thus if we define the total angular momentum as

$$\overleftrightarrow{\boldsymbol{J}} = \overleftrightarrow{\boldsymbol{S}} + \boldsymbol{L}, \tag{1.82}$$

$\boldsymbol{E}_{LG}$ is an eigenfunction of $J_z = \overleftrightarrow{\boldsymbol{J}} \cdot \boldsymbol{u}_z$ with eigenvalue

$$m = l + s. \tag{1.83}$$

1.4.2 Beyond the paraxial approximation

Helicity and total angular momentum

We consider a field that is non-paraxial, such as, a strongly focused beam or the field scattered by a nanoparticle. In this case, the orbital and the spin angular momentum become ill-defined because the polarization and the direction of propagation become position-dependent, and the orbital and spin angular momentum values are defined as the eigenvalues with respect to the orbital and spin angular momentum operators projected onto the direction of propagation. To avoid these issues, we can use two alternative quantities to describe the angular momentum properties of the field. On the one hand, it is convenient to work directly with the total angular momentum [55], as the eigenvalues from J_z are well defined for some solutions of Maxwell's equations, such as the Mie's multipoles (see below). On the other hand, we can address the polarization properties of light by defining the helicity as the spin projected in the direction of propagation. Formally, the helicity operator is

$$\overleftrightarrow{\boldsymbol{\Lambda}} = \overleftrightarrow{\boldsymbol{S}} \cdot \boldsymbol{u}_k = \frac{\nabla\times}{k}, \tag{1.84}$$

where in the last identity, we have used Eq. (1.77) and the fact that $\boldsymbol{u}_k$, the unity vector along the direction of propagation can be found using the operator $\overleftrightarrow{\boldsymbol{u}}_k = -i\nabla/k$ [36,64]. Notably, the eigenvectors of these operators are the Riemann-Silberstein vectors as defined in Eq. (1.8). Thus, any electromagnetic field that can be written as a $\boldsymbol{F}_+$ or $\boldsymbol{F}_-$ Riemann-Silberstein vectors has a well-defined helicity.

Multipoles with well-defined total angular momentum

We can redefine the standard Mie theory multipoles described in section 1.3 to obtain multipoles with a well-defined total angular momentum operator. According

to reference [65], these multipoles are

$$\boldsymbol{A}^{(M)}_{b,n,m}(\boldsymbol{r},\omega) = \\ = \frac{i(-1)^m}{(\mathrm{sign}(m))^m\sqrt{n(n+1)}}\sqrt{\frac{2n+1}{4\pi}\frac{(n-|m|)!}{(n+|m|)!}}(\boldsymbol{M}_{b,n,|m|,e} + i\mathrm{sign(m)}\boldsymbol{M}_{b,n,|m|,e}) \tag{1.85}$$

$$\boldsymbol{A}^{(E)}_{b,n,m}(\boldsymbol{r},\omega) = \\ = \frac{(-1)^m}{(\mathrm{sign}(m))^m\sqrt{n(n+1)}}\sqrt{\frac{2n+1}{4\pi}\frac{(n-|m|)!}{(n+|m|)!}}(\boldsymbol{N}_{b,n,|m|,e} + i\mathrm{sign(m)}\boldsymbol{N}_{b,n,|m|,o}) \tag{1.86}$$

where $\mathrm{sign}(m) = 1$ for $m \geq 0$ and $\mathrm{sign}(m) = -1$ for $m < 0$. $\boldsymbol{A}^{(E)}_{b,n,m}$ and $\boldsymbol{A}^{(M)}_{b,n,m}$ are a combination of electric ($\boldsymbol{N}_{b,n,m,\sigma}$) and magnetic ($\boldsymbol{M}_{b,n,|m|,\sigma}$) multipoles, respectively and they, hence, maintain their respective electric or magnetic character. Because of the orthogonal relationships between $\boldsymbol{M}_{b,n,|m|,\sigma}$ and $\boldsymbol{N}_{b,n,|m|,\sigma}$, $\boldsymbol{A}^{(M)}_{b,n,m}$ are $\boldsymbol{A}^{(E)}_{b,n,m}$ also orthogonal, *i.e.*,

$$\iiint drd\Omega \boldsymbol{A}^{(X)}_{b,n,m}(\boldsymbol{r},\omega)\boldsymbol{A}^{(X')}_{b',n',m'}(\boldsymbol{r},\omega) = 0, \tag{1.87}$$

for $b \neq b'$, $n \neq n'$, $m \neq m'$, or $X \neq X'$, with $X = M$ or E. The new $\boldsymbol{A}^{(M)}_{b,n,m}$ and $\boldsymbol{A}^{(E)}_{b,n,m}$ electric multipoles are eigenvalues of J_z, the z-component of the total angular momentum operator,

$$J_z\boldsymbol{A}^{(M)}_{b,n,m}(\boldsymbol{r},\omega) = m\boldsymbol{A}^{(M)}_{b,n,m}(\boldsymbol{r},\omega), \tag{1.88}$$

and

$$J_z\boldsymbol{A}^{(E)}_{b,n,m}(\boldsymbol{r},\omega) = m\boldsymbol{A}^{(E)}_{b,n,m}(\boldsymbol{r},\omega). \tag{1.89}$$

Further analysis of the angular momentum properties of $\boldsymbol{A}^{(M)}_{b,n,m}$ and $\boldsymbol{A}^{(E)}_{b,n,m}$ can be found in references [65, 66].

Multipoles with well-defined helicity

The $\boldsymbol{A}^{(M)}_{b,n,m}$ and $\boldsymbol{A}^{(E)}_{b,n,m}$ multipoles have well-defined total angular momentum, but not well-defined helicity. Next, we define a set of combinations of $\boldsymbol{A}^{(M)}_{b,n,m}$ and $\boldsymbol{A}^{(E)}_{b,n,m}$ that results in a new basis of multipoles with well-defined helicity. To find these combinations, we use the expressions of the Riemann-Silberstein vectors, which are the eigenfunctions of the helicity operator (Eq. (1.8)), and are combinations of electric and magnetic fields (Eq. (1.7)). Thus, we first write the

electric and magnetic fields using the $\boldsymbol{A}^{(M)}_{b,n,m}$ and $\boldsymbol{A}^{(E)}_{b,n,m}$ multipoles[iv],

$$\boldsymbol{E}(\boldsymbol{r},\omega) = \sum_{n,m}[iC^{(E)}_{n,m}\boldsymbol{A}^{(E)}_{b,n,m}(\boldsymbol{r},\omega) + C^{(M)}_{n,m}\boldsymbol{A}^{(M)}_{b,n,m}(\boldsymbol{r},\omega)]. \tag{1.90}$$

By using this expression of the electric field and applying Eqs. (1.63), (1.85) and (1.86) on Maxwell's equations (Eq. (1.5)), we can obtain the expression of the magnetic field,

$$\boldsymbol{B}(\boldsymbol{r},\omega) = \frac{1}{c_0}\sum_{n,m}[C^{(M)}_{n,m}\boldsymbol{A}^{(E)}_{b,n,m}(\boldsymbol{r},\omega) - iC^{(E)}_{n,m}\boldsymbol{A}^{(E)}_{b,n,m}(\boldsymbol{r},\omega)]. \tag{1.91}$$

Using these expressions of $\boldsymbol{E}$ and $\boldsymbol{B}$ we can write the Riemann-Silberstein vectors in Eq. (1.9) as,

$$\boldsymbol{F}_{\pm}(\boldsymbol{r},\omega) = \sum_{n,m}(C^{(E)}_{l,m} + C^{(M)}_{l,m})[\boldsymbol{A}^{(M)}_{b,n,m}(\boldsymbol{r},\omega) \pm i\boldsymbol{A}^{(E)}_{b,n,m}(\boldsymbol{r},\omega)]. \tag{1.92}$$

$\boldsymbol{F}_{\pm}$ are eigenfunctions of the helicity operator with eigenvalue Λ. It can be proved [65–67] that each term in the sum of Eq. (1.92),

$$\boldsymbol{A}^{(\Lambda)}_{b,n,m}(\boldsymbol{r},\omega) = \boldsymbol{A}^{(M)}_{b,n,m}(\boldsymbol{r},\omega) + \Lambda i\boldsymbol{A}^{(E)}_{b,n,m}(\boldsymbol{r},\omega), \tag{1.93}$$

are also eigenfunctions of the helicity operator, $\overleftrightarrow{\boldsymbol{\Lambda}}$, with the same eigenvalue $\Lambda = \pm 1$, *i.e.* $\boldsymbol{A}^{(+)}_{b,n,m}$ satisfies $\overleftrightarrow{\boldsymbol{\Lambda}}\boldsymbol{A}^{(+1)}_{b,n,m}(\boldsymbol{r},\omega) = \boldsymbol{A}^{(+1)}_{b,n,m}(\boldsymbol{r},\omega)$, and $\boldsymbol{A}^{(-1)}_{b,n,m}$ satisfies $\overleftrightarrow{\boldsymbol{\Lambda}}\boldsymbol{A}^{(-1)}_{b,n,m}(\boldsymbol{r},\omega) = -\boldsymbol{A}^{(-1)}_{b,n,m}(\boldsymbol{r},\omega)$. Further, the $\boldsymbol{A}^{(\Lambda)}_{b,n,m}$ multipoles are also the z-components of total angular momentum, $J_z = \overleftrightarrow{\boldsymbol{J}}\cdot\boldsymbol{u}_z$. Thus, $\boldsymbol{A}^{(\Lambda)}_{b,n,m}$ constitutes the new multipoles we are looking for, which allows for decomposing any electromagnetic field on a basis well-suited to directly address the helicity and total angular momentum properties.

1.4.3 Scattering of a beam with well-defined angular momentum by a spherical nanoparticle

In chapter 5 we study the scattering of a focused light beam with well-defined angular momentum properties by a spherical nanoparticle. In this section, we show that the Mie's formalism described in section 1.4.2 allows for tackling this scattering process. We show in Fig. 1.12 a scheme of this scattering problem, an incident circularly-polarized Laguerre-Gauss beam focused by a high-numerical-aperture lens at the center of a spherical nanoparticle. Before focusing, the Laguerre-Gauss beam is a paraxial beam and thus has a well-defined value of the spin and the orbital angular momentum (see subsection 1.4.1). For example, we can consider

[iv] Note that for convenience, in equations (1.90) and (1.91) we chose to add a $\pi/2$ phase (*i.e.*, a i factor) between the electric and magnetic multipoles.

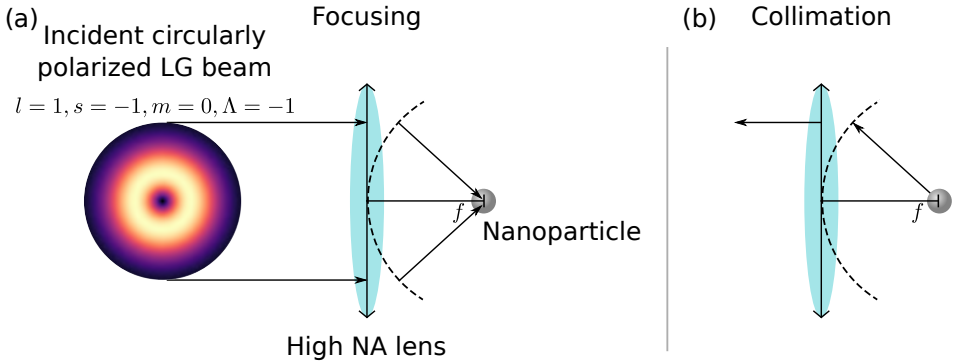

Figure 1.12: Scheme of the scattering process studied in section 1.4.3. (a) Scheme of the illumination: an incident circularly polarized Laguerre-Gauss (LG) beam is focused on the center of a small spherical nanoparticle by using a high numerical aperture lens. In the scheme we plot the amplitude distribution of a LG_l^0 beam with $l = 1$ and $s = -1$ (corresponding to circular right-polarization). These values result in a total angular momentum $m = 0$. (b) Scheme of the collimation process: the light back-scattered by the nanoparticle is collected and collimated by the same lens used for focusing. In the focusing process the field (in (a)) incident on the aperture of the lens (vertical arrow in the shaded blue area) is mapped onto a spherical surface of radius f (dashed line) and then rotated as described in section 1.4.3. The collimation (in (b)) corresponds to the inverse process, so that the field is evaluated in the same spherical surface, rotated, and then mapped onto the aperture of the lens.

a circularly right-polarized beam with a spatial distribution following a LG_1^0 (see Eq. (1.73)) Laguerre-Gauss, resulting in $s = -1$, $l = +1$, and $m = l + s = 0$. We consider that the beam propagates in the z-direction so that $\overleftrightarrow{\boldsymbol{\Lambda}} = S_z$ (Eq. (1.84)), and thus $s = \Lambda = -1$.

The scattered beam in the backward direction (*i.e.*, opposite to the propagation of the incident beam) is collimated with the same lens used to focus the incident beam. After the collimation we separate the field into two contributions, one with the same helicity as the incident beam, and another contribution with opposite helicity. The collimated beams are paraxial, and thus, we can also address the s, l, of the scattered fields. We next describe the equations that we use to implement all these steps of the scattering process.

The incident Laguerre-Gauss beam follows Eq. (1.81). This beam is focused by the lens at the plane $z_c = 0$. The first step is to write the focused field as an expansion of multipoles with well-defined helicity $\boldsymbol{A}^{(\Lambda)}_{b,n,m}$ of different order n. The multipoles $\boldsymbol{A}^{(\Lambda)}_{b,n,m}$ are defined in Eq. (1.93). In particular, we use multipoles with $b = 1$ ($\boldsymbol{A}^{(\Lambda)}_{1,n,m}$) (see section 1.3). The focused electric field is:

$$\boldsymbol{E}_{\text{foc}}(\boldsymbol{r}, \omega) = \sum_{n=0}^{\infty} \sqrt{2} C_n(\omega) \boldsymbol{A}^{(\Lambda)}_{1,n,m}(\boldsymbol{r}, \omega), \tag{1.94}$$

where, ω is the angular frequency of the light, Λ is the helicity of the incident beam

(corresponding to its circular polarization, see subsection 1.4.1), and we only need to sum over multipoles with m equal to the angular momentum of the beam. For convenience, the $\boldsymbol{r}$ coordinates in Eq. (1.94) are chosen to be centered at the focal point of the lens (not to be confused with the r_c, ϕ_c, and θ_c coordinates of the LG beam in Eq. (1.73)). The coefficients C_n are,

$$C_n = i^{(n-1)} k\sqrt{2\pi}\sqrt{2n+1}\int_0^{\theta_{\max}} \mathfrak{d}^n_{m,\Lambda}(\theta)\sin(\theta) LG^l_q(f\sin(\theta),0,0)\sqrt{\cos(\theta)} f e^{-ikf} d\theta, \tag{1.95}$$

where $\mathfrak{d}^n_{m,\Lambda}$ is the small Wigner d-function [68] and $\theta_{\max}$ is the maximal half-angle of the lens of numerical aperture $NA = n\sin(\theta_{\max})$ (n is the refractive index of the medium after the lens). These coefficients are derived in reference [67] using the aplanatic lens model [35] (see scheme on Fig. 1.12a). In brief, the modeling of the focusing process can be separated into three steps. First, the incident electric field in the aperture of the lens is mapped onto a reference surface with coordinates $r = f$, $\varphi_s \in [0, 2\pi]$, and $\theta \in [\pi - \theta_{\max}, \pi]$ (*i.e.* a spherical cap situated at the focal distance, f, from the nanoparticle). Second, the mapped (vectorial) electric field is rotated such that from each point of the reference surface emerges a plane wave that propagates toward the focal point. This rotation results in the $\mathfrak{d}^n_{m,\Lambda}$ function in Eq. (1.95). Third, we obtain the field at the focal point as the sum of all these plane waves. The sum of these plane waves leads to the integration in Eq. (1.95).

We next calculate the fields scattered by the spherical nanoparticle under the illumination of the strongly focused Laguerre-Gauss beams. Equation (1.61) describes the response of a spherical nanoparticle under plane wave illumination. The extension of this solution to our case is [67],

$$\boldsymbol{E}^{\text{sca}}_{LG}(\boldsymbol{r},\omega) = \sum_{n=0}^{\infty} C_n(\omega)\left(V_n(\omega)\boldsymbol{A}^{(\Lambda)}_{3,n,m}(\boldsymbol{r},\omega) + W_n(\omega)\boldsymbol{A}^{(-\Lambda)}_{3,n,m}(\boldsymbol{r},\omega)\right), \tag{1.96}$$

where V_n and W_n correspond to combinations of the a_n and b_n coefficients (in Eqs. (1.62a) and (1.62b), respectively),

$$V_n(\omega) = -\frac{a_n(\omega)+b_n(\omega)}{2}, \tag{1.97}$$

$$W_n = \frac{a_n(\omega)-b_n(\omega)}{2}. \tag{1.98}$$

Note that due to the angular momentum properties of the $\boldsymbol{A}^{(\Lambda)}_{b,n,m}$ multipoles (see Eqs. (1.88), (1.89), and (1.93)) the scattered field in Eq. (1.96) preserves the total angular momentum of the incoming and focused beam. This preservation is a consequence of the rotational symmetry of the nanoparticle and will be exploited in chapter 5.

The backscattered field in Eq. (1.96) is collimated through the same lens that focuses the incident beam. To model this collimation using the aplanatic lens model, we follow the inverse process of the focusing. The backscattered field is evaluated at the same spherical reference surface as for the focus (dashed line in Fig. 1.12b). We then perform the inverse rotation compared to the focusing process so that the Poynting vectors of the scattered field become perpendicular to the aperture of the

lens at all points. Finally, we map the rotated field of the reference aperture onto the surface of the lens. This collimation process corresponds mathematically to:

$$\boldsymbol{E}_{LG}^{\mathrm{Col}}(r_{\mathrm{c}}, \varphi_{\mathrm{c}}, z_{\mathrm{c}} = 0, \omega) = \hat{R}(f, \varphi_{\mathrm{s}}, \theta_{\mathrm{s}}) \cdot \boldsymbol{E}_{LG}^{\mathrm{sca}}(f, \varphi_{\mathrm{s}}, \theta_{\mathrm{s}}, \omega) \cos(\theta_{\mathrm{s}})^{-1}, \tag{1.99}$$

where $\boldsymbol{E}_{LG}^{\mathrm{Col}}$ is the collimated field, (r_{c}, φ_{c}, z_{c}) are the cylindrical coordiantes in the aperture of the lens (with $z_{\mathrm{c}} = 0$ and $r_{\mathrm{c}} = f \sin(\theta_{\mathrm{s}})$), and $\hat{R}(f, \varphi_{\mathrm{s}}, \theta_{\mathrm{s}})$ is the position-dependent Euler rotation matrix:

$$\begin{aligned} \hat{R}(f, \varphi_{\mathrm{s}}, \theta_{\mathrm{s}}) = &\begin{pmatrix} \sin(\varphi_{\mathrm{s}}) & -\cos(\varphi_{\mathrm{s}}) & 0 \\ \cos(\varphi_{\mathrm{s}}) & \sin(\varphi_{\mathrm{s}}) & 0 \\ 0 & 0 & 1 \end{pmatrix} \cdot \\ &\begin{pmatrix} 1 & 0 & 0 \\ 0 & \cos(\theta_{\mathrm{s}}) & -\sin(\theta_{\mathrm{s}}) \\ 0 & \sin(\theta_{\mathrm{s}}) & \cos(\theta_{\mathrm{s}}) \end{pmatrix} \cdot \begin{pmatrix} \sin(\varphi_{\mathrm{s}}) & \cos(\varphi_{\mathrm{s}}) & 0 \\ -\cos(\varphi_{\mathrm{s}}) & \sin(\varphi_{\mathrm{s}}) & 0 \\ 0 & 0 & 1 \end{pmatrix}. \end{aligned} \tag{1.100}$$

Last, the $\cos(\theta_{\mathrm{s}})^{-1}$ factor in Eq. (1.99) accounts for the differences between the differential area at the reference spherical surface, dA_S, and the differential area at the aperture of the lens, dA_L ($dA_S = dA_L / \cos(\theta_{\mathrm{s}})$, see chapter 3 of reference [35]).

CHAPTER 2

FUNDAMENTALS OF THE QUANTUM DESCRIPTION OF THE INTERACTION OF LIGHT AND OPTICAL RESONATORS

Motivated by the quick development of the maser and the laser in the 1950s and 1960s, the photonic community developed a quick interest in developing a general quantum optics framework. One of the outstanding achievements of many scientists (Roy J. Glauber, John R. Klauder, E. C. George Sudarshan, and Leonard Mandel, among others) was to introduce such a quantum optics framework and show that this framework is not only limited to describe quantum effects, but it can also describe classical optics phenomena [69–71]. This chapter is devoted to lay down some fundamental concepts on the quantum optics foundations used in this thesis. We begin by reviewing the basis of the quantum formalism (section 2.1) and how it can be applied to describe the quantization of light (section 2.2). In section 2.3, we present a quantum approach to study the interaction of both classical and quantum states of light with a beam splitter, which is the basis of the work presented in chapter 5. Furthermore, the beam splitter is the main element in many interferometers, including the Hanbury-Brown and Twiss (HBT) interferometer, a device that enables the characterization of the number of photons emitted by a source. In section 2.4, we introduce the quantum formalism of the HBT interferometer, and use it to analyze the response of the HBT to four different types of light source: a thermal (classical) source, a coherent (classical) source, a single photon (quantum) source, and a realistic two-photon (quantum) source.

In sections 2.5 and 2.6 we lay down the theoretical framework that we use in chapter 4 to analyze the quantum response of a standard cavity-quantum

electrodynamics (cavity-QED) system composed by a two-level-system (*e.g.*, a molecule or a quantum dot) interacting with an optical cavity (*e.g.*, a plasmonic nanostructure). This system comprises the same elements as those introduced in chapter 1, *i.e.*, light interacting with a nanostructure (cavity) and a two-level-system (TLS). However, in contrast with chapter 1 where the focus is placed on the classical response of the cavity and of the TLS independently, here we focus on the quantum description of the joint cavity-TLS (CTS). In section 2.5, we review the derivation of the state-of-the-art description of the Hamiltonian of a CTS, valid for any value of the interaction strength between the cavity and the TLS. Last, in section 2.6 we address the dynamical evolution of a generic quantum system (such as a CTS) taking into account its interaction with the environment. In particular, in this section, we review the derivation of the master equation formalism, which is one of the most widely used descriptions of the interaction of a quantum system with its environment [21, 72, 73].

2.1 States of light and observables

Before describing the quantization of light or how quantized light interacts with matter, we briefly introduce the main building blocks of the quantum mechanics formalism. In quantum mechanics, physical systems are characterized by their state. In particular, the quantum states of the system can be interpreted as a probability distribution for the outcomes of possible measurements.

In a simple situation, a quantum state can be written as a "ket-vector" (or simply "ket"), $|\Psi\rangle$, or as a "bra-vector (or simply "bra"), $\langle\Psi| = |\Psi\rangle^\dagger$, where $\dagger$ indicates the complex conjugate operation [74]. A quantum state that can be written as a single ket $|\Psi\rangle$ (or bra) is said to be pure. However, not all systems can be described as pure states. To address this situation, we introduce next a more general description, given by the density matrix formalism. For a pure $|\Psi\rangle$ state, the density matrix operator is simply the projector of $|\Psi\rangle$ [74], *i.e.*,

$$\hat{\rho}_{\text{Pure}} = |\Psi\rangle\langle\Psi| . \tag{2.1}$$

Because every state must satisfy the normalization $\langle\Psi|\Psi\rangle = 1$, the density matrix of a pure state is idempotent, $\hat{\rho}^n_{\text{Pure}} = \hat{\rho}_{\text{Pure}}$ (for any positive integer n).

Crucially, the density matrix formalism is also well suited to describe mixed or non-pure states. The density matrix operator of mixed states describes statistical ensembles of pure states, and can be written as

$$\hat{\rho}_{\text{Mix}} = \sum_i p_i |\Psi_i\rangle\langle\Psi_i| , \tag{2.2}$$

where p_i (with $\sum_i p_i = 1$ and $p_i < 1$ for all i) is the probability of finding the system in the $|\Psi_i\rangle$ pure state. Equation (2.2) implies that the density matrix operator of a mixed system is not idempotent, $\hat{\rho}^n_{\text{Mix}} \neq \hat{\rho}_{\text{Mix}}$ (for any integer $n > 1$). To quantify how much a mixed state departs from a pure state, we evaluate the

loss of purity

$$\mathcal{L} = 1 - \mathrm{Tr}\{\hat{\rho}^2\} = 1 - \sum_i \langle \Psi_i | \, \hat{\rho}^2 \, | \Psi_i \rangle \tag{2.3}$$

where $\hat{\rho}$ is constituted by either a mixed ($\hat{\rho}_{\mathrm{Mix}}$) or a pure ($\hat{\rho}_{\mathrm{Pure}}$) state. For pure states,

$$\mathrm{Tr}\{\hat{\rho}^2_{\mathrm{Pure}}\} = 1, \tag{2.4}$$

and then $\mathcal{L} = 0$. However, for mixed states,

$$\mathrm{Tr}\{\hat{\rho}^2_{\mathrm{Mix}}\} \neq 1. \tag{2.5}$$

Moreover, it can be shown that $\mathrm{Tr}\{\hat{\rho}^2_{\mathrm{Mix}}\} < 1$ and $\mathrm{Tr}\{\hat{\rho}^2_{\mathrm{Mix}}\} = 1/\mathcal{N}$ corresponds to maximally mixed states where $\mathcal{N}$ is the number of states in the basis of the $\hat{\rho}_{\mathrm{Mix}}$ state. Thus, $\mathcal{L} < 1$ for mixed states, and $\mathcal{L} = 1 - 1/\mathcal{N}$ for a maximally mixed state.

As mentioned above, quantum states describe the probability distribution of different outcomes of a possible measurement of a system. Observables, on the other hand, describe a measurable physical quantity. The observables are represented by operators $\hat{O}$ acting on its Hilbert space [74]. Using the density matrix formalism, we can describe the mean value (or expected value) of measurement as

$$\langle \hat{O} \rangle = \mathrm{Tr}\{\hat{\rho}\hat{O}\}, \tag{2.6}$$

which for pure states simplifies to

$$\langle \hat{O} \rangle = \langle \Psi | \hat{O} | \Psi \rangle \, . \tag{2.7}$$

2.2 Quantization of light

In this section, we derive the quantized Hamiltonian that describes the energy and time evolution of an electromagnetic plane wave in vacuum that either propagates freely or is confined in a cavity. We start by considering a single mode corresponding to a plane wave with wave vector $\boldsymbol{k}$,

$$\boldsymbol{E}_{\boldsymbol{k}}(\boldsymbol{r}, \omega) = E_{\boldsymbol{k}}(\omega) e^{i\boldsymbol{k}\cdot\boldsymbol{r}} \boldsymbol{u}_{\boldsymbol{k}}, \tag{2.8}$$

where ω is the frequency of the field, and $\boldsymbol{u}_{\boldsymbol{k}}$ is the unity vector of $\boldsymbol{E}_{\boldsymbol{k}}$ (the expressions here can be extended to more complex fields by describing them as a superposition of single mode plane waves). The classical energy $\mathcal{E}_{\boldsymbol{k}}$ of this single-mode wave is described by the classical Hamiltonian of the electromagnetic wave, $\mathcal{H}_{\boldsymbol{k}}$, in a volume $\mathcal{V}$,

$$\mathcal{E}_{\boldsymbol{k}} = \mathcal{H}_{\boldsymbol{k}} = \iiint_{\mathcal{V}} \frac{1}{2} \left(\varepsilon_0 \mathrm{Re}\{\boldsymbol{E}_{\boldsymbol{k}}(\boldsymbol{r}, \omega)^2\} + \frac{1}{\mu_0} \mathrm{Re}\{\boldsymbol{B}_{\boldsymbol{k}}(\boldsymbol{r}, \omega)^2\} \right) d\boldsymbol{r}, \tag{2.9}$$

where $\mathrm{Re}\{\boldsymbol{E}_{\boldsymbol{k}}(\boldsymbol{r},\omega)\}$ and $\mathrm{Re}\{\boldsymbol{B}_{\boldsymbol{k}}(\boldsymbol{r},\omega)\}$ are the real part of the complex electric and magnetic field, respectively. Using the equality between electric and magnetic energy of a plane wave[v] and considering that $\boldsymbol{E}_{\boldsymbol{k}}(\boldsymbol{r},\omega)$ is orthogonal for modes of different $\boldsymbol{k}$[vi], Eq. (2.9) simplifies to

$$\mathcal{H}_{\boldsymbol{k}} = \varepsilon_0 \mathcal{V} |E(\omega)|^2. \tag{2.10}$$

Next, we redefine the electric field in terms of two conjugate variables,

$$\tilde{\Pi}_{\boldsymbol{k}}(\omega) = \frac{\sqrt{\varepsilon_0 \mathcal{V}}}{\omega} \mathrm{Re}\{E_{\boldsymbol{k}}(\omega)\}, \tag{2.11}$$

and

$$\tilde{p}_{\boldsymbol{k}}(\omega) = \sqrt{\varepsilon_0 \mathcal{V}} \mathrm{Im}\{E_{\boldsymbol{k}}(\omega)\}, \tag{2.12}$$

where $\tilde{p}_{\boldsymbol{k}}(\omega)$ plays the role of the classical linear momentum and $\tilde{\Pi}_{\boldsymbol{k}}(\omega)$ is an analogue of the position (note that these variables are real valued). We can then write the electric field as

$$E_{\boldsymbol{k}}(\omega) = \sqrt{\varepsilon_0 \mathcal{V}} (\omega \tilde{\Pi}_{\boldsymbol{k}}(\omega) + i \tilde{p}_{\boldsymbol{k}}(\omega)), \tag{2.13}$$

Using Eq. (2.13), the classical Hamiltonian in Eq. (2.10) becomes

$$\mathcal{H}_{\boldsymbol{k}} = \frac{1}{2} (\omega^2 \tilde{\Pi}_{\boldsymbol{k}}(\omega)^2 + \tilde{p}_{\boldsymbol{k}}(\omega)^2), \tag{2.14}$$

which corresponds to the canonical Hamiltonian of a harmonic oscillator.

To find the quantum description of the Hamiltonian given in Eq. (2.14), we use the correspondence principle and convert the classical variables $\tilde{\Pi}_{\boldsymbol{k}}$ and $\tilde{p}_{\boldsymbol{k}}$ into quantum momentum and position operators, $\hat{\Pi}_{\boldsymbol{k}}$ and $\hat{p}_{\boldsymbol{k}}$, respectively. Thus the quantum Hamiltonian reads:

$$\hat{\mathcal{H}}_{\boldsymbol{k}} = \frac{1}{2} (\omega^2 \hat{\Pi}_{\boldsymbol{k}}(\omega)^2 + \hat{p}_{\boldsymbol{k}}(\omega)^2), \tag{2.15}$$

where $\hat{\Pi}_{\boldsymbol{k}}(\omega)$ and $\hat{p}_{\boldsymbol{k}}(\omega)$ satisfy the commutation relation $[\hat{\Pi}_{\boldsymbol{k}}(\omega), \hat{p}_{\boldsymbol{k}}(\omega)] = \hat{\Pi}_{\boldsymbol{k}}(\omega)\hat{p}_{\boldsymbol{k}}(\omega) - \hat{p}_{\boldsymbol{k}}(\omega)\hat{\Pi}_{\boldsymbol{k}}(\omega) = i\hbar$, $\hbar$ being the reduced Plank constant (this relation corresponds to the uncertainty principle) [70].

So far we have quantized the fields by expressing the electromagnetic fields in terms of quantized physical quantities with the "$\hat{\Pi}_{\boldsymbol{k}}$-position" and "$\hat{p}_{\boldsymbol{k}}$-momentum" operators. However, it is really convenient to introduce next the so-called "second-

[v] The equality between electric and magnetic energy assumes the absence of external charges and currents. In this situation, evaluating Faraday's law (first Maxwell's equation in Eq. (1.5)) with monochromatic fields ($\boldsymbol{E}(t) \propto e^{i\omega t}$ and $\boldsymbol{B}(t) \propto e^{i\omega t}$) results in $c_0^2 \mathrm{Re}\{\boldsymbol{B}_{\boldsymbol{k}}\}^2 = \mathrm{Re}\{\boldsymbol{E}_{\boldsymbol{k}}\}^2$. This result can also be extended to polychromatic waves by describing them as a superposition of monochromatic waves.

[vi] The orthogonal light-modes satisfy $\iiint_V \boldsymbol{E}_{\boldsymbol{k}}(\omega) \boldsymbol{E}_{\boldsymbol{k}'}(\omega')^* d\boldsymbol{r} = \mathcal{V} |E(\omega_{\boldsymbol{k}})|^2 \delta^K_{\omega,\omega'} \delta^K_{\boldsymbol{k},\boldsymbol{k}'}/2$ (where δ^K is the Kronecker delta).

quantization" operators. These operators establish a framework to describe fields in terms of particles, which can be created or destroyed. These second quantization operators can be written as a combination of $\hat{\Pi}_{\boldsymbol{k}}(\omega)$ and $\hat{p}_{\boldsymbol{k}}(\omega)$,

$$\hat{a}_{\boldsymbol{k}}(\omega) = \sqrt{2\hbar\omega_{\boldsymbol{k}}}(\omega\hat{\Pi}_{\boldsymbol{k}}(\omega) + i\hat{p}_{\boldsymbol{k}}(\omega)), \tag{2.16}$$

and

$$\hat{a}^{\dagger}_{\boldsymbol{k}}(\omega) = \sqrt{2\hbar\omega_{\boldsymbol{k}}}(\omega\hat{\Pi}_{\boldsymbol{k}}(\omega) - i\hat{p}_{\boldsymbol{k}}(\omega)), \tag{2.17}$$

respectively. The operators $\hat{a}^{\dagger}_{\boldsymbol{k}}(\omega)$ and $\hat{a}_{\boldsymbol{k}}(\omega)$ correspond to the creation and annihilation of a quantum of light, *i.e.*, a photon. Applying $\hat{a}^{\dagger}_{\boldsymbol{k}}(\omega)$ and $\hat{a}_{\boldsymbol{k}}(\omega)$ to a state with n-photons, $|n\rangle$, results in increasing or decreasing of the number of photons in the state by one unit:

$$\hat{a}_{\boldsymbol{k}}(\omega)\,|n\rangle = \sqrt{n}\,|n-1\rangle\,, \tag{2.18}$$

$$\hat{a}^{\dagger}_{\boldsymbol{k}}(\omega)\,|n\rangle = \sqrt{n+1}\,|n+1\rangle\,. \tag{2.19}$$

Hence, we can define the number of photons operator as $\hat{n}(\omega) = \hat{a}^{\dagger}_{\boldsymbol{k}}(\omega)\hat{a}_{\boldsymbol{k}}(\omega)$, where

$$\langle n|\,\hat{a}^{\dagger}_{\boldsymbol{k}}(\omega)\hat{a}_{\boldsymbol{k}}(\omega)\,|n\rangle = n. \tag{2.20}$$

Another crucial property of the operators $\hat{a}_{\boldsymbol{k}}(\omega)$ and $\hat{a}^{\dagger}_{\boldsymbol{k}}(\omega)$ is their commutator relationship,

$$[\hat{a}_{\boldsymbol{k}}(\omega), \hat{a}^{\dagger}_{\boldsymbol{k}}(\omega)] = 1, \tag{2.21}$$

which is a consequence of the commutation properties of $\hat{q}_{\boldsymbol{k}}(\omega)$ and $\hat{p}_{\boldsymbol{k}}(\omega)$.

Finally, we write the quantum Hamiltonian in terms of the creation and destruction operators,

$$\hat{\mathcal{H}}_{\boldsymbol{k}} = \hbar\omega\hat{a}^{\dagger}_{\boldsymbol{k}}(\omega)\hat{a}_{\boldsymbol{k}}(\omega) + \frac{1}{2}\hbar\omega, \tag{2.22}$$

The $1/2$ term corresponds to the energy of the vacuum state, and it is common to renormalize it to zero, so the Hamiltonian $\hat{\mathcal{H}}_{\boldsymbol{k}}$ becomes

$$\hat{\mathcal{H}}_{\boldsymbol{k}} \to \hbar\omega\hat{a}^{\dagger}_{\boldsymbol{k}}(\omega)\hat{a}_{\boldsymbol{k}}(\omega). \tag{2.23}$$

2.3 Quantum transformations by a lossless and a lossy beam splitter

One of the simplest devices to manipulate states of light (classical or quantum) is a beam splitter. Beam splitters are a fundamental tool in optics that split the incoming light into two paths of propagation, as we show in the schematics of Fig. 2.1. Beam splitters are extensively used to control both classical and quantum states of light. In this subsection we first briefly review the standard description of the classical and quantum transformations induced by a standard lossless beam

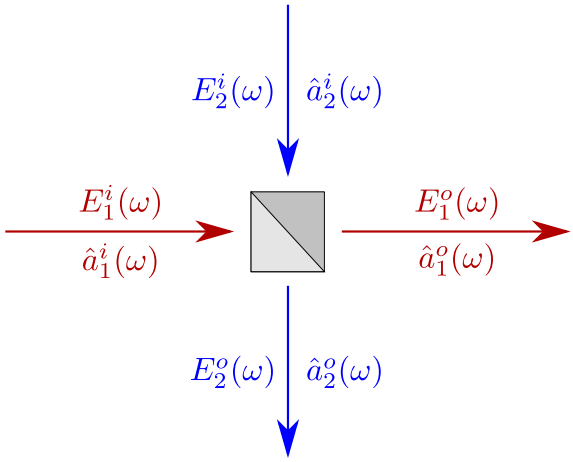

Figure 2.1: Sketch of the classical and quantum transformation of light induced by a standard beam splitter. In the classical description, the input E_1^i and E_2^i modes are transformed onto the output E_1^o and E_2^o modes. In the quantum formalism, the input quantum $\hat{a}_1^i$ and $\hat{a}_2^i$ operators are transformed onto the output $\hat{a}_1^o$ and $\hat{a}_2^o$ operators.

splitter. We then extend this formalism to describe the transformation by a lossy beam splitter, *i.e.*, a beam splitter that can dissipate the incident photons and thus making it *lose* their corresponding energy. In this thesis we use the quantum transformation of beam splitters to describe the process occurring in a Hanbury-Brown Twiss interferometer in section 2.4, and to study the interaction between quantum states of light and a nanostructure in chapter 5.

Classical transformation by a beam splitter

We first consider the standard description of the classical transformation of light by a standard (lossless) beam splitter. This transformation can be understood as a change of basis between two input modes at the beam splitter, $E_1^i(\omega)$ and $E_2^i(\omega)$, and the two output modes of the beam splitter $E_1^o(\omega)$ and $E_2^o(\omega)$. The input and output channels with the corresponding fields are shown in the scheme of Fig. 2.1. The input $E_1^i(\omega)$ and $E_2^i(\omega)$ and output $E_1^o(\omega)$ and $E_2^o(\omega)$ modes are related by a unitary transformation [75],

$$\begin{aligned} E_1^o(\omega) &= t_1(\omega)E_1^i(\omega) + r_1(\omega)E_2^i(\omega), \\ E_2^o(\omega) &= r_2(\omega)E_1^i(\omega) + t_2(\omega)E_2^i(\omega), \end{aligned} \tag{2.24}$$

where t_1 and t_2 are the transmittance coefficients, and r_1 and r_2 are the reflectance coefficients of the beam splitter [76]. For a lossy beam splitter, t_1, t_2, r_1, and r_2 can take any arbitrary value as long the energy of the fields at the output of the beam splitter is lower than the value of the energy of the fields at the input of the beam splitter, *i.e.*, $|E_1^o(\omega)|^2 + |E_2^o(\omega)|^2 < |E_1^i(\omega)|^2 + |E_2^i(\omega)|^2$.

On the other hand, for a lossless beam splitter, the energy of the input fields is the same as the output fields, *i.e.*, $|E_1^o(\omega)|^2 + |E_2^o(\omega)|^2 = |E_1^i(\omega)|^2 + |E_2^i(\omega)|^2$. The conservation of energy imposes the transmittance t-coefficients and the reflectance r-coefficients to satisfy [75, 76]

$$|t_1(\omega)|^2 + |r_1(\omega)|^2 = |t_2(\omega)|^2 + |r_2(\omega)|^2 = 1, \tag{2.25}$$

and

$$t_1(\omega)r_2(\omega)^* + r_1(\omega)t_2(\omega)^* = 0. \tag{2.26}$$

These constraints on t_1, t_2, r_1, and r_2 allow us to write Eq. (2.24) in terms of a single transmittance, and a single reflectance coefficient [75, 77, 78],

$$\begin{aligned} E_1^o(\omega) &= t(\omega)E_1^i(\omega) + r(\omega)E_2^i(\omega), \\ E_2^o(\omega) &= r(\omega)E_1^i(\omega) + t(\omega)E_2^i(\omega), \end{aligned} \tag{2.27}$$

where t and r must satisfy $|r(\omega)|^2 + |t(\omega)|^2 = 1$ and $r(\omega)t(\omega) = -(r(\omega)t(\omega))^*$.

Quantum transformation by an energy-conserving beam splitter

In quantum optics, the beam splitter transformation also corresponds to a change of basis between the output and the input states. Importantly, in quantum optics, this change of basis is defined by the annihilation operators and not directly by the quantum states [70, 77, 78]. Following the procedure of quantization of electromagnetic fields used in section 2.2, we introduce a set of $\hat{a}_1^i(\omega)$ and $\hat{a}_2^i(\omega)$ annihilation operators that define the orthogonal input modes of the beam splitter and another set of $\hat{a}_1^o(\omega)$ and $\hat{a}_2^o(\omega)$ annihilation operators that define the orthogonal output modes (Fig. 2.1). The relationship between the input and output quantum operators of a lossless beam splitter is analogous to the classical transformation introduced in Eq. (2.27) [70, 77, 78],

$$\begin{aligned} \hat{a}_1^o(\omega) &= t(\omega)\hat{a}_1^i(\omega) + r(\omega)\hat{a}_2^i(\omega), \\ \hat{a}_2^o(\omega) &= r(\omega)\hat{a}_1^i(\omega) + t(\omega)\hat{a}_2^i(\omega), \end{aligned} \tag{2.28}$$

where t and r are the same transmittance and reflectance coefficients as in the classical description. The close connection between the classical and quantum transformation is due to the fact that Maxwell's equations determine the evolution of electromagnetic modes both in the classical and quantum regimes [64].

Quantum transformation by a lossy beam splitter

We next consider the quantum transformation of a lossy beam splitter. In this case, the output state of the lossy beam splitter does not conserve the energy of the incident quantum state, which means that the output state can have the same or fewer photons than the incident state. We model the "dissipation" modes (also called "ancilla" modes [79]) by introducing the Langevin $\hat{L}_1$ and $\hat{L}_2$ operators associated

with losses due, for example, to fluctuating currents in the beam splitter [78]. These operators are added directly to the quantum transformation in Eq. (2.28), leading to the quantum transformation of a lossy beam splitter [78],

$$\begin{aligned}\hat{a}_1^o(\omega) &= t_1(\omega)\hat{a}_1^i(\omega) + r_1(\omega)\hat{a}_2^i(\omega) + \hat{L}_1(\omega),\\ \hat{a}_2^o(\omega) &= r_2(\omega)\hat{a}_1^i(\omega) + t_2(\omega)\hat{a}_2^i(\omega) + \hat{L}_2(\omega).\end{aligned} \tag{2.29}$$

In the lossy beam splitter, there is no imposition for $t_1 = t_2$ or $r_1 = r_2$. However, t_1, t_2, r_1, and r_2 still correspond to the classical values of the transmittance and reflectance coefficients in Eq. (2.24). On the other hand, the Langevin operators in Eq. (2.29) must satisfy three requirements [78, 80, 81]: (i) their expected value must vanish,

$$\langle \hat{L}_1(\omega)\rangle = \langle \hat{L}_1^\dagger(\omega)\rangle = \langle \hat{L}_2(\omega)\rangle = \langle \hat{L}_2^\dagger(\omega)\rangle = 0, \tag{2.30}$$

(ii) the Langevin operators must commute with the input operators (*e.g.*, $[\hat{L}_1(\omega), \hat{a}_1^i(\omega)] = 0$), as the input fields and noise sources inside the beam splitter must be independent, and (iii) the Langevin operators do not change the canonical commutation relationships between the bosonic operators in Eq. (2.21). Additional properties of Langevin operators and their explicit form for a one-dimensional beam splitter (a very thin one-layer beam splitter) can be found in references [78, 80, 81].

2.4 The Hanbury-Brown and Twiss interferometer

The Hanbury-Brown and Twiss (HBT) interferometer is a simple device typically composed of a beam splitter and two detectors. The HBT has played a crucial role in the history of quantum optics because it enables to characterize the different states of light and it has shown how photons composing a state of light can interfere between them [69, 70, 82, 83]. In this section, we briefly review the measurements that can be performed with an HBT interferometer and how they relate to the statistics of the number of photons emitted by a light source. We first derive a mathematical formalism that describes the transformations produced in the HBT measurements (subsection 2.4.1). We then illustrate how to interpret the results from the HBT interferometry by applying this formalism to analyze the emission from a variety of canonical light sources (subsections 2.4.2-2.4.5).

2.4.1 General description of the Hanbury-Brown and Twiss interferometer

Figure 2.2 shows the schematics of a standard HBT interferometer: light incident along one input path of a beam splitter is divided into two paths. At the end of both paths, a detector, D_1 and D_2, is located for the horizontal and vertical paths, respectively. The HBT measures intensity correlations of light: the detection of

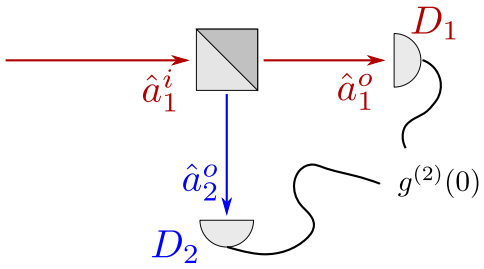

Figure 2.2: Sketch of a standard HBT interferometer. The input light, which can be a classical or quantum state of light, is splitted into two output paths by a beam splitter. In this section, we choose a "50-50" beam splitter, where light is reflected or transmitted with equal probability. We indicate this transformation with the input $\hat{a}_1^i$ and output $\hat{a}_1^o$ and $\hat{a}_2^o$ operators introduced in Fig. 2.1. Light leaving the beam splitter is converted into an electric current at two photodetectors D_1 and D_2, each of them at the end of the output paths. Both detectors are placed at the same distance from the beam splitter. The electric signal of both detectors is manipulated in an additional device to obtain the correlation measurement, $g^{(2)}(0)$.

light simultaneously at both detectors normalized to the individual detection at each detector. The resulting measurement of the HBT is the intensity correlation, $g^{(2)}(\tau)$, where τ indicates the time delay between light traveling from the beam-splitter to each detector. This thesis considers only the zero-delayed case with $\tau = 0$, corresponding to a situation where both detectors are set at the same distance from the beam splitter.

In a typical experiment based on HBT interferometry, $g^{(2)}(0)$ is obtained by taking the average of the intensity measured at each detector ($\langle \hat{I}_1 \rangle$ and $\langle \hat{I}_2 \rangle$ at D_1 and D_2, respectively) and the average of the multiplication of the intensity at both detectors ($\langle \hat{I}_1 \hat{I}_2 \rangle$). The resulting intensities correlation corresponds to

$$g^{(2)}(0)(\omega_1, \omega_2) = \frac{\langle \hat{I}_1(\omega_1) \hat{I}_2(\omega_2) \rangle}{\langle \hat{I}_1(\omega_1) \rangle \langle \hat{I}_2(\omega_2) \rangle}, \tag{2.31}$$

where ω_1 and ω_2 are the frequencies of detection of each detector (they correspond, for example, to the central frequency of a filter placed at the aperture of each detector) [83]. In this thesis we consider that the detectors are color-blind, *i.e.*, all photons are detected independently of their frequency. Thus we write the "color-blind" intensity correlations as

$$g^{(2)}(0) = \frac{\langle \hat{I}_1 \hat{I}_2 \rangle}{\langle \hat{I}_1 \rangle \langle \hat{I}_2 \rangle}, \tag{2.32}$$

where we are tracing out over the frequency degree of freedom.

The intensity operators are proportional to the corresponding number of photons operator: $\hat{I}_1 \propto \hat{a}_1^{o\dagger} \hat{a}_1^o$ and $\hat{I}_2 \propto \hat{a}_2^{o\dagger} \hat{a}_2^o$. Next, we consider that the beam splitter is a lossless, frequency independent, "50-50" beam splitter, which corresponds to setting $t(\omega) \to t = 1/\sqrt{2}$ and $r(\omega) \to r = i/\sqrt{2}$ [77, 78]. Assuming monochromatic

illumination, using the beam splitter transformation introduced in Eq. (2.28), and considering that there is no input state on the vertical path, we can write Eq. (2.32) in terms of the input operators as

$$g^{(2)}(0) = \frac{\langle \hat{a}_1^{i\,\dagger} \hat{a}_1^{i\,\dagger} \hat{a}_1^i \hat{a}_1^i \rangle}{\langle \hat{a}_1^{i\,\dagger} \hat{a}_1^i \rangle^2} = \frac{\langle \hat{a}^\dagger \hat{a}^\dagger \hat{a} \hat{a} \rangle}{\langle \hat{a}^\dagger \hat{a} \rangle^2}, \tag{2.33}$$

where in the last equality, we have simplified our notation, $\hat{a}_1^i \equiv \hat{a}$. It can be shown (see, for example, chapter 5 in reference [70]) that $g^{(2)}(0)$ can be directly connected with the statistics of emission from a light source

$$g^{(2)}(0) = 1 + \frac{\langle (\Delta \hat{n})^2 \rangle - \langle \hat{n} \rangle}{\langle \hat{n} \rangle^2}, \tag{2.34}$$

where $\langle \hat{n} \rangle$ is the mean number of photons emitted by the source in a time interval. The time interval that defines the number of photons in each "packet" of photons emitted by the source is called coherence time, τ_C, and it is inversely related to the natural line width of the spectral lines of the source. In our theoretical description, we are considering that the detectors in the HBT detect the number of photons arriving in time windows of τ_C[vii] [70]. $\langle (\Delta \hat{n})^2 \rangle = |\langle \hat{n}^2 \rangle - \langle \hat{n} \rangle^2|$ in Eq. (2.34) are the fluctuations in the average number of emitted photons. In the following subsections (subsections 2.4.2 to 2.4.5), we discuss the relationship between $g^{(2)}(0)$ and the statistical nature of the emission from four canonical light sources: a coherent source, a thermal source, a quantum single-photon source, and a quantum realistic two-photon source.

2.4.2 Statistics of light emitted by a coherent source

Coherent sources of light, such as a laser, emit photons with the same frequency and same wavefronts. The statistics of the number of photons emitted from a coherent light source follows a characteristic Poisson's distribution with fluctuations $\langle (\Delta \hat{n})^2 \rangle = \langle \hat{n} \rangle$ [70]. Thus, using Eq. (2.34), we find that the HBT interferometer results in

$$g^{(2)}(0) = 1. \tag{2.35}$$

To illustrate this result, we analyze in Fig. 2.3 the statistics and intensity correlations of a coherent light source with an average emission of $\langle \hat{n} \rangle = 5$ photons. Figure 2.3a shows the distribution of the number of photons emitted by this source (a Poisson distribution with average $\langle \hat{n} \rangle = 5$ and fluctuations $\langle (\Delta \hat{n})^2 \rangle = 5$) at a time interval. Figure 2.3b shows a sketch illustrating the response of the HBT interferometer to this input source. In this sketch, the packets of photons arrive at the beam splitter at relatively regular intervals and are split towards the two detectors. Note that the beam splitter divides the incident states into a superposition of states with different

[vii] For larger time windows, counting the photons in each packet can result in a statistical Poisson distribution, and at shorter time windows, the information in the photon intensity correlations can be lost [77, 83].

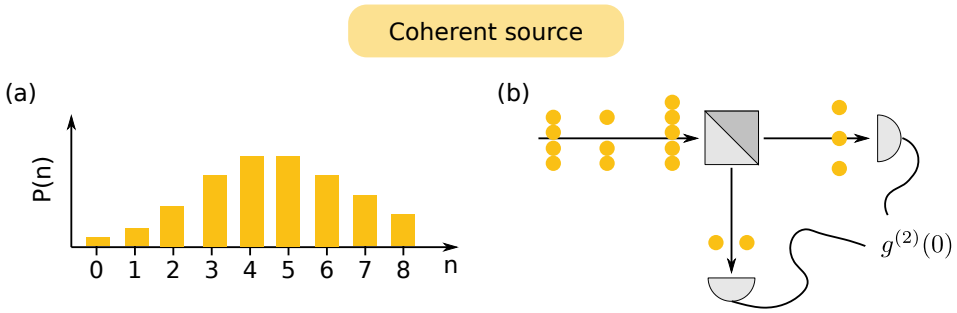

(c)

Measurement number	$\bar{I}_1$	$\bar{I}_2$	$\bar{I}_1\bar{I}_2$	Number of photons
1	2	2	4	4
2	1	3	3	4
3	6	3	18	9
4	2	3	6	5
5	3	2	6	5
6	4	2	8	6
7	2	2	4	4
8	3	3	9	6
9	2	2	4	4
10	6	2	12	8
Average	3.1	2.4	7.4	

$$\overline{g^{(2)}(0)} = 0.99$$

Figure 2.3: Example of the measurement of the intensity correlations $g^{(2)}(0)$ of a coherent source. (a) Poissonian distribution with mean occupation number $\langle n \rangle = 5$ representing the statistics of the number of photons emitted by a coherent source. The graph shows the probability distribution evaluated up to $n = 8$ photons. (b) Sketch of the response of the HBT interferometer under coherent illumination, where each orange circle represents an individual photon. In the figure, we represent one of the possible outcomes from the beam splitter. (c) Simulated measurement by a HBT interferometer. In the first ten rows we show (from left to right columns): the measurement number, the intensity measured by the detector in the horizontal path, $\bar{I}_1$, the intensity measured by the detector in the vertical path, $\bar{I}_2$, the multiplication of the intensity measured by both detectors, $\bar{I}_1\bar{I}_2$, and the number of photons emitted by the coherent source. These values are obtained with random number generators based on the number of photons statistically emitted by the coherent source and on the response of the beam splitter (see discussion in the text). In the last row of the table, we show the average value of $\bar{I}_1$, $\bar{I}_2$, and $\bar{I}_1\bar{I}_2$. Below the table we show the value of $g^{(2)}(0)$ obtained from the average values.

numbers of photons at each output branch of the beam splitter. For example, in the figure, an incident state with $N = 5$ photons is split into a superposition of all possible $|n_1, n_2\rangle$ states with $n_1 + n_2 = N = 5$, where n_1 and n_2 indicate the number of photons at each output path of the beam splitter. When measured, this superposition of states collapses into a single state; for example, in the figure, we chose it to be the $|3, 2\rangle$ state.

In Fig. 2.3c, we show a table that simulates the behavior of the HBT interferometer. The first ten rows correspond to ten simulated measurements under coherent illumination (measurement number in the first column). For this table and the following examples in Figs. 2.4-2.6, we first use a random number generator to obtain N, the number of photons emitted by the source in a given time interval (corresponding to each individual simulated measurement). This random number generator follows the statistic distribution of the source, *i.e.*, a Poisson distribution in the case of Fig. 2.3. Next, we obtain the intensity of an individual measurement by each detector, $\bar{I}_1$ and $\bar{I}_2$, shown in the second and third columns, respectively (the line over a variable indicates simulated values for a single measurement). We assign $\bar{I}_1$ to $\bar{n}_1$, a randomly generated number of photons that arrive at the D_1 detector. To obtain $\bar{n}_1$ we take into account that, using the beam splitter transformation in Eq. (2.28), the output state at each detector of the HBT is $|\Psi^o_{\text{HBT}}\rangle = [(\hat{a}^\dagger_1 + i\hat{a}^\dagger_2)/\sqrt{2}]^N |0\rangle$, with $|0\rangle$ being the vacuum state (with zero photons). We can then obtain the probability of measuring n_1 photons in the D_1 detector as $|\langle\Psi^o_{\text{HBT}}|n_1, n_2\rangle|^2$, where the $|n_1, n_2\rangle$ describe having n_1 and n_2 photons at the horizontal and vertical output paths of the beam splitter, respectively. The value of $\bar{n}_1$ results from using a random number generator following the statistical distribution given by the $|\langle\Psi^o_{\text{HBT}}|n_1, n_2\rangle|^2$ probabilities. Then we assign $\bar{I}_2$ to $\bar{n}_2 = N - \bar{n}_1$. Using these values of $\bar{I}_1$ and $\bar{I}_2$ we show the resulting $\bar{I}_1\bar{I}_2$ product in the fourth column. Finally, in the last row, we give the mean values $\langle\bar{I}_1\rangle$, $\langle\bar{I}_2\rangle$, and $\langle\bar{I}_1\bar{I}_2\rangle$, which corresponds to the average of the individual simulated measurements, $\bar{I}_1$, $\bar{I}_2$, and $\bar{I}_1\bar{I}_2$, respectively, in the rows above. The result of the HBT interferometer corresponds to

$$\overline{g^{(2)}(0)} = \frac{\langle\bar{I}_1\bar{I}_2\rangle}{\langle\bar{I}_1\rangle\langle\bar{I}_2\rangle}. \tag{2.36}$$

For the table in Fig. 2.3 we obtain $\overline{g^{(2)}(0)} \approx 0.99$ (indicated at the bottom of the figure), which is very close to the theoretical value $g^{(2)}(0) = 1$ expected from Eq. (2.35) (larger sampling results in $\overline{g^{(2)}(0)} \approx 1$, not shown here). This simple example illustrates not only the performance of a standard HBT but also how the intensity correlations measured by an HBT interferometer are directly connected to the statistics of the emission of a source.

2.4.3 Statistics of light emitted by a thermal source

We next consider an HBT interferometer under thermal illumination, such as light emitted by a gas discharge lamp. The number of photons emitted by a thermal

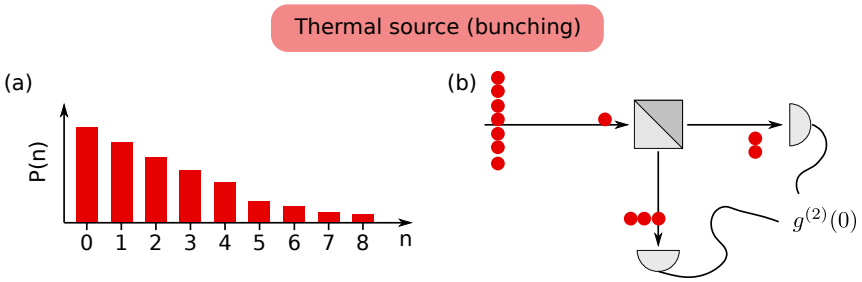

(c)

Measurement number	$\bar{I}_1$	$\bar{I}_2$	$\bar{I}_1\bar{I}_2$	Number of photons
1	0	1	0	1
2	2	3	6	5
3	0	2	0	2
4	1	0	0	1
5	0	1	0	1
6	0	1	0	1
7	0	0	0	0
8	3	0	0	3
9	6	7	42	13
10	4	3	13	7
Average	1.6	1.8	6.0	

$$\overline{g^{(2)}(0)} \approx 2.08$$

Figure 2.4: Example of the measurement of the intensity correlations $g^{(2)}(0)$ of a thermal source. (a) Bose-Einstein distribution with mean occupation number $\langle n \rangle = 5$ representing the statistics of the number of photons emitted by a coherent source. The graph shows the probability distribution evaluated up to $n = 8$ photons. (b) Sketch of the response of the HBT interferometer under coherent illumination, where each red circle represents an individual photon. In the figure, we represent one of the possible outcomes from the beam splitter. (c) Simulated measurement by a HBT interferometer. In the first ten rows we show (from left to right columns): the measurement number, the intensity measured by the detector in the horizontal path, $\bar{I}_1$, the intensity measured by the detector in the vertical path, $\bar{I}_2$, the multiplication of the intensity measured by both detectors, $\bar{I}_1\bar{I}_2$, and the number of photons emitted by the thermal source. These values are obtained with random number generators based on the number of photons statistically emitted by the thermal source and on the response of the beam splitter (see discussion in the text). In the last row of the table, we show the average value of $\bar{I}_1$, $\bar{I}_2$, and $\bar{I}_1\bar{I}_2$. Below the table we show the value of $g^{(2)}(0)$ obtained from the average values.

light source follows a Bose-Einstein, positive-definite, half-normal distribution (a normal distribution, $P(n)$, but only defined for positive values, $n \geq 0$) [70]. Figure 2.4a shows the evaluation of such distribution with a $\langle(\Delta\hat{n})^2\rangle = 5$ variance. A half-normal distribution satisfies $\langle(\Delta\hat{n})^2\rangle = \langle\hat{n}\rangle^2 + \langle\hat{n}\rangle$ [70], and, $g^{(2)}(0)$ in Eq. (2.34) becomes,

$$g^{(2)}(0) = 2. \tag{2.37}$$

Figure 2.4b shows a sketch of the emission of a thermal source onto an HBT interferometer. The sketch emphasizes how this source often emits photon packages containing a significant number of photons, with a relatively long period of time between these groups with no photon emission. This behavior contrasts with the more regular emission of a coherent source (Fig. 2.3b). Statistically, if the incident photon package to the beam splitter contains many photons, the output detected state would contain a similar number of photons at each detector.

Figure 2.4c shows a simulation of the HBT interferometer measurements for a thermal source. The values shown in the figure are obtained using the same methodology presented when discussing Fig. 2.3c, except for the use of the Bose-Einstein statistics for the photons emitted by the thermal source (Fig. 2.4a). Consistent with the previous discussion, the number of photons emitted by the thermal source in a time interval (last column of Fig. 2.4c) is very irregular, with some intervals containing many photons and others very few or none. This type of behavior, where photons are emitted in "bunches" (packets with large numbers of photons), corresponds to a bunched emission and results in $g^{(2)}(0) > 1$.[viii]. The last row of the table shows the average value of the intensities measured at each detector of the HBT after ten simulated measurements in the rows above. Using these average values in Eq. (2.36) we obtain $\overline{g^{(2)}(0)} \approx 2.08$ (indicated at the bottom of the figure), a value very close to the theoretical $g^{(2)}(0) = 2$ result in Eq. (2.37).

2.4.4 Statistics of light emitted by a single photon source

We study in this section the intensity correlations and statistics of light showing a very different behavior as compared to the bunched thermal emission: the emission from a single photon source. In Fig. 2.5a, we show the distribution of the number of photons emitted by a realistic single-photon source, which can emit one photon at each time interval, but can also emit zero photons. As illustrated by the sketch in Fig. 2.5b, the output state from the beam splitter can only be detected in a single output path. Thus, the intensity measured by one of the detectors is zero, so that $\langle\hat{I}_h\hat{I}_v\rangle = 0$, and according to Eq. (2.32), in this case,

$$g^{(2)}(0) = 0. \tag{2.38}$$

The table in Fig. 2.5c shows the results of a simulated measurement (performed as in previous sections) for a single photon source. In the last row of the table, we

[viii] More technically, "bunching" occurs when $g^{(2)}(\tau) < g^{(2)}(0)$. In any case, the statistical behavior of the emission of photons in bunches results in $g^{(2)}(0) > 1$, and for the rest of this thesis, we refer to $g^{(2)}(0) > 1$ as "bunching".

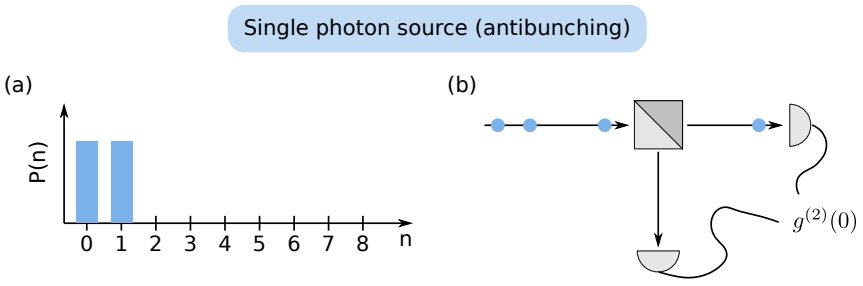

(c)

Measurement number	$\bar{I}_1$	$\bar{I}_2$	$\bar{I}_1\bar{I}_2$	Number of photons
1	0	0	0	0
2	0	1	0	1
3	0	1	0	1
4	0	1	0	1
5	0	0	0	0
6	0	0	0	0
7	0	0	0	0
8	0	0	0	0
9	1	0	0	1
10	0	0	0	0
Average	0.3	0.1	0	

$$g^{(2)}(0) = 0$$

Figure 2.5: Example of the measurement of the intensity correlations $g^{(2)}(0)$ of a single photon source. (a) Statistic distribution of the number of photons emitted by a single photon source. (b) Sketch of the response of the HBT interferometer under single photon illumination, where each blue circle represents an individual photon. In the figure, we represent one of the possible outcomes from the beam splitter. (c) Simulated measurement by a HBT interferometer. In the first ten rows we show (from left to right columns): the measurement number, the intensity measured by the detector in the horizontal path, $\bar{I}_1$, the intensity measured by the detector in the vertical path, $\bar{I}_2$, the multiplication of the intensity measured by both detectors, $\bar{I}_1\bar{I}_2$, and the number of photons emitted by the single-photon source. These values are obtained with random number generators based on the number of photons statistically emitted by the single photon source and on the response of the beam splitter (see discussion in the text). In the last row of the table, we show the average value of $\bar{I}_1$, $\bar{I}_2$, and $\bar{I}_1\bar{I}_2$. Below the table we show the value of $g^{(2)}(0)$ obtained from the average values.

show the average values $\langle \bar{I}_1 \rangle$ and $\langle \bar{I}_2 \rangle$, which are non-zero, but we indeed find that $\langle \bar{I}_1 \bar{I}_2 \rangle = 0$, thus, $\overline{g^{(2)}(0)} = 0$ in perfect agreement with Eq. (2.38).

This characteristic $g^{(2)}(0) = 0$ value can also be obtained from the statistical properties of the number of photons emitted. For the single-photon source analyzed in Fig. 2.5, the average value of the number of photons emitted is $\langle \hat{n} \rangle = 0.5$, and the fluctuations of the distribution shown in Fig. 2.5a are $\langle (\Delta \hat{n})^2 \rangle = 0.25$, which, according to Eq. (2.34) results in the expected $g^{(2)}(0) = 0$ value of the intensity correlations. Note that in this case the fluctuations are lower than the fluctuations of a Poisson distribution with the same expected value (*i.e.*, $\langle (\Delta \hat{n})^2 \rangle < \langle \hat{n} \rangle$), and thus, this type of distribution of emitted photons is often called "sub-Poissonian". From Eq. (2.34) it is straightforward to prove that only sub-Poissonian distributions result in $g^{(2)}(0) < 1$. These sources with $g^{(2)}(0)$ are often referred to as "antibunched", as they rarely emit bunches of more than one photon (in the case of $g^{(2)}(0) = 0$ only one or zero photons are emitted at each time interval)[ix].

2.4.5 Statistics of light emitted by a realistic two-photon source

It is interesting to compare the "antibunching" result just described with the emission of a highly-correlated two-photon source. Most textbooks argue that a n-photon source result in $g^{(2)}(0) = 1 - 1/n$ with $n > 1$ [70], but this statement needs to be more precise. In this statement it is implied that the n-photon source that results in $g^{(2)}(0) = 1 - 1/n$ must emit exactly n photons (and no less than n photons) at any interval of time. However, these types of sources are very hard to obtain experimentally[x]. In the following, we focus on a realistic n-photon source that can emit two photons or less, and we show that, in this case, we can obtain a strong, unbound bunching with $g^{(2)}(0) > 2$, in stark contrast with the $g^{(2)}(0) = 1 - 1/n < 1$ prediction.

Figure 2.6a shows the statistical distribution of the number of photons emitted by a two-photon source with a 80% probability of no-emission, a 5% probability of emitting one photon, and a 15% probability of emitting two photons. This probability has a variance $\langle (\Delta \hat{n})^2 \rangle = 0.53$ higher than its average $\langle \hat{n} \rangle = 0.35$. From Eq. (2.34),

$$g^{(2)}(0) = 2.44, \tag{2.39}$$

a value indicating a bunched or superpoissonian emission.

Figure 2.6b shows a sketch of the emission of this system onto an HBT interferometer. If two photons are emitted after the beam splitter, they can be detected at a single detector, resulting in $\bar{I}_1 \bar{I}_2 = 0$ at a single time interval. However, the most probable output state has one photon at each output path of the beam splitter (this is the state depicted in the sketch), resulting in $\bar{I}_1 \bar{I}_2 = 1$.

[ix] We use this terminology in this thesis, although, technically, the "antibunching" term is defined for $g^{(2)}(0) < g^{(2)}(\tau)$.

[x] Experiments can perform a post-selection measurement neglecting all emission that does not contain the exact number of photons desired, thus recovering the statistics of emission of a perfect n-photon source.

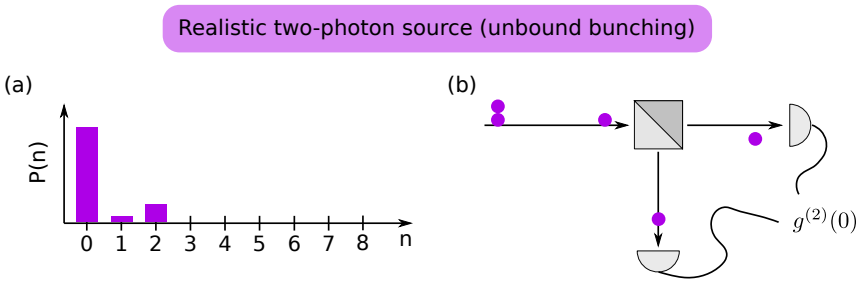

(c)

Measurement number	$\bar{I}_1$	$\bar{I}_2$	$\bar{I}_1\bar{I}_2$	Number of photons
1	0	0	0	0
2	2	0	0	2
3	0	0	0	0
4	0	0	0	0
5	0	0	0	0
6	0	0	0	0
7	1	1	0	2
8	0	0	0	0
9	0	0	0	0
10	0	0	0	0
Average	0.3	0.1	0.1	

$$\overline{g^{(2)}(0)} \approx 3.33$$

Figure 2.6: Example of the measurement of the intensity correlations $g^{(2)}(0)$ of a realistic two-photon source. (a) Statistic distribution of the number of photons emitted by the two-photon source. (b) Sketch of the response of the HBT interferometer under the illumination from the two-photon source, where each purple circle represents an individual photon. In the figure, we represent one of the possible outcomes from the beam splitter. (c) Simulated measurement by a HBT interferometer. In the first ten rows we show (from left to right columns): the measurement number, the intensity measured by the detector in the horizontal path, $\bar{I}_1$, the intensity measured by the detector in the vertical path, $\bar{I}_2$, the multiplication of the intensity measured by both detectors, $\bar{I}_1\bar{I}_2$, and the number of photons emitted by the two-photon source. These values are obtained with random number generators based on the number of photons statistically emitted by the two-photon source and on the response of the beam splitter (see discussion in the text). In the last row of the table, we show the average value of $\bar{I}_1$, $\bar{I}_2$, and $\bar{I}_1\bar{I}_2$. Below the table we show the value of $g^{(2)}(0)$ obtained from the average values.

In Fig. 2.6c, we show a simulation of a HBT interferometer measurement obtained with random number generators (we use the same methodology introduced in the previous sections). The simulation in Fig. 2.6c shows that the most common emission from the source has zero photons and that the measurements with non-zero photons usually correspond to the emission of a packet (or a bunch) of two photons. Moreover, after averaging the intensity measured by each detector and its product, we find a correlation

$$\overline{g^{(2)}(0)} \approx 3.33, \tag{2.40}$$

close to the expected $g^{(2)}(0) = 2.44$ value in Eq. (2.39) (larger samplings results in $\overline{g^{(2)}(0)} \approx 2.44$). Notice that this $g^{(2)}(0)$ value is higher than the standard $g^{(2)}(0) = 2$ bunching obtained by a thermal source. This larger value is due to the highly-correlated emission of the system, which favors the emission of two-photon pairs over a single-photon emission. In fact, we can obtain an arbitrarily large, unbounded correlation by increasing the probability of no emission and decreasing the probability of single-photon and two-photon emission. For example, for a source of 98% probability of no-emission, a 0.1% probability of emitting one photon, and a 1.9% probability of emitting two photons, we obtain (using fifty thousand simulated measurements) $\overline{g^{(2)}(0)} \approx 25$[xi], more than one order of magnitude larger than the thermal bunching $g^{(2)}(0) = 2$ in Eq. (2.37).

2.5 The Hamiltonian of cavity-QED systems

In this section, we review in detail the derivation of the quantum Rabi model (QRM) Hamiltonian, which describes the interactions between a cavity (such as a metallic nanostructure, see chapter 1) and a QE (such as a quantum dot or a molecule) modeled as a two-level-system (TLS). This derivation is based on recent work discussing the corrections necessary to ensure the gauge-invariance of the QRM [84–88]. We conclude this section by describing how the QRM Hamiltonian simplifies into the Hamiltonian of the Jaynes-Cummings model (JCM), a canonical model to describe the response of cavity-TLS (CTS) in the regime where the interaction between the cavity and the emitter is weak.

The derivation of the QRM Hamiltonian is organized as follows: first, in subsection 2.5.1 we attempt to derive the QRM Hamiltonian directly in the Coulomb gauge (our gauge of choice in this thesis). This derivation presents some difficulties when separating the response of the unperturbed emitter from the interaction between the emitter and the cavity. To overcome these issues, we adopt the dipole gauge in subsection 2.5.2. Within the dipole gauge, we are able to successfully derive the QRM Hamiltonian. Finally, in subsection 2.5.3, we transform the QRM Hamiltonian from the dipole to the Coulomb gauge.

[xi] In this case, the distribution of the number of photons emitted by the source results in an average $\langle \hat{n} \rangle = 0.04$ and variance $\langle (\Delta \hat{n})^2 \rangle = 0.0784$, and thus, using Eq. (2.34) the theoretical value of the intensity correlations is $g^{(2)}(0) = 25$, in perfect agreement with the simulation.

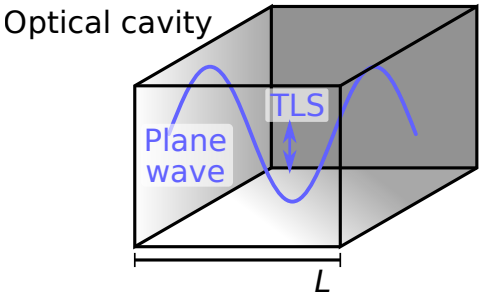

Figure 2.7: Sketch of the CTS studied in section 2.5. The optical cavity corresponds to a box made of conducting walls of length L. The optical cavity supports a single electromagnetic mode, corresponding to a plane wave propagating between two walls. A TLS (emitter) is placed in the middle of the cavity.

2.5.1 From the classical Lagrangian to the first quantization of the Coulomb gauge quantum Rabi Hamiltonian

Most descriptions of the QRM Hamiltonian are given in the Coulomb gauge and in the dipole gauge. In this section, we derive the QRM Hamiltonian in both gauges. In particular, we follow the derivation of the QRM Hamiltonian for a simple system composed of an optical cavity and a single quantum emitter. The optical cavity is a square box with perfectly conducting walls of length L (see the sketch in Fig. 2.7). Further, we assume that this cavity supports a single plane wave mode [70]. The results obtained for this simple cavity can be extended to more complex photonic cavities, including plasmonic cavities with multiple modes [13, 89–91].

A single quantum emitter (QE) is located in the middle of the cavity, interacting with the electromagnetic field inside the cavity (see sketch in Fig. 2.7). In subsection 1.2.1, we discussed that the classical electromagnetic response of a QE can be modeled as the response of an electric point-like dipole. In this derivation, we explicitly consider that the point-like dipole is composed of two charged particles, both with mass m, placed at a time-dependent distance z_+ and $z_-(t) = -z_+(t)$ from the center of the emitter, along one axis of reference (chosen to be z). The particle at position z_+ has a charge q, the particle at position z_- has a charge $-q$, and the distance between the particles, $d_\sigma(t) = z_+(t) - z_-(t)$ oscillates with a frequency ω_σ.

We next derive the quantum Hamiltonian of an oscillatory point-like dipole QE (latter approximated as the TLS) interacting with a single-mode electromagnetic field (generated by the cavity) within the Coulomb gauge, as obtained directly from the Lagrangian operator. The classical Lagrangian for an electric dipole interacting

with an electromagnetic field is (see Chapter 2 of reference [92]):

$$L = \frac{1}{2}m\dot{z}_+(t)^2 + \frac{1}{2}m\dot{z}_-(t)^2 + V(d_\sigma) + \\ + \int \left[\frac{\varepsilon_0}{2}(|\boldsymbol{A}(\dot{\boldsymbol{r}},t)|^2 - c_0^2|\nabla\times\boldsymbol{A}(\boldsymbol{r},t)|^2) + \boldsymbol{j}\cdot\boldsymbol{A}(\boldsymbol{r},t)\right] d^3\boldsymbol{r}. \tag{2.41}$$

Here V is the total potential experienced by the charges of the electric dipole. For example, V could be the Coulomb potential of attraction of the positive and negative charges. $\boldsymbol{j} = q\boldsymbol{u}_z[\dot{z}_+(t)\delta(\boldsymbol{r}-\boldsymbol{u}_z z_+(t)) - \dot{z}_-(t)\delta(\boldsymbol{r}-\boldsymbol{u}_z z_-(t))]$ in Eq. (2.41) is the current density of the dipole, and $\boldsymbol{A}$ is the potential vector of the electromagnetic field of the single mode of the cavity. For the simple cavity box we are considering here (see the sketch in Fig. 2.7), $\boldsymbol{A}$ corresponds to a single plane wave oscillating as $\boldsymbol{A}(\boldsymbol{r},t) = \boldsymbol{A}(t)e^{i(\boldsymbol{k}_c\cdot\boldsymbol{r})}$, where $\boldsymbol{A}$ is perpendicular to its direction of propagation $\boldsymbol{k}_c/k_c$ [70, 92], and thus $|\nabla\times\boldsymbol{A}(\boldsymbol{r},t)|^2 = k_c^2|\boldsymbol{A}(t)|^2$, with $k_c = |\boldsymbol{k}_c|$. This simplification allows us to write the Lagrangian in Eq. (2.41) as

$$L = \frac{1}{4}m\dot{d}_\sigma^2 + V(d_\sigma) + \frac{1}{2}\varepsilon_0\mathcal{V}_{\text{Eff}}\dot{A}^2 - \frac{1}{2}\varepsilon_0\mathcal{V}_{\text{Eff}}\omega_c^2A^2 + q\dot{d}_\sigma A, \tag{2.42}$$

where $A = |\boldsymbol{A}(t)|$, $\omega_c = c_0k_c$, and we have used that $\dot{z}_+(t)^2 + \dot{z}_-(t)^2 = \dot{d}_\sigma^2/2$[xii]. $\mathcal{V}_{\text{Eff}}$ is the effective mode volume of the cavity mode, which strongly depends on the type of cavity that we are studying[xiii]. For the simple cavity box we are considering here, $\mathcal{V}_{\text{Eff}} = L^3$. The first two terms in the sum of Eq. (2.42) describe the kinetic and potential energy of the unperturbed emitter. The third and fourth terms describe the electromagnetic energy of the cavity mode unperturbed by the emitter. The fifth (last) term describes the energy of the cavity-emitter interaction.

The classical Hamiltonian in the Coulomb gauge can be obtained from Eq. (2.42) by introducing the canonical momenta for each time-derivate variable,

$$p = \frac{\partial L}{\partial\dot{d}_\sigma} = \frac{1}{2}m\dot{d}_\sigma + qA, \tag{2.43}$$

$$\Pi = \frac{\partial L}{\partial\dot{A}} = \varepsilon_0\mathcal{V}_{\text{Eff}}\dot{A}. \tag{2.44}$$

Importantly, p in Eq. (2.43) is not the momentum of the unperturbed emitter ($m\dot{d}_\sigma$), as p includes a term dependent on the external electromagnetic field of the cavity, qA (thus the momentum of the unperturbed emitter becomes $m\dot{d}_\sigma = p - qA$). As we show at the end of this subsection and in subsection 2.5.2, the dependence of p on A does not allow us to perform a direct quantization of the excitations of the emitter.

[xii] This is because $(\dot{z}_+(t) + \dot{z}_-(t))^2 = 0$, *i.e.*, we assume that the center of charges of the emitter does not displace, which implies that $-2\dot{z}_+(t)\dot{z}_-(t) = \dot{z}_+(t)^2 + \dot{z}_-(t)^2$, and thus, $\dot{d}_\sigma^2 = (\dot{z}_+(t) - \dot{z}_-(t))^2 = 2(\dot{z}_+(t)^2 + \dot{z}_-(t)^2)$.

[xiii] For example, for a plasmonic cavity with a single mode in a vacuum, $\mathcal{V}_{\text{Eff}} \approx 3/(4\pi)\lambda^3Q/P_{\text{F}}$ [23, 93, 94], where Q is the quality factor of the resonance of the cavity, and P_{F} is the Purcell factor of the plasmonic nanocavity (see definition of P_{F} in chapter 3) [35, 95, 96].

The choice of the canonical momenta in Eqs. (2.43) and (2.44) is called the minimal replacement rule, which allows us to define the classical Hamiltonian,

$$\mathcal{H}_{\text{C-Class.}} = \dot{d}_\sigma p + \dot{A}\Pi - L, \tag{2.45}$$

which (after some algebraic manipulation) results in

$$\mathcal{H}_{\text{C-Class.}} = \frac{(p - qA)^2}{m} + V(d_\sigma) + \frac{\Pi^2}{2\varepsilon_0 \mathcal{V}_{\text{Eff}}} + \frac{1}{2}\varepsilon_0 \mathcal{V}_{\text{Eff}} \omega_c^2 A^2, \tag{2.46}$$

where again, $(p - qA)$ is equivalent to the momentum of the unperturbed emitter.

To obtain the quantum Hamiltonian, we convert the classical variables p, d_σ, A, and Π into operators $\hat{p}$, $\hat{d}_\sigma$, $\hat{A}$, and $\hat{\Pi}$ that satisfy the commutation relations $[\hat{d}_\sigma, \hat{p}] = [\hat{A}, \hat{\Pi}] = i\hbar$. Hence, we obtain the Coulomb-gauge quantum Hamiltonian:

$$\hat{\mathcal{H}}_{\text{C}}^{(N)} = \frac{(\hat{p} - q\hat{A})^2}{m} + \hat{V} + \frac{\hat{\Pi}^2}{2\varepsilon_0 \mathcal{V}_{\text{Eff}}} + \frac{1}{2}\varepsilon_0 \mathcal{V}_{\text{EFf}} \omega_c^2 \hat{A}^2, \tag{2.47}$$

where $\hat{V}$ indicates the quantized potential energy, which depends on the distance operator between the charges of the emitter, $\hat{d}_\sigma$. The operator $\hat{V}$ can be projected on the distance basis as [84]

$$\hat{V} = \iint V(d_\sigma, d'_\sigma) \left|d_\sigma\right\rangle \left\langle d'_\sigma\right| dd_\sigma dd'_\sigma, \tag{2.48}$$

where $|d_\sigma\rangle$ and $|d'_\sigma\rangle$ are a continuous set of eigenstates of the distance $\hat{d}_\sigma$ operator, and $V(d_\sigma, d'_\sigma) = \langle d_\sigma|\hat{V}|d'_\sigma\rangle$. In the beginning of section 2.5.2 we discuss in more detail the properties of the $V(d_\sigma, d'_\sigma)$ function, and how it connects with the classical potential $V(d_\sigma)$ (in Eq. (2.41)).

Next, we introduce the second-quantization creation $\hat{c}^\dagger$ and annihilation $\hat{c}$ operators associated with the electromagnetic mode of the cavity, such that

$$\hat{A} = \sqrt{\frac{\hbar}{2\varepsilon_0 \mathcal{V}_{\text{Eff}} \omega_c}} (\hat{c} + \hat{c}^\dagger), \tag{2.49}$$

$$\hat{\Pi} = -i\sqrt{\frac{\hbar \varepsilon_0 \mathcal{V}_{\text{Eff}} \omega_c}{2}} (\hat{c} - \hat{c}^\dagger), \tag{2.50}$$

and write Eq. (2.47) as

$$\hat{\mathcal{H}}_{\text{C}}^{(N)} = \frac{(\hat{p} - q\hat{A})^2}{m} + \hat{V} + \hbar\omega_c \hat{c}^\dagger \hat{c} + \frac{\hbar\omega_c}{2}. \tag{2.51}$$

We renormalize the energy in $\hat{\mathcal{H}}_{\text{C}}^{(N)}$ by subtracting the $\hbar\omega_c/2$ term, *i.e.*, we introduce $\hat{\mathcal{H}}_{\text{C}} = \hat{\mathcal{H}}_{\text{C}}^{(N)} - \hbar\omega_c/2$, and we separate the resulting $\hat{\mathcal{H}}_{\text{C}}$ Hamiltonian into two additive terms:

$$\hat{\mathcal{H}}_{\text{C}} = \hat{\mathcal{H}}_\sigma + \hat{\mathcal{H}}_{\text{C}}^{(0)}, \tag{2.52}$$

where

$$\hat{\mathcal{H}}_{\mathrm{C}}^{(0)} = \hbar\omega_c \hat{c}^\dagger \hat{c} \tag{2.53}$$

is the Hamiltonian of the cavity unperturbed by the emitter, and

$$\hat{\mathcal{H}}_\sigma = \frac{(\hat{p} - q\hat{A})^2}{m} + \hat{V}, \tag{2.54}$$

corresponds, *a priori*, to the Hamiltonian of the emitter unperturbed by the cavity, where the second term ($\hat{V}$) is the potential energy experienced by the charges of the emitter, and the first term ($(\hat{p} - q\hat{A})^2/m$) is equivalent to the kinetic energy of the emitter (see discussion of the $(p - qA)$ term in Eq. (2.46)). This means that in this Hamiltonian, derived in the Coulomb-gauge, $\hat{\mathcal{H}}_{\mathrm{C}}$, we can not directly identify an independent term describing the interaction between the emitter and the cavity (the cavity-emitter interaction term is hidden in the energy of the "unperturbed" emitter).

So far, we have introduced the creation and annihilation operators of the cavity, and the next natural step in the quantization scheme requires introducing the analogous "creation" and "annihilation" operators of the emitter. The standard procedure to introduce these operators requires truncating the Hilbert space of the emitter, and, in order to do so, $\hat{\mathcal{H}}_\sigma$ (Eq. (2.54)) should describe the energy of the emitter unperturbed by the presence of the cavity. However, the $\hat{\mathcal{H}}_\sigma$ Hamiltonian includes the action of the cavity with terms $\propto \hat{A}$. The latter $\propto \hat{A}$ terms appears from the description of the classical momentum p in Eq. (2.43), and it does not allow us to derive further the quantization of $\hat{\mathcal{H}}_\sigma$ [84]. Moreover, if we directly truncate the $\hat{V}$ term in $\hat{\mathcal{H}}_\sigma$ (Eq. (2.54)), $\hat{V}$ will also become dependent on the field of the cavity. Before entering into details on how to avoid this issue, let us consider what would happen if we directly truncate the Hilbert space of the emitter.

The truncation of the Hilbert space of the emitter is a very common approximation in which the response of an emitter, such as a molecule or a quantum dot, is described by only considering the transition between two electronic levels with the lowest energy of the emitter. After reducing the response of the emitter to only its two lowest electronic levels, the emitter is referred to as a "two-level-system". The two lowest energetic states of the unperturbed emitter are termed as the ground $|g\rangle$ state and the excited $|e\rangle$ state, and the energy structure of the emitter can be approximated by these two states if two main conditions are met: (i) that the two states are well separated from the higher energy levels, and (ii) that the energy difference $\Delta E_{CTS} = \hbar|\omega_c - \omega_\sigma|$ given by the transition defined by these two levels, $\hbar\omega_\sigma$, and the energy of the electromagnetic mode of the cavity, $\hbar\omega_c$, is much smaller than the energy difference between $\hbar\omega_c$ and the energy of the other electric transitions of the emitter. In this thesis, we always consider that these two conditions are met. Then, the Hamiltonian of the "unperturbed" emitter in Eq. (2.52) is effectively approximated as $\hat{\mathcal{H}}_\sigma = \hbar\omega_\sigma(|e\rangle\langle e| - |g\rangle\langle g|)/2$, implying that the energy of the unperturbed TLS becomes $\hbar\omega_\sigma/2$ if excited or $-\hbar\omega_\sigma/2$ otherwise. It is straightforward to foresee that replacing this expression of $\hat{\mathcal{H}}_\sigma$ in Eq. (2.52) completely neglects the cavity-TLS interaction, and thus, it is not

correct. On the other hand, references [84,97] point out another common effective approach to describe the "unperturbed" Hamiltonian of the emitter, which consists in substituting

$$\frac{\hat{p}^2}{m} + \hat{V} \to \hbar\frac{\omega_\sigma}{2}(|e\rangle\langle e| - |g\rangle\langle g|) \tag{2.55}$$

in $\hat{\mathcal{H}}_\sigma$. However, this approximation introduces two crucial sources of error. First, the $\hat{p}$ operator in Eq. (2.55) depends on the action of the cavity via a $q\hat{A}$ term (Eq. (2.43)). Second, in the Coulomb gauge, the Hilbert space truncation of the emitter (onto the $|g\rangle$ and $|e\rangle$ states) causes the potential $\hat{V}$ to gain dependence also on the field $\hat{A}$ (see the beginning of the next subsection). Thus, nor the kinetic $\hat{p}^2$ term, nor the potential $\hat{V}$ term in Eq. (2.55) are suited to describe the energy of the unperturbed emitter. In the following subsections, we briefly review a solution to successfully truncate the Hilbert space of the emitter and obtain a correct expression of the QRM Hamiltonian in the Coulomb gauge.

2.5.2 Truncation of the Hilbert space of the emitter, loss of locality, and quantum Rabi Hamiltonian in the dipole gauge

Loss of locality of the emitter potential

Next we briefly review the general discussion in reference [84] to explain how the potential of the unperturbed emitter becomes dependent on $\hat{A}$ due to the truncation of the Hilbert space of the emitter in the Coulomb gauge. After Eq. (2.48) we discussed that the potential operator $\hat{V}$ could be written in the distance basis in terms of the function $V(d_\sigma, d'_\sigma)$. We expect that $V(d_\sigma, d'_\sigma) = V(d_\sigma)\delta(d_\sigma - d'_\sigma)$ with $V(d_\sigma)$ the value of the classical potential that we introduced in the beginning of the previous subsection (Eq. (2.41)). This is because we initially consider that $V(d_\sigma, d'_\sigma)$ is a local potential in the quantum context[xiv]. However, as we show next, when truncating the response of the QE to only its two lowest energy levels, the locality of this potential can be lost.

We first consider a complete basis of the eigenstates of the emitter,

$$|n_\sigma\rangle \in \{|g\rangle, |e\rangle, |e_2\rangle, |e_3\rangle, ...\}, \tag{2.56}$$

where $|g\rangle$ is the ground state, $|e\rangle$ is the first excited state, and $|e_2\rangle, |e_3\rangle, ...$ are the higher excited states. Then we write $V(d_\sigma, d'_\sigma)$ in Eq. (2.48) in this $|n_\sigma\rangle$ basis,

$$V(d_\sigma, d'_\sigma) = V(d_\sigma)\delta(d_\sigma - d'_\sigma) = \sum_{n_\sigma \neq n'_\sigma}^{\infty} V(d_\sigma)\langle d_\sigma|n_\sigma\rangle\langle d'_\sigma|n'_\sigma\rangle, \tag{2.57}$$

where in a realistic emitter, the $\langle d_\sigma|n_\sigma\rangle$ and $\langle d'_\sigma|n'_\sigma\rangle$ terms correspond to smooth

[xiv] Note that here we discuss locality and non-locality in a quantum context, where quantum non-locality describes the *instantaneous* propagation of correlations between entangled systems, or in Albert Einstein's words "spooky action-at-a-distance" [98–100].

wave functions representing the spatial distribution of the eigenstates of the emitter (note that the d_σ distance is a continuous variable). Next, we truncate the sum on the $|n_\sigma\rangle$ states to the first two eigenstates, $|n_\sigma\rangle \in \{|g\rangle, |e\rangle\}$, and thus,

$$V(d_\sigma, d'_\sigma) \approx V(d_\sigma)(\langle d_\sigma|g\rangle \langle d'_\sigma|e\rangle + \langle d_\sigma|e\rangle \langle d'_\sigma|g\rangle). \tag{2.58}$$

The two terms added inside the parenthesis in Eq. (2.58) cannot result in $\delta(d_\sigma - d'_\sigma)$, because the Dirac delta is the sum of all the elements of the basis; in other words, the Dirac delta cannot simply be factorized as the product of two smooth wavefunctions. Thus, Eq. (2.58) results in a loss of locality of the potential. Furthermore, any non-local potential $V(d_\sigma, d'_\sigma)$ can be expressed as a momentum-dependent potential, $V(d_\sigma, d'_\sigma) \to V(d_\sigma, p)$ [84, 101–103], and this dependence on the momentum is a significant issue in the Coulomb gauge because, according to Eq. (2.43), p depends on the potential vector A of the electromagnetic cavity mode. As we discussed above, if the potential operator $\hat{V}$ has a dependence on the field of the cavity, it is not suited to describe the potential energy of the unperturbed emitter.

The method to avoid introducing the dependence of $\hat{V}$ on $\hat{A}$ consists in changing from the Coulomb to the dipole gauge. In the dipole gauge, p only describes the properties of the unperturbed emitter, allowing one to truncate the Hamiltonian of the unperturbed emitter. After this change, it becomes possible to apply a transformation onto the Hamiltonian of the emitter in the dipole gauge and return to the Coulomb gauge.

From the Coulomb gauge Lagrangian to the dipole gauge Hamiltonian

The Lagrangian introduced in Eq. (2.42) is written in the Coulomb gauge. To change from the Coulomb to the dipole gauge without affecting the equations of motion of the system, we must perform a transformation of the type $L_D = L + dG_L/dt$, where G_L is a function of the position variables (d_σ), the field variables (A and Π), and time (t). In particular, the G_L function that describes the transformation from the Coulomb gauge to the dipole gauge is $G_L = -qd_\sigma A$, resulting in

$$L_D = L - q(\dot{d}_\sigma A + d_\sigma \dot{A}) = \frac{1}{4}m\dot{d}_\sigma^2 + V(d_\sigma) + \frac{1}{2}\varepsilon_0 \mathcal{V}_{\text{Eff}} \dot{A}^2 - \frac{1}{2}\varepsilon_0 \mathcal{V}_{\text{Eff}} \omega_c^2 A^2 - qd_\sigma \dot{A}. \tag{2.59}$$

This change of gauge affects the choice of the canonical momenta from p and Π in Eqs. (2.43) and (2.44) to

$$p_D = \frac{\partial L}{\partial \dot{d}_\sigma} = \frac{1}{2}m\dot{d}_\sigma, \tag{2.60}$$

$$\Pi_D = \frac{\partial L}{\partial \dot{A}} = \varepsilon_0 \mathcal{V}_{\text{Eff}} \dot{A} - qd_\sigma. \tag{2.61}$$

Importantly, the new canonical momentum p_D in the dipole gauge does not depend on any property of the external field. Using Eqs. (2.59)-(2.61) we can obtain the

classical Hamiltonian in the dipole gauge:

$$\mathcal{H}_{\text{D-Class.}} = \frac{p_D^2}{m} + V(d_\sigma) + \frac{(\Pi_D + q d_\sigma)^2}{2\varepsilon_0 \mathcal{V}_{\text{Eff}}} + \frac{1}{2}\varepsilon_0 \mathcal{V}_{\text{Eff}} \omega_c^2 A. \tag{2.62}$$

Next we use the correspondence principle and convert p_D, Π_D, d_σ, and A in Eq. (2.62) into quantum operators,

$$\hat{\mathcal{H}}_{\text{D}}^{(N)} = \frac{\hat{p}_D^2}{m} + \hat{V} + \frac{(\hat{\Pi}_D + q\hat{d}_\sigma)^2}{2\varepsilon_0 \mathcal{V}_{\text{Eff}}} + \frac{1}{2}\varepsilon_0 \mathcal{V}_{\text{Eff}} \omega_c^2 \hat{A}. \tag{2.63}$$

In a similar manner to the Coulomb gauge (Eqs. (2.49) and (2.50)) we can introduce the second-quantization creation $\hat{c}^\dagger$ and annihilation $\hat{c}$ operators associated to the electromagnetic mode of the cavity,

$$\hat{A} = \sqrt{\frac{\hbar}{2\varepsilon_0 \mathcal{V}_{\text{Eff}} \omega_c}}(\hat{c} + \hat{c}^\dagger), \tag{2.64}$$

and

$$\hat{\Pi}_D = -i\sqrt{\frac{\hbar \varepsilon_0 \mathcal{V}_{\text{Eff}} \omega_c}{2}}(\hat{c} - \hat{c}^\dagger). \tag{2.65}$$

By substituting these expressions on $\hat{\mathcal{H}}_{\text{D}}$ we obtain,

$$\hat{\mathcal{H}}_{\text{D}}^{(N)} = \hat{\mathcal{H}}_\sigma^{(D)} + \hbar\omega_c \hat{c}^\dagger \hat{c} + \frac{(q\hat{d}_\sigma)^2}{2\varepsilon \mathcal{V}_{\text{Eff}}} - i\frac{q\hat{d}_\sigma \sqrt{\hbar\omega_c}}{\sqrt{2\varepsilon_0 \text{V}_{\text{Eff}}}}(\hat{c} - \hat{c}^\dagger) + \frac{\hbar\omega_c}{2}, \tag{2.66}$$

where we have defined $\mathcal{H}_\sigma^{(D)} = \hat{p}_D^2/m + \hat{V}$, as the Hamiltonian of the unperturbed emitter.

Next, we truncate the Hilbert space of the emitter. We introduce this truncation on the Hamiltonian of the system $\hat{\mathcal{H}}_{\text{D}}$ in four steps [84, 97]: (i) We first consider the complete basis of the eigenstates of the emitter in Eq. (2.56), and truncate it to the first two states, the ground $|g\rangle$ and the excited $|e\rangle$ state. (ii) We introduce the annihilation (or lowering) operator

$$\hat{\sigma} = |g\rangle \langle e| , \tag{2.67}$$

and the creation (or rising) operator

$$\hat{\sigma}^\dagger = |e\rangle \langle g| . \tag{2.68}$$

$\hat{\sigma}$ describes the decay from the excited $|e\rangle$ state to the ground $|g\rangle$ state of the emitter, and $\hat{\sigma}^\dagger$ describes the excitation from $|g\rangle$ to $|e\rangle$. (iii) We write the Hamiltonian of the unperturbed emitter, $\mathcal{H}_\sigma^{(D)}$, as the energy difference between the excited and ground state,

$$\hat{\mathcal{H}}_\sigma^{(D)} = \frac{\hbar\omega_\sigma}{2}\hat{\sigma}_z, \tag{2.69}$$

where $\hat{\sigma}_z = [\hat{\sigma}^\dagger, \hat{\sigma}]$. (iv) We write $\hat{d}_\sigma$ and $\hat{p}_D$ in terms of $\hat{\sigma}$ and $\hat{\sigma}^\dagger$,

$$\hat{d}_\sigma = \sqrt{\frac{\hbar}{2m\omega_\sigma}}(\hat{\sigma} + \hat{\sigma}^\dagger), \tag{2.70}$$

$$\hat{p}_D = -i\sqrt{\frac{\hbar m\omega_\sigma}{2}}(\hat{\sigma} - \hat{\sigma}^\dagger). \tag{2.71}$$

Then, the Hamiltonian in Eq. (2.66) can be written as,

$$\hat{\mathcal{H}}_D^{(N)} = \frac{\hbar\omega_\sigma}{2}\hat{\sigma}_z + \hbar\omega_c\hat{c}^\dagger\hat{c} - i\hbar g\sqrt{\frac{\omega_c}{\omega_\sigma}}(\hat{c} - \hat{c}^\dagger)(\hat{\sigma} + \hat{\sigma}^\dagger) + \frac{\hbar q^2}{4m\omega_\sigma\varepsilon_0\mathcal{V}_{\text{Eff}}} + \frac{\hbar\omega_c}{2}, \tag{2.72}$$

with [84]

$$g = \frac{q}{2\sqrt{m\varepsilon_0\mathcal{V}_{\text{Eff}}}}. \tag{2.73}$$

After re-normalizing (neglecting the constant terms in the Hamiltonian), we find the well-known formula of the Rabi Hamiltonian in the dipole gauge,

$$\hat{\mathcal{H}}_D = \hat{\mathcal{H}}_D^{(N)} - \left(\frac{\hbar q^2}{4m\omega_\sigma\varepsilon_0\mathcal{V}_{\text{Eff}}} + \frac{\hbar\omega_c}{2}\right) = \frac{\hbar\omega_\sigma}{2}\hat{\sigma}_z + \hbar\omega_c\hat{c}^\dagger\hat{c} - i\hbar g\sqrt{\frac{\omega_c}{\omega_\sigma}}(\hat{c} - \hat{c}^\dagger)(\hat{\sigma} + \hat{\sigma}^\dagger). \tag{2.74}$$

2.5.3 From the dipole gauge to the Coulomb gauge

So far we have shown the derivation of the QRM Hamiltonian in the dipole gauge. Our next and final goal is to obtain this Hamiltonian in the Coulomb gauge. In Eq. (2.59) we introduced the change of gauge as a transformation on the Lagrangian operator. However, we can also directly change between the dipole and coulomb gauges by performing a unitary transformation on the Hamiltonian of the system [84, 85, 87, 92, 104],

$$\hat{\mathcal{H}}_C = \hat{U}\hat{\mathcal{H}}_D\hat{U}^\dagger + i\dot{\hat{U}}\hat{U}^\dagger, \tag{2.75}$$

with

$$\hat{U} = \exp(i(-\hat{G}_L)), \tag{2.76}$$

being a unitary matrix, and $\hat{G}_L = -q\hat{d}_\sigma\hat{A}$ corresponds to applying the quantum correspondence principle to the same G_L function that we use to transform the Lagrangian from the Coulomb gauge to the dipole gauge. Using the expressions of $\hat{A}$ and $\hat{d}_\sigma$ in Eqs. (2.64) and (2.70), $\hat{U}$ results in

$$\hat{U} = \exp\left[i\frac{g}{\sqrt{\omega_\sigma\omega_c}}(\hat{\sigma} + \hat{\sigma}^\dagger)(\hat{c} + \hat{c}^\dagger)\right]. \tag{2.77}$$

Note that the $\hat{U}$ transformation does not depend explicitly on time, and thus the $i\dot{\hat{U}}\hat{U}^\dagger$ term in Eq. (2.75) vanish, and we obtain

$$\hat{\mathcal{H}}_C = \hbar\omega_c \hat{c}^\dagger \hat{c} + \hat{U}\left(\frac{\hbar\omega_\sigma}{2}\hat{\sigma}_z\hat{\sigma}\right)\hat{U}^\dagger \tag{2.78}$$

For simplicity, we focus on the resonant case with $\omega_0 \equiv \omega_\sigma = \omega_c$, where Eq. (2.78) becomes

$$\hat{\mathcal{H}}_C = \hbar\omega_0 \hat{c}^\dagger \hat{c} + \frac{\hbar\omega_0}{2}\left\{\hat{\sigma}_z \cos[2\eta(\hat{c}+\hat{c}^\dagger)] + \hat{\sigma}_y \sin[2\eta(\hat{c}+\hat{c}^\dagger)]\right\}, \tag{2.79}$$

with $\hat{\sigma}_y = i(\hat{\sigma}^\dagger - \hat{\sigma})$, and $\eta = g/\omega_0$. This is the expression of the QRM Hamiltonian in the Coulomb gauge.

From this derivation, it might seem easier to work in the dipole gauge, where the truncation of the Hilbert space of the basis of the emitter is straightforward, and hence, the derivation of the Hamiltonian is direct. However, we note that working in the dipole gauge also presents some disadvantages. For instance, whereas in the Coulomb gauge the operator of the electric field generated by the cavity is simply proportional to $\hat{c}$, in the dipole gauge it becomes proportional to $\hat{c} + i\eta(\hat{\sigma} + \hat{\sigma}^\dagger)$ [85,87]. This change in the electric field operator affects, for example, the operators describing the emission and the dissipation of the system, which is very inconvenient for analyzing the dynamics in cavity-QED systems.

2.5.4 Jaynes-Cummings model Hamiltonian

Many cavity-QED setups show coupling strengths that are much smaller than the natural frequency of the cavity, *i.e.*, $g \ll \omega_0$. In this case, the Hamiltonian in Eq. (2.79) can be simplified in the limit of very small coupling $\eta = g/\omega_0 \to 0$. In this limit, we can expand the sine and cosine functions to the first order, and we obtain

$$\hat{\mathcal{H}}_C \approx \hbar\omega_0 \hat{c}^\dagger \hat{c} + \frac{\hbar\omega_0}{2}\hat{\sigma}_z + \hbar g \hat{\sigma}_y(\hat{c}+\hat{c}^\dagger). \tag{2.80}$$

Further, we can perform the rotating wave approximation (RWA), which consists in neglecting the double rotating, no-number conserving terms, *i.e.*, $\hat{\sigma}\hat{c}$ and $\hat{\sigma}^\dagger\hat{c}^\dagger$. This approximation results in the widely-used Jaynes-Cummings Hamiltonian [21,105]:

$$\hat{\mathcal{H}}_{\mathrm{JC}} = \hbar\omega_0 \hat{c}^\dagger \hat{c} + \hbar\frac{\omega_0}{2}\hat{\sigma}_z + i\hbar g(\hat{\sigma}^\dagger \hat{c} - \hat{c}^\dagger \hat{\sigma}). \tag{2.81}$$

2.6 Quantum dynamics in open quantum systems: the quantum master equation

Every quantum system interacts with its environment, for example with phonons at a specific temperature or simply with vacuum fluctuations. Often we know very

little about this environment, and we approximate it as a Markovian reservoir (a Markovian reservoir has no memory of its previous interactions with the quantum system, nor is it able to create coherences due to its interaction with the system). In this section, we focus on describing how the interaction of a quantum system with its environment affects its dynamics, *i.e.*, the time evolution of the state of the quantum system. For that purpose, we introduce the quantum master equation formalism, which allows us to describe the dynamics of the system without giving a complete description of the environment (we just approximate the environment as a Markovian reservoir). In the following subsections 2.6.1 and 2.6.2, we review the critical steps in deriving the master equation (for a complete and pedagogical derivation of the master equation, including a detailed discussion of the approximations involved, references [72, 73, 106] are good options).

2.6.1 From the Von Neumann equation to the Markovian master equation

In quantum mechanics, there are three pictures to understand the time evolution of a system: the Schrödinger, the Interaction, and the Heisenberg pictures. The studies presented in this thesis (chapters 5 and 4) are given in the Schrödinger picture, where the states describe the evolution of a system. In the Schrödinger picture, the evolution of a state (described by its density matrix, $\hat{\rho}$) follows the Von Neumann equation [72],

$$\frac{d}{dt}\hat{\rho}(t) = \frac{-i}{\hbar}[\hat{\mathcal{H}}, \hat{\rho}(t)], \tag{2.82}$$

being $\hat{\mathcal{H}}$ the Hamiltonian describing the energy of the quantum system, the energy of the environment, and the system-environment interaction. Our aim in this section is to operate the Von Neumann equation (Eq. (2.82)) to obtain the so-called quantum master equation, an expression that focuses only on the evolution of the state of the system, described by the density matrix $\hat{\rho}_S$, and the interaction between the system and the environment is conveniently simplified. $\hat{\rho}_S$ is contained in the total density matrix $\hat{\rho}$ (in Eq. (2.82)), which describes both the state of the system (independently of the environment) and of the state of the environment (independently of the system). We can extract $\hat{\rho}_S$ from $\hat{\rho}$ as,

$$\hat{\rho}_S(t) = \mathrm{Tr}_R\{\hat{\rho}(t)\}, \tag{2.83}$$

where Tr_R denotes the trace over the Hilbert space of the environment (or reservoir), [72–74, 106].

Before starting the derivation of the master equation, we need to introduce $\hat{\mathcal{H}}$ (in Eq. (2.82)), which is the Hamiltonian of the system and the environment. This Hamiltonian can be split into three terms,

$$\hat{\mathcal{H}} = \hat{\mathcal{H}}_S + \hat{\mathcal{H}}_R + \hat{\mathcal{H}}_{SR}, \tag{2.84}$$

where $\hat{\mathcal{H}}_S$ describes the energy of the system that we are interested in studying. For convenience, our derivation of the master equation is carried out on the basis of the $|\nu\rangle$ eigenstates of $\hat{\mathcal{H}}_S$, such that

$$\hat{\mathcal{H}}_S = \sum_\nu \hbar\omega_\nu |\nu\rangle \langle\nu| , \tag{2.85}$$

where $\hbar\omega_\nu$ is the eigenvalue of the $|\nu\rangle$ eigenstate. $\hat{\mathcal{H}}_R$ in Eq. (2.84) describes the energy of the environment of the system, and $\hat{\mathcal{H}}_{SR}$ describes the interaction energy between the system and the environment. The most general form of the $\hat{\mathcal{H}}_{SR}$ Hamiltonian describing the interaction between the environment and the system is [72],

$$\hat{\mathcal{H}}_{SR} = \hbar \sum_\alpha \hat{\mathcal{S}}_\alpha \otimes \hat{\mathcal{R}}_\alpha, \tag{2.86}$$

where $\hat{\mathcal{S}}_\alpha = \hat{\mathcal{S}}_\alpha^\dagger$ and $\hat{\mathcal{R}}_\alpha = \hat{\mathcal{R}}_\alpha^\dagger$ are hermitian operators of the system and of the environment, respectively. The subindex α runsover the different components of the Hamiltonian of the system. For instance, in the cavity-QED systems studied in this thesis, we consider two different α terms, one for the interaction between the cavity with the environment, and another term accounting for the interaction between the TLS and the environment.

We now proceed to operate the Von Neumann equation (Eq. (2.82)) to obtain the master equation. For this derivation, it is most convenient to operate Eq. (2.82) in the interaction picture. In the interaction picture, both the states and the Hamiltonian evolve in time, and the Von Neumann equation in the interaction picture reads as [72],

$$\frac{d}{dt}\hat{\rho}^{(i)}(t) = \frac{-i}{\hbar}[\hat{\mathcal{H}}^{(i)}(t), \hat{\rho}^{(i)}(t)]. \tag{2.87}$$

Along this section we use the label "(i)" to indicate that the Hamiltonian and the density matrix of the system, $\hat{\mathcal{H}}^{(i)}$ and $\hat{\rho}^{(i)}(t)$, respectively, are written in the interaction picture. $\hat{\mathcal{H}}^{(i)}$ and $\hat{\rho}^{(i)}(t)$ are connected with the operators in the Schrödinger picture by a unitary transformation [72, 73, 106]:

$$\hat{\mathcal{H}}^{(i)}(t) = \hat{U}^\dagger_{(s-i)}(t)\hat{\mathcal{H}}_{SR}\ \hat{U}_{(s-i)}(t), \tag{2.88}$$

and

$$\hat{\rho}^{(i)}(t) = \hat{U}^\dagger_{(s-i)}(t)\hat{\rho}\ \hat{U}_{(s-i)}(t). \tag{2.89}$$

with the unitary transformation being

$$\hat{U}_{(s-i)}(t) = \exp[i(\hat{\mathcal{H}}_S + \hat{\mathcal{H}}_R)t/\hbar]. \tag{2.90}$$

We next re-express Eq. (2.87) by integrating it,

$$\hat{\rho}^{(i)}(t) = \hat{\rho}^{(i)}(0) - \frac{i}{\hbar}\int_0^t [\hat{\mathcal{H}}^{(i)}(t'), \hat{\rho}^{(i)}(t')]dt', \tag{2.91}$$

and then substituting $\hat{\rho}^{(i)}(t)$ in Eq. (2.91) back into the right-hand side of Eq. (2.87),

$$\frac{d}{dt}\hat{\rho}^{(i)}(t) = -\frac{i}{\hbar}[\hat{\mathcal{H}}^{(i)}(t), \hat{\rho}^{(i)}(0)] - \frac{1}{\hbar^2}\left[\hat{\mathcal{H}}^{(i)}(t), \int_0^t [\hat{\mathcal{H}}^{(i)}(t'), \hat{\rho}^{(i)}(t')]dt'\right]. \quad (2.92)$$

As stated above, we are interested only in the time evolution of the state of the system, which we can extract from Eq. (2.92) using the partial trace over the Hilbert space of the environment (Eq. (2.83)),

$$\frac{d}{dt}\hat{\rho}_S^{(i)}(t) = -\mathrm{Tr}_R\left\{\frac{i}{\hbar}[\hat{\mathcal{H}}^{(i)}(t), \hat{\rho}^{(i)}(0)] + \frac{1}{\hbar^2}\left[\hat{\mathcal{H}}^{(i)}(t), \int_0^t [\hat{\mathcal{H}}^{(i)}(t'), \hat{\rho}^{(i)}(t')]dt'\right]\right\}. \quad (2.93)$$

To operate Eq. (2.93) we need to introduce our first approximation in this derivation: we assume that the environment corresponds to a Markovian reservoir, where we assume that the dissipation of the correlations of the reservoir is much faster than any variation of the system. Mathematically this implies that [72,73,106]:

$$\langle\hat{\mathcal{R}}_\alpha^{(i)}(t)\rangle = \mathrm{Tr}\{\hat{\mathcal{R}}_\alpha^{(i)}(t)\hat{\rho}^{(i)}(0)\} \approx 0, \quad (2.94)$$

for all α, where

$$\hat{\mathcal{R}}_\alpha^{(i)}(t) = \hat{U}^\dagger_{(s-i)}(t)\hat{\mathcal{R}}_\alpha\ \hat{U}_{(s-i)}(t) \quad (2.95)$$

are the operators of the reservoir in the interaction picture. This is the main approximation that we are going to use for the derivation of the master equation.

It can be proven that the assumption in Eq. (2.94) implies [72],

$$\mathrm{Tr}_R\{[\hat{\mathcal{H}}^{(i)}(t), \hat{\rho}^{(i)}(0)]\} \approx 0. \quad (2.96)$$

Thus, Eq. (2.93) simplifies to

$$\frac{d}{dt}\hat{\rho}_S^{(i)}(t) \approx -\mathrm{Tr}_R\left\{\frac{1}{\hbar^2}\left[\hat{\mathcal{H}}^{(i)}(t), \int_0^t [\hat{\mathcal{H}}^{(i)}(t'), \hat{\rho}^{(i)}(t')]dt'\right]\right\}. \quad (2.97)$$

Next, we introduce two further approximations in Eq. (2.97): we first assume that the state of the system at a time t' does not depend on the history of the interaction with the reservoir at previous times t', and thus,

$$[\hat{\mathcal{H}}^{(i)}(t'), \hat{\rho}^{(i)}(t')] \approx [\hat{\mathcal{H}}^{(i)}(t'), \hat{\rho}^{(i)}(t)]. \quad (2.98)$$

This approximation simplifies Eq. (2.97) to

$$\frac{d}{dt}\hat{\rho}_S^{(i)}(t) \approx -\mathrm{Tr}_R\left\{\frac{1}{\hbar^2}\left[\hat{\mathcal{H}}^{(i)}(t), \int_0^t [\hat{\mathcal{H}}^{(i)}(t'), \hat{\rho}^{(i)}(t)]dt'\right]\right\}. \quad (2.99)$$

Note that in this last equation $\hat{\rho}^{(i)}$ depends on t instead of t' as in Eq. (2.97). Second, we introduce the Born approximation, which states that for a weak interaction

between the system and the reservoir, we can factorize the total density matrix

$$\hat{\rho}^{(i)}(t) \approx \hat{\rho}_S^{(i)}(t) \otimes \hat{\rho}_R^{(i)}, \tag{2.100}$$

where the state of the reservoir, described by the density matrix $\hat{\rho}_R^{(i)}$, is considered to be constant in time because we assume that the time scales at which coherences of the reservoir are dissipated are much faster than the time scales at which the system varies, and thus, $\hat{\rho}_R$ is not affected by the dynamics of the system (same approximation as for Eq. (2.94)). Using the Born approximation (Eq. (2.100)) in Eq. (2.99), we can arrive at the so-called Redfield equation [107],

$$\frac{d}{dt}\hat{\rho}_S^{(i)}(t) = -\mathrm{Tr}_R\left\{\frac{1}{\hbar^2}\left[\hat{\mathcal{H}}^{(i)}(t), \int_0^t [\hat{\mathcal{H}}^{(i)}(t'), \hat{\rho}_S^{(i)}(t) \otimes \hat{\rho}_R^{(i)}]dt'\right]\right\}. \tag{2.101}$$

If we again assume that the reservoir correlations disappear very fast in comparison with the evolution of the system, we can consider that the $[\hat{\mathcal{H}}^{(i)}(t'), \hat{\rho}_S(t)^{(i)} \otimes \hat{\rho}_R^{(i)}]$ term in Eq. (2.101) is only determined by the evaluation of t' close to t, and thus, we can approximate the lower limit of the integral in time by $-\infty$ [72,73,106]. This results in the Born-Markov or Markovian master equation,

$$\frac{d}{dt}\hat{\rho}_S^{(i)}(t) = -\mathrm{Tr}_R\left\{\frac{1}{\hbar^2}\left[\hat{\mathcal{H}}^{(i)}(t), \int_0^\infty [\hat{\mathcal{H}}^{(i)}(t-s), \hat{\rho}_S^{(i)}(t) \otimes \hat{\rho}_R^{(i)}]ds\right]\right\}, \tag{2.102}$$

where we have substituted $t' \to t - s$ for convenience.

2.6.2 From the Markovian master equation to the Lindbladian master equation

The integral in Eq. (2.102) does not ensure that $\hat{\rho}_S^{(i)}$ is a positive-definite matrix, which is a requisite for any quantum density matrix. To ensure that $\hat{\rho}_S^{(i)}$ is positive-definite, we need to perform one last approximation, the rotating wave approximation on the interaction between the system and the reservoir (RRWA[xv]). To better explain the RRWA, let us first find the expression of $\hat{\mathcal{H}}^{(i)}$, the Hamiltonian in the interaction picture. We first introduced $\hat{\mathcal{H}}^{(i)}$ in Eq. (2.88), where it is shown to explicitly depend on $\hat{\mathcal{H}}_{SR}$, the Hamiltonian describing the system-reservoir interaction in the Scrhrödinger picture. $\hat{\mathcal{H}}_{SR}$ is written directly in terms of the $\hat{\mathcal{S}}_\alpha$ operators of the system and the $\hat{\mathcal{R}}_\alpha$ operators of the reservoir (Eq. (2.86)). In the interaction picture, $\hat{\mathcal{H}}^{(i)}$ can also be directly expressed in terms of the operators of the system and the reservoir [72],

$$\hat{\mathcal{H}}^{(i)}(t) = \sum_\alpha \hat{\mathcal{S}}_\alpha^{(i)}(t) \otimes \hat{\mathcal{R}}_\alpha^{(i)}(t), \tag{2.103}$$

[xv] Do not confuse with the RWA of the Jaynes-Cummings model introduced in subsection 2.5.4.

where $\hat{\mathcal{R}}_\alpha^{(i)}(t)$ are the reservoir operators in the interaction picture (Eq. (2.95)), and

$$\hat{\mathcal{S}}_\alpha^{(i)}(t) = \hat{U}_{(s-i)}^\dagger(t)\hat{\mathcal{S}}_\alpha\hat{U}_{(s-i)}(t), \tag{2.104}$$

are the system operators in the interaction picture, where $\hat{U}_{(s-i)}(t)$ is given in Eq. (2.90).

Dressed operator formalism

Next, we simplify the $\hat{\mathcal{S}}_\alpha^{(i)}(t)$ operators in Eq. (2.104). To do so, we need first to express the $\hat{\mathcal{S}}_\alpha$ operators in the Schrödinger picture in the basis of the $|\nu\rangle$ eigenstates of the Hamiltonian of the system $\hat{\mathcal{H}}_S$ (Eq. (2.85)),

$$\hat{\mathcal{S}}_\alpha = \sum_\omega \hat{\mathcal{S}}_\alpha(\omega), \tag{2.105}$$

with

$$\hat{\mathcal{S}}_\alpha(\omega) = \sum_{\omega_\mu-\omega_\nu=\omega} |\nu\rangle\langle\nu|\hat{\mathcal{S}}_\alpha|\mu\rangle\langle\mu|, \tag{2.106}$$

where $|\mu\rangle$ are also eiegenstates of $\hat{\mathcal{H}}_S$. The $|\nu\rangle$ and $|\mu\rangle$ eigenstates have eigenvalues $\hbar\omega_\nu$ and $\hbar\omega_\mu$, respectively, and the sum in the equation extends for any $|\mu\rangle$ and $|\nu\rangle$ such that their eigenvalues satisfy $(\omega_\mu - \omega_\nu = \omega)$. $\hat{\mathcal{S}}_\alpha(\omega)$ are called *dressed operators*, and they satisfy,

$$[\hat{\mathcal{H}}_S, \hat{\mathcal{S}}_\alpha(\omega)] = -\omega\hat{\mathcal{S}}_\alpha(\omega), \tag{2.107}$$

and

$$\hat{\mathcal{S}}_\alpha^\dagger(\omega) = \hat{\mathcal{S}}_\alpha(-\omega). \tag{2.108}$$

Using Eqs. (2.105) and (2.107) we can directly express the operators of the system in the interaction picture, $\hat{\mathcal{S}}_\alpha^{(i)}$ (Eq. (2.104)), in terms of the dressed operators in the Schrödinger picture,

$$\hat{\mathcal{S}}_\alpha^{(i)} = \sum_\omega \hat{U}_{(s-i)}^\dagger(t)\hat{\mathcal{S}}_\alpha(\omega)\hat{U}_{(s-i)}(t) = e^{-i\omega t}\hat{\mathcal{S}}_\alpha(\omega), \tag{2.109}$$

and thus, the Hamiltonian in the interaction picture $\hat{\mathcal{H}}^{(i)}$ (Eq. (2.103)) results in

$$\hat{\mathcal{H}}^{(i)}(t) = \sum_{i,\omega} e^{-i\omega t}\hat{\mathcal{S}}_\alpha(\omega)\otimes\hat{\mathcal{R}}_\alpha^{(i)}(t). \tag{2.110}$$

Reservoir rotating wave approximation

We then substitute $\hat{\mathcal{H}}^{(i)}$ in the Markovian master equation (Eq. (2.102)), and after expanding the commutators and a lengthy algebraic manipulation [72, 106]

we arrive at

$$\frac{d}{dt}\hat{\rho}_S^{(i)}(t) = \sum_{\omega,\omega',\alpha,\beta} e^{i(\omega-\omega')t}\Gamma_{\alpha,\beta}(\omega)\left[\hat{\mathcal{S}}_\beta(\omega)\hat{\rho}_S^{(i)}(t)\hat{\mathcal{S}}_\alpha^\dagger(\omega') - \hat{\mathcal{S}}_\alpha^\dagger(\omega')\hat{\mathcal{S}}_\beta(\omega)\hat{\rho}_S^{(i)}(t)\right] + \text{h.c.}, \tag{2.111}$$

where h.c. denotes the hermitian conjugate of the previous term in the sum, and

$$\Gamma_{\alpha,\beta}(\omega) = \int_0^\infty e^{i\omega s}\text{Tr}_R\{\hat{\mathcal{R}}_\alpha^{(i)\dagger}(t)\hat{\mathcal{R}}_\beta^{(i)}(t-s)\hat{\rho}_R^{(i)}\}ds. \tag{2.112}$$

Finally, we introduce the RRWA, from which we ignore all $\omega \neq \omega'$ terms in Eq. (2.111). The RRWA is valid as long as the time scale given by $\sim 1/|\omega - \omega'|$ (for $\omega \neq \omega'$) is larger than the time scale at which the state system varies appreciably [72]. This approximation results in

$$\frac{d}{dt}\hat{\rho}_S^{(i)}(t) \approx \sum_{\omega,\alpha,\beta} \Gamma_{\alpha,\beta}(\omega)\left[\hat{\mathcal{S}}_\beta(\omega)\hat{\rho}_S^{(i)}(t)\hat{\mathcal{S}}_\alpha^\dagger(\omega) - \hat{\mathcal{S}}_\alpha^\dagger(\omega)\hat{\mathcal{S}}_\beta(\omega)\hat{\rho}_S^{(i)}(t)\right] + \text{h.c.}. \tag{2.113}$$

Lamb shift and Lindblad super operators

After the RRWA, it is guaranteed that solving $\hat{\rho}_S^{(i)}$ in Eq. (2.113) results in a positive-definite matrix [73]. Furthermore, Eq. (2.113) addresses the dynamics of the state of the system almost exclusively by using only the dressed operators of the system, which do not depend on the reservoir (the only information about the reservoir is encoded in $\Gamma_{\alpha,\beta}$, Eq. (2.112)). Moving back to the Schrödinger picture we can express Eq. (2.113) as [72, 73]

$$\frac{d}{dt}\hat{\rho}_S(t) = \frac{-i}{\hbar}[(\hat{\mathcal{H}}_S + \hat{\mathcal{H}}_{R\Delta\omega}), \hat{\rho}_S(t)] + \sum_{\alpha,\beta,\omega} \gamma_{\alpha,\beta}(\omega)\mathcal{D}_{\hat{S}_\alpha(\omega),\hat{S}_\beta(\omega)}[\hat{\rho}_S(t)], \tag{2.114}$$

where

$$\gamma_{\alpha,\beta}(\omega) = \Gamma_{\alpha,\beta}(\omega) + \Gamma_{\alpha,\beta}^*(\omega), \tag{2.115}$$

$\mathcal{D}_{\hat{S}_\alpha(\omega),\hat{S}_\beta(\omega)}$ are the so-called Lindblad or Gorini–Kossakowski–Sudarshan–Lindblad (GKSL) superoperators and $\hat{\mathcal{H}}_{R\Delta\omega}$ is the so-called reservoir Lamb-shift Hamiltonian (see discussion below). Let us start by describing the Lindblad superoperators. In this thesis we only study systems where $\gamma_{\alpha,\beta}$ becomes diagonal, *i.e.*, $\gamma_{\alpha,\beta}(\omega) = \delta_{\alpha,\beta}^K\gamma_{\alpha,}(\omega)$, and thus Eq. (2.114) simplifies to,

$$\frac{d}{dt}\hat{\rho}_S(t) = \frac{-i}{\hbar}[(\hat{\mathcal{H}}_S + \hat{\mathcal{H}}_{R\Delta\omega}), \hat{\rho}_S(t)] + \sum_{\alpha,\omega} \gamma_\alpha(\omega)\mathcal{D}_{\hat{S}_\alpha(\omega)}[\hat{\rho}_S(t)], \tag{2.116}$$

where the $\mathcal{D}_{\hat{S}_\alpha(\omega)}[\hat{\rho}_S(t)]$ Lindblad superoperators read as

$$\mathcal{D}_{\hat{S}_\alpha(\omega)}[\hat{\rho}_S(t)] = \left(\hat{\mathcal{S}}_\alpha(\omega)\hat{\rho}_S(t)\hat{\mathcal{S}}^\dagger_\alpha(\omega_k) - \frac{1}{2}\{\hat{\mathcal{S}}^\dagger_\alpha(\omega)\hat{\mathcal{S}}_\alpha(\omega), \hat{\rho}_S(t)\}\right). \tag{2.117}$$

$\mathcal{D}$ are also sometimes called dissipation superoperators because they are often used to model only the energetic dissipation of the quantum system due to its interaction with the reservoir. However, the Lindblad superators are not restricted to modeling the dissipation of the system, they can also model an incoherent or a thermal pump, or they can also model the pure-dephasing of the quantum system, *i.e.*, an interaction of the quantum system with the reservoir that does not induce a direct mechanism for loss (nor gain) of energy of the quantum system.

On the other hand, the reservoir Lamb-shift Hamiltonian corresponds to

$$\hat{\mathcal{H}}_{R\Delta\omega} = \hbar \sum_{\alpha,\beta} \Delta\omega_{\alpha,\beta}(\omega)\hat{\mathcal{S}}^\dagger_\alpha(\omega)\hat{\mathcal{S}}_\beta(\omega), \tag{2.118}$$

where

$$\Delta\omega_{\alpha,\beta}(\omega) = \frac{-i}{2}(\Gamma_{\alpha,\beta}(\omega_k) - \Gamma^*_{\alpha,\beta}(\omega_k)), \tag{2.119}$$

The reservoir Lamb-shift Hamiltonian in Eq. (2.118) has the role of renormalizing the energies of the system due to its interaction with the reservoir. This effect is usually incorporated in the definition of the energies of the Hamiltonian of the system, and $\hat{\mathcal{H}}_{R\Delta\omega}$ is neglected [72, 73]. Thus, we arrive at the final form of the master equation

$$\frac{d}{dt}\hat{\rho}_S(t) = \frac{-i}{\hbar}[\hat{\mathcal{H}}_S, \hat{\rho}_S(t)] + \sum_{\alpha,\omega} \gamma_\alpha(\omega)\mathcal{D}_{S_\alpha(\omega)}[\hat{\rho}_S(t)], \tag{2.120}$$

also called the Lindbladian master equation.

CHAPTER 3

FANO ASYMMETRY IN ZERO–DETUNED EXCITON–PLASMON SYSTEMS

3.1 Introduction

In chapter 1, we describe how metallic nanoparticles (or nanoantennas) support plasmonic resonances, which allows for confining light in small hot spots located in their surroundings [3, 23–26]. On of the advantages of this field confinement is that it can lead to very efficient interaction with quantum emitters, such as quantum dots, solid-state color centers, or molecules. The interaction can modify the optical properties of the optical transition of a quantum emitter (QE), for example enhancing its emission rate, which can be exploited in a variety of applications in nanophotonics [108–110]. For example, in surface-enhanced spectroscopy, the coupling with the plasmonic nanoantennas enables the optical characterization of very small amounts or even single molecules [3, 5, 8, 25, 111–117].

In this context, the elastic response of QEs interacting with nanoantennas often results in a distinctive narrow spectral feature, the so-called Fano resonance, that has been characterized in many different nanophotonic systems [8, 118–121]. The Fano resonance can consist in a symmetric dip in the spectrum or in a very asymmetric lineshape [113, 115, 122–124]. It is generally well understood that the asymmetry of the Fano features depends strongly on the detuning between the resonance of the QEs and that of the plasmonic nanoantenna. A symmetric Fano dip is typically expected when the detuning of the QE and the nanoantenna resonances is zero (resonant system), and it becomes increasingly asymmetric as the detuning is increased [112–115]. However, it has been recently emphasized [8]

that clear asymmetric Fano lineshapes can also be found for zero detuning. In this chapter, we analyze in detail the origin of the additional asymmetry of the Fano lineshape in the spectra of resonant plasmon-exciton systems. We consider an exciton of a single QE in resonance with an optical mode of a metallic nanoantenna, but the conclusions can be extended to other similar systems.

In this study, we first focus (sections 3.2-3.4) on the extinction cross-section spectrum of a spherical nanoparticle interacting resonantly with a QE. We first introduce a simple model that identifies why a symmetric Fano feature is typically expected under resonant conditions [112–115], and then we use rigorous electromagnetic calculations to show that an asymmetry in the spectrum can be present in a realistic configuration. The different phenomena that lead to the asymmetry are introduced and analyzed in detail in section 3.4, where we first develop an analytical expression that decomposes the Fano asymmetry factor into two different contributions. Furthermore, we implement a series of simple models to analyze how the Fano asymmetry is influenced by aspects in the nanoparticle-QE interaction, such as retardation, direct illumination and emission of the QE, and the contribution to the dielectric permittivity of the nanoantenna from the band structure of d-electrons. Finally, in section 3.5 we illustrate the general validity of our study by analyzing a more complex nanoantenna, a dimer composed of two spherical gold nanoparticles. This study can help to better understand the asymmetry in Fano features beyond the detuning between exciton and plasmon resonances.

3.2 Fano asymmetry under resonant conditions

To illustrate why a symmetric Fano dip is expected under resonant conditions of excitation of a nanoantenna and a QE, and to expose how this expectation is not always fulfilled, we first compare (i) the extinction cross-section of a canonical nanoantenna-QE system obtained using a simple model that results in a symmetric Fano dip with (ii) the exact calculations giving an asymmetric Fano lineshape. We consider a silver spherical nanoparticle (nanoantenna) of radius $R = 20$ nm coupled to a QE under weak illumination. The QE is placed at a position (in Cartesian coordinates), $\boldsymbol{r}_{\mathrm{e}} = ((R+d)_x, 0_y, 0_z)$. We treat the QE as a point-like dipole, representing an excitonic transition with polarizability along the direction perpendicular to the surface of the plasmonic nanoantenna (x-axis). The dipolar plasmon mode of the nanoantenna (see section 1.2) and the excitonic transition of the QE are resonant at the same wavelength λ_0 (frequency $\omega_0 = 2\pi c_0/\lambda_0$). The system is situated in a vacuum, and it is excited by a plane wave of amplitude E_0 polarized parallel to the dipole orientation (Fig. 3.1a).

To obtain the extinction spectrum of the hybrid QE-nanoantenna system, we first consider a simple dipole-dipole interaction model that treats the spherical nanoantenna as a second point-like dipole positioned at its center (the center of coordinates), representing the dipolar plasmon mode. This model is based on the response of small spherical nanoparticles introduced in section 1.2. In typical

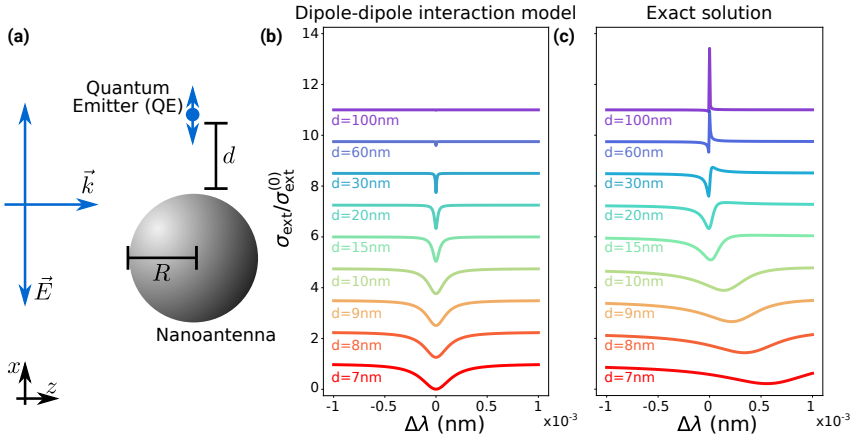

Figure 3.1: Fano asymmetry under resonant nanoantenna-QE conditions. (a) Scheme of the system studied in sections 3.2 and 3.4. A QE is placed at a distance d from the surface of a silver spherical nanoparticle of radius R. An excitonic transition couples resonantly with the dipolar mode of the nanoparticle. The excitonic transition in the QE is polarized along the x-axis that joins the center of the nanoantenna and the QE. The system is illuminated by a plane wave propagating along the z-axis with electric field polarized along the x-axis. (b) and (c) Extinction cross-section of the hybrid system, $\sigma_{\rm ext}$, normalized to the spectra of the bare sphere, $\sigma_{\rm ext}^{(0)}$ as obtained within (b) the simple dipole-dipole interaction model described in sections 3.2 and 3.4 and (c) within rigorous Mie theory calculations. The spectra are vertically displaced by 1.25 for clarity and plotted as a function of the wavelength detuning ($\Delta\lambda = \lambda - \lambda_0$) with respect to the resonance of both nanoantenna and QE (λ_0). Each spectral line is evaluated for different distances, d, between the QE and the surface of the antenna (indicated in the figure). In both calculations, the radius of the silver spherical nanoparticle is $R = 20$ nm. The exact calculations consider the experimental permittivity of silver [41] to model the response of the nanoantenna (leading to $\lambda_0 = 359.78$ nm). On the other hand, in the approximated dipole-dipole interaction model we use the Drude model to describe the dielectric function of the nanoantenna, $\varepsilon_{\rm a} = 1 - \omega_{\rm p}^2/[\omega(\omega + i\kappa)]$, with $\hbar\omega_{\rm p} = 6.06$ eV and $\hbar\kappa = 0.62$ eV, obtaining $\lambda_0 = 354.59$ nm for the dipolar excitation.

plasmonic systems, the fields induced by the nanoantenna at the position of the QE are much larger than the incident field [3, 111], so that the direct illumination of the QE can be neglected. Using this assumption and the quasistatic approximation, we obtain the following coupled equations for the dipole moments (oriented along the x-axis) induced in the QE, $p_{\rm e}$, and in the nanoantenna, $p_{\rm a}$:

$$p_{\rm e}(\omega) = \alpha_{\rm e}(\omega) G^{\rm qs}_{x,x}(\boldsymbol{r}_{\rm e}) p_{\rm a}(\omega), \tag{3.1a}$$

$$p_{\rm a}(\omega) = \alpha_{\rm a}(\omega)(E_0 + G^{\rm qs}_{x,x}(\boldsymbol{r}_{\rm e}) p_{\rm e}(\omega)), \tag{3.1b}$$

with $G^{\rm qs}_{x,x}$ the $\{x,x\}$–component of the quasistatic near-field Green's function, which describes the field propagation between dipoles and was already introduced in section 1.2.1. In Eqs. (3.1a) and (3.1b) we have used that the field propagation from the nanoantenna (centered at $\boldsymbol{r}_{\rm a} = 0$) to the QE is equivalent to the propagation

from the QE to the nanoantenna, *i.e.*, $G^{\rm qs}_{x,x}(\boldsymbol{r}_{\rm e}) \equiv G^{\rm qs}_{x,x}(\boldsymbol{r}_{\rm e},\boldsymbol{r}_{\rm a}) = G^{\rm qs}_{x,x}(\boldsymbol{r}_{\rm a},\boldsymbol{r}_{\rm e})$ (see Eq. (1.27)). $\alpha_{\rm a}$ and $\alpha_{\rm e}$ in Eqs. (3.1a) and (3.1b) are the polarizability of the nanoantenna and of the QE, respectively. Within a Drude model description of the permittivity of the metal, and using a Drude-Lorentz model for the optical response of the QE, the $\alpha_{\rm e}$ and $\alpha_{\rm a}$ polarizabilities become:

$$\alpha_{\rm e}(\omega) = \frac{A_{\rm e}}{\omega_0^2 - \omega^2 - i\gamma_0\omega}, \tag{3.2a}$$

$$\alpha_{\rm a}(\omega) = \frac{A_{\rm a}}{\omega_0^2 - \omega^2 - i\kappa\omega}, \tag{3.2b}$$

where the strength of the coupling between the two dipoles is determined by the polarizability amplitude of the QE, $A_{\rm e}$, and that of the plasmonic nanoantenna, $A_{\rm a}$. The frequency $\omega_R = \omega_p/\sqrt{3}$ is the frequency of the dipolar plasmon resonance in the nanoantenna (with ω_p the Drude plasma frequency). Here we chose ω_R to match ω_0 ($\omega_R = \omega_0$), the resonant excitation frequency of the QE. Last, γ_0 and κ are the spontaneous decay rate of the QE and the plasmonic intrinsic decay rate, respectively. Throughout this chapter we consider that the dipole moment of the excitonic transition is $f_0 = 0.05e{\cdot}$nm (e is the electron charge), which sets the polarizability amplitude of the QE $A_{\rm e} = 2\omega_0 f_0^2/\hbar$ and the spontaneous decay rate $\gamma_0 = \omega_0^3 f_0^2/(3\pi\varepsilon_0\hbar c_0^3)$ (see section 1.2.4). We do not consider other intrinsic molecular losses beyond γ_0. Substituting Eqs. (3.2a) and (3.2b) into Eqs. (3.1a) and (3.1b) one obtains:

$$(\omega_0^2 - \omega^2)p_{\rm e}(\omega) - i\omega\gamma_0 p_{\rm e}(\omega) = A_{\rm e}G^{\rm qs}_{x,x}(\boldsymbol{r}_{\rm e})p_{\rm a}(\omega), \tag{3.3a}$$

$$(\omega_0^2 - \omega^2)p_{\rm a}(\omega) - i\omega\kappa p_{\rm a}(\omega) = A_{\rm a}G^{\rm qs}_{x,x}(\boldsymbol{r}_{\rm e})p_{\rm e}(\omega) + A_{\rm a}E_0. \tag{3.3b}$$

Here, the polarizability amplitude of the nanoantenna determines how efficiently the system is excited (via the term $A_{\rm a}E_0$). Eqs. (3.1a)-(3.3b) and the expression used to obtain $A_{\rm a}$ are discussed in more detail in section 3.4.2.

We note that Eqs. (3.3a) and (3.3b) are very similar to those obtained with phenomenological models that assume that the QE and the plasmonic nanoparticle can be treated as two coupled harmonic oscillators. This coupled-harmonic-oscillators model has been frequently used to describe the interaction between quantum emitters and nanoantennas [8, 125, 126].

We show in Fig. 3.1b the extinction cross-section spectrum of the hybrid QE-nanoantenna system obtained using Eqs. (3.3a) and (3.3b) for different values of the separation distance d between the QE and the surface of the nanoantenna (the value of d affects the quasistatic Green's function, $G^{\rm qs}_{x,x}$, and, thus, the QE-nanoantenna interaction). The extinction cross section $\sigma_{\rm ext}$ is normalized to the corresponding value of the bare nanoantenna $\sigma^{(0)}_{\rm ext}$ and it is obtained assuming that the direct emission of the QE is negligible ($p_{\rm a} \gg p_{\rm e}$), which is a typical situation

in plasmonic systems. In this case, the optical theorem (Eq. (1.41)) [40] gives

$$\sigma_{\mathrm{ext}}^{\mathrm{simp}}(\omega) = \frac{2\pi}{\lambda\varepsilon_0}\mathrm{Im}\{p_{\mathrm{a}}(\omega)/E_0\}, \tag{3.4}$$

where the super index "simp" emphasizes that this is a simplified expression that only considers the emission from the nanoantenna.

The normalized extinction cross-section in Fig. 3.1b features an almost constant background and the emergence of a spectrally narrow dip at the resonant wavelength λ_0 for all the separation distances d considered. The background corresponds to the very broad plasmonic response and the dip to the Fano feature. Importantly, the Fano dip obtained within this simple dipole-dipole interaction model (Eqs. (3.3a)-(3.4)) is always perfectly symmetric.

We next obtain the exact electromagnetic response of the hybrid system, which we calculate from the optical theorem (Eq. (1.41)) by obtaining the total scattered field within the rigorous Mie theory formalism introduced in section 1.3 (see also references [40, 45, 127]). In particular, we use Mie theory to calculate the response of the spherical nanoantenna illuminated by the incoming plane wave (section 1.3.2) and by the induced dipole moment of the QE (section 1.2.4). For all Mie theory calculations shown in this chapter, we have used an expansion of 60 multipoles, which we verified that ensures convergence. The details of the calculation of the extinction cross-section are given in section 3.3.1.

Figure 3.1c shows the resulting extinction cross section obtained for the same system and distances d as in Fig. 3.1b. These exact calculations exhibit again a broad background, due to the response of the bare plasmonic nanoantenna, and a narrow Fano feature caused by the coupling between the QE exciton and the plasmonic resonance of the nanoantenna. However, the Fano lineshapes show clear differences compared to those obtained with the simple dipole-dipole interaction model (Eqs. (3.3a)-(3.4) and Fig. 3.1b). Overall, the Fano features are broader for the exact calculations than for the simple dipole model. Further, the exact calculation also results in a shift of the Fano features, induced by the photonic lamb shift, not included in the simple model. The shift and larger broadening are clearer for small nanoantenna-QE separation distances ($d < 20$ nm) and are mainly a consequence of the coupling between the QE exciton and the higher-order modes of the nanoantenna [35, 95, 96, 128–136]. Crucially, the Fano feature obtained within the exact calculations is not necessarily a perfectly symmetric dip, but it can take different lineshapes. This shape evolves from a broad and almost symmetric dip at short separation distances ($d < 15$ nm) towards a narrow and almost symmetric peak at large separation distances ($d > 60$ nm). In the range between these two extremes, the Fano feature becomes clearly asymmetric.

Thus, we have shown that the prediction of a symmetric Fano dip obtained with a simple dipole-dipole interaction model can strongly differ from the results of the exact calculations, where significantly asymmetric lineshapes emerge. We emphasize that this asymmetry is not due to plasmon-exciton detuning as the resonance condition of zero detuning is preserved in all cases. In the following, we

analyze in detail the different physical mechanisms that lead to asymmetric Fano lineshapes for QE-nanoantenna systems under resonant conditions.

3.3 Fano lineshape

3.3.1 Analytical derivation of the Fano lineshape in the extinction cross-section

First, we show that the extinction cross-section spectrum σ_{ext} of a QE interacting with a nanoantenna follows the modified Fano lineshape discussed in references [118, 119],

$$\frac{\sigma_{\text{ext}}(\omega)}{\sigma_{\text{ext}}^{(0)}} \approx \frac{(\Omega(\omega)+q)^2+B}{\Omega(\omega)^2+1}, \tag{3.5}$$

where q is the Fano asymmetry factor (the key parameter that we analyze in this chapter), B is the zero-dip parameter, and

$$\Omega(\omega) = \frac{{\omega_0'}^2-\omega^2}{\omega\gamma'}, \quad \omega_0' = \omega_0 + \Delta\omega, \tag{3.6}$$

with $\Delta\omega$ the Lamb shift. γ' is the enhanced decay rate of the QE in the presence of the nanoantenna, which can be written in terms of the Purcell Factor P_{F} as

$$\gamma' = (P_{\text{F}}+1)\gamma_0 + \gamma_i^{\text{NR}} \tag{3.7}$$

where γ_i^{NR} are other intrinsic (non-radiative) losses of the QE (in this chapter we consider $\gamma_i^{\text{NR}} = 0$). q, B, $\Delta\omega$, and P_{F} are the main parameters defining the Fano lineshape. In the first part of this subsection, we focus on deriving simple analytical expressions to calculate them in an arbitrary QE-nanoantenna system. In the second part of this subsection, we evaluate them for a QE interacting with a silver spherical nanoparticle and discuss in more depth their physical origin.

To obtain the extinction cross-section of the QE–nanoantenna system using the optical theorem [40], evaluated for our system and illumination

$$\sigma_{\text{ext}}(\omega) = \frac{4\pi}{k^2}\text{Re}\left\{(-ikz_{\text{d}})e^{-ikz_{\text{d}}}\frac{E_x^{\text{FF}}(\boldsymbol{r}_{\text{d}},\omega)}{E_0}\right\}, \tag{3.8}$$

where E_x^{FF} is the x-component of the scattered electric field that the QE-nanoantenna system induces on a point-like detector placed in the far-field region, at the (Cartesian) coordinates $\boldsymbol{r}_{\text{d}} = (0_x, 0_y, (z_{\text{d}})_z)$. σ_{ext} is independent of the chosen value of z_{d} since $E_x^{\text{FF}}(\boldsymbol{r}_{\text{d}},\omega) \propto e^{ikz_{\text{d}}}/z_{\text{d}}$ [40]. We note that throughout this derivation, it is only necessary to calculate the x-component of all of the considered electric fields because of the geometry considered [35, 40]. Thus, to avoid repetition, we do not always state explicitly in the discussion below that we are referring to the x-component of the fields, or the (x,x)-component of the Green's functions,

but we indicate this by an x (or (x,x)) subindex.

E_x^{FF} can be expressed as the sum of two contributions,

$$E_x^{\mathrm{FF}}(\boldsymbol{r}_{\mathrm{d}},\omega) = E_x^{\mathrm{A}}(\boldsymbol{r}_{\mathrm{d}},\omega) + E_x^{\text{E-Tot}}(\boldsymbol{r}_{\mathrm{d}},\omega), \tag{3.9}$$

where E_x^{A} is the field directly scattered by the nanoantenna in the absence of the QE and $E_x^{\text{E-Tot}}$ is the total electric field that the QE induces at the detector considering the presence of the nanoantenna. By defining the far-field enhancement factor at the position of the detector as $K^{\mathrm{FF}}(\boldsymbol{r}_{\mathrm{d}},\omega) = E_x^{\mathrm{A}}(\boldsymbol{r}_{\mathrm{d}},\omega)/E_0$ we can write E_x^{A} as

$$E_x^{\mathrm{A}}(\omega) = K^{\mathrm{FF}}(\omega)E_0. \tag{3.10}$$

On the other hand, $E_x^{\text{E-Tot}}$ can be written using the Green's function formalism as

$$E_x^{\text{E-Tot}}(\boldsymbol{r}_{\mathrm{d}},\omega) = G_{x,x}^{\mathrm{FF}}(\boldsymbol{r}_{\mathrm{d}},\boldsymbol{r}_{\mathrm{e}},\omega)p_{\mathrm{e}}(\omega), \tag{3.11}$$

where p_{e} is the induced dipole moment of the QE (oriented along the x-axis) and $G_{x,x}^{\mathrm{FF}}$ is the Green's function that describes the emission of the QE towards the detector in the presence of the nanoantenna.

We decompose $G_{x,x}^{\mathrm{FF}}$ as a sum of two contributions

$$G_{x,x}^{\mathrm{FF}}(\boldsymbol{r}_{\mathrm{d}},\boldsymbol{r}_{\mathrm{e}},\omega) = G_{0_{x,x}}^{\mathrm{FF}}(\boldsymbol{r}_{\mathrm{d}},\boldsymbol{r}_{\mathrm{e}},\omega) + S_{x,x}^{\mathrm{FF}}(\boldsymbol{r}_{\mathrm{d}},\boldsymbol{r}_{\mathrm{e}},\omega), \tag{3.12}$$

where $G_{0_{x,x}}^{\mathrm{FF}}$ (already introduced in Eq. (1.24)) is the vacuum Green's function that describes the field E_x^{E} that the QE induces in the detector when no nanoantenna is present,

$$E_x^{\mathrm{E}}(\boldsymbol{r}_{\mathrm{d}},\omega) = G_0^{\mathrm{FF}}{}_{x,x}(\boldsymbol{r}_{\mathrm{d}},\boldsymbol{r}_{\mathrm{e}},\omega)p_{\mathrm{e}}(\omega), \tag{3.13}$$

where we can approximate $\boldsymbol{r}_{\mathrm{e}} \approx 0$ in the evaluation of $G_0^{\mathrm{FF}}{}_{x,x}$ (*i.e.*, the effect of this change becomes negligible small in the detector situated in the far-field), so that

$$G_{0_{x,x}}^{\mathrm{FF}}(\boldsymbol{r}_{\mathrm{d}},\boldsymbol{r}_{\mathrm{e}},\omega) \approx G_{0_{x,x}}^{\mathrm{FF}}(\boldsymbol{r}_{\mathrm{d}},0,\omega) = \frac{k^2}{4\pi\varepsilon_0 z_{\mathrm{d}}}e^{ikz_{\mathrm{d}}}, \tag{3.14}$$

On the other hand, $S_{x,x}^{\mathrm{FF}}$ is the dyadic function that describes the electric fields induced by the QE on the detector via the nanoantenna E_x^{EA} [137] (*i.e.* the electric fields that the nanoantenna scatters towards the detector when it is illuminated only by the QE),

$$E_x^{\mathrm{EA}}(\boldsymbol{r}_{\mathrm{d}},\omega) = S_{x,x}^{\mathrm{FF}}(\boldsymbol{r}_{\mathrm{d}},\boldsymbol{r}_{\mathrm{e}},\omega)p_{\mathrm{e}}(\omega). \tag{3.15}$$

For the exact results obtained with Mie theory, we calculate $S_{x,x}^{\mathrm{FF}}$ using Mie theory as discussed in reference [127]. To evaluate Eqs. (3.11), (3.13), and (3.15) we need first to obtain the value of the induced dipole moment p_{e}. p_{e} is given by (see

section 1.2.4),

$$p_{\mathrm{e}}(\omega) = \alpha_{\mathrm{e}}(\omega) E_x^{\mathrm{NF}}(\boldsymbol{r}_{\mathrm{e}}, \omega), \tag{3.16}$$

where α_{e} is given in Eq. (3.2a). E_x^{NF} is the field that excites the QE,

$$E_x^{\mathrm{NF}}(\boldsymbol{r}_{\mathrm{e}}, \omega) = E_0 + E_x^{\mathrm{AE}}(\boldsymbol{r}_{\mathrm{e}}, \omega) + E_x^{\mathrm{EAE}}(\boldsymbol{r}_{\mathrm{e}}, \omega), \tag{3.17}$$

which we write as the sum of the field E_0 due to the direct illumination of the plane wave, and two additional contributions induced by the presence of the nanoantenna, E_x^{AE} and E_x^{EAE}. E_x^{AE} corresponds to the electric field that the nanoantenna induces at the QE position in the absence of the QE due to the illumination by the incident plane wave, *i.e.* E_x^{AE} depends only on the response of the isolated nanoantenna. If we use a typical definition of the near-field enhancement factor at the position of the QE, $K(\boldsymbol{r}_{\mathrm{e}}, \omega) = E_x^{\mathrm{AE}}(\boldsymbol{r}_{\mathrm{e}}, \omega)/E_0$, we can write

$$E_x^{\mathrm{AE}}(\boldsymbol{r}_{\mathrm{e}}, \omega) = K(\boldsymbol{r}_{\mathrm{e}}, \omega) E_0. \tag{3.18}$$

On the other hand, E_x^{EAE} is the electric field that the QE induces at its own position via the nanoantenna, that is, the field scattered by the nanoantenna at the QE position when the only source is the QE. We write this contribution as a function of p_{e} by using again the Green's function formalism. For doing so, we introduce the dyadic function $S_{x,x}^{\mathrm{NF}}$ that describes the emission of the QE onto itself via the nanoantenna [137],

$$E_x^{\mathrm{EAE}}(\boldsymbol{r}_{\mathrm{e}}, \omega) = S_{x,x}^{\mathrm{NF}}(\boldsymbol{r}_{\mathrm{e}}, \omega) p_{\mathrm{e}}(\omega). \tag{3.19}$$

Using Eqs. (3.17), (3.18), and (3.19) we find the expression for p_{e},

$$p_{\mathrm{e}}(\omega) = \frac{A_{\mathrm{e}}}{\omega_0'(\omega)^2 - \omega^2 - i\gamma'(\omega)\omega} [K(\boldsymbol{r}_{\mathrm{e}}, \omega) + 1] E_0, \tag{3.20}$$

with

$$\omega_0'(\omega)^2 = \omega_0^2 - A_{\mathrm{e}} \mathrm{Re}\{S_{x,x}^{\mathrm{NF}}(\boldsymbol{r}_{\mathrm{e}}, \omega)\}, \quad \gamma'(\omega) = \gamma_0 + \gamma_i^{\mathrm{NR}} + \frac{1}{\omega} A_{\mathrm{e}} \mathrm{Im}\{S_{x,x}^{\mathrm{NF}}(\boldsymbol{r}_{\mathrm{e}}, \omega)\}, \tag{3.21}$$

where γ_i^{NR} is the non-radiative decay rate of the QE (in this chapter, we consider $\gamma_i^{\mathrm{NR}} = 0$). We observe that the $A_{\mathrm{e}}/[\omega_0'(\omega)^2 - \omega^2 - i\gamma'(\omega)\omega]$ prefactor in Eq. (3.20) follows a similar expression to the original α_{e} polarizability of the QE (Eq. (3.2a)) but for the central frequency, which is shifted from ω_0 to ω_0' in Eq. (3.21) (see Eq. (3.6)) and for the decay rate of the QE, which is augmented from γ_0 to γ' in Eq. (3.21) (see Eq. (3.7)).

By using Eqs. (3.10), (3.11), and (3.20) we can write E_x^{FF} as

$$E_x^{\mathrm{FF}}(\boldsymbol{r}_\mathrm{d},\omega) = \\ = \Big\{K^{\mathrm{FF}}(\boldsymbol{r}_\mathrm{d},\omega) + \underbrace{[G_0^{\mathrm{FF}}{}_{x,x}(\boldsymbol{r}_\mathrm{d},\boldsymbol{r}_\mathrm{e},\omega) + S_{x,x}^{\mathrm{FF}}(\boldsymbol{r}_\mathrm{d},\boldsymbol{r}_\mathrm{e},\omega)]}_{G_{x,x}^{\mathrm{FF}}(\boldsymbol{r}_\mathrm{d},\boldsymbol{r}_\mathrm{e},\omega)} \frac{A_\mathrm{e}[K(\boldsymbol{r}_\mathrm{e},\omega)+1]}{\omega_0'(\omega)^2-\omega^2-i\gamma'(\omega)\omega}\Big\}E_0, \tag{3.22}$$

and by substituting Eq. (3.22) into Eq. (3.8) we obtain

$$\sigma_{\mathrm{ext}}(\omega) = \\ = \frac{4\pi}{k^2}\mathrm{Re}\left\{(-ikz_\mathrm{d})e^{-ikz_\mathrm{d}}\left[K^{\mathrm{FF}}(\boldsymbol{r}_\mathrm{d},\omega) + G_{x,x}^{\mathrm{FF}}(\boldsymbol{r}_\mathrm{d},\boldsymbol{r}_\mathrm{e},\omega)\frac{A_\mathrm{e}(K(\boldsymbol{r}_\mathrm{e},\omega)+1)}{\omega_0'(\omega)^2-\omega^2-i\gamma'(\omega)\omega}\right]\right\}. \tag{3.23}$$

We normalize this expression by the extinction cross-section of the bare nanoantenna $\sigma_{\mathrm{ext}}^{(0)}$ (that can be calculated using the optical theorem as $\sigma_{\mathrm{ext}}^{(0)}(\omega) = (4\pi/k^2)\mathrm{Re}\{(-ikz_\mathrm{d})e^{-ikz_\mathrm{d}}K^{\mathrm{FF}}(\boldsymbol{r}_\mathrm{d},\omega)\}$), and obtain the normalized extinction cross-section of the hybrid system as:

$$\frac{\sigma_{\mathrm{ext}}(\omega)}{\sigma_{\mathrm{ext}}^{(0)}(\omega)} = \\ = \mathrm{Re}\Big\{1 + \frac{1}{\frac{k^2}{4\pi}\sigma_{\mathrm{ext}}^{(0)}(\omega)}(-ikz_\mathrm{d})e^{-ikz_\mathrm{d}}G_{x,x}^{\mathrm{FF}}(\boldsymbol{r}_\mathrm{d},\boldsymbol{r}_\mathrm{e},\omega)\frac{A_\mathrm{e}(K(\boldsymbol{r}_\mathrm{e},\omega)+1)}{\omega_0'(\omega)^2-\omega^2-i\gamma'(\omega)\omega}\Big\}. \tag{3.24}$$

Next, we define

$$\Omega(\omega) = \frac{\omega_0'(\omega)^2-\omega^2}{\gamma'(\omega)\omega}, \tag{3.25}$$

$$q(\omega) = \frac{1}{2}\frac{1}{\frac{k^2}{4\pi}\sigma_{\mathrm{ext}}^{(0)}(\omega)}\frac{A_\mathrm{e}}{\gamma'(\omega)\omega}\mathrm{Re}\left\{(-ikz_\mathrm{d})e^{-ikz_\mathrm{d}}G_{x,x}^{\mathrm{FF}}(\boldsymbol{r}_\mathrm{d},\boldsymbol{r}_\mathrm{e},\omega)(K(\boldsymbol{r}_\mathrm{e},\omega)+1)\right\}, \tag{3.26}$$

$$B(\omega) = \\ = 1 - q(\omega)^2 - \frac{1}{\frac{k^2}{4\pi}\sigma_{\mathrm{ext}}^{(0)}(\omega)}\frac{A_\mathrm{e}}{\gamma'(\omega)\omega}\mathrm{Im}\left\{(-ikz_\mathrm{d})e^{-ikz_\mathrm{d}}G_{x,x}^{\mathrm{FF}}(\boldsymbol{r}_\mathrm{d},\boldsymbol{r}_\mathrm{e},\omega)(K(\boldsymbol{r}_\mathrm{e},\omega)+1)\right\}, \tag{3.27}$$

and, taking into account that A_e, γ_0, ω, ω_0, and $\sigma_\mathrm{ext}^{(0)}(\omega)$ are real numbers, we can simplify Eq. (3.24) as

$$\frac{\sigma_\mathrm{ext}(\omega)}{\sigma_\mathrm{ext}^{(0)}(\omega)} = \left[1 + \frac{2q(\omega)\Omega}{\Omega^2+1} + \frac{-1+q(\omega)^2+B(\omega)}{\Omega^2+1}\right] = \frac{[\Omega+q(\omega)]^2+B(\omega)^2}{\Omega^2+1}. \quad (3.28)$$

For generality, we have kept in this derivation the explicit frequency dependence of the parameters $\sigma_\mathrm{ext}^{(0)}(\omega)$, $\gamma'(\omega)$, $\omega_0'(\omega)^2$, $q(\omega)$, and $B(\omega)$, so that Eq. (3.28) is exact. If we consider that the spectral width of the Fano feature (determined by γ') is much smaller than the spectral width of the plasmon resonance of the nanoantenna we can evaluate all these parameters at the excitonic resonant frequency ω_0,

$$\sigma_\mathrm{ext}^{(0)} \approx \sigma_\mathrm{ext}^{(0)}(\omega_0), \quad \gamma' \approx \gamma'(\omega_0), \quad {\omega_0'}^2 \approx \omega_0'(\omega_0)^2, \quad q \approx q(\omega_0), \quad B \approx B(\omega_0), \quad (3.29)$$

and approximate[xvi] Eq. (3.28) as the modified Fano lineshape [8,118,119],

$$\frac{\sigma_\mathrm{ext}(\omega)}{\sigma_\mathrm{ext}^{(0)}} \approx \frac{(\Omega(\omega)+q)^2+B^2}{\Omega(\omega)^2+1}, \quad (3.30)$$

with $\Omega(\omega) = ({\omega_0'}^2-\omega^2)/(\omega\gamma')$. To ensure that the approximation of Eq. (3.29) is justified, we consider in this chapter a dipolar oscillator strength f_0 of the QE sufficiently small so that the Fano features remain very narrow [138,139] (in our calculations we use $f_0 = 0.05e\cdot$ nm, e being the electron charge).

Next we summarize the expressions of the parameters present in Eq. (3.30),

$$\sigma_\mathrm{ext}^{(0)} = \frac{4\pi}{k_0^2}\mathrm{Re}\left\{(-ik_0z_\mathrm{d})e^{-ik_0z_\mathrm{d}}K^\mathrm{FF}(\boldsymbol{r}_\mathrm{d},\omega_0)\right\}, \quad (3.31a)$$

$$\Delta\omega = \omega_0' - \omega_0 = \sqrt{\omega_0 - A_\mathrm{e}\mathrm{Re}\{S_{x,x}^\mathrm{NF}(\boldsymbol{r}_\mathrm{e},\omega_0)\}} - \omega_0, \quad (3.31b)$$

$$P_\mathrm{F} = \frac{\gamma'-\gamma_i^\mathrm{NR}}{\gamma_0} - 1 = \frac{1}{\omega}A_\mathrm{e}\mathrm{Im}\{S_{x,x}^\mathrm{NF}(\boldsymbol{r}_\mathrm{e},\omega_0)\}, \quad (3.31c)$$

$$q = \frac{1}{2}\frac{1}{\frac{k_0^2}{4\pi}\sigma_\mathrm{ext}^{(0)}}\frac{A_\mathrm{e}}{\gamma'\omega_0}\mathrm{Re}\left\{(-ik_0z_\mathrm{d})e^{-ik_0z_\mathrm{d}}G_{x,x}^\mathrm{FF}(\boldsymbol{r}_\mathrm{d},\boldsymbol{r}_\mathrm{e},\omega_0)(K(\boldsymbol{r}_\mathrm{e},\omega_0)+1)\right\}, \quad (3.31d)$$

$$B = 1 - q^2 - \frac{1}{\frac{k_0^2}{4\pi}\sigma_\mathrm{ext}^{(0)}}\frac{A_\mathrm{e}}{\gamma'\omega_0}\mathrm{Im}\left\{(-ik_0z_\mathrm{d})e^{-ik_0z_\mathrm{d}}G_{x,x}^\mathrm{FF}(\boldsymbol{r}_\mathrm{d},\boldsymbol{r}_\mathrm{e},\omega_0)(K(\boldsymbol{r}_\mathrm{e},\omega_0)+1)\right\}, \quad (3.31e)$$

where $k_0 = \omega_0 c_0$ is the wavevector at the resonant frequency ω_0. We have verified that Eqs. (3.30)-(3.31e) describe all the spectra that we present in this chapter very accurately (*i.e.* the approximation given in Eq. (3.29) is valid). We note that all the parameters in Eqs. (3.31a)-(3.31e) can be obtained from standard classical

[xvi] In the systems studied in this chapter $\omega_0 \approx \omega_0'$, and thus, evaluating the parameters $\sigma_\mathrm{ext}^{(0)}$, γ', q, and B parameters in Eq. (3.29) at ω_0 or ω_0' gives very similar results.

electromagnetic calculations.

Finally, we simplify Eq. (3.31d) using the reciprocity theorem [140–142]. According to this theorem, near-field enhancement factor $K(\boldsymbol{r}_\mathrm{e},\omega) = E_x^\mathrm{A}(\boldsymbol{r}_\mathrm{e},\omega)/E_0$ is connected with the fields that the QE induces at the detector directly (E_x^E) and via the nanoantenna (E_x^EA) by the following equation,

$$K(\boldsymbol{r}_\mathrm{e},\omega) = \frac{E_x^\mathrm{EA}(\boldsymbol{r}_\mathrm{e},\omega)}{E_x^\mathrm{E}(\boldsymbol{r}_\mathrm{e},\omega)}. \tag{3.32}$$

Using Eqs. (3.13), (3.15), and (3.32) we write the reciprocity theorem as

$$\frac{S_{x,x}^\mathrm{FF}(\boldsymbol{r}_\mathrm{d},\boldsymbol{r}_\mathrm{e},\omega)}{{G_0^\mathrm{FF}}_{x,x}(\boldsymbol{r}_\mathrm{d},\boldsymbol{r}_\mathrm{e},\omega)} = K(\boldsymbol{r}_\mathrm{e},\omega). \tag{3.33}$$

In principle, the reciprocity theorem [140–142] relates the field enhancement induced by a plane-wave with the emission of the QE in the backward direction (*i.e.* in the negative z-direction for the considered systems), while ${G_0^\mathrm{FF}}_{x,x}$ and $S_{x,x}^\mathrm{FF}$ in Eq. (3.31d) describe the emission of the QE in the forward direction (*i.e.* in the positive z-direction). However, the symmetry of our system implies that ${G_0^\mathrm{FF}}_{x,x}$ and $S_{x,x}^\mathrm{FF}$ are identical in the forward and backward direction, and Eqs. (3.32) and (3.33) are valid. By using Eq. (3.12) we can write Eq. (3.33) as

$$G_{x,x}^\mathrm{FF}(\boldsymbol{r}_\mathrm{d},\boldsymbol{r}_\mathrm{e},\omega) = {G_0^\mathrm{FF}}_{x,x}(\boldsymbol{r}_\mathrm{d},\boldsymbol{r}_\mathrm{e},\omega)(K(\boldsymbol{r}_\mathrm{e},\omega)+1). \tag{3.34}$$

Last, using Eqs. (3.14), (3.31d), and (3.34) we obtain

$$q = \frac{A_\mathrm{e}}{2\sigma_\mathrm{ext}^{(0)}\gamma' c_0 \varepsilon_0}\left(\mathrm{Im}\{K(\boldsymbol{r}_\mathrm{e},\omega_0)\} + \mathrm{Re}\{K(\boldsymbol{r}_\mathrm{e},\omega_0)\}\mathrm{Im}\{K(\boldsymbol{r}_\mathrm{e},\omega_0)\}\right), \tag{3.35}$$

3.3.2 Evaluation of the Fano lineshape

In the subsection above, we have shown that the extinction cross-section of a QE-nanoantenna system excited by a plane wave can be described by a modified Fano lineshape [8, 118, 119] (assuming that the spectral width of the QE emission is much smaller than the width of the spectral response of the nanoantenna). For convenience, we repeat here the formula of the modified Fano lineshape in Eq. (3.30)

$$\frac{\sigma_\mathrm{ext}(\omega)}{\sigma_\mathrm{ext}^{(0)}} \approx \frac{(\Omega(\omega)+q)^2+B}{\Omega(\omega)^2+1},$$

where $\Omega(\omega) = ({\omega_0'}^2-\omega^2)/(\omega\gamma')$ (Eq. (3.25)).

The modified Fano lineshape in Eq. (3.30) depends on three parameters, q, $\Omega(\omega)$, and B (calculated from Eqs. (3.31a)-(3.31e) and (3.35)). As introduced above, q is the total asymmetry factor (also called Fano-parameter) that captures the asymmetry of the Fano lineshape of the extinction cross-section spectrum, and it is the main focus of this chapter. Ω is a normalized frequency given in Eq. (3.6).

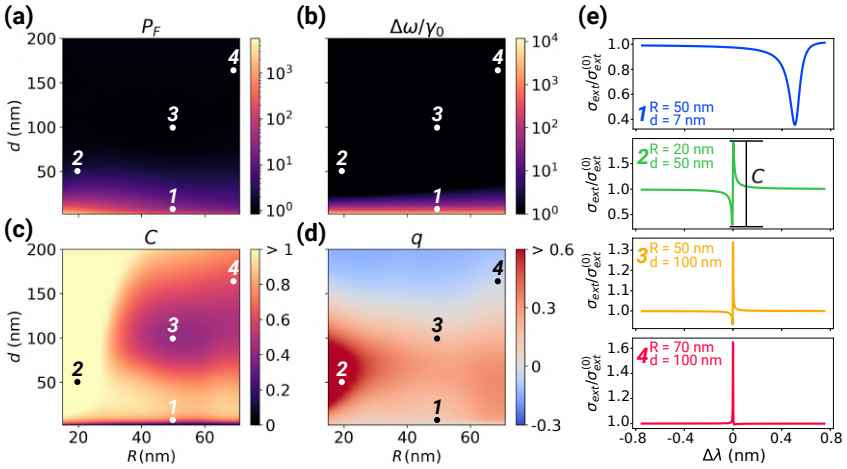

Figure 3.2: (a-d) Contour plots of the parameters defining the Fano lineshape, obtained within Mie theory. (a) Purcell Factor, P_F, (b) Lamb Shift, $\Delta\omega$, (c) contrast, C, and (d) total asymmetry factor, q, as a function of the distance, d (the minimum distance in the panels is $d = 2$ nm), from the QE to the surface of a silver spherical antenna with different radius, R. The resonance of the QE is chosen to match the frequency of resonance of the nanoantenna for all sizes of particles, R. (e) Normalized extinction spectra of the hybrid system are evaluated at points marked as 1, 2, 3, and 4 in panels (a)-(d). The values of R and d for each point are indicated in the labels of panel (e).

$\Delta\omega$ is the photonic Lamb Shift (Eq. (3.6)) that corresponds to a slight shift in the resonant frequency from ω_0 to ω_0', and $\gamma' = (P_F + 1)\gamma_0$ are the enhanced losses of the QE (Eq. (3.7)), which describes the broadening of the Fano dip. Both effects can be clearly observed in the spectra of Fig. 3.1c. The expression of γ' assumes no intrinsic losses beyond γ_0, but it can be modified in a straightforward manner to include additional intrinsic losses. Last, B in Eq. (3.30) is the zero-dip parameter (Eq. (3.31e)) that can be related to the factor q and the contrast $C = \sqrt{2(B+1)q^2 + (B-1)^2 + q^4}$. Here, we define the contrast C of the Fano feature as the difference between the maximum and the minimum of the Fano feature in the normalized extinction cross-section spectrum (see inset in panel 2 of Fig. 3.2e).

Thus, changes on the Fano spectral lineshape can be understood by analyzing the parameters, q, C, P_F, and $\Delta\omega$ (the last two determining Ω). Note that these parameters can be obtained from the classical Green's function and the field enhancement of the plasmonic antenna at the position of the emitter according to Eqs. (3.31a)-(3.31e). In Fig. 3.2a-d, we systematically study the dependence of these parameters with the radius of the silver spherical nanoparticle, R, and the distance between the antenna and the emitter, d. All values are obtained from exact Mie theory calculations using the experimental values of the silver permittivity [41] and assuming resonant conditions; *i.e.*, for each radius, we find the frequency of the dipolar plasmonic resonance of the antenna (lowest-energy peak in the extinction

cross-section spectrum of the bare nanoantenna), and we modify the energy of the QE transition accordingly. To illustrate the resulting Fano lineshape described by the parameters in Figs. 3.2a-b, we also show, in Fig. 3.2e, the extinction cross section spectrum for four different points indicated in Figs. 3.2a-d (the values of R and d for each point are given in the labels of Fig. 3.2e).

For all the radii considered, the Purcell Factor, P_{F}, (Fig. 3.2a), and the photonic Lamb shift $\Delta\omega$ (Fig. 3.2b) strongly increase when the QE approaches the antenna, as shown in previous studies [35, 95, 96, 128–133]. This increase is due to the more efficient coupling of the QE with the plasmonic modes of the nanoantenna, particularly with high-order modes. On the other hand, the contrast, C, shows a more complex dependence with the radius, R, and the distance, d (Fig. 3.2c). We can distinguish three different distance regimes in this figure. For short distances ($d \lesssim 10$ nm), the QE couples very efficiently to the higher-order modes of the spherical nanoparticle, and the resulting quenching of the emission [134–136] leads to the disappearance of the Fano dip (small contrast). For intermediate distances (compared to the radius, *i.e.* 10 nm $\lesssim d \lesssim 3R$), the quenching becomes less significant, and the Fano feature emerges with a reasonably big contrast ($1 \gtrsim C \gtrsim 0.5$, purple-reddish region in Fig. 3.2c). In this regime of distances, the contrast is smaller for spheres with $R \gtrsim 40$ nm, which is mainly a consequence of two destructive interference effects, the first between the excitation of the QE by the illumination plane–wave and by the antenna-induced near fields, and the second between the light emitted by the QE directly and via the nanoantenna. Last, as the separation distance is made significantly larger than the radius ($d \gtrsim 3R$), the QE progressively decouples from the nanoantenna, and the extinction cross-section of the whole system evolves toward the superposition of the peak of the extinction cross-section of the QE in a vacuum on top of the broad background spectrum of the bare spherical nanoparticle. We can then express the extinction cross–section of the whole system at very long separation distances as $(\sigma_{\mathrm{ext}}^{(0)} + \sigma_{\mathrm{ext}}^{\mathrm{QE}})/\sigma_{\mathrm{ext}}^{(0)}$, where $\sigma_{\mathrm{ext}}^{\mathrm{QE}}$ is the extinction cross-section of the QE in a vacuum. As we have considered that the QE only has radiative losses due to the spontaneous decay, $\sigma_{\mathrm{ext}}^{\mathrm{QE}}$ is larger than the extinction cross-section of the bare spherical nanoparticle $\sigma_{\mathrm{ext}}^{(0)}$ [36] ($\sigma_{\mathrm{ext}}^{\mathrm{QE}} = 6\pi(\omega_0/c_0)^2 > \sigma_{\mathrm{ext}}^{(0)}$), and the contrast becomes higher than one, $C > 1$.

Last, Fig. 3.2d shows the relatively complex dependence of the total asymmetry factor q with radius R and distance d. The Fano asymmetry is small ($|q| < 0.2$) for $d \lesssim 10$ nm (corresponding to a symmetric dip) and for large distances, $d \gtrsim 150$ nm, (corresponding to an almost symmetric peak). At intermediate distances (10 nm $\lesssim d \lesssim 150$ nm) the asymmetry is significantly larger, with a maximum value at a distance $d \sim 50$ nm, which is strongly dependent on the radius. We also find that at large distances ($d \gtrsim 150$ nm) the asymmetry can take negative values and show a damped oscillatory behavior of q with d (the dependence of q for a larger range of distance is studied in section 3.4.3). Understanding this complex behavior is the main objective of this chapter and it is analyzed in detail next.

3.4 Dissection of the asymmetry

To analyze the Fano asymmetry in more detail, we show in subsection 3.4.1 that the expression of the asymmetry factor (Eq. (3.35)) can be decomposed into two contributions, each of them described by a simple analytical expression, and describing the effect in the asymmetry of a collection of different physical mechanisms. In subsections 3.4.2 and 3.4.3, we evaluate the asymmetry factor and its contributions using a series of analytical dipole-dipole interaction models of increasing accuracy to understand how different aspects of the interaction affect the Fano profile.

3.4.1 Analytical expression of the total asymmetry factor

To further analyze the total asymmetry factor q of the Fano lineshape, we first separate its analytical expression in Eq. (3.35) into two main contributions, q_{E} and q_{R} (derivation in appendix A):

$$q = \underbrace{\left(\frac{A_{\mathrm{e}}}{2\sigma_{\mathrm{ext}}^{(0)} c_0 \varepsilon_0} \frac{\mathrm{Im}\{K(\boldsymbol{r}_{\mathrm{e}}, \omega_0)\}}{\gamma'}\right)}_{q_{\mathrm{E}}} + \underbrace{\left(\frac{A_{\mathrm{e}}}{2\sigma_{\mathrm{ext}}^{(0)} c_0 \varepsilon_0} \frac{\mathrm{Re}\{K(\boldsymbol{r}_{\mathrm{e}}, \omega_0)\}\mathrm{Im}\{K(\boldsymbol{r}_{\mathrm{e}}, \omega_0)\}}{\gamma'}\right)}_{q_{\mathrm{R}}}. \tag{3.36}$$

We focus first on analyzing the q_{R} contribution to the asymmetry factor. In appendix A, we demonstrate that this factor fully describes the asymmetry in resonant conditions if we ignore the direct excitation and emission of the QE ($q \to q_{\mathrm{R}}$). If we decompose explicitly the field enhancement into its amplitude $|K|$ and phase φ_{A}, we obtain:

$$q_{\mathrm{R}} = \frac{A_{\mathrm{e}}}{2\sigma_{\mathrm{ext}}^{(0)} c_0 \varepsilon_0} \frac{|K(\boldsymbol{r}_{\mathrm{e}}, \omega_0)|^2 \sin(2\varphi_{\mathrm{A}}(\boldsymbol{r}_{\mathrm{e}}, \omega_0))}{\gamma'}. \tag{3.37}$$

We can further simplify Eq. (3.37) by connecting $|K|$ with the enhanced decay rate γ' as:

$$\frac{|K(\boldsymbol{r}_{\mathrm{e}}) + 1|^2}{\gamma'} = \frac{\eta_{\mathrm{R}}}{\mathcal{D}\gamma_0}, \tag{3.38}$$

where η_{R} is the radiative yield (defined as the ratio between the radiative and the total decay rate of the QE in the presence of the nanoantenna) [134]. $\mathcal{D}$ is the directivity (as defined in Eq. (1.37)) of the fields emitted by the QE in the presence of the nanoantenna normalized by the directivity of the bare QE [42, 130] and it is typically close to one ($\mathcal{D} \sim 1$). We show in appendix B how to derive Eq. (3.38) by using reciprocity [140–142] and provide the exact definition of $\mathcal{D}$. For plasmonic nanostructures $|K|$ is often much larger than 1 and we can then

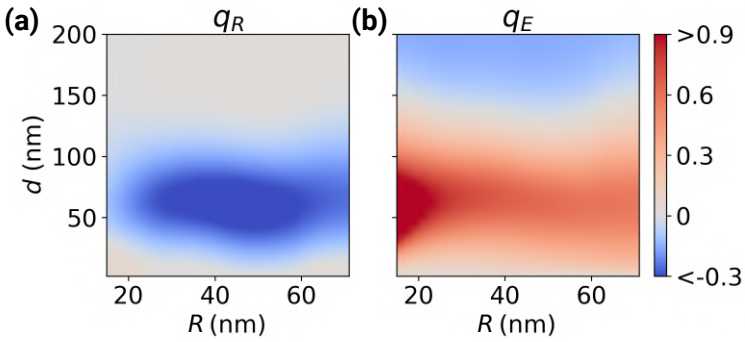

Figure 3.3: Values of the two asymmetry factors q_{R} and q_{E}. The values of (a) q_{R} and (b) q_{E} given in Eq. (3.36) are shown for different radius R and distances of the QE to the surface d (the minimum distance in the panels is 2 nm). These results are obtained using Mie theory and the experimental permittivity of silver [41]. For each radius, R, the resonance of the QE is chosen to match the frequency of the resonance of the nanoantenna.

approximate the equality in Eq. (3.38) as $|K(\boldsymbol{r}_{\mathrm{e}})|^2/\gamma' \approx \eta_{\mathrm{R}}/\mathcal{D}\gamma_0$, which results in

$$q_{\mathrm{R}} \approx \frac{A_{\mathrm{e}}}{2\sigma_{\mathrm{ext}}^{(0)} c_0 \varepsilon_0} \frac{\eta_{\mathrm{R}}}{\mathcal{D}\gamma_0} \sin(2\varphi_{\mathrm{A}}(\boldsymbol{r}_{\mathrm{e}}, \omega_0)). \tag{3.39}$$

Thus, the asymmetry factor q_{R} only depends in this case on the phase of the field enhancement φ_{A}, but not on its amplitude. In the simplified dipole-dipole interaction model considered in section 3.2 (Eqs. (3.3a)-(3.4)), $\varphi_{\mathrm{A}}(\boldsymbol{r}_{\mathrm{e}}, \omega_0) = \pi/2$, and thus $q_{\mathrm{R}} = 0$. When φ_{A} deviates from $\pi/2$ (for example, due to retardation) $q_{\mathrm{R}} \neq 0$, introducing an asymmetry in the Fano feature.

Figure 3.3a shows the values of q_{R} calculated using the full electromagnetic Mie theory to describe the scattering of the silver spherical nanoparticle. q_{R} is again plotted in resonant conditions as a function of the radius of the silver spherical nanoparticle R and the distance d between the emitter and the surface of the nanoparticle. $|q_{\mathrm{R}}|$ is largest for intermediate distances (20 nm $\lesssim d \lesssim$ 80 nm) where retardation is significant (and thus, φ_{A} becomes substantially different than $\pi/2$) and $|K|$ is of the order of 1 (see Eq. (3.37)). At shorter distances, $|K|$ increases so that Eq. (3.39) becomes more accurate, and at the same time $\sin(2\varphi_{\mathrm{A}}(\boldsymbol{r}_{\mathrm{e}}, \omega_0))$ takes values close to 0, since retardation becomes negligible. As a consequence, $|q_{\mathrm{R}}|$ strongly decreases. On the other hand, at larger distances, $|K|^2$ becomes very small and γ' becomes similar to the intrinsic decay rate γ_0. Thus, $|q_{\mathrm{R}}|$ gradually approaches 0, according to Eq. (3.37).

We next analyze the second asymmetry contribution, $q_{\mathrm{E}} \propto \mathrm{Im}\{K(\boldsymbol{r}_{\mathrm{e}}, \omega_0)\}/\gamma'$ (Eq. (3.36)), which appears when the direct excitation and emission of the QE is considered. The results of the Mie's calculation of q_{E} are shown in Fig. 3.3b. q_{E} is small for long QE–nanoantenna distances ($d > 100$ nm) because $|K|$ approaches 0 and $\gamma' \approx \gamma_0$ (we focus here on the absolute value of q_{E} and we discuss the change of

sign for $d \approx 150$ nm below). Indeed, for long distances the system starts to decouple and we can approximately consider the response of the QE and the nanoantenna separately. These two contributions interfere constructively so that we can directly add up their respective extinction cross-sections according to the optical theorem. Thus, the final extinction cross-section spectrum is given by a symmetric peak due to the QE emission added to the broad plasmonic peak (panel 4 in Fig. 3.2e), corresponding to low values of q_{E} and q.

Furthermore, q_{E} is also small at short distances ($d \lesssim 20$ nm). In this case $|K| \gg 1$ so that $q_{\mathrm{E}} \propto \mathrm{Im}\{K(\boldsymbol{r}_{\mathrm{e}}, \omega_0)\}/\gamma' \to 0$ because $\gamma' \propto |K(\boldsymbol{r}_{\mathrm{e}}, \omega_0) + 1|^2 \gamma_0$ (from Eq. (3.38)). These low values of q_{E} for small d could be expected since q_{E} is given by the direct excitation of the QE; therefore q_{E} becomes negligible if the direct excitation is very small in comparison with the excitation via the nanoantenna.

On the other hand, q_{E} becomes largest for intermediate separation distances (20 nm $\lesssim d \lesssim$ 80 nm), as Fig. 3.3b shows. In this range of distances, the field induced by the spherical nanoparticle is of similar strength as the field of the incident plane-wave ($|K| \approx 1$). The excitation of the QE is then given by an interplay between the direct and the antenna-mediated illumination, which carry a different phase leading to large values of the asymmetry factor $q_{\mathrm{E}} \gtrsim 0.6$. We note that in all this discussion, we have focused on the direct excitation, but a similar analysis can also be developed in terms of the direct emission of the antenna, according to reciprocity, which was adopted in the derivation of the expression of q_{E} in Eq. (3.36). The analysis of the q_{E} and q_{R} factors thus already gives insights into the general behavior of the total asymmetry factor q (Eq. (3.36)) shown in Fig. 3.2d. Notably, the relatively low values of q obtained for intermediate radius (40 nm $\lesssim R \lesssim$ 60 nm) in the 20 nm $\lesssim d \lesssim$ 80 nm separation distance range, which results in a characteristic "saddle" shape, are due to the addition of two asymmetry factors, $q = q_{\mathrm{E}} + q_{\mathrm{R}}$ of similar absolute value but opposite sign.

3.4.2 Effect of different optical response approximations on the asymmetry

To further understand the origin of the asymmetry q and its contributions, q_{E} and q_{R}, under resonant conditions, we adopt different analytical dipole-dipole interaction models of increasing levels of complexity. A general dipole-dipole description of the QE-nanoantenna system introduced in section 3.2 (Fig. 3.1) is given by

$$p_{\mathrm{e}}(\omega) = \alpha_{\mathrm{e}}(\omega)(E_0 + \mathcal{G}_{x,x}(\boldsymbol{r}_{\mathrm{e}}, \omega) p_{\mathrm{a}}(\omega)), \tag{3.40a}$$

$$p_{\mathrm{a}}(\omega) = \alpha_{\mathrm{a}}(\omega)(E_0 + \mathcal{G}_{x,x}(\boldsymbol{r}_{\mathrm{e}}, \omega) p_{\mathrm{e}}(\omega)), \tag{3.40b}$$

where E_0 is the amplitude of the excitation field and p_{a} and α_{a} are the induced dipole and the polarizability of a single plasmonic mode of the nanoantenna (in our case the dipolar plasmonic mode), respectively. p_{e} and α_{e} are the corresponding magnitudes of the exciton of the QE. α_{e} is given by Eq. (3.2a) and during this section we use different models to describe α_{a}. $\mathcal{G}_{x,x}$ is the $\{x, x\}$-component

of the Green's function that describes the interaction between the QE and the nanoantenna (either the quasistatic or the fully retarded expression). As already introduced, due to the geometry chosen, we can treat the induced dipoles and polarizabilities of the QE and nanoantenna as scalars.

Finally, the extinction cross section of the QE-nanoantenna system can be obtained from the optical theorem (Eq. (1.41)) [40] as:

$$\sigma_{\text{ext}} = \frac{2\pi}{\lambda\varepsilon_0}\text{Im}\left\{\frac{p_{\text{a}}+p_{\text{e}}}{E_0}\right\}. \tag{3.41}$$

In the following, we introduce different approximations in Eqs. (3.40a)-(3.41). We first discuss the simplifications necessary to reproduce the simple model discussed in section 3.2 (Eqs. (3.1a)-(3.3b)). We then systematically modify this model to progressively build up a more rigorous model that nicely reproduces the results obtained with Mie theory (Figs. 3.3 and 3.2d). In this manner we can better identify how different effects contribute to each of the features of the total asymmetry factor in resonance.

We show in Fig. 3.4a-g the total asymmetry factor q and its contributions q_{R} and q_{E} when different modifications of the dipole-dipole interaction models are implemented. Each column of the figure shows the results for particular assumptions in the model (as indicated by labels at the bottom) and the first, second, and third row of the figure provide the values of q_{R}, q_{E}, and q (respectively) evaluated for the same ranges of radius R and distances d as those in Figs. 3.3 and 3.2a-d.

Simple reference model

We consider first the simple dipole-dipole interaction model introduced in section 3.2 (Eqs. (3.3a)-(3.4)). This simple model describes the optical response of the coupled QE-nanoantenna system using four simplifications in Eqs. (3.40a)-(3.41):

(i) The polarizability of the spherical nanoantenna, α_{a}, is obtained using the quasistatic approximation (Eq. (1.29)),

$$\alpha_{\text{a}}(\omega) = 4\pi\varepsilon_0 R^3 \frac{\varepsilon_{\text{a}}(\omega)-1}{\varepsilon_{\text{a}}(\omega)+2}, \tag{3.42}$$

where ε_{a} is the relative dielectric permittivity of the nanoantenna.

(ii) We describe the permittivity of the metallic nanoantenna using the Drude's model, $\varepsilon_{\text{a}}(\omega) = 1-\omega_{\text{p}}^2/[\omega(\omega+i\kappa)]$, where ω_{p} is the plasma frequency, and κ are the plasmon losses. Inserting ε_{a} into Eq. (3.42), directly recovers the expression of the polarizability given in Eq. (3.2b), with $A_{\text{a}} = 4\pi\omega_{\text{p}}^2\varepsilon_0 R^3/3$ and $\omega_0 = \omega_{\text{p}}/\sqrt{3}$. This expression of α_{a} is purely imaginary at resonance ($\omega = \omega_0$).

(iii) The QE is only excited by the field created by the nanoantenna (corresponding to $\mathcal{G}_{x,x}(\boldsymbol{r}_{\text{e}},\omega)p_{\text{a}}(\omega)$ in Eq. (3.40a)), neglecting the direct excitation of the QE by the incident plane wave. Further, we also neglect the direct emission of the QE to the far-field as it is usually smaller than the emission mediated by the nanoantenna. According to the optical theorem, the extinction cross-section is

then directly given by the induced dipole at the nanoantenna, $\sigma_{\rm ext} \propto {\rm Im}\{p_{\rm a}\}$.

(iv) The interaction between the QE and the nanoantenna is described using the quasistatic Green's function (Eq. (1.27))

$$G^{\rm qs}_{x,x}(\boldsymbol{r}_{\rm e}) = \frac{1}{2\pi\varepsilon_0(R+d)^3}, \tag{3.43}$$

which is real-valued (and frequency-independent).

In the following, it is useful to summarize the optical response of the QE-nanoantenna system assumed in this simple model by displaying the set of equations summarizing the model:

$$p_{\rm a}(\omega) = \alpha_{\rm a}(\omega)(E_0 + G^{\rm qs}_{x,x}(\boldsymbol{r}_{\rm e})p_{\rm e}(\omega)), \tag{3.44a}$$

$$p_{\rm e}(\omega) = \alpha_{\rm e}(\omega)K(\boldsymbol{r}_{\rm e},\omega)E_0, \tag{3.44b}$$

$$K(\boldsymbol{r}_{\rm e},\omega)E_0 = G^{\rm qs}_{x,x}(\boldsymbol{r}_{\rm e})p_{\rm a}(\omega), \tag{3.44c}$$

$$\gamma' = \left[1 + {\rm Im}\left\{\frac{A_{\rm e}\alpha_{\rm a}(\omega)}{\gamma_0\omega_0}(G^{\rm qs}_{x,x}(\boldsymbol{r}_{\rm e}))^2\right\}\right]\gamma_0, \tag{3.44d}$$

$$\sigma_{\rm ext}(\omega) = \frac{2\pi}{\lambda\varepsilon_0}{\rm Im}\left\{\frac{p_{\rm a}(\omega)}{E_0}\right\}, \tag{3.44e}$$

where we have introduced the connection of the field enhancement factor K at the position of the QE with the induced dipole moment of the nanoantenna and the Green's function (Eq. (3.44c)). We also include the expression of the enhanced effective decay rate of the QE, γ' (Eq. (3.44d)). Both K and γ' are key parameters to understand the changes on the asymmetry of the Fano feature. This simple reference model always predicts a zero asymmetry factor ($q = 0$, $q_{\rm E} = 0$, and $q_{\rm R} = 0$), as shown in section 3.2 and, thus, it is not included in Fig. 3.4.

Contribution of *d*-electrons to the permittivity

The first modification to the simple dipole-dipole interaction model consists in changing the dielectric permittivity of the nanoantenna from the simple Drude model $\varepsilon_{\rm a}(\omega) = 1 - \omega_{\rm p}^2/[\omega(\omega + i\kappa)]$ into a modified Drude expression $\varepsilon_{\rm a}^{\rm MD}(\omega) = \varepsilon_\infty - \omega_{\rm p}^2/[\omega(\omega + i\kappa)]$ (with $\varepsilon_\infty = 6$, $\hbar\omega_{\rm p} = 9.17$ eV, and $\hbar\kappa = 21$ meV). $\varepsilon_{\rm a}^{\rm MD}$ approximately includes the effect of the d-electrons of silver, which allows for better describing the optical response of the silver nanoantenna. Within this description, Eqs. (3.44a)-(3.44e) remain valid except that the polarizability of the nanoantenna is now $\alpha_{\rm a}^{\rm MD}(\omega) = 4\pi R^3(\varepsilon_{\rm a}^{\rm MD}(\omega) - 1)/(\varepsilon_{\rm a}^{\rm MD}(\omega) + 2)$, so that $\alpha_{\rm a}^{\rm MD}$ is no longer a perfect Lorentzian function. As a consequence, the induced field enhancement K is not purely imaginary at resonance and the Fano feature at resonance becomes slightly asymmetric, $q = q_{\rm R} \neq 0$, according to Eq. (3.39) ($q_{\rm E} = 0$ because we are not considering yet the contribution of the direct emission and excitation of the QE). We show in Fig. 3.4a the results of the total asymmetry factor q and its contributions $q_{\rm E}$ and $q_{\rm R}$ obtained within this model as a function

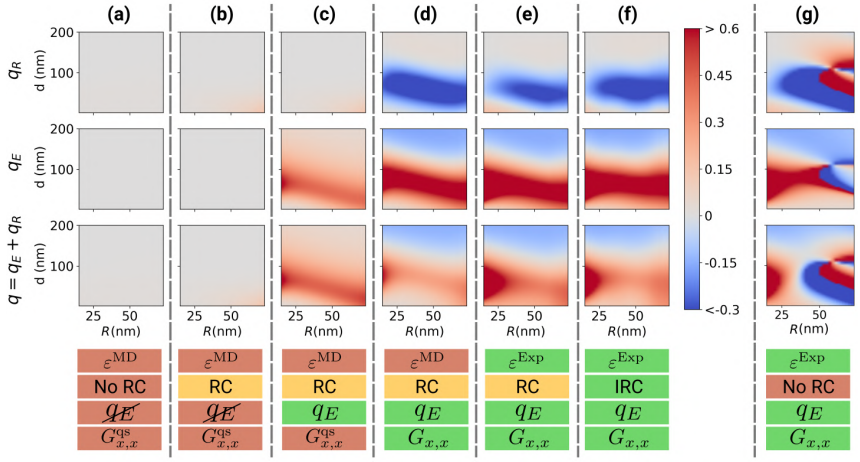

Figure 3.4: Behavior of the asymmetry factors in the extinction cross-section in resonant conditions (zero detuning between the nanoantenna and QE resonances). Each (a)-(g) column contains three panels showing the values of the asymmetry factors q_R (first row), q_E (second row), and the total asymmetry factor, $q = q_E + q_R$, (third row). The asymmetry factors are calculated for different values of the radius R of the silver spherical nanoantenna, and the distance d between the nanoantenna and the QE. The resonance of the QE is chosen to match the frequency of the dipolar resonance of the nanoantenna for each radius R. The values shown in each (a)-(g) column are obtained using the different models described in subsection 3.4.2. The values of the asymmetry factors are saturated to values larger than 0.6 and smaller than -0.3. At the bottom of each (a)-(g) column, we indicate the main features of the considered model with four labels colored in green, yellow, or red. The red labels indicate a less accurate description of a given feature, while the yellow and green indicate a progressively more accurate description. The label "ε^{MD}" indicates that we use the modified Drude expression to describe the permittivity of the nanoantenna. "ε^{Exp}" indicates that we use the experimental values of the permittivity of the nanoantenna [41]. "No RC" indicates that we do not consider the radiative correction. "RC" indicates that we consider a simple radiative correction. "IRC" indicates that we use an improved version of the radiative correction (3.46) [47]. "$\not{q_E}$" indicates that we do not consider the direct excitation and emission of the QE (and thus $q_E = 0$). "q_E" indicates that we do consider the direct and emission of the QE. "$G^{qs}_{x,x}$" indicates that we use the quasistatic Green's function described in section 3.2. "$G_{x,x}$" indicates that we use the full expression of the Green's function (Eq. (1.21)).

of the radius R of the spherical nanoparticle and the distance d between the QE and the surface of the nanoparticle. We observe how, although within this model $q \neq 0$ and $q_R \neq 0$, the asymmetry remains very small with $q \leq 0.01$.

Simple radiative correction

We next consider a simple radiative correction to the nanoantenna polarizability in Eq. (1.36): $\alpha_a^{RC}(\omega) = \alpha_a^{MD}(\omega)/[1 - i\alpha_a^{MD}(\omega)(2\pi/\lambda)^3/(6\pi\varepsilon_0)]$ [35, 47, 143], which accounts for the radiation damping of the nanoantenna in a vacuum (see section 1.2.2). This correction incorporates the scattering losses that broaden the resonance, which was neglected in the previous quasistatic description (Fig. 3.4a).

We note that, once the radiative correction is introduced, the maximum of the extinction cross-section $\sigma_{\text{ext}}^{(0)}$ of the bare nanoantenna dipolar resonance red-shifts spectrally with increasing size and is found at a slightly shorter wavelength than the corresponding maximum of the near–field enhancement $|K|$ [144, 145]. When not stated otherwise, we consider by default that the resonance frequency of the QE, ω_0, matches the frequency at which $\sigma_{\text{ext}}^{(0)}$ is maximum. Below, in section 3.4.3, we show that the effect of setting ω_0 to the maximum of $|K|$ is weak.

We show in Fig. 3.4b (second column of the figure) the resulting total asymmetry factor q (and its contributions, q_{E} and q_{R}) obtained after substituting $\alpha_{\text{a}}^{\text{MD}}$ by $\alpha_{\text{a}}^{\text{RC}}$ in the simplest dipole-dipole interaction model (3.44a)-(3.44c). This change mainly affects the value of K, which acquires a larger real part at resonance as compared to the previous model (the phase of K deviates further from $\pi/2$) and, thus, $q = q_{\text{R}}$ increases (Eq. (3.37)), with q_{E} remaining equal to zero. In particular, q_{R} becomes larger with increasing R, as the effect of the radiative correction increases with the size of the nanoantenna. q_{R} also increases for shorter d due to the stronger enhancement $|K|$. However, the asymmetry remains small (hardly noticeable in Fig. 3.4b, with $\max(q_{\text{R}}) \approx 0.14$). Last, we note that this low value of q may lead to think that the radiative correction is of little importance in the description of the total asymmetry factor. However, we emphasize in the last model presented in this section that, once we go beyond the quasistatic approximation, it is critical to consider a correct description of the radiative correction.

Direct excitation and emission of the QE

In the next step we introduce the direct excitation of the QE by the plane wave and the direct emission of the QE to the far field (third column, Fig. 3.4c). These two effects are introduced at the same time because, due to reciprocity [140–142], their contribution to the asymmetry is identical (demonstration in appendix A). After all these changes the response of the system is given by the following modified equations:

$$p_{\text{a}}(\omega) = \alpha_{\text{a}}^{\text{RC}}(\omega)(E_0 + G_{x,x}^{\text{qs}}(\boldsymbol{r}_{\text{e}})p_{\text{e}}(\omega)), \tag{3.45a}$$

$$p_{\text{e}}(\omega) = \alpha_{\text{e}}(\omega)(1 + K(\boldsymbol{r}_{\text{e}}, \omega))E_0, \tag{3.45b}$$

$$K(\boldsymbol{r}_{\text{e}}, \omega)E_0 = G_{x,x}^{\text{qs}}(\boldsymbol{r}_{\text{e}})p_{\text{a}}(\omega), \tag{3.45c}$$

$$\gamma' = \left[1 + \text{Im}\left\{\frac{A_{\text{e}}\alpha_{\text{a}}^{\text{RC}}(\omega)}{\gamma_0\omega_0}(G_{x,x}^{\text{qs}}(\boldsymbol{r}_{\text{e}}, \omega))^2\right\}\right]\gamma_0, \tag{3.45d}$$

$$\sigma_{\text{ext}}(\omega) = \frac{2\pi}{\lambda\varepsilon_0}\text{Im}\left\{\frac{p_{\text{a}}(\omega) + p_{\text{e}}(\omega)}{E_0}\right\}. \tag{3.45e}$$

The direct excitation of the QE by the incident plane wave of amplitude E_0 is described by the term $\alpha_{\text{e}}E_0$ in Eq. (3.45b). Similarly, the direct contribution from the QE to the extinction cross section is given by the term $\propto \text{Im}\{p_{\text{e}}\}$ in Eq. (3.45e). In this scenario, the q_{E} contribution to the asymmetry is no longer zero, and the full expression of the total asymmetry factor, $q = q_{\text{E}} + q_{\text{R}}$, needs to be

considered (Eq. (3.36)). On the other hand, q_{R} remains unchanged as compared to the previous model.

As shown in Fig. 3.4c the resulting q_{E} dominates the total asymmetry factor q, and follows similar trends with distance as those described when discussing the results of the exact calculation in Fig. 3.3. q_{E} is small at long separation distances ($d > 100$ nm) because the QE and the nanoantenna start to behave independently, and also at short distances ($d \lesssim 20$ nm) because the direct excitation of the QE is very small compared to the excitation via the nanoantenna. q_{E} is thus maximum at intermediate distances within this model (20 nm $\lesssim d \lesssim$ 80 nm) where the excitation of the QE via the nanoantenna is of the same order of magnitude than the direct excitation by the incident plane wave. The distance that maximizes q_{E} follows a linear dependence with increasing radius R. More precisely, the maxima are found for an approximately constant distance between the QE and the center of the nanoantenna ($d + R$). This behavior occurs because in this description the near fields are evaluated using the quasistatic Green's function, which only depends on $(d + R)^3$. Further, despite the similar behavior of q_{E} obtained with this model, and that obtained with the rigorous calculation (compare Figs. 3.4c and 3.3b), some differences still remain. In particular the latter decays more slowly with distance, it changes its sign as the distance increases, and the maximum of q_{E} is found at a similar distance d for all radii. Moreover, the current model, given by Eqs. (3.45b)-(3.45e), is clearly insufficient to reproduce the exact q_{R} contribution (compare Figs. 3.4c and 3.3a).

Full retarded Green's function

In order to further approach the exact response of the interacting system, we replace the quasistatic near-field Green's function in Eqs. (3.45a)-(3.45e) with the full expression of the Green's function $G_{x,x}$ in Eq. (1.21) [35]. $G^{\mathrm{qs}}_{x,x}(\boldsymbol{r}_{\mathrm{e}}) = 1/[(2\pi)\varepsilon_0(R+d)^3]$ (Eq. (3.43)) is always a real number but $G_{x,x}$ is complex, with a phase that changes with distance d largely due to the retardation phase associated with the propagation of the fields. Furthermore, $G_{x,x}$ decays more slowly than $G^{\mathrm{qs}}_{x,x}$ with d because it includes terms decaying as $1/(R+d)$ and $i/(R+d)^2$ (corresponding to the far- and intermediate-field contributions, respectively). These changes directly affect the phase and the modulus of the enhancement factor ($K(\boldsymbol{r}_{\mathrm{e}}, \omega) = G_{x,x}(\boldsymbol{r}_{\mathrm{e}}, \omega) p_{\mathrm{a}}(\omega)/E_0$) and thus both q_{E} and q_{R} (Eq. (3.36)), as shown in Fig. 3.4d (fourth column).

We first observe that the distance-dependence of the amplitude and phase of K induces the change of sign of q_{E} for $d \approx 150$ nm (change from red to blue color), and also the overall slower decay of its absolute value ($|q_{\mathrm{E}}|$) with d discussed above. We show in section 3.4.3 that q_{E} oscillates for larger separation distances. The maxima values of q_{E} are larger than those in the previous model, mainly due to the far- and intermediate field contributions.

Further, we obtain clearly larger values of $|q_{\mathrm{R}}|$ than in the previous model, with values of up to $|q_{\mathrm{R}}| \approx 0.45$, as compared to $|q_{\mathrm{R}}| \lesssim 0.14$ in Fig. 3.4c. According to Eq. (3.37) we can directly relate these high values of q_{R} to changes of phase

of the field enhancement, φ_{A}. When the full Green's function $G_{x,x}$ is used, φ_{A} can considerably differ from $\pi/2$ for moderate and large d, which explains the relatively large values of $|q_{\mathrm{R}}|$. $|q_{\mathrm{R}}|$ is maximum for $(R+d) \approx 100$ nm and it decays for larger distances because the field enhancement becomes very small and, thus, $|q_{\mathrm{R}}| \propto |K(\boldsymbol{r}_{\mathrm{e}}, \omega)|^2/\gamma'$ (Eq. (3.37)) progressively approaches zero.

The asymmetry contributions q_{E} and q_{R} take similar absolute values of opposite signs at intermediate distances (20 nm $< d <$ 100 nm). As a consequence, the total asymmetry $q = q_{\mathrm{E}} + q_{\mathrm{R}}$ partially cancels in this regime, specially for radius 25 nm $\lesssim R \lesssim$ 70 nm. Thus, q presents a saddle point centered at $R \approx 40$ nm and $d \approx 80$ nm. The qualitative dependence of q with radius and distance within this model is in good agreement with the rigorous Mie theory results (Fig. 3.2d). We thus conclude that this improved model contains the fundamental elements to capture the main features of the behavior of the total asymmetry factor.

Experimental permittivity

We can further increase the agreement with the results obtained with the Mie theory calculations by using the same experimental values $\varepsilon_{\mathrm{a}}^{\mathrm{Exp}}$ of the permittivity of silver used in that Mie calculations (instead of the modified Drude model). The polarizability of the nanoantenna then becomes $\alpha_{\mathrm{a}}^{\mathrm{RC\text{-}Exp}}(\omega) = \alpha_{\mathrm{a}}^{\mathrm{Exp}}(\omega)[1/(1 - i\alpha_{\mathrm{a}}^{\mathrm{Exp}}(\omega)k^3/(6\pi\varepsilon_0))]$ with $\alpha_{\mathrm{a}}^{\mathrm{Exp}}(\omega) = 4\pi R^3(\varepsilon_{\mathrm{a}}^{\mathrm{Exp}}(\omega) - 1)/(\varepsilon_{\mathrm{a}}^{\mathrm{Exp}}(\omega) + 2)$. Figure 3.4e (fifth column) shows the asymmetry contributions calculated with this assumption. The changes as compared with the previous model (Fig. 3.4d) are relatively small and are mostly found for small spheres ($R < 25$ nm), where we find an increase of $|q_{\mathrm{E}}|$ and a decrease of $|q_{\mathrm{R}}|$. Indeed, smaller spheres resonate at shorter wavelengths, for which the contribution of the d-electrons to the experimental permittivity significantly modifies the plasmonic response. The changes on the asymmetry due to the influence of the d-electrons can be larger in other materials, such as gold. For example, we show in section 3.4.3 that including this effect is crucial to accurately describe the asymmetry factor for a QE interacting with a gold nanoantenna.

Improved description of the radiative correction

Last we introduce a more accurate description of the radiative–corrected polarizability following reference [47]:

$$\alpha_{\mathrm{a}}^{\mathrm{IRC}}(\omega) = \frac{\alpha_{\mathrm{a}}^{\mathrm{Exp}}(\omega)}{1 - \frac{3}{5}\zeta^2 \frac{\varepsilon_{\mathrm{a}}^{\mathrm{Exp}}(\omega)-2}{\varepsilon_{\mathrm{a}}^{\mathrm{Exp}}(\omega)+2} - i\alpha_{\mathrm{a}}^{\mathrm{Exp}}(\omega)\frac{(2\pi/\lambda)^3}{6\pi\varepsilon_0} - 3\frac{\zeta^4}{350}\frac{(\varepsilon_{\mathrm{a}}^{\mathrm{Exp}}(\omega))^2 - 24\varepsilon_{\mathrm{a}}^{\mathrm{Exp}}(\omega)+16}{\varepsilon_{\mathrm{a}}^{\mathrm{Exp}}(\omega)+2}} \tag{3.46}$$

with $\zeta = 2\pi R/\lambda$.

We implement this improvement to the dipole-dipole interaction model, which can be summarized in a set of equations as:

$$p_{\mathrm{a}}(\omega) = \alpha_{\mathrm{a}}^{\mathrm{IRC}}(\omega)(E_0 + G_{x,x}(\boldsymbol{r}_{\mathrm{e}}, \omega)p_{\mathrm{e}}(\omega)), \tag{3.47a}$$

$$p_{\mathrm{e}}(\omega) = \alpha_{\mathrm{e}}(\omega)(E_0 + K(\boldsymbol{r}_{\mathrm{e}}, \omega)), \tag{3.47b}$$

$$K(\boldsymbol{r}_{\mathrm{e}}, \omega)E_0 = G_{x,x}(\boldsymbol{r}_{\mathrm{e}}, \omega)p_{\mathrm{a}}(\omega), \tag{3.47c}$$

$$\gamma' = \left[1 + \mathrm{Im}\left\{\frac{A_{\mathrm{e}}\alpha_{\mathrm{a}}^{\mathrm{IRC}}(\omega)}{\gamma_0\omega_0}(G_{x,x}(\boldsymbol{r}_{\mathrm{e}}, \omega))^2\right\}\right]\gamma_0, \tag{3.47d}$$

$$\sigma_{\mathrm{ext}}(\omega) = \frac{2\pi}{\lambda\varepsilon_0}\mathrm{Im}\left\{\frac{p_{\mathrm{a}}(\omega) + p_{\mathrm{e}}(\omega)}{E_0}\right\}. \tag{3.47e}$$

For ease of reference, we summarize all the aspects that are included in Eqs. (3.47a)-(3.47e) but not in Eqs. (3.44a)-(3.44e) (the latter corresponding to the simplest model considered in this section): (i) the direct excitation and emission of the QE are included in Eqs. (3.47b) and (3.47e), respectively, (ii) the propagation of the fields beyond the quasistatic approximation is included by the full Green's function in Eqs. (3.47a), (3.47c), and (3.47d), and (iii) we use a modified version of the polarizability of the spherical nanoparticle $\alpha_{\mathrm{a}}^{\mathrm{IRC}}$ in Eqs. (3.47a) and (3.47d) that incorporates the effect of the radiation damping of the nanoantenna and considers the influence of d-electrons on the permittivity of the material.

Figure 3.4f (sixth column) shows that by introducing the improved radiative correction (Eq. (3.46)) the values of the asymmetry change very little, with the largest changes occurring for $R > 50$ nm (as compared to the results of the previous model in Fig. 3.4e). In particular the maxima of $|q_{\mathrm{R}}|$ and q_{E} for $R > 50$ nm have been displaced in Fig. 3.4f towards slightly larger distances d. The reason for this displacement is that the new radiative correction redshifts the resonant wavelength for large particles, which changes the ratio between the QE-nanoantenna distance and the wavelength, $(R + d)/\lambda$ (affecting the full Green's function $G_{x,x}$).

The resulting values of the total asymmetry factor q and the q_{R} and q_{E} contributions that are obtained within this improved model (Fig. 3.4f) are in very good agreement with the exact results shown in Figs. 3.2d and 3.3a-b for the radius and distances considered. The main difference occurs in the shortest range of distances, $d < 10$ nm. For such distances the Mie theory calculation results in a very large increase of the decay rate γ' due to the coupling with the high-order modes of the plasmonic response [134], which is not included in the dipole-dipole description analyzed here. The large increase of γ' strongly reduces the asymmetry by increasing the denominator in Eq. (3.36). However, this decrease is hard to appreciate in the figures, as the value of q predicted by the most refined dipole-dipole interaction model (Eqs. (3.47b)-(3.47e)) is already small for these short distances.

Equations (3.47b)-(3.47e) allow for a simple quantitative description of the total asymmetry factor that enables to identify the different effects that influence the value of q. However, it is instructive to further analyze the importance of the radiative correction. In the discussion above, the introduction of the simpler radiative correction only led to a very small change of the asymmetry (compare Fig. 3.4a and Fig. 3.4b), but this effect is small only when considering very simple dipole-dipole interaction models. If the radiative correction is neglected in the final expressions (Eqs. (3.47b)-(3.47e)) we obtain a completely inaccurate response

for the total asymmetry factor (and its contributions). This can be observed by comparing Fig. 3.4g (seventh column) with Fig. 3.4f, where the only difference between the two is that Fig. 3.4g ignores the radiative correction. We have verified that including the radiative correction is necessary for all the models that use the full Green's function.

We have thus shown, in this subsection, how each approximation in the dipole-dipole interaction affects the description of the Fano asymmetry for zero-detuning. This has allowed us to associate the different aspects of the asymmetry with relevant physical effects.

3.4.3 The Fano asymmetry factor in additional scenarios

In sections 3.2, 3.3, and 3.4 we study the asymmetry factor of the Fano feature present in the extinction cross-section spectrum of a QE placed at a distance $d \in [2, 200]$ nm from the surface of a single spherical nanoparticle. In particular, we studied the situation where the plasmonic mode of the nanoantenna and the exciton of the QE are resonant are the same wavelength λ_0, with λ_0 the wavelength that maximizes the extinction cross-section of the bare nanoantenna (in the spectral region where the dipolar plasmonic resonance dominates the response). However, some of the dependencies of the Fano asymmetry predicted (such as the oscillatory behavior of q with the separation distance d or the influence of the d-electrons) are hard to appreciate in the situations considered so far. Therefore, we explore in this subsection three additional clarifying scenarios. First, we consider a larger range of distances $d \in [2, 1200]$ nm. Second, we change the material of the spherical nanoparticle from silver to gold. Last, to assess the robustness of our results, we analyze the effect of tuning the resonant wavelength of the QE to match the maximum value of the near-field enhancement factor $|K|$ associated with the dipolar mode instead of the maximum of the cross-section.

The analysis presented here follows the same procedure as in subsection 3.4.2, *i.e.* we calculate the asymmetry factor q and its contributions q_{R} and q_{E} (Eq. (3.36)) with a series of simple models based on the dipole-dipole approximation. The simplest model always predicts an almost negligible asymmetry factor, and we progressively incorporate different physical effects that increase the accuracy of the description. Columns a-f of Figs. 3.5, 3.7, and 3.6 correspond to the same models as those developed for Fig. 3.4a-f. We note that all the models in this subsection do not include the quenching effect due to the coupling with higher order plasmonic modes [134] that strongly decrease q for $d < 10$ nm.

Longer range of distances

So far we have focused on the behavior of the asymmetry for a range of distances $d \in [2, 200]$ nm for the different dipole-dipole interaction models. We show in Fig. 3.5a-f the values of the asymmetry factor q and its contributions q_{R} and q_{E} calculated for a larger range of distances, $d \in [2, 1200]$ nm. Figure 3.5f shows the values of q, q_{R}, and q_{E} using the most accurate dipole-dipole interaction model

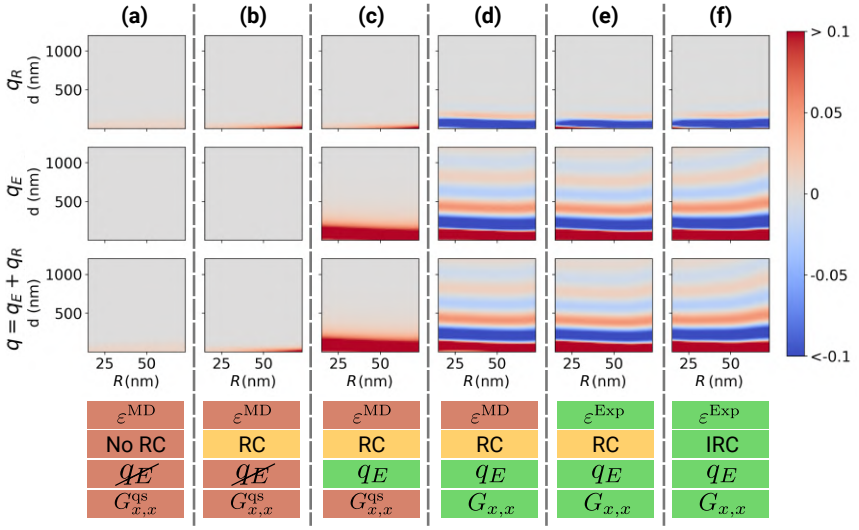

Figure 3.5: Values of the asymmetry factor calculated for a QE in the proximity of a spherical silver nanoparticle of different radius R. The system is identical as in Fig. 3.4, except that the asymmetry is calculated for a larger range of distances between the QE and the surface of the nanoparticle $d \in [2, 1200]$ nm. (a)-(f) Asymmetry factor q (panels in the third row) and its contributions q_{E} (first row) and q_{R} (second row) calculated as a function of R and d. Each column corresponds to a different model, as indicated by the labels at the bottom, following the same scheme as used in Fig. 3.4a-f (see caption of that figure for further details).

using the improved description of the radiative correction (Eqs. (3.47a)-(3.47e)). Consistently with the discussion in subsection 3.4.2, as we increase d we can observe a clear oscillatory behavior (superimposed to a general tendency to decrease) of q, q_{R}, and q_{E}. The oscillatory behavior causes changes of the sign of these three factors. Comparing the results for the different models in Fig. 3.5 we find that the oscillations appear when we include the full Green's function $G_{x,x}$ in our model (compare Figs. 3.5c and d).

Last, we note that Fig. 3.5a (corresponding to the simplest dipole-dipole interaction model) also shows a small but clearly non-zero value of asymmetry, $q \neq 0$ for $d \lesssim 100$ nm, which was harder to appreciate in Fig. 3.4a because of the chosen color scheme.

Gold spherical nanoparticle

Figure 3.6a-f shows the analysis of the asymmetry factor q of the Fano feature in the extinction cross-section spectrum and its contributions q_{R} and q_{E} when the single spherical nanoparticle is made of gold. The QE resonant frequency is again set to the value that maximizes the extinction cross-section spectrum near the dipolar resonance. Figure 3.6f, corresponding to the most precise dipole-dipole interaction model consider, shows that q is relatively big for a large range of

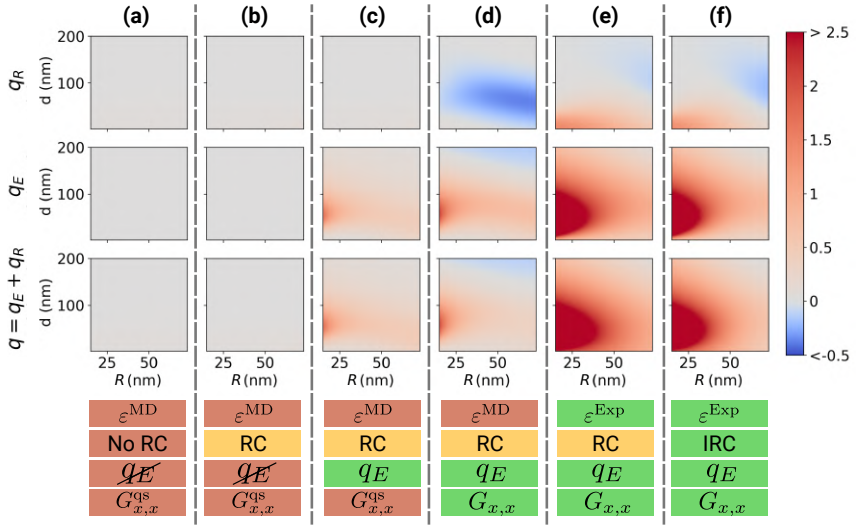

Figure 3.6: Values of the asymmetry factor calculated for a QE in the proximity of a spherical gold nanoparticle of different radius R of the nanoparticle and different distances d between the QE and the surface of the nanoparticle. (a)-(f) Asymmetry factor q (panels in the third row) and its contributions q_{E} (first row) and q_{R} (second row) calculated as a function of R and d. Each column corresponds to a different model, as indicated by the labels at the bottom, following the same scheme as used in Fig. 3.4a-f (see caption of that figure for further details).

distances, $q > 0.25$ for $d \lesssim 200$ nm (whereas in the silver case $q > 0.25$ for 20 nm $\lesssim d \lesssim 100$ nm, see Fig. 3.4d and 3.4f). Further, the dependence of q with d for the gold nanoparticles shows a broad single maximum and does not change its sign in the range of distances considered. This is in contrast with the silver results, where there is a change of sign of q following an oscillatory pattern. Additionally, for the gold spherical nanoparticle (Fig. 3.6f) $|q_{\mathrm{E}}|$ is overall much larger than $|q_{\mathrm{R}}|$, so that it dominates the dependence of the total asymmetry factor q with R and d, while in the silver nanoparticles $|q_{\mathrm{E}}|$ and$|q_{\mathrm{R}}|$ are of the same order of magnitude and both contributions strongly influence the values of q. Last, Fig. 3.6f shows that the q_{R} contributions takes large positive values ($q > 0.25$) for $d \lesssim 50$ nm when considering gold as the plasmonic material, whereas for silver, q_{R} is overall negative for the same range of distances (see Fig. 3.4f).

The differences between the calculations for silver and gold nanoparticles are mostly due to the contribution of the d-electrons of the material to the dielectric permittivity, which is much larger for gold. This can be confirmed by looking at Fig. 3.6d, which was obtained using the modified Drude model for gold. Specifically, we use

$$\varepsilon_{\mathrm{a}}^{\mathrm{MD}} = \varepsilon_{\infty} - \frac{\omega_p^2}{\omega(\omega + i\kappa)}, \tag{3.48}$$

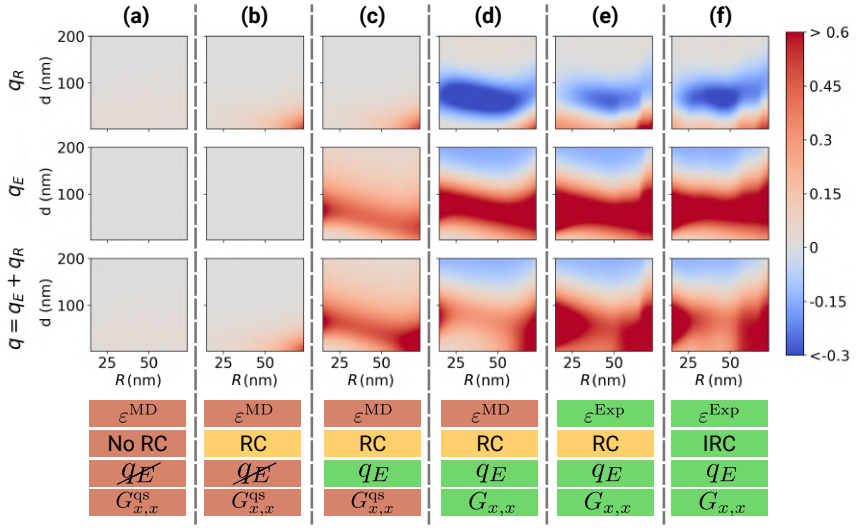

Figure 3.7: Values of the asymmetry factor calculated for a QE in the proximity of a spherical silver nanoparticle of different radius R of the nanoparticle and different distances d between the QE and the surface of the nanoparticle. The asymmetry factor is calculated by tuning the QE resonance to match the frequency at which the nanoantenna near-field enhancement is maximized due to the dipolar resonance for each particular set of R and d (in contrast, in Fig. 3.4 the QE resonance was matched to the extinction maximum of the plasmonic dipolar resonance). (a)-(f) Asymmetry factor q (panels in the third row) and its contributions q_{E} (first row) and q_{R} (second row) calculated as a function of R and d. Each column corresponds to a different model, as indicated by the labels at the bottom, following the same scheme as used in Fig. 3.4a-f (see caption of that figure for further details).

with $\varepsilon_\infty = 9$, $\hbar\omega_p = 9.07$eV, and $\hbar\kappa = 71$ meV for gold. These values are obtained from fitting the experimental data [40] for large ω. The dependence of the asymmetry factor with R and d shown in Fig. 3.6d (modified Drude model) are very similar to the results for the silver nanosphere (Fig. 3.4f).

QE tuned to the frequency of the maximum field enhancement

All the results presented in this chapter except for Fig. 3.7 are obtained considering that the resonant frequency of the QE matches the maximum of the extinction cross-section of the bare nanoantenna. In Fig. 3.7a-f we show the analysis of the Fano asymmetry in the extinction cross-section spectrum for the case where the resonant frequency of the QE matches the maximum of the field enhancement induced by the nanoantenna at the position of the QE (in both cases we consider the maximum that is mostly determined by the dipolar plasmonic mode).

Overall, the values of $|q|$, $|q_{\mathrm{R}}|$, and $|q_{\mathrm{E}}|$ are slightly higher in Fig. 3.7a-f than in Fig. 3.4a-f. However, these differences are small and the trends of the dependence of q, q_{R}, and q_{E} with the distance d and the radius of the nanoparticle R are the

same in Fig. 3.7a-f and in Fig. 3.4a-f.

3.5 Fano resonance in dimers

In the previous sections we have analyzed in detail the asymmetry of the Fano lineshape that is revealed in the extinction cross section spectrum of a QE placed near a spherical metallic nanoparticle (Fig. 3.1a), chosen as an example of a canonical nanoantenna. To demonstrate that a similar analysis can be applied to more general nanostructures, we consider next the Fano asymmetry for a QE situated in a junction between two spherical gold nanoparticles (a dimer nanoantenna). This dimer configuration has been intensely studied because it induces a much larger near–field enhancement than the single spherical nanoparticle, as sought, for example, in surface-enhanced spectroscopy [25, 26, 146–151].

We show in Fig. 3.8a a scheme of the dimer configuration. The system is driven by an incident plane wave of amplitude E_0 that propagates along the z-axis, and polarized along the x-axis parallel to the orientation of the point-like dipole that represents the QE and to the axis of symmetry of the two spherical nanoparticles. We consider gold instead of silver nanoparticles in this section. Despite having larger absorption losses, gold is widely used in surface-enhanced spectroscopy because it does not oxidize and it is more handleable in experiments. The permittivity of gold is taken from reference [41], the two spherical nanoparticles have a radius of $R = 40$ nm, and we vary their surface-to-surface distance $2d$. The emitter is placed in the middle of the gap between the two nanoparticles (at distance d from the surface of each of them), and its properties are the same as in the previous sections (strength $f_0 = 0.05$ e·nm, intrinsic decay rate corresponding to the spontaneous radiative decay, and resonance frequency tuned as a function of d to always match the dipolar resonance of the nanoantenna [152], as given by the maximum of the extinction cross-section), *i.e.*, we keep the condition of zero-detuning in all cases analyzed and shown here.

Fig. 3.8b shows the extinction cross-section spectrum of this hybrid system calculated for different values of d, as obtained from Eq. (3.8). In this section, the value of all the necessary input electromagnetic parameters (such as the near-field enhancement and the self-interaction Green's function) are obtained from the solution of Maxwell's equations under plane-wave of dipolar illumination as given by the Matlab package *MNPBEM17* [153–155] (the details of these calculations are given in appendix C). A clear Fano feature is observed in all spectra, showing a qualitatively similar dependence with distance as the results of the single spherical nanoparticle (Fig. 3.1c). In both situations the Fano lineshape obtained at small distances $d \lesssim 10$ nm corresponds to a broadened and almost symmetric dip, while at much larger separation distances, $d \gtrsim 200$ nm, we observe an almost symmetric narrow peak. Thus, $q \approx 0$ in these two situations. For values of d between these two extremes, the Fano spectrum shows various degrees of asymmetry.

Despite these qualitative similarities, the results obtained for the dimer nanoantenna (Fig. 3.8b) and a single silver nanoparticle (Fig. 3.1c) show some

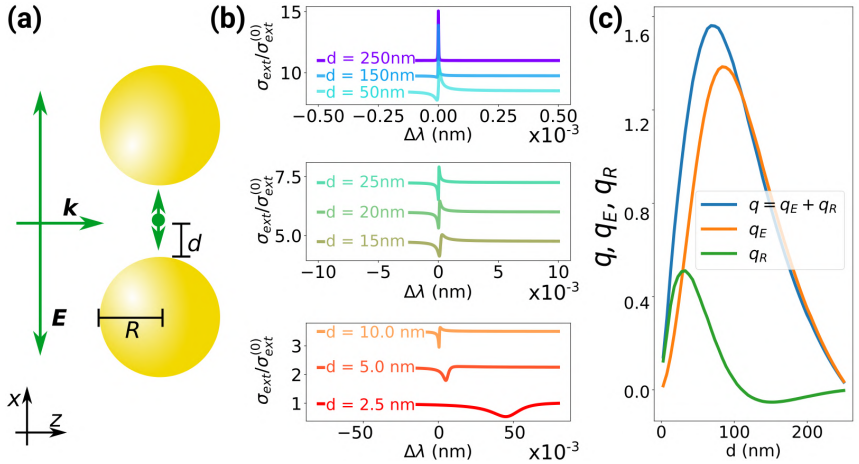

Figure 3.8: Characterization of the Fano asymmetry in the extinction cross–section of a QE coupled to a metallic dimer obtained at zero detuning (resonant conditions). (a) Scheme of the dimer nanostructure. A QE with dipole momentum polarized along the x-axis is placed between two gold spherical nanoparticles of radius $R = 40$ nm at a distance d from the surface of each of them (the separation between the center of the two nanoparticles is $2(d + R)$). The dimer axis is parallel to the x-axis. The system is illuminated by a plane wave propagating along the z-axis and with the electric field polarized along the x-axis. (b) Normalized extinction cross-section spectra $\sigma_{\rm ext}/\sigma^{(0)}_{\rm ext}$ of the coupled emitter-dimer nanoantenna system. The spectra are vertically displaced by 1.5 for clarity. Each Fano lineshape is evaluated for different values of d that range from $d = 2.5$ nm to $d = 250$ nm (see labels in the figure). The spectra are grouped in three separate panels, each of them plotted over a different spectral range, $\Delta\lambda$. (c) Dependence with distance d of the Fano total asymmetry factor q (blue line) together with its contributions $q_{\rm E}$ (orange line) and $q_{\rm R}$ (green line). For each separation distance d of the calculations in (b) and (c) we have set the resonance of the QE to match the frequency of resonance of the nanoantenna.

clear quantitative differences. For instance, the Purcell factor $P_{\rm F}$ and the photonic Lamb shift $\Delta\omega$ experienced by the emitter, which describe the broadening and shift of the Fano feature, respectively, are much larger in the case of the dimer due to the stronger field confinement [25,146,151] ($P_{\rm F} \approx 1.4\times10^4$ and $\Delta\omega/\gamma \approx 3.2\times10^5$ for the dimer and $d = 2.5$ nm, to be compared with $P_{\rm F} \approx 4.3 \times 10^2$ and $\Delta\omega/\gamma \approx 4.4 \times 10^3$ for the single silver spherical nanoparticle system of the same radius R and distance d). We also observe that there is a clear asymmetry for a larger range of distances in the dimer as compared to the single silver nanoantenna of the same radius (compare the three panels in Fig. 3.8b and Fig. 3.1c)

To study the Fano asymmetry of the dimer system in more detail, we show in Fig. 3.8c the dependence with d of the total asymmetry factor q (blue line) and its two components $q_{\rm E}$ (orange line) and $q_{\rm R}$ (green line), as obtained from Eq. (3.36) (with $q = q_{\rm E} + q_{\rm R}$). For separation distances $d \gtrsim 30$ nm the total asymmetry factor q is mainly influenced by the $q_{\rm E}$ contribution, *i.e.* it is mostly due to the direct excitation and emission of the QE. In a similar way as for the single spherical nanoparticle, $q_{\rm E}$ is larger at intermediate distances (20 nm $\lesssim d \lesssim$ 200 nm for the

dimer), when the excitation and emission of the QE via the nanoantenna has a magnitude comparable to the direct excitation by the incident plane wave and the direct emission of the QE to the far field, respectively. Outside this range of distances this condition is not verified and q_{E} is small.

On the other hand, the q_{R} contribution (green line in Fig. 3.8c) dominates the total asymmetry factor for $d \lesssim 30$ nm. The distance dependence of q_{R} can again be explained using Eq. (3.37), which indicates that $q_{\mathrm{R}} \propto |K(\boldsymbol{r}_{\mathrm{e}}, \omega)|^2 \sin(2\varphi_{\mathrm{A}}(\boldsymbol{r}_{\mathrm{e}}, \omega))/\gamma'$. The $|K(\boldsymbol{r}_{\mathrm{e}}, \omega)|^2/\gamma'$ factor in this expression explains many aspects of the general tendency of $|q_{\mathrm{R}}|$. For long separation distances, $d \gtrsim 200$ nm, the field-enhancement factor $|K|$ approaches zero, leading to small values of $|q_{\mathrm{R}}|$. For short distances $d \lesssim 10$ nm, the quenching induced by the coupling of the emitter with the high–order modes of the plasmonic dimer also becomes important [134]. As a consequence, the plasmon-enhanced decay rate $\gamma' = (1 + P_{\mathrm{F}})\gamma_0$ takes significantly higher values than the enhancement of the intensity $|K|^2$, leading to small values of $|q_{\mathrm{R}}|$. Between these two regimes of d, $|K(\boldsymbol{r}_{\mathrm{e}}, \omega)|^2/\gamma'$ is maximized so that $|q_{\mathrm{R}}|$ can be relatively large. Additionally, q_{R} is also influenced by the phase φ_{A} of the enhancement, which changes with distance largely due to propagation effects. The resulting $\sin(2\varphi_{\mathrm{A}}(\boldsymbol{r}_{\mathrm{e}}, \omega))$ factor has an oscillatory behavior with the separation distance with an approximated period of 200 nm, and the changes of the sign are directly reflected in the oscillation of q_{R}, as shown in Fig. 3.8c (green line). Further, $\sin(2\varphi_{\mathrm{A}}(\boldsymbol{r}_{\mathrm{e}}, \omega))$ decreases sharply if the distance becomes smaller than $d \lesssim 10$ nm, emphasizing the rapid decrease of q_{R} for this range of distances.

Overall the general trends of $|q_{\mathrm{R}}|$ obtained for the dimer system as a function of separation distance d (Fig. 3.8c) resemble the result obtained for the silver spherical nanoparticle (Fig. 3.3a), both showing a clear maximum for intermediate distances. However, some significant differences can be pointed out. The range of distances where $|q_{\mathrm{R}}|$ is large extends towards significantly smaller d in the case of the gold dimer ($|q_{\mathrm{R}}| > 0.25$ for 10 nm $\lesssim d \lesssim$ 70 nm) as compared to the single silver spherical nanoparticle ($|q_{\mathrm{R}}| > 0.25$ for 40 nm $\lesssim d \lesssim$ 80 nm and $R = 40$ nm). Further, q_{R} takes relatively large positive values in the dimer structure ($d \lesssim 100$ nm in Fig. 3.8c), in contrast to the negative values of q_{R} calculated for the single spherical nanoparticle of the same radius ($d \lesssim 100$ nm in Fig. 3.3c). This last difference mostly occurs due to the stronger influence of the d-electrons in the permittivity of gold (used for the dimer material) as compared to silver (see section 3.4.3) The contribution of the d-electrons significantly modifies the phase of the field enhancement φ_{A}, and thus the asymmetry.

3.6 Conclusions

We analyze in detail the asymmetry of the Fano feature found in the extinction cross-section spectrum of a nanoantenna interacting with a QE resonantly, *i.e.* the QE and the nanoantenna have the same resonant excitation frequency, and thus, the asymmetry is not due to the detuning. We have focused on the coupling with an exciton of a single QE but the conclusions also apply to coupling with many

QEs or with molecular vibrations. We first consider a spherical silver nanoantenna under laser illumination as a canonical nanoantenna. We show that the spectra obtained with exact electromagnetic calculations of the optical response of the hybrid QE-nanoantenna system under zero detuning present an asymmetry not found in a very simple dipole-dipole interaction description.

The asymmetry of the Fano feature is quantified through a parameter q. We derive an analytical expression of q that depends mainly on the field-enhancement and the plasmon-enhanced-losses of the QE. This expression can be decomposed into two contributions, $q = q_{\mathrm{E}} + q_{\mathrm{R}}$, where q_{E} is mainly connected with the direct emission and excitation of the QE, while q_{R} mostly captures other phenomena (such as retardation) that affect the phase of the field enhancement that the nanoantenna induces on the QE.

The analytical expression of q evaluated with different dipole-dipole interaction models (with an increasing degree of complexity) allow us to analyze in detail the origin of the asymmetry. These models improve the description of the polarizability of the spherical nanoparticle and that of the Green's function that governs the QE-nanoantenna interaction. The implementation of these models enables to identify the influence of five effects on the asymmetry: (i) the radiation damping of the nanoantenna, which makes it necessary to introduce a radiative correction to its response. Ignoring this correction results in a completely unreliable description of the optical response of large nanoparticles and thus of the resulting asymmetry; (ii) the influence of d-electrons on the permittivity of the plasmonic material, and thus of the polarizability of the nanoantenna. This contribution is particularly important for nanoantennas that resonate at shorter wavelengths (for example, small spherical nanoparticles); (iii) the direct excitation of the QE by the incident field exciting the system and the direct emission of the QE to the far-field, *i.e.* the two contributions to the q_{E} asymmetry factor discussed above; (iv) the propagation of the fields beyond the quasistatic near-field approximation. The asymmetry can be affected by the slowly-decaying terms of the vacuum Green's function (intermediate and far-field terms) and, especially, by the retardation-induced changes of the phase of the fields induced by the nanoantenna at the position of the emitter (and vice–versa); (v) the changes of the optical response of the nanoantenna due to its high–order modes. The high–order modes of the nanoantenna are not included in the dipole-dipole interaction models analyzed in this chapter, but their influence is revealed by comparing our most complete dipole-dipole interaction model with the rigorous calculations. These rigorous calculations show reduced values of the asymmetry for short distances between the QE and the nanoantenna due to the quenching induced by the coupling of the QE exciton to the high-order plasmonic modes of the nanoantenna [134].

Further, we note that although the effect of the high-order modes for moderate and large separation distances is relatively small for a single nanoantenna under laser illumination, it could be more important when the illumination is a point-like source (tunneling current or a transition dipole moment in a molecule) that can couple very efficiently to highly-confined modes. This aspect could explain, for instance, the asymmetry observed in recent experiments that analyzed the

emission spectrum of a QE placed in a plasmonic nanocavity formed between the metallic tip of a scanning tunneling microscope and a metallic substrate, with the system being excited by the localized fluctuation of the tunneling current at optical frequencies [8].

Last, we show that the asymmetry analysis can also be applied to more complex nanostructures. Specifically, we show that the modifications of the Fano features obtained for the single silver spherical nanoantenna is similar to the results obtained for a gold dimer nanoantenna, with some quantitative differences. As an example of these differences, the asymmetry contribution q_{R} is mainly positive for the gold dimer system and mainly negative of the single silver spherical nanoparticle (of the same radius), which is mostly due to the larger influence of the *d*-electrons in the permittivity of gold. However, we emphasize that the effects behind the origin of the asymmetry are similar in both systems. Thus we conclude that the analysis proposed in this chapter provides insights into the origin of the asymmetry of the Fano lineshape applicable to very general systems in nanophotonics.

CHAPTER 4

UNBOUND STRONG BUNCHING AND BREAKDOWN OF THE ROTATING WAVE APPROXIMATION IN THE QUANTUM RABI MODEL

4.1 Introduction

Many systems studied in cavity quantum optics are variations of its fundamental workhorse: a quantum emitter (such as a single molecule [156, 157], or a quantum dot [158–160]) coupled to an optical cavity [161, 162]. In chapter 3, we have studied classically the optical response of such a system when the cavity and the QE interact weakly. In this chapter, we focus on studying the excitation and emission pathways of the very same configuration for any arbitrarily large interaction strength between the QE and the cavity. In contrast with chapter 3 where we addressed the optical behavior of the QE in a linear regime, here we treat it as a two-level-system (TLS, see discussion in section 2.5), incorporating to our description non-linear effects caused by the photon blockade of the TLS[xvii].

The behavior of the cavity-TLS (CTS) is dictated by the relationships between the coupling strength (g) and the characteristic resonant frequencies (ω_σ and ω_c) and dissipation rates (γ and κ) of the TLS and the cavity, respectively. In particular, if g is smaller than the dominant losses of the system (usually $\gamma \lesssim \kappa/2$, $g \lesssim \kappa/2$, defining the *weak coupling* (WC) regime), any energy that enters the system is likely lost before the exchange of excitations between the cavity and the

[xvii] The photon blockade describes the situation where the excitation of the TLS prevents the interaction of the TLS with further photons until the excited state decays to the ground state.

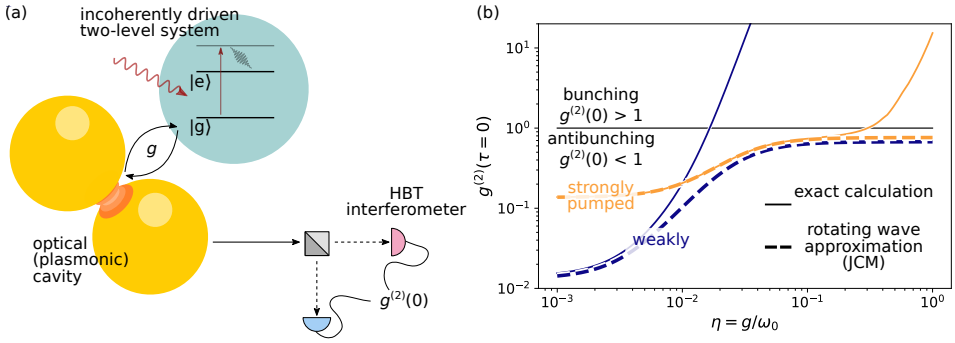

Figure 4.1: (a) Setup of the system studied in chapter 4. An incoherently driven TLS interacts with an optical cavity, such as a plasmonic dimer. The emission of the cavity is analyzed with a Hanbury Brown and Twiss (HBT) interferometer (further discussed in the text), giving the intensity correlations $g^{(2)}(0)$. (b) Intensity correlations $g^{(2)}(0)$ as a function of the coupling parameter $\eta = g/\omega_0$, calculated using the QRM (solid lines; see details in section 4.2.1) and the JCM (dashed lines; section 4.2.2). Under a strong incoherent pumping rate ($\Gamma/\gamma = 10$, orange lines), the results of the two models coincide in the WC regime ($\eta \lesssim 2.5 \times 10^{-2}$), and become very different for USC $\eta \gtrsim 0.1$. For a weak pumping rate ($\Gamma/\gamma = 10^{-6}$, dark blue lines), correlations obtained with the JCM and the QRM differ in the USC and WC regimes, for any $\eta \gtrsim 5 \times 10^{-3}$.

TLS can occur. On the other hand, in the *strong coupling* (SC) regime for which g exceeds the losses of the system (usually $g \gtrsim \kappa/2$ when γ is small), the cavity and the TLS can coherently exchange excitations before the energy is dissipated, inducing a hybridization in the response of the cavity-TLS (CTS) [139, 163, 164].

Further increasing the coupling strength of the system leads to the so-called *ultra-strong coupling* (USC) regime, where g becomes comparable to the resonant frequencies of the cavity and TLS. The phenomenological limit for the onset of the USC is typically defined as $g \gtrsim 0.1\omega_c$, or $g \gtrsim 0.1\omega_\sigma$ (USC systems are typically studied in a resonant configuration where $\omega_c = \omega_\sigma$). In the USC, some of the usual approximations used in the WC regime — most importantly — the Rotating Wave Approximation (RWA), yield incorrect results. As a result, USC systems exhibit new characteristics and non-trivial properties, such as the existence of a non-vacuum ground state [165, 166].

The response of quantum systems is typically accessed by measuring the *one-photon spectrum* $S^{(1)}(\omega)$ of the emitted light, and tracing the strength and frequency of the emerging spectral features. To further characterise the emitted light, and access its *statistics*, we can measure its intensity correlation $g^{(2)}(\tau)$, through the Hanbury Brown and Twiss (HBT) interferometer [21, 167–169] as introduced in section 2.4 (see schematics in Fig. 4.1a). In particular, the intensity correlations can highlight the effects of the non-number-conserving terms in the Rabi Hamiltonian [170] (see Eq. (2.79)). Consequently, $g^{(2)}(\tau)$ might prove to be a far more sensitive probe of the effects of USC than the one-photon spectra.

In this chapter, we analyze the emission of an incoherently-pumped CTS, operating from the WC to the USC regimes. We focus on studying the intensity

correlations $g^{(2)}(\tau = 0)$ obtained within two models: the Quantum Rabi model (QRM), and its widely used approximation — the Jaynes-Cummings model (JCM). We embrace the formulation of the QRM derived in section 2.5. This derivation was recently introduced in a series of papers which have reconciled long-standing questions about ensuring gauge invariance [84–88], and proposed a complete description of the interaction between an USC system and the environment. Further, this formulation of the gauge-invariant QRM offers an opportunity to carefully study two questions: (i) how the statistics of emission from a CTS changes as one transitions between different coupling regimes, and (ii) how the JCM breaks down in the USC regime. To illustrate these effects, in Fig. 4.1b we plot $g^{(2)}(0)$ calculated using the QRM (solid lines) and the JCM (dashed lines), under two different incoherent pumping rates (details of the models and excitation schemes are discussed in section 4.2). In contrast to previously reported works on the emission from a thermally pumped CTS [171,172], we find that under incoherent illumination of the TLS, the emission of the CTS appears to exhibit a seemingly unbounded bunching $g^{(2)}(0) \gg 1$. Furthermore, we find that the two models (JCM and QRM) can deviate significantly both in the USC (see the orange lines in Fig. 4.1b, $\eta = g/\omega_0 \gtrsim 0.1$), as well as in the WC regime (blue lines; for the parameters used in Fig. 4.1, the WC is defined as $\eta \lesssim 2.5 \times 10^{-2}$, see section 4.2.1 for details), depending on the incoherent pumping rate.

This chapter is structured as follows: in section 4.2 we formally introduce the Quantum Rabi and Jaynes-Cumming Hamiltonians, and describe the formulation of the excitation, emission, and dissipation of the system. In section 4.3 we identify the key mechanism that gives rise to the strong bunching in the emission. Finally, in section 4.4 we probe the extent of this effect in the USC, SC, and WC regimes, and discuss how the intensity correlations can help to identify the breakdown of the RWA.

4.2 Cavity-two-level-system Hamiltonian models

In this section, we summarize the two models used to calculate the intensity correlations of the CTS (which allows us to characterize the emission from the system): the general QRM and its well-known approximation, the JCM. These models are based on the quantum master equation formalism introduced in section 2.6, which describes the dynamics of a quantum system interacting with its environment.

We focus our description of the dynamics of the CTS. We choose a pumping mechanism and a set of parameters that correspond to recent experiments with plasmonic CTS systems, which have reportedly reached values of η close to 0.1 [125, 156–160, 173–176]. In particular, we explore the emission from a CTS under incoherent pumping of the TLS, corresponding to a TLS driven by a laser blue-detuned from the TLS resonance, exciting higher-order levels of the emitter, followed by a spontaneous cascade to the excited $|e\rangle$ state of the TLS (see scheme in 4.1a). To obtain the dynamics from such a system, we need the following

seven elements to characterize the dynamics of the system in the master equation introduced in section 2.6 (Eq. (2.120)): (i) the Hamiltonian describing the energy of the CTS, (ii) the operators describing the losses of the cavity, (iii) the decay rate of the cavity, (iv) the operators describing the losses of the TLS, (v) the decay rate of the TLS, (vi) the operators describing the incoherent excitation of the TLS, and (vii) the pumping rate of the TLS. In subsections 4.2.1 and 4.2.2 we introduce these seven elements in the complete QRM and in the approximated JCM, respectively.

4.2.1 Quantum Rabi model

Interaction and dynamics in the quantum Rabi model

In section 2.5, we derived the QRM Hamiltonian $\hat{\mathcal{H}}_C$ describing the energy in the CTS for any arbitrary coupling strength $\eta = g/\omega_0$ between the cavity and the TLS. For convenience, we repeat here the formula of $\hat{\mathcal{H}}_C$, (Eq. (2.79)),

$$\hat{\mathcal{H}}_C = \hbar\omega_0 \hat{c}^\dagger \hat{c} + \frac{\hbar\omega_0}{2}\left\{\hat{\sigma}_z \cos[2\eta(\hat{c}+\hat{c}^\dagger)] + \hat{\sigma}_y \sin[2\eta(\hat{c}+\hat{c}^\dagger)]\right\},$$

where, again, $\hat{c}$ is the annihilation operator of the cavity mode, ω_0 is the resonant frequency of the cavity and of the TLS, $\hat{\sigma}_z = [\sigma^\dagger, \sigma]$, and $\hat{\sigma}_y = i(\hat{\sigma}^\dagger - \hat{\sigma})$, being $\hat{\sigma}$ the lowering operator of the TLS (see Eq. (2.67)). Note that the $\hat{\mathcal{H}}_C$ Quantum Rabi Hamiltonian does not conserve the *excitation number*, but $\hat{\mathcal{H}}_C$ conserves the *parity* of excitations.

As mentioned above, the Hamiltonian is the first element that we need to address the dynamics of the state of our system, described by the time evolution of the density matrix of the CTS, $\hat{\rho}$. Next, we characterize the dissipation of the cavity. To do so, we use the dressed operators formalism introduced in subsection 2.6.2, where the dressed operators appeared in the Lindblad terms of the master equation (Eqs. (2.117) and (2.120)). We use this same formalism applied to the $\hat{\mathcal{S}}_{\hat{c}} = i(\hat{c}^\dagger - \hat{c})$ operators describing the interaction between the cavity and the environment [85,86]. As in the derivation of the master equation in section 2.6.2, it is convenient to decompose $\hat{\mathcal{S}}_{\hat{c}}$ in the basis of the eigenstates of the QRM Hamiltonian (see also Eq. (2.106)),

$$\hat{\mathcal{S}}_{\hat{c}} = \hat{x}_{\hat{c}}^{(0)} + \sum_{\omega}[\hat{x}_{\hat{c}}(\omega) + \hat{x}_{\hat{c}}^\dagger(\omega)], \tag{4.1}$$

where

$$\hat{x}_{\hat{c}}^{(0)} = \sum_{\mu} |\mu\rangle_{\mathrm{R}\ \mathrm{R}}\langle\mu|\, i(\hat{c}^\dagger - \hat{c})\, |\mu\rangle_{\mathrm{R}\ \mathrm{R}}\langle\mu|\,, \tag{4.2}$$

and

$$\hat{x}_{\hat{c}}(\omega) = |\nu\rangle_{\mathrm{R}\ \mathrm{R}}\langle\nu|\, i(\hat{c}^\dagger - \hat{c})\, |\mu\rangle_{\mathrm{R}\ \mathrm{R}}\langle\mu|\,, \tag{4.3}$$

where $\omega = \omega_\mu - \omega_\nu > 0$, and the kets $|\nu\rangle_{\mathrm{R}}$ and $|\mu\rangle_{\mathrm{R}}$ are the eigenvectors of the QRM Hamiltonian, and $\hbar\omega_\nu > \hbar\omega_\mu$ are their respective eigenvalues. We plot $\Delta E = \hbar(\omega_\nu - \omega_{\mathrm{G}})$ (being $\hbar\omega_{\mathrm{G}}$ the eigenenergy of the CTS ground state) as a

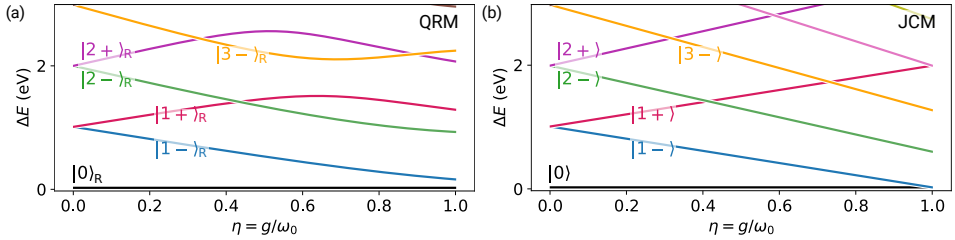

Figure 4.2: Eigenvalues of the CTS obtained as function of the coupling parameter $\eta = g/\omega_0$ within (a) the JCM and (b) the QRM. For each $|\nu\rangle$ (for the JCM) or $|\nu\rangle_{\mathrm{R}}$ (for the QRM) eigenstate, we show ΔE: the difference between its eigenenergy ($\hbar\omega_\nu$) and the ground state energy ($\hbar\omega_{\mathrm{G}}$).

function of η in Fig. 4.2a. The notation for QRM eigenstates used throughout this chapter, $|\nu\rangle_{\mathrm{R}} \in \{|0\rangle_{\mathrm{R}}, |1-\rangle_{\mathrm{R}}, |1+\rangle_{\mathrm{R}}, |2-\rangle_{\mathrm{R}}, |2+\rangle_{\mathrm{R}}, \dots\}$, is chosen to recall the JCM polaritons ($|n\pm\rangle = (|n, g\rangle \pm |n-1, e\rangle)/\sqrt{2}$), as the two match in the limit of vanishing coupling g. In Fig. 4.2a, we can observe how the eigenvalues of $|n+\rangle_{\mathrm{R}}$ ($|n-\rangle_{\mathrm{R}}$) increase (decrease) linearly with η for $\eta \lesssim 0.1$. This same behavior is followed by the JCM polaritons ($|n\pm\rangle$). However, whereas the JCM polaritons keep increasing or decreasing linearly with η for $\eta \gtrsim 0.1$, the eigenvalues of the QRM show a more complex dependence with η, presenting crossings and anticrossings with the eigenvalues of other eigenstates. Note that throughout this chapter we keep the labeling of the eigenstates even after the eigenvalues crossing points (see color code in the figure).

Each term on the right hand side of Eq. (4.1) represents a different process in the interaction of the system with its environment; $\hat{x}_{\hat{c}}$ describes the dissipation (the cavity gives energy to the environment), $\hat{x}_{\hat{c}}^\dagger$ describes the incoherent pumping (the environment gives energy to the cavity), and $\hat{x}_{\hat{c}}^{(0)}$ describes the so-called dephasing (there is no direct energy transfer between the cavity and the environment) [21,72,86]. In the systems studied in this thesis, we are interested in the dissipation of the cavity, described by the $\hat{x}_{\hat{c}}$ terms. These operators are then used to build the $\mathcal{D}_{\hat{x}_{\hat{c}}(\omega)}$ dissipation Lindblad superoperators according to Eq. (2.117), where each dissipation superoperator has associated a frequency-dependent dissipation rate, $\gamma_{\hat{c}}$ in the final master equation (Eq. (2.120)). In general, $\gamma_{\hat{c}}$ can be strongly dependent on the energy $\hbar\omega$ of the transitions between the eigenstates. However, in this thesis, we consider simple dissipation mechanisms, where $\gamma_{\hat{c}}$ becomes constant, *i.e.*, $\gamma_{\hat{c}}(\omega) \to \kappa$, with κ being the classical plasmonic losses introduced in section 1.2, when the cavity is a plasmonic resonator. In the plasmonic CTS considered in this chapter, the cavity is characterized by resonant frequency ω_0 (set to $\hbar\omega_0 = 1$ eV), and a low quality factor $Q = \omega_0/\kappa$, defined by the dissipation rate κ, and set to $Q = 20$ (thus $\kappa = 50$ meV). Thus, we only need a single Lindblad term to describe the dissipation of the cavity,

$$\kappa\mathcal{D}_{\hat{x}_{\hat{c}}}[\hat{\rho}(t)] = \frac{\kappa}{2}\left(2\hat{x}_{\hat{c}}\hat{\rho}(t)\hat{x}_{\hat{c}}^\dagger - \{\hat{x}_{\hat{c}}^\dagger\hat{x}_{\hat{c}}, \hat{\rho}(t)\}\right) \tag{4.4}$$

with

$$\hat{x}_{\hat{c}} = \sum_{\omega_\mu > \omega_\nu} |\nu\rangle_{\mathrm{R}\ \mathrm{R}}\langle\nu|\, i(\hat{c}^\dagger - \hat{c})\, |\mu\rangle_{\mathrm{R}\ \mathrm{R}}\langle\mu|\,. \tag{4.5}$$

Next, we use this same approach to address the dissipation and incoherent pumping of the TLS. We first consider the operator $\hat{\mathcal{S}}_{\hat{\sigma}} = (\hat{\sigma}^\dagger + \hat{\sigma})$ describing the interaction between the TLS and the environment [85, 86]. Then we decompose $\hat{\mathcal{S}}_{\hat{\sigma}}$ in the basis of the QRM eigenvalues:

$$\hat{\mathcal{S}}_{\hat{\sigma}} = \hat{x}^{(0)}_{\hat{\sigma}} + \sum_{\omega} [\hat{x}_{\hat{\sigma}}(\omega) + \hat{x}^\dagger_{\hat{\sigma}}(\omega)], \tag{4.6}$$

where,

$$\hat{x}^{(0)}_{\hat{\sigma}} = \sum_{\mu} |\mu\rangle_{\mathrm{R}\ \mathrm{R}}\langle\mu|\, (\hat{\sigma}^\dagger + \hat{\sigma})\, |\mu\rangle_{\mathrm{R}\ \mathrm{R}}\langle\mu|\,, \tag{4.7}$$

and

$$\hat{x}_{\hat{\sigma}}(\omega) = |\nu\rangle_{\mathrm{R}\ \mathrm{R}}\langle\nu|\, (\hat{\sigma}^\dagger + \hat{\sigma})\, |\mu\rangle_{\mathrm{R}\ \mathrm{R}}\langle\mu|\,, \tag{4.8}$$

with $\omega = \omega_\mu - \omega_\nu > 0$ (as in Eq. (4.3)). $\hat{x}_{\hat{\sigma}}$ and $\hat{x}^\dagger_{\hat{\sigma}}$ in Eq. (4.6) are used in Lindblad superoperators to address the dissipation, and the incoherent pumping, respectively [85, 86]. For the CTS consider in this chapter, we consider frequency-independent dissipation and pumping rates of the TLS, so we use a single Lindblad term to describe the losses of the TLS,

$$\gamma \mathcal{D}_{\hat{x}_{\hat{\sigma}}}[\hat{\rho}(t)] = \frac{\gamma}{2}\left(2\hat{x}_{\hat{\sigma}}\hat{\rho}(t)\hat{x}^\dagger_{\hat{\sigma}} - \{\hat{x}^\dagger_{\hat{\sigma}}\hat{x}_{\hat{\sigma}}, \hat{\rho}(t)\}\right), \tag{4.9}$$

and a single Lindblad term to describe the incoherent pumping of the TLS,

$$\Gamma \mathcal{D}_{\hat{x}^\dagger_{\hat{\sigma}}}[\hat{\rho}(t)] = \frac{\Gamma}{2}\left(2\hat{x}^\dagger_{\hat{\sigma}}\hat{\rho}(t)\hat{x}_{\hat{\sigma}} - \{\hat{x}_{\hat{\sigma}}\hat{x}^\dagger_{\hat{\sigma}}, \hat{\rho}(t)\}\right). \tag{4.10}$$

Here γ and Γ are the decay and incoherent pumping rates of the TLS, respectively, and

$$\hat{x}_{\hat{\sigma}} = \sum_{\omega_\mu > \omega_\nu} |\nu\rangle_{\mathrm{R}\ \mathrm{R}}\langle\nu|\, (\hat{\sigma}^\dagger + \hat{\sigma})\, |\mu\rangle_{\mathrm{R}\ \mathrm{R}}\langle\mu|\,. \tag{4.11}$$

In particular, we chose a decay rate of the TLS $\gamma/\omega_0 = 10^{-3}$, negligible compared to the decay rate of the cavity κ. Thus, we can establish the upper limit for the WC regime as $\eta = g/\omega_0 \lesssim \kappa/(2\omega_0) = 0.025$.

We now have all the elements to describe the dynamical evolution of $\hat{\rho}$ as follows from the master equation in Eq. (2.120),

$$\frac{d}{dt}\hat{\rho}(t) = \frac{-i}{\hbar}[\hat{\mathcal{H}}_C, \hat{\rho}(t)] + \kappa \mathcal{D}_{\hat{x}_{\hat{c}}}[\hat{\rho}(t)] + \gamma \mathcal{D}_{\hat{x}_{\hat{\sigma}}}[\hat{\rho}(t)] + \Gamma \mathcal{D}_{\hat{x}^\dagger_{\hat{\sigma}}}[\hat{\rho}(t)]. \tag{4.12}$$

Correlations in the quantum Rabi model

To characterize the statistical properties of the emission of the CTS, we study the intensity correlations of the emitted photons, $g^{(2)}(\tau = 0)$, as measured by an HBT interferometer, introduced in section 2.4. The measurement of a HBT interferometer corresponds to,

$$g^{(2)}(\tau) = \frac{\langle I_1(t+\tau) I_2(t) \rangle}{\langle I_1(t+\tau) \rangle \langle I_2(t) \rangle}, \tag{4.13}$$

where $I_1(t+\tau)$ and $I_2(t)$ are the photocurrents registered by the two detectors of the HBT interferometer, and τ is the time delay between the detection events (see Fig. 4.1a).

For zero time delay ($\tau = 0$) and sufficiently large t (so the system reaches the steady state), this quantity is related to the statistics of photons *inside* the cavity as [21, 85]:

$$g^{(2)}(0) = \frac{\langle \hat{x}_{\hat{c}}^\dagger \hat{x}_{\hat{c}}^\dagger \hat{x}_{\hat{c}} \hat{x}_{\hat{c}} \rangle_{ss}}{\langle \hat{x}_{\hat{c}}^\dagger \hat{x}_{\hat{c}} \rangle_{ss}^2}. \tag{4.14}$$

Crucially, within the QRM, $g^{(2)}(0)$ depends on the $\hat{x}_{\hat{c}}$ dressed operators introduced in Eq. (4.5), ensuring Gauge-invariance. On the other hand, $\langle \hat{O} \rangle_{ss}$ in the expression of $g^{(2)}(0)$ denotes the expectation value of operator $\hat{O}$ in the steady state (ss). Then, by using Eq. (4.12) we can obtain the steady state of the system via the density operator $\hat{\rho}_{ss}$ such that $\partial_t \hat{\rho}_{ss} = 0$.

This framework is used to calculate the dependence of $g^{(2)}(0)$ (Eq. (4.14)) on the coupling parameter $\eta = g/\omega_0$, plotted in Fig. 4.1b as solid orange and blue lines, for the case of strong ($\Gamma/\gamma = 10$), and weak ($\Gamma/\gamma = 10^{-6}$) pumping, respectively. All calculations of the evolution of the steady state and expectation values in the system that we obtain in this chapter have been carried out using the Python package QuTiP [177, 178]. We have considered in all of our QuTiP calculations an expansion of the Fock states of the cavity up to $N_c = 10$, which we verified ensures convergence.

4.2.2 Jaynes-Cummings model

In section 2.5.4 we derived the JCM Hamiltonian by taking two approximations. First, we expand the interaction term in the QRM Hamiltonian as

$$\hat{\sigma}_z \cos\left[2\eta(\hat{c} + \hat{c}^\dagger)\right] + \hat{\sigma}_y \sin\left[2\eta(\hat{c} + \hat{c}^\dagger)\right] = \hat{\sigma}_z + 2\eta\hat{\sigma}_y(\hat{c} + \hat{c}^\dagger) + O(\eta^2), \tag{4.15}$$

and drop the nonlinear terms in η. Next, we introduce the rotating wave approximation (RWA) by removing the so-called non-number-conserving terms $\hat{\sigma}\hat{c} + \hat{\sigma}^\dagger\hat{c}^\dagger$, to obtain the JCM Hamiltonian in Eq. (2.81) that we reproduce here for convenience,

$$\hat{\mathcal{H}}_{\mathrm{JC}} = \hbar\omega_0 \hat{c}^\dagger \hat{c} + \hbar \frac{\omega_0}{2} \hat{\sigma}_z + i\hbar g(\hat{\sigma}^\dagger \hat{c} - \hat{c}^\dagger \hat{\sigma}).$$

Further, the JCM introduces additional approximations regarding the emission, dissipation, and absorption of the system.

Dynamics in the Jaynes Cummings model

In the JCM, the interaction between the system and the environment is simplified by treating the dissipation of the cavity and of the TLS as separate elements. Let us first explore the dissipation of the cavity in the absence of the TLS. The Hamiltonian of the single cavity mode is (see Eq. (2.53)),

$$\hat{\mathcal{H}}_{\text{Cavity}} = \hbar\omega_0 \hat{c}^\dagger \hat{c}. \tag{4.16}$$

The eigenstates of these Hamiltonians are the Fock number states $|n\rangle$ (see section 2.2), with eigenvalues $\hbar n\omega_0$, ($n \geq 0$ any integer number). The dissipation of the cavity is described using the same dressed operators formalism introduced in the section above (Eqs. (4.1)-(4.5)). However, the dressed operators are built using the $|n\rangle$ eigenstates of the Hamiltonian of the bare cavity. Thus, the $\hat{x}_{\hat{c}}$ dressed operators in Eq. (4.5) now result in

$$\hat{x}_{\hat{c}} \to \sum_{\omega_m > \omega_n} |n\rangle \langle n| \, i(\hat{c}^\dagger - \hat{c}) \, |m\rangle \langle m| = -i \sum_n \sqrt{n} \, |n-1\rangle \langle n| = -i\hat{c}, \tag{4.17}$$

where, in the last identity, we have simply used the definition of the $\hat{c}$ annihilation operators in Eq. (2.18). Hence, the Lindblad dissipation term of the cavity becomes,

$$\begin{aligned} &\kappa \mathcal{D}_{\hat{x}_{\hat{c}}}[\hat{\rho}^{(\text{JC})}(t)] \to \kappa \mathcal{D}_{(-i\hat{c})}[\hat{\rho}^{(\text{JC})}(t)] = \kappa \mathcal{D}_{\hat{c}}[\hat{\rho}^{(\text{JC})}(t)] = \\ &= \frac{\kappa}{2}\left(2\hat{c}\hat{\rho}^{(\text{JC})}(t)\hat{c}^\dagger - \{\hat{c}^\dagger\hat{c}, \hat{\rho}^{(\text{JC})}(t)\}\right). \end{aligned} \tag{4.18}$$

Note that here we use the label "(JC)" to differentiate the density matrix describing the state in the QRM and that in the JCM.

Similarly, the dissipation of the TLS is described in the absence of the cavity. The Hamiltonian of the bare TLS is (see Eq. (2.69)),

$$\hat{\mathcal{H}}_{\text{TLS}} = \hbar \frac{\omega_0}{2} \hat{\sigma}_z, \tag{4.19}$$

with eigenstates $|g\rangle$ and $|e\rangle$, and eigenvalues $-\omega_0/2$ for $|g\rangle$ and $\omega_0/2$ for $|e\rangle$. As for the case of the cavity, the dissipation and incoherent excitation of the TLS is described using the same dressed operator formalism introduced for the QRM (Eqs. (4.6)-(4.11)). However, the dressed operators are built using only the decomposition on the $|g\rangle$ and $|e\rangle$ eigenstates. Thus, the $\hat{x}_{\hat{\sigma}}$ dressed operators in Eq. (4.11) become,

$$\hat{x}_{\hat{\sigma}} \to \sum_{\omega_e > \omega_g} |g\rangle \langle g| \, (\hat{\sigma}^\dagger + \hat{\sigma}) \, |e\rangle \langle e| = \hat{\sigma}. \tag{4.20}$$

Substituting this expression of $\hat{x}_{\hat{\sigma}}$ into the dissipation and incoherent pumping

terms in Eqs. (4.9) and (4.10), we obtain

$$\gamma\mathcal{D}_{\hat{x}_{\hat{\sigma}}}[\hat{\rho}^{(\mathrm{JC})}(t)] \to \gamma\mathcal{D}_{\hat{\sigma}}[\hat{\rho}^{(\mathrm{JC})}(t)] = \frac{\gamma}{2}\left(2\hat{\sigma}\hat{\rho}^{(\mathrm{JC})}(t)\hat{\sigma}^{\dagger} - \{\hat{\sigma}^{\dagger}\hat{\sigma}, \hat{\rho}^{(\mathrm{JC})}(t)\}\right), \quad (4.21)$$

for the TLS dissipation term, and

$$\Gamma\mathcal{D}_{\hat{x}_{\hat{\sigma}}^{\dagger}}[\hat{\rho}^{(\mathrm{JC})}(t)] \to \Gamma\mathcal{D}_{\hat{\sigma}^{\dagger}}[\hat{\rho}^{(\mathrm{JC})}(t)] = \frac{\Gamma}{2}\left(2\hat{\sigma}^{\dagger}\hat{\rho}^{(\mathrm{JC})}(t)\hat{\sigma} - \{\hat{\sigma}\hat{\sigma}^{\dagger}, \hat{\rho}^{(\mathrm{JC})}(t)\}\right), \quad (4.22)$$

for the TLS incoherent pumping term.

In summary, we can write the master equation with all the contributions to the system dynamics as introduced here, as:

$$\frac{d}{dt}\hat{\rho}_{\mathrm{JC}}(t) = \frac{-i}{\hbar}[\hat{\mathcal{H}}_{\mathrm{JC}}, \hat{\rho}^{(\mathrm{JC})}(t)] + \kappa\mathcal{D}_{\hat{c}}[\hat{\rho}^{(\mathrm{JC})}(t)] + \gamma\mathcal{D}_{\hat{\sigma}}[\hat{\rho}^{(\mathrm{JC})}(t)] + \Gamma\mathcal{D}_{\hat{\sigma}^{\dagger}}[\hat{\rho}^{(\mathrm{JC})}(t)]. \quad (4.23)$$

Intensity correlations in the Jaynes Cummings model

As for the QRM (in Eq. (4.14)), the correlations arising in the JCM are also related to the statistics of photons inside of the cavity and, can be expressed in terms of the dressed cavity operators [21]. However, the operator that describes the photons of the cavity corresponding to the dressed operators in Eq. (4.17) reduce to $\hat{x}_{\hat{c}} \to -i\hat{c}$, and thus, in the JCM the intensity correlations become

$$g^{(2)}_{\mathrm{JC}}(0) = \frac{\langle\hat{c}^{\dagger}\hat{c}^{\dagger}\hat{c}\hat{c}\rangle_{ss}}{\langle\hat{c}^{\dagger}\hat{c}\rangle^{2}_{ss}}. \quad (4.24)$$

The expected values in Eq. (4.24) are obtained with the steady-state $\hat{\rho}^{(\mathrm{JC})}_{ss}$, which we calculate from the solution of $\partial_t\hat{\rho}^{(\mathrm{JC})}_{ss} = 0$ in the standard master equation introduced in Eq. (4.23).

Figure 4.1b (dashed lines) shows the intensity correlations $g^{(2)}_{\mathrm{JC}}(0)$ obtained applying Eq. (4.24) in the JCM for strong (dashed orange line) and weak (dashed blue line) pumping. In the former case, the JCM correctly reproduces the results of the exact QRM below the USC threshold $\eta \lesssim 0.1$, but completely fails for larger η, where the $g^{(2)}_{\mathrm{JC}}(0)$ obtained with the JCM saturates, $g^{(2)}_{\mathrm{JC}}(0) \lesssim 2/3$, while, in the exact QRM, $g^{(2)}(0)$ keeps increasing strongly with η. Furthermore, for the weak incoherent pumping (blue lines), we find significant differences between the JCM and QRM even in the WC regime (the JCM and QRM differ for $\eta \gtrsim 5 \times 10^{-3}$). This unexpected breakdown of the JCM for small η is discussed in detail in section 4.4.

Analytical limit of the correlations in the Jaynes-Cummings Hamiltonian

The JCM has been extensively used to describe the properties of weakly-coupled CTSs [21]. In this chapter, it establishes a point of comparison to identify new features that can arise in the QRM. Further, we show next that the simplifications introduced by the JCM allow us to obtain an approximate analytical expression of $g^{(2)}(0)$ in the weak-illumination case, where the incoherent pumping of the TLS has a rate much lower than the TLS losses, $\Gamma \ll \gamma$.

As a first step, we identify the minimum set of operators for which the master equations form an almost closed system: $\mathbf{v} = \left(\hat{c}^\dagger\hat{c}, \hat{\sigma}^\dagger\hat{\sigma}, \hat{c}^\dagger\hat{\sigma}, \hat{c}\hat{\sigma}^\dagger, \hat{c}^\dagger\hat{c}\hat{\sigma}^\dagger\hat{\sigma}, \hat{c}^\dagger\hat{c}\hat{c}\hat{\sigma}^\dagger, \hat{c}^\dagger\hat{c}^\dagger\hat{c}\hat{\sigma}, \hat{c}^\dagger\hat{c}^\dagger\hat{c}\hat{c}\right)^T$. The equations of motion for the expectation values of these operators can be approximately expressed as

$$\frac{d}{dt}\langle\mathbf{v}\rangle = M\langle\mathbf{v}\rangle + \mathbf{b}, \tag{4.25}$$

with $\mathbf{b} = (0, \Gamma, 0, 0, 0, 0, 0, 0)^T$, and

$$M = \begin{pmatrix} -\kappa & 0 & -g & -g & 0 & 0 & 0 & 0 \\ 0 & -\gamma & g & g & 0 & 0 & 0 & 0 \\ g & -g & -\mathcal{M}_1 & 0 & -g & 0 & 0 & 0 \\ g & -g & 0 & -\mathcal{M}_1 & -g & 0 & 0 & 0 \\ \Gamma & 0 & 0 & 0 & -(\gamma+\kappa) & g & g & 0 \\ 0 & 0 & 0 & 0 & -2g & -\mathcal{M}_2 & 0 & g \\ 0 & 0 & 0 & 0 & -2g & 0 & -\mathcal{M}_2 & g \\ 0 & 0 & 0 & 0 & 0 & -2g & -2g & -2\kappa \end{pmatrix}, \tag{4.26}$$

where $\mathcal{M}_1 = (\Gamma+\kappa+\gamma)/2$ and $\mathcal{M}_2 = (\Gamma+\gamma+3\kappa)/2$. To derive Eqs. (4.25)-(4.26) we truncated the set of equations by considering that the pumping rate of the system, Γ, is very small. Thus, in the steady-state, the TLS is mostly in the ground state, and we approximate [179] (i) $\langle\hat{\sigma}\hat{\sigma}^\dagger\rangle \approx 1$, (ii) $\langle\hat{c}^\dagger\hat{c}^\dagger\hat{c}\hat{c}\hat{\sigma}\hat{\sigma}^\dagger\rangle \approx \langle\hat{c}^\dagger\hat{c}^\dagger\hat{c}\hat{c}\rangle$, and (iii) $\langle\hat{c}^\dagger\hat{c}^\dagger\hat{c}\hat{c}\hat{\sigma}^\dagger\hat{\sigma}\rangle \approx 0$.

In the steady state $\partial_t\langle\mathbf{v}\rangle_{ss} = 0$, and we can derive closed expressions for $\langle\hat{c}^\dagger\hat{c}\rangle_{ss}$ and $\langle\hat{c}^\dagger\hat{c}^\dagger\hat{c}\hat{c}\rangle_{ss}$.

$$\begin{aligned}\langle\hat{c}^\dagger\hat{c}\rangle_{ss} \approx & -4g^2\Gamma(4g^2\gamma + 12g^2\kappa + \Gamma\gamma\kappa + \gamma^2\kappa + \Gamma\kappa^2 + 4\gamma\kappa^2 + 3\kappa^3)\times \\ & \times\big[16g^4\Gamma\gamma - 16g^4\gamma^2 - 64g^4\gamma\kappa + 4g^2\Gamma^2\gamma\kappa - 4g^2\Gamma\gamma^2\kappa - 8g^2\gamma^3\kappa - 48g^4\kappa^2 - \\ & - 8g^2\Gamma\gamma\kappa^2 - 36g^2\gamma^2\kappa^2 - \Gamma^2\gamma^2\kappa^2 - 2\Gamma\gamma^3\kappa^2 - \gamma^4\kappa^2 - 4g^2\Gamma\kappa^3 - 40g^2\gamma\kappa^3 - \\ & - \Gamma^2\gamma\kappa^3 - 6\Gamma\gamma^2\kappa^3 - 5\gamma^3\kappa^3 - 12g^2\kappa^4 - 4\Gamma\gamma\kappa^4 - 7\gamma^2\kappa^4 - 3\gamma\kappa^5\big]^{-1}, \end{aligned} \tag{4.27}$$

$$\langle \hat{c}^\dagger \hat{c}^\dagger \hat{c}\hat{c} \rangle_{ss} \approx 32 g^4 \Gamma^2 \left[-16 g^4 \Gamma\gamma + 16 g^4 \gamma^2 + 64 g^4 \gamma\kappa - 4 g^2 \Gamma^2 \gamma\kappa + 4 g^2 \Gamma \gamma^2 \kappa + \right.$$
$$+ 8 g^2 \gamma^3 \kappa + 48 g^4 \kappa^2 + 8 g^2 \Gamma \gamma \kappa^2 + 36 g^2 \gamma^2 \kappa^2 + \Gamma^2 \gamma^2 \kappa^2 + 2\Gamma\gamma^3\kappa^2 + \gamma^4 \kappa^2 +$$
$$+ 4 g^2 \Gamma \kappa^3 + 40 g^2 \gamma \kappa^3 + \Gamma^2 \gamma \kappa^3 + 6\Gamma\gamma^2\kappa^3 + 5\gamma^3\kappa^3 +$$
$$\left. + 12 g^2 \kappa^4 + 4\Gamma\gamma\kappa^4 + 7\gamma^2\kappa^4 + 3\gamma\kappa^5 \right]^{-1}. \tag{4.28}$$

In particular, we are interested only in the values of $\langle \hat{c}^\dagger \hat{c} \rangle_{ss}$ and $\langle \hat{c}^\dagger \hat{c}^\dagger \hat{c}\hat{c} \rangle_{ss}$ in the two opposite limits of $g \ll \Gamma$ (vanishing coupling), and $g \gg \kappa$ (beyond the SC regime). We obtain an expression that is valid in both limits by retaining the terms dependent on the leading powers of the two free parameters, Γ and g, in Eqs. (4.27) and (4.28):

$$\langle \hat{c}^\dagger \hat{c} \rangle_{ss} \approx \frac{4g^2(4g^2+\kappa^2)\Gamma}{\kappa^3 (4g^2 + \gamma\kappa)} = \Gamma \frac{C}{C+1} \frac{4g^2+\kappa^2}{\kappa^3}, \tag{4.29}$$

where $C = 4g^2/(\kappa\gamma)$ is the cooperativity, and

$$\langle \hat{c}^\dagger \hat{c}^\dagger \hat{c}\hat{c} \rangle_{ss} \approx \frac{32 g^4 \Gamma^2}{3\kappa^2 (16 g^4 + \gamma\kappa^3)}. \tag{4.30}$$

The intensity correlations are found, in the two limits of interest, as

$$g^{(2)}_{\mathrm{JC}}(0) \xrightarrow{\kappa \gg \gamma \gg \Gamma \gg g} \frac{2}{3}\frac{\gamma}{\kappa}, \tag{4.31}$$

$$g^{(2)}_{\mathrm{JC}}(0) \xrightarrow{g \gg \kappa \gg \gamma \gg \Gamma} \frac{2}{3}. \tag{4.32}$$

Note that $g^{(2)}_{\mathrm{JC}}(0)$ is derived here by neglecting the direct emission from the TLS, which is an invalid approximation for very small g in equation (4.31) (unless the emission of the TLS is filtered-out). If direct emission of the TLS is included (4.31) should be modified, as it is clearest in the limit of $g = 0$. In this case, the emission of the system is only given by the TLS, which emits one photon at a time resulting in $g^{(2)}_{\mathrm{JC}} = 0$.

Importantly, both limits in Eqs. (4.31) and (4.32) are antibunched, *i.e.*, for all coupling strengths, we expect the JCM to result in an antibunching signal. This is confirmed by the results in Fig. 4.1b (dashed blue line), which shows the intensity correlations $g^{(2)}_{\mathrm{JC}}(0)$ obtained applying Eq. (4.24) for the JCM for weak incoherent pumping. The results of this figure also validates the limits in Eqs. (4.31) and (4.32), with $g^{(2)}(0) = 1.33 \times 10^{-2} = (2/3)(\gamma/\kappa)$ for $\eta = 10^{-3}$ and $g^{(2)}(0) = 2/3$ for $\eta = 1$.

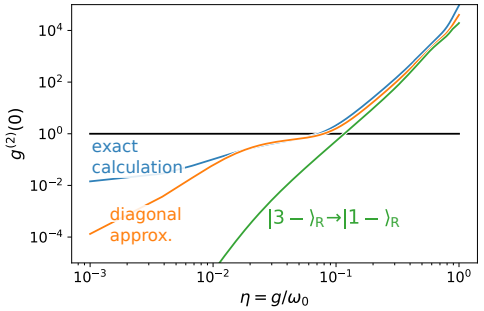

Figure 4.3: Intensity correlations as a function of the coupling parameter $\eta = g/\omega_0$ obtained within several approximations: exact values of $g^{(2)}(0)$ (solid blue line); the diagonal approximation truncated to the states $\{|0\rangle_R, |1-\rangle_R, |1+\rangle_R, |2-\rangle_R, |2+\rangle_R, |3-\rangle_R\}$ in Eq. (4.33) (solid orange line); the diagonal approximation considering only the ${}_R\langle 3-|\,\hat{x}_{\hat{c}}\hat{x}_{\hat{c}}\,|1-\rangle_R$ term in the numerator of $g^{(2)}(0)$ in Eq. (4.37) ($|3-\rangle_R \to |1-\rangle_R$, solid green line). The calculations shown in this figure are obtained within the QRM for $\Gamma/\gamma = 10^{-3}$.

4.3 Origin of the bunching in ultrastrongly coupled systems

In this section, we demonstrate that the strong bunching identified in the USC regime in Fig. 4.1b can be related to the characteristics (decay pathways and population) of the single $|3-\rangle_R$ eigenstate. To justify the focus on that particular eigenstate of the QRM Hamiltonian, we plot in Fig. 4.3 the exact values of $g^{(2)}(0)$ (solid blue line) obtained for an intermediate pumping $\Gamma/\gamma = 10^{-3}$ together with approximated results. We start by approximating the steady-state density matrix as being diagonal in the basis of the $|\nu\rangle_R$ eigenstates of the QRM Hamiltonian,

$$\hat{\rho}_{ss} \approx \sum_{\nu} R_\nu \;\; |\nu\rangle_R \; {}_R\langle\nu|\,, \tag{4.33}$$

where R_ν is the population of the $|\nu\rangle_R$ eigenstate. Thus, we can write the expected value of any operator $\hat{O}$ in the steady state as:

$$\langle\hat{O}\rangle_{ss} = \mathrm{Tr}\{\hat{O}\hat{\rho}_{ss}\} \approx \mathrm{Tr}\left\{\hat{O}\left(\sum_{\nu} R_\nu\,|\nu\rangle_R\;{}_R\langle\nu|\right)\right\} = \sum_{\nu} R_\nu\;{}_R\langle\nu|\,\hat{O}\,|\nu\rangle_R. \tag{4.34}$$

We then apply this formula to the expected value of $\langle(\hat{x}_{\hat{c}}^\dagger)^n(\hat{x}_{\hat{c}})^n\rangle_{ss}$ ($n = 1$ and $n = 2$ for the numerator and denominator of $g^{(2)}(0)$, respectively), resulting in:

$$\langle(\hat{x}_{\hat{c}}^\dagger)^n(\hat{x}_{\hat{c}})^n\rangle_{ss} \approx \sum_{\nu} R_\nu\;{}_R\langle\nu|\,(\hat{x}_{\hat{c}}^\dagger)^n(\hat{x}_{\hat{c}})^n\,|\nu\rangle_R = \sum_{\nu} R_\nu\;{}_R\langle\nu|\,(\hat{x}_{\hat{c}}^\dagger)^n\hat{\mathbb{I}}(\hat{x}_{\hat{c}})^n\,|\nu\rangle_R, \tag{4.35}$$

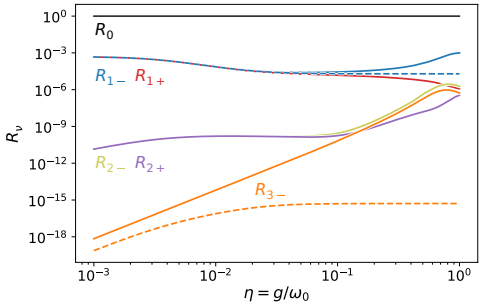

Figure 4.4: Populations of the polaritonic states R_ν (see labels) of a CTS calculated with the QRM (solid lines) and JCM (dashed lines) as a function of the coupling parameter $\eta = g/\omega_0$, for the intermediate pumping $\Gamma/\gamma = 10^{-3}$.

where we have included in the last step the identity matrix $\hat{\mathbb{I}}$. Because the eigenstates of the QRM Hamiltonian are orthonormal we can write the identity matrix as $\hat{\mathbb{I}} = \sum_\mu |\mu\rangle_{\mathrm{R}}\ {}_{\mathrm{R}}\langle\mu|$, and thus:

$$\sum_\nu R_\nu\ {}_{\mathrm{R}}\langle\nu|\,(\hat{x}_{\hat{c}}^\dagger)^n \hat{\mathbb{I}} (\hat{x}_{\hat{c}})^n\,|\nu\rangle_{\mathrm{R}} =$$
$$= \sum_{\mu,\nu} R_\nu\ {}_{\mathrm{R}}\langle\nu|\,(\hat{x}_{\hat{c}}^\dagger)^n\,|\mu\rangle_{\mathrm{R}}\ {}_{\mathrm{R}}\langle\mu|\,(\hat{x}_{\hat{c}})^n\,|\nu\rangle_{\mathrm{R}} = \sum_{\mu,\nu} R_\nu |{}_{\mathrm{R}}\langle\mu|\,(\hat{x}_{\hat{c}})^n\,|\nu\rangle_{\mathrm{R}}\,|^2, \tag{4.36}$$

where we have used the property $\langle b|\hat{O}^\dagger|a\rangle = (\langle a|\hat{O}|b\rangle)^*$. Applying Eq. (4.36) to $n = 1$ (denominator of $g^{(2)}(0)$ in Eq. (4.14)) and $n = 2$ (numerator of $g^{(2)}(0)$), results in

$$g^{(2)}(0) \approx \frac{\sum_{\nu,\mu} R_\nu\ |{}_{\mathrm{R}}\langle\mu|\,\hat{x}_{\hat{c}}\hat{x}_{\hat{c}}\,|\nu\rangle_{\mathrm{R}}\,|^2}{\left(\sum_{\nu,\mu} R_\nu\ |{}_{\mathrm{R}}\langle\mu|\,\hat{x}_{\hat{c}}\,|\nu\rangle_{\mathrm{R}}\,|^2\right)^2}, \tag{4.37}$$

The intensity correlations calculated by truncating the double sum in the numerator up to $|3-\rangle_{\mathrm{R}}$ are shown with the solid orange line in Fig. 4.3 — this approximation gives a very good agreement with the exact calculation for $\eta \gtrsim 2.5 \times 10^{-2}$; as we have numerically verified, the deviation observed in the WC regime $\eta \lesssim 2.5 \times 10^{-2}$ is not due to the truncation of the basis, but rather due to the effect of the off-diagonal terms of $\hat{\rho}_{ss}$.

We can further approximate $g^{(2)}(0)$ by limiting the double sum in Eq. (4.37) over ν and μ to the $|\nu\rangle = |3-\rangle_{\mathrm{R}}$ and $|\mu\rangle = |1-\rangle_{\mathrm{R}}$ term:

$$g^{(2)}(0) \approx \frac{R_{3-}\ |{}_{\mathrm{R}}\langle 1-|\,\hat{x}_{\hat{c}}\hat{x}_{\hat{c}}\,|3-\rangle_{\mathrm{R}}\,|^2}{\left(\sum_{\nu,\mu} R_\nu\ |{}_{\mathrm{R}}\langle\mu|\,\hat{x}_{\hat{c}}\,|\nu\rangle_{\mathrm{R}}\,|^2\right)^2}. \tag{4.38}$$

This approximation explores the role of the correlated two-photon emission from $|3-\rangle_{\mathrm{R}}$ to the $|1-\rangle_{\mathrm{R}}$ state. We show in Fig. 4.3 (green line) the resulting $g^{(2)}(0)$

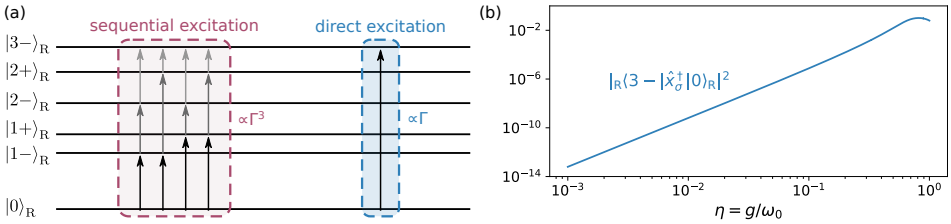

Figure 4.5: (a) Schematics and (b) dependence of the direct excitation pathways of the $|3-\rangle_R$ polariton in the QRM with η. (a) The sequential and direct excitation mechanisms are characterised by a cubic and linear dependence of the process on the incoherent driving rate Γ, respectively. (b) Efficiency of the direct excitation of $|3-\rangle_R$ state directly from the $|0\rangle_R$ state, quantified as $|_R\langle 3-|\,\hat{x}_\sigma^\dagger\,|0\rangle_R\,|^2$, which grows approximately as η^4 (until $\eta \approx 0.5$), and matching the dependence of R_{3-} shown in Fig. 4.4.

obtained by using Eq. (4.38), which is in good agreement with the exact calculations (blue line in the figure) for large coupling strength, $\eta \gtrsim 0.1$.

Equation (4.38) shows that the singular role of the $|3-\rangle_R$ polariton in the onset of bunching can be ascribed to two effects: the presence of a two-photon emission pathway from $|3-\rangle_R$ towards $|1-\rangle_R$, and a comparatively large, non-thermal population of $|3-\rangle_R$, expressed in our model as R_{3-}.

To analyse the latter effect in more detail, we plot in Fig. 4.4 the populations R_ν of all the relevant eigenstates of the QRM Hamiltonian (solid lines) as a function of the normalized coupling η for the intermediate pumping $\Gamma/\gamma = 10^{-3}$. Initially, the eigenstates are populated according to their respective eigenvalues, with the lower-energy states being more populated. While this mechanism holds for $\eta < 0.05$, Fig. 4.4 shows that for larger coupling the population R_{3-} (orange solid line) rapidly grows at a rate proportional to η^4, becoming larger than R_{2+} (purple solid line), and eventually approaching R_{1+} (red solid line) for $\eta > 0.1$. This increase of R_{3-} far exceeds that observed within the JCM (see the orange dashed line denoting the population of the $|3-\rangle$ polariton).

This large population of the $|3-\rangle_R$ polariton can be attributed to the new, *direct excitation* pathway introduced in the QRM (see Fig. 4.5a). In this model, the $|3-\rangle_R$ polariton can be directly driven from the ground state $|0\rangle_R$, through the $\Gamma/2\mathcal{D}_{\hat{x}_\sigma^\dagger}$ incoherent pumping term introduced in the master equation (4.12). We illustrate this effect in Fig. 4.5(b), by plotting the $|_R\langle 3-|\,\hat{x}_\sigma^\dagger\,|0\rangle_R|^2$ matrix element which quantifies the efficiency of the direct excitation pathway, as a function of η. We identify a clear scaling with η^4 until $\eta \approx 0.5$, similarly to the behavior of R_{3-}.

The direct excitation pathway should be proportional to the incoherent pumping rate Γ, and compete with the *sequential excitation* pathway $|0,g\rangle_R \to |1\pm\rangle_R \to |2\pm\rangle_R \to |3-\rangle_R$, with total rate $\propto \Gamma^3$. We can identify this competition in Fig. 4.6, where we plot the population R_{3-} as a function of Γ, for a range of coupling parameters η. The direct mechanism dominates the pumping for small Γ, where its linear dependence on the pumping rate makes it more efficient than the sequential pumping mechanism. Only when we increase Γ, does the latter process become

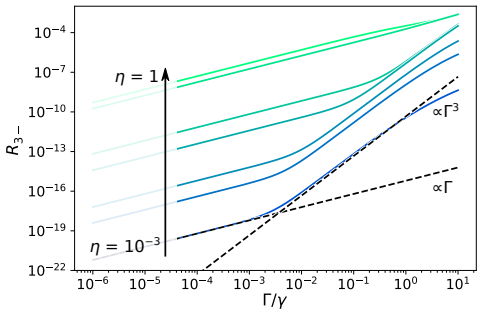

Figure 4.6: Populations of the $|3-\rangle_{\mathrm{R}}$ eigenstate as a function of the normalized incoherent pumping rate Γ/γ, for a range of coupling parameters η (from bottom to top, $\eta = 10^{-3}, 5\times 10^{-3}, 10^{-2}, 5\times 10^{-2}, 0.1, 0.5, 1$). The dashed lines highlights the regions where $|R_{3-}|$ evaluated for $\eta = 10^{-3}$ is $\propto \Gamma$ or $\propto \Gamma^3$.

more efficient and we recover $R_{3-} \propto \Gamma^3$ [xviii]. The transition from the linear to the cubic dependence on Γ, or from the direct to sequential excitation mechanisms, shifts towards larger Γ as we increase the coupling strength η. This is because the overall efficiency of the direct excitation, governed by the matrix element $|_{\mathrm{R}}\langle 3-|\,\hat{x}^{\dagger}_{\sigma}\,|0\rangle_{\mathrm{R}}|^2$, grows rapidly with η (see Fig. 4.5b).

4.4 Probing the breakdown of the RWA

In section 4.3 we identified and traced the emergence of the bunching in the USC regime, as observed in Fig. 4.1b and in Fig. 4.3 and connected with the direct excitation and two-photon emission from the $|3-\rangle_{\mathrm{R}}$ polariton. Here, we explore the extent of this new effect, and identify the coupling and pumping thresholds for the deviation between the JCM and the QRM to emerge. Figures 4.7a and b compare the values of $g^{(2)}(0)$ calculated within the QRM and the JCM, respectively, for a range of the normalized coupling strengths η and pumping rates Γ, and demonstrate that the deviation between the JCM and the QRM also depends strongly on the latter parameter (Γ), in a manner consistent with the formulation laid out in section 4.3.

4.4.1 Qualitative dependence of the bunching on the pumping

The map of intensity correlation shown in Fig. 4.7a indicates that the bunching observed in the QRM (and not in the JCM) depends on the rate of incoherent pumping Γ for a wide range of coupling parameters η. In Fig. 4.7a the bunching appears at $\Gamma/\gamma = 10^{-6}$ for $\eta \gtrsim 2\times 10^{-2}$ and at $\Gamma/\gamma = 10$ for $\eta \gtrsim 0.3$. We explore

[xviii] We also numerically verify that the populations $R_{2\pm}$ are proportional to Γ^2 throughout this regime, pointing to a sequential driving mechanism.

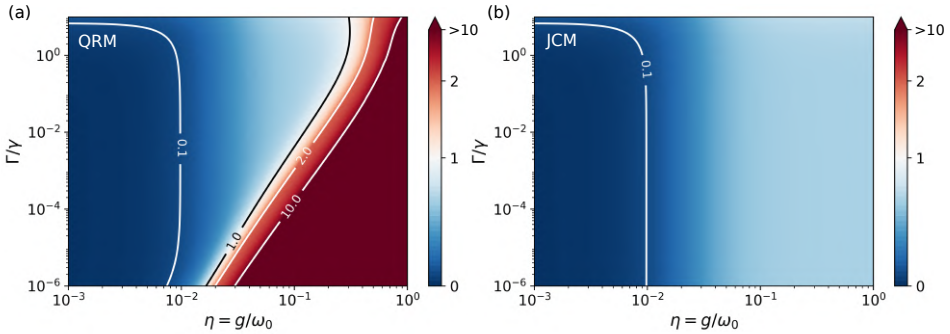

Figure 4.7: Dependence of $g^{(2)}(0)$ on the normalized pumping rate Γ/γ and coupling strength η obtained within the (a) QRM and (b) JCM. The colormap indicates in blue and red the antibunching ($g^{(2)}(0) < 1$) and bunching ($g^{(2)}(0) > 1$) regions, respectively. The color scale of $g^{(2)}(0)$ is linear from $g^{(2)}(0) = 0$ to 2 and logarithmic from $g^{(2)}(0) = 2$ to 10, where it saturates.

this effect in more detail in Fig. 4.8a, where we plot vertical cuts of Fig. 4.7a — dependence of $g^{(2)}(0)$ on Γ —, for $\eta = 0.1$ to 1, and find that for sufficiently small Γ the intensity correlations follow

$$g^{(2)}(0) \propto \frac{1}{\Gamma}. \tag{4.39}$$

This dependence extends towards larger Γ for larger η and results from the direct excitation mechanism of the polariton $|3-\rangle_{\mathrm{R}}$. In the USC regime, the contribution from this polariton dominates the numerator of $g^{(2)}(0)$, as approximated in Eq. (4.38), with the numerator proportional to $R_{3-} \propto \Gamma$ (as discussed in section 4.3). Conversely, the denominator of Eq. (4.38) is dominated by the contribution from the $|1\pm\rangle_{\mathrm{R}}$ eigenstates $\propto R_{1\pm}$. Since both $|1-\rangle_{\mathrm{R}}$ and $|1+\rangle_{\mathrm{R}}$ are populated directly from the ground state, we find $R_{1\pm} \propto \Gamma$. Thus we recover the $g^{(2)}(0) \propto R_{3-}/(R_{1\pm})^2 \propto 1/\Gamma$ dependence, and $g^{(2)}(0)$ is therefore found to be unbounded.

Equation (4.39) can be used as a marker for the breakdown of the JCM, since in that model, the direct pumping mechanism of high-order polaritons is absent, and consequently the intensity correlations are largely constant for small Γ (see Fig. 4.7b). In the following subsection, we further explore the breakdown of the JCM.

4.4.2 Breakdown of the JCM Hamiltonian in the WC regime

Figure 4.7a shows that in the QRM, the strong bunching region can also appear for η in the WC and SC regimes. In particular, for very weak incoherent pumping ($\Gamma/\gamma \lesssim 10^{-5}$), the strong bunching appears for couplings as small as $\eta \approx 2.5 \times 10^{-2}$, highlighting a significant deviation from the predictions of the JCM (where

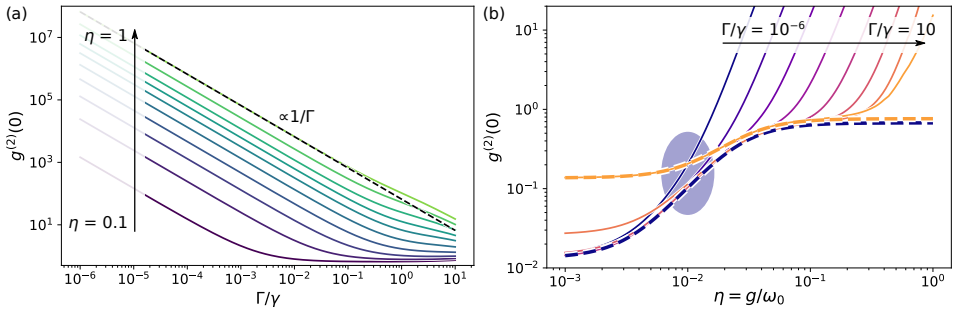

Figure 4.8: Landscape of $g^{(2)}(0)$ as a function of the (a) normalized incoherent pumping rate Γ/γ, and (b) coupling parameter $\eta = g/\omega_0$. In (a) the collection of lines represents results for the coupling parameter varied linearly in the range $\eta \in [0.1, 1]$. In (b) we exponentially increase the pumping rates from $\Gamma/\gamma = 10^{-6}$ to 10. The solid lines are obtained with the QRM, and the dashed orange and blue lines in (b) show the results obtained within the JCM for $\Gamma/\gamma = 10^{-6}$ and 10, respectively. The marked blue area in panel (b) indicates the WC region where a difference between the results obtained with both models becomes noticeable for a $\Gamma/\gamma = 10^{-6}$ pumping rate.

$g^{(2)}(0) < 1$ for all η). To demonstrate this effect more clearly, in Fig. 4.8b we plot horizontal cuts of Fig. 4.7 — the dependence of $g^{(2)}(0)$ on η calculated for different pumping rates Γ using the QRM (solid lines) and in the JCM (dashed lines). Note that in Fig. 4.8b only the cases $\Gamma/\gamma = 10^{-6}$ and $\Gamma/\gamma = 10$ are evaluated within the JCM (deashed lines), but other pumping rates follow the same antibunched emission for all the coupling regimes within this model (see Fig. 4.7).

The difference between the QRM and JCM in the WC and SC regimes has the same origin as in the USC regime: the direct excitation of the $|3-\rangle_{\mathrm{R}}$ eigenstate in the QRM. As we discuss in section 4.3, this direct mechanism can be dominant for any η, including the WC regime, providing that the pumping is sufficiently small. Notice, for instance, the blue marked area highlighting the differences between the solid and dashed blue lines in Fig. 4.8b. This difference can be traced back to the excitation mechanism within the JCM: for small Γ ($\Gamma \ll \gamma$), $g^{(2)}(0)$ in the JCM is determined by the population of the polariton with two-photon terms $|2\pm\rangle$ (we neglect the far smaller contribution from $|3\pm\rangle$), and, since this polariton is excited through a sequential process, its population is then proportional to Γ^2. Normalized by the square of the population of the $|1\pm\rangle$ states ($\propto \Gamma^2$), the intensity correlation in the weak pumping and coupling limit of the JCM is independent of Γ, and does not support bunched emission pathways.

It is worthwhile to consider how these striking differences can emerge also in the WC limit, where the QRM and JCM would be conventionally expected to match. To derive the Jaynes-Cummings Hamiltonian, $\hat{\mathcal{H}}_{\mathrm{JC}}$ in Eq. (2.81), we (i) performed the expansion of the QRM Hamiltonian $\hat{\mathcal{H}}_C$ in a power series of η, and dropped terms scaling with higher powers of η, and (ii) applied the RWA to remove the non-number-conserving terms. Figure 4.7 shows that QRM and JCM can get very different for arbitrarily small η, suggesting that the error in $g^{(2)}_{\mathrm{JC}}(0)$ introduced by

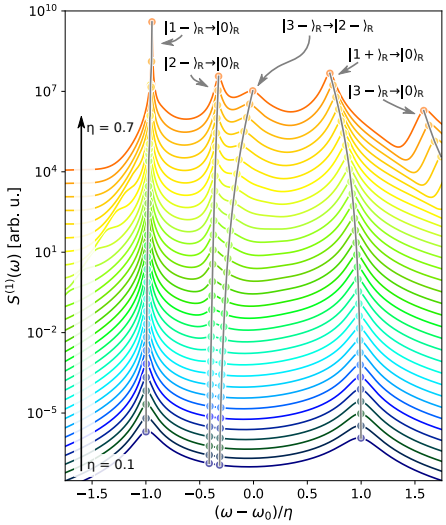

Figure 4.9: Emission spectra from the USC system for the parameter η changing linearly from 0.1 to 0.7, in $\Delta\eta = 0.02$ steps. The spectra are shifted vertically for clarity. Features describing transitions between eigenstates of the QRM Hamiltonian are traced and marked. The spectra are calculated within the QRM for an intermediate pumping rate $\Gamma/\gamma = 10^{-3}$.

the series truncation in (i) can be made arbitrarily small. Thus, we can trace the observed differences to the application of the RWA.

This is, to our knowledge, a singular situation for observing the breakdown of the RWA in the WC limit. An experimental assessment of this effect would constitute a serious challenge, as it would require the realization of a very weak incoherent pumping scheme for the two-level system, and simultaneous building of a significant two-photon statistics from a faint emission from the single cavity mode. On the other hand, its partial verification through the observation of $g^{(2)}(0) \propto 1/\Gamma$ dependence, should be more accessible.

4.4.3 Emission spectra

To conclude our characterization of the QRM, we study the dependence of the one-photon emission spectrum $S^{(1)}(\omega)$ on the coupling strength. We show that the differences between the QRM and the JCM for a coupling below the USC, are much smaller for $S^{(1)}(\omega)$ than for the intensity correlations $g^{(2)}(0)$, emphasizing the interest of using the intensity correlation to identify the breakdown of the JCM.

In Fig. 4.9, we plot the emission spectra $S^{(1)}(\omega)$ for a range of coupling strengths η. We calculate $S^{(1)}(\omega)$ within the QRM as [72, 85, 87]

$$S^{(1)}(\omega) \propto \int_{-\infty}^{\infty} \langle \hat{x}_{\hat{c}}^{\dagger}(\tau)\hat{x}_{\hat{c}}(0)\rangle_{ss}\, e^{-i\omega\tau} d\tau, \tag{4.40}$$

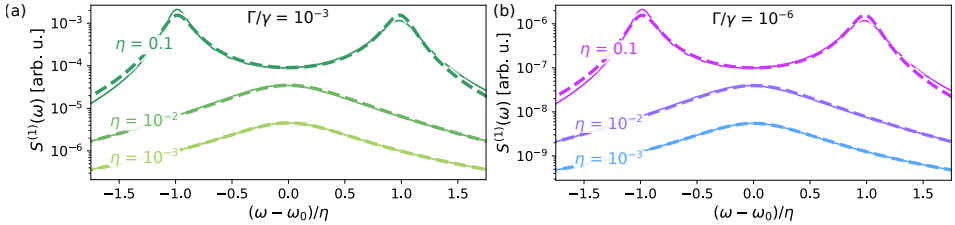

Figure 4.10: Comparison between the emission spectra obtained within the QRM (solid lines) and JCM (dashed lines) for different couplings strengths, as indicated in the figure. Panels (a) and (b) correspond to different pumping rate, $\Gamma/\gamma = 10^{-3}$ and $\Gamma/\gamma = 10^{-6}$, respectively.

where $\hat{x}_{\hat{c}}$ and $\hat{x}^{\dagger}_{\hat{c}}$ are the dressed annihilation and creation operators of the cavity, respectively. Each spectral feature in the figure corresponds to a transition between the eigenstates of the system, which we identify by matching the frequency of the peak with the difference between the eigenfrequencies of the system (see Fig. 4.2a). We plot these spectra as a function of the rescaled frequency $(\omega-\omega_0)/\eta$ to (partially) compensate for the η-dependence of the Rabi splitting between the polaritons.

The smallest coupling strength considered in Fig. 4.9 corresponds to the low limit of the USC, $\eta = 0.1$. This spectrum displays two peaks of similar intensity which, as in the JCM, correspond to the emission of a single photon via the $|1-\rangle_{\mathrm{R}} \to |0\rangle_{\mathrm{R}}$ (lower frequency feature) and $|1+\rangle_{\mathrm{R}} \to |0\rangle_{\mathrm{R}}$ (higher frequency) transitions. Only when one increases the coupling strength to about $\eta \approx 0.3$, do the spectra develop additional features: the strength of the spectral peak corresponding to the $|1-\rangle_{\mathrm{R}} \to |0\rangle_{\mathrm{R}}$ transition increases, and two new peaks, corresponding to the $|3-\rangle_{\mathrm{R}} \to |2-\rangle_{\mathrm{R}}$ and $|2-\rangle_{\mathrm{R}} \to |0\rangle_{\mathrm{R}}$ transitions (as labelled in the figure), emerge. The visibility of each peak can be compared to the populations of the initial states participating in the emission processes. For instance, the two new peaks follow the same dependence on η as the populations R_{3-} and R_{2-}, respectively (Fig. 4.4), so that, for $\eta \gtrsim 0.05$, the two populations grow very rapidly with increasing η. Simultaneously, as we increase the coupling η, spectral features continuously shift, reflecting the changes in the spectrum of the QRM Hamiltonian (Fig. 4.2a).

These additional peaks emerge only in the USC regime, for $\eta \gtrsim 0.3$. To check whether this threshold can be significantly modified, as we observed for the intensity correlations, in Fig. 4.10 we compare the spectra obtained from the JCM (dashed lines) and the QRM (solid lines) using weaker incoherent pumping Γ, and various couplings $\eta = 10^{-3}$, 10^{-2}, and 0.1 (note that $\eta = 10^{-3}$ and 10^{-2} are below the minimum value considered in Fig. 4.9, and give no peak-splitting). In the JCM the emission spectrum is calculated as

$$S^{(1)}(\omega) \propto \int_{-\infty}^{\infty} \langle \hat{c}^{\dagger}(\tau)\hat{c}(0)\rangle_{ss}\, e^{-i\omega\tau} d\tau, \tag{4.41}$$

where $\hat{c}$ and $\hat{c}^{\dagger}$ are the annihilation operators of the cavity, respectively.

The spectra point to small differences between the two models for the largest η

in both considered pumping rates considered, but these differences would be likely difficult to identify in experimental settings. On the other hand, as shown in Figs. 4.7 and 4.8b, the $g^{(2)}(0)$ obtained for $\Gamma/\gamma = 10^{-3}$ and $\Gamma/\gamma = 10^{-6}$ show strong qualitative differences for $\eta \gtrsim 2.5 \times 10^{-2}$ due to the direct excitation pathway of the state $|3-\rangle_{\mathrm{R}}$ introduced in section 4.3. The lack of sensitivity of $S^{(1)}(\omega)$ to this direct excitation pathway is due to the fact that the emission from the lower $|1-\rangle_{\mathrm{R}}$ and $|1+\rangle_{\mathrm{R}}$ states predominantly govern the emission spectra for $\eta \lesssim 0.3$. The excitation and emission from these eigenstates are not impacted by the direct excitation mechanism discussed above, and do not lead to the breakdown of the RWA. We thus conclude that the characterization of the correlations is a more powerful tool than measuring the one-photon emission spectra for the identification of phenomena caused by the non-number-conserving terms of the QRM Hamiltonian for coupling below the traditional USC threshold $\eta \approx 0.1$.

4.5 Conclusions

In this chapter, we analyze the statistics of the emission from a generic quantum system comprising an incoherently driven two-level emitter interacting with a cavity. We identify the emergence of unbounded bunching as the system approaches the USC regime. By expressing the dynamics of the system in the basis of the polaritonic eigenstates of the quantum Rabi Hamiltonian, we can attribute the bunching to the singular behavior of the individual eigenstate $|3-\rangle_{\mathrm{R}}$, which (i) decays through a correlated two-photon emission, and (ii) is very strongly populated by a new, direct excitation mechanism from the ground state.

We show that intensity correlations $g^{(2)}(0)$ are a much more sensitive tool for observing the phenomena induced by the non-number-conserving terms in the QRM, than the one-photon emission spectra. Indeed, we find that the intensity correlations can identify a breakdown of the rotating wave approximation far below the conventional limit of the USC, with the exact limit determined by the rate of incoherent pumping.

These findings call for experimental verification, and further theoretical studies, to verify the robustness of the identified excitation and emission mechanisms. Our model can be extended to account for more complex decay dynamics and energy structure of the quantum emitter, involving dark excitonic states, or pure dephasing, as well as the interaction with a structured reservoir.

CHAPTER 5

PRESERVATION AND DESTRUCTION OF THE PURITY OF TWO-PHOTON STATES IN THE INTERACTION WITH A NANOSCATTERER

5.1 Introduction

Classical light beams can carry well-defined angular momentum, as described in chapter 1. Similarly, quantum states of light (introduced in chapter 2) can also carry well-defined angular momentum. This aspect opens up a variety of potential benefits for quantum technologies. For instance, the angular momentum of quantum states of light can be used to encode information [15–18]. This is particularly useful for quantum information applications as quantum states of light are very resilient to lose their entanglement and purity during propagation [180–182]. Thus, the states of light with well-defined angular momentum are ideal candidates as quantum information carriers.

On the other hand, photons do not interact strongly with material particles and structures, limiting the possibilities of processing photonic quantum information [183, 184]. Several techniques are being developed in order to enhance photon interactions, such as the use of quantum optomechanical interaction, optical metamaterials, high-density gases, slow-light materials and several others [185–189]. Engineering nanophotonic nanostructures for quantum information processing offers the possibility to, not only enhancing light-matter interactions, but also manipulating light in devices with a footprint of the order of the wavelength. While the use of nanostructures and the study of their optical resonances to enhance

the classical interaction of light and matter has a long tradition [49, 111, 190], a formal study of the effect of the interaction of quantum states of light with such nanostructures is still needed.

In this chapter, we provide a framework to study the interaction between quantum states of light with well defined angular momentum and a nanostructure. Our approach is general, but we focus on an experimentally relevant situation: the scattering of two-photon states of light by a rotationally symmetric nanostructure. Crucially, the rotational symmetry imposes the conservation of the total angular momentum $m = l + s$, where l and s represent the orbital and spin angular momentum, respectively. Thus, these nanostructures allow for the manipulation of states of light with a fixed and well-defined total angular momentum in a controlled manner [20, 191].

5.2 Input and output states

The theoretical framework used to describe the quantum scattering process is based on an input/output general formalism [78, 79, 191, 192]. We consider that the input and output states of the system are quantum states of light composed by two entangled photons, where the two photons have total angular momentum $m = 0$, and the information is encoded in their helicity Λ (defined as the projection of the spin operator $\overleftrightarrow{\boldsymbol{S}}$ on the direction of propagation, see Eq. (1.84)), which takes $\Lambda = +1$ or $\Lambda = -1$ values (see section 1.4) [191]. We consider a basis of four input two-photon modes that completely describes any input monochromatic two-photon states:

$$|\psi^i_\pm(\omega_1, \omega_2)\rangle = \frac{1}{2}\left\{\hat{a}^\dagger_i(\omega_1)\hat{a}^\dagger_i(\omega_2) \pm \hat{b}^\dagger_i(\omega_1)\hat{b}^\dagger_i(\omega_2)\right\}|0\rangle\,, \tag{5.1a}$$

$$|\chi^i_\pm(\omega_1, \omega_2)\rangle = \frac{1}{2}\left\{\hat{a}^\dagger_i(\omega_1)\hat{b}^\dagger_i(\omega_2) \pm \hat{b}^\dagger_i(\omega_1)\hat{a}^\dagger_i(\omega_2)\right\}|0\rangle\,, \tag{5.1b}$$

where $|0\rangle$ is the vacuum state, and ω_1 and ω_2 are the frequencies of the two-photons. The basis of the two-photon output monochromatic modes also has four elements, $|\psi^o_\pm(\omega_1, \omega_2)\rangle$ and $|\chi^o_\pm(\omega_1, \omega_2)\rangle$, whcih follow Eqs. (5.1a) and (5.1b), respectively, but the input "i" labels are substituted by the output "o" labels,

$$|\psi^o_\pm(\omega_1, \omega_2)\rangle = \frac{1}{2}\left\{\hat{a}^\dagger_o(\omega_1)\hat{a}^\dagger_o(\omega_2) \pm \hat{b}^\dagger_o(\omega_1)\hat{b}^\dagger_o(\omega_2)\right\}|0\rangle\,, \tag{5.2a}$$

$$|\chi^o_\pm(\omega_1, \omega_2)\rangle = \frac{1}{2}\left\{\hat{a}^\dagger_o(\omega_1)\hat{b}^\dagger_o(\omega_2) \pm \hat{b}^\dagger_o(\omega_1)\hat{a}^\dagger_o(\omega_2)\right\}|0\rangle\,. \tag{5.2b}$$

The modes of light are described by the input(output) $\hat{a}^\dagger_{i(o)}(\omega)$ and $\hat{b}^\dagger_{i(o)}(\omega)$ operators that indicate the creation of an input(output) photon with helicity $\Lambda = +1$ or $\Lambda = -1$, respectively. The properties of the creation and annihilation operators describing the quantization of light were discussed in section 2.2. Notably, the $\hat{a}^\dagger_{i(o)}(\omega)$ and $\hat{b}^\dagger_{i(o)}(\omega)$ bosonic operators satisfy the canonical commutation relations (Eq. (2.21)) and operate on a single frequency ω.

Recent experiments have measured a degradation of input quantum states (quantified below by means of the loss of purity) after scattering off a nanostructure [191]. In particular, in these (and other similar) experiments, the incident photon pairs are generated in a superposition of states of different frequencies, typically by a standard spontaneous parametric down-conversion (SPDC) process. In this chapter, we analyze the mechanism by which the scattering of these non-monochromatic states can result in a loss of purity. With this purpose, we first focus on the scattering of states that are frequency superpositions of the monochromatic two-photon state $|\psi_+^i(\omega_1,\omega_2)\rangle$ (in section 5.3.3 we study the scattering of the rest of the elements in the basis),

$$|\Psi_+^i\rangle = \iint d\omega_1 d\omega_2 \phi(\omega_1,\omega_2)\,|\psi_+^i(\omega_1,\omega_2)\rangle\,. \tag{5.3}$$

where $\phi(\omega_1,\omega_2)$ is the two-photon spectral function that we approximate as the product of two Gaussian functions both centered at the central frequency ω_{in} (or central wavelength $\lambda_{\text{in}} = 2\pi c/\omega_{\text{in}}$) and variance $\sigma = 3$ THz (this value is chosen to be similar to the one used in recent experiments [193, 194]),

$$\phi(\omega_1,\omega_2) = \frac{1}{\sigma\sqrt{\pi}} \exp\left(-\frac{(\omega_1-\omega_{\text{in}})^2}{2\sigma^2}\right) \exp\left(-\frac{(\omega_2-\omega_{\text{in}})^2}{2\sigma^2}\right). \tag{5.4}$$

Note that this expression of $\phi(\omega_1,\omega_2)$ implies that the two photons are indistinguishable, since $\phi(\omega_1,\omega_2) = \phi(\omega_2,\omega_1)$.

Experimentally-accesible density matrix

In order to approach a realistic experimental characterization of quantum states, we consider that the scattered states are measured through a post-selection of two-photon states, where the scattered states with less than two photons are ignored. We also consider in the following that the detectors are "blind" to the frequency degree of freedom. Then, the input and output quantum states are best described with the experimentally-accessible post-selected density matrix, $\hat{\varrho}$, resulting from tracing out the frequency degree of freedom. Thus, the elements $\langle\xi|\hat{\varrho}|\xi'\rangle$ of the density matrix corresponds to the results of standard quantum state tomography measurements [74, 195],

$$\langle\xi|\hat{\varrho}^{i(o)}|\xi'\rangle = \mathcal{K} \iint d\omega_1 d\omega_2\, \langle\xi(\omega_1,\omega_2)\,|\Psi_+^{i(o)}\rangle\,\langle\Psi_+^{i(o)}|\,\xi'(\omega_1,\omega_2)\rangle\,, \tag{5.5}$$

where $\mathcal{K}$ is a normalization constant that ensures $\text{Tr}\{\hat{\varrho}^{i(o)}\} = 1$. $|\xi(\omega_1,\omega_2)\rangle$ and $|\xi'(\omega_1,\omega_2)\rangle$ can be any of the $|\psi_\pm^{i(o)}(\omega_1,\omega_2)\rangle$ and $|\chi_\pm^{i(o)}(\omega_1,\omega_2)\rangle$ states given in Eqs. (5.1a) and (5.1b), respectively. For example, Fig. 5.1 shows the density matrix $\hat{\varrho}^i$ of the incident state $|\Psi_+^i\rangle$ (Eq. (5.3)) calculated using Eq. (5.5). $\hat{\varrho}^i$ is characterized by a single non-zero element corresponding to $\langle\psi_+|\hat{\varrho}^i|\psi_+\rangle$, and there is no contribution from the other elements of the basis (Eqs. (5.1a) and

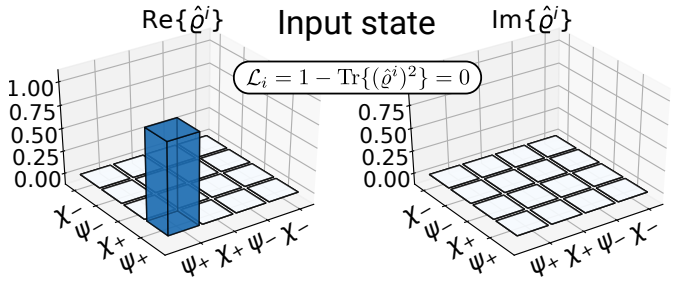

Figure 5.1: Real (left) and imaginary (right) components of $\hat{\varrho}^i$, the density matrix associated to the input state $|\Psi^i_+\rangle$. The two-photon spectral function is centered at $\omega_{\mathrm{in}} = 17.5 \times 10^{14}$ rad/s and has a variance of $\sigma = 3$ THz. $\mathcal{L}_i = 0$ indicates that the input state is pure.

(5.1b)). The loss of purity of such a quantum state can then be quantified using $\mathcal{L}_{i(o)} = 1 - \mathrm{Tr}\{(\hat{\varrho}^{i(o)})^2\}$ (introduced in Eq. (2.3)), where $\mathcal{L}_{i(o)} = 0$ indicates a pure state and $\mathcal{L}_{i(o)} > 0$ a mixed state. The input density matrix $\hat{\varrho}^i$ in Fig. 5.1 satisfies $\mathcal{L}_i = 1 - \mathrm{Tr}\{(\hat{\varrho}^i)^2\} = 0$, which confirms that $\hat{\varrho}^i$ is a pure state [74].

5.3 Quantum transformation

We next discuss how to analyze the loss of purity due to the scattering of $m = 0$ photons by a rotationally symmetric nanostructure. As discussed in section 1.4.3, rotationally symmetric structures conserve the total angular momentum of the incident light. However, the conservation of the total angular momentum does not imply the conservation of the vectorial degree of freedom of light, which is determined by the helicity Λ. Since the states of light studied in this chapter are determined by m and Λ (see section 1.4.2), the input electromagnetic modes with $m = 0$ and $\Lambda = +1$ (or $\Lambda = -1$) can only be scattered into two different output electromagnetic modes with $m = 0$ (due to m conservation) and $\Lambda = +1$ or $\Lambda = -1$. Further, we consider that photons can be lost or dissipated in the scattering process. This situation where two input electromagnetic modes are either lost or transformed into two other output electromagnetic modes is analogous to the situation produced in a lossy beam splitter [78, 79, 192]. Thus, we can directly adapt the transformation of lossy beam splitters that was introduced in section 2.3 (Eq. (2.29)) to our system, resulting in the following equations connecting the output and input annihilation operators:

$$\begin{aligned} \hat{a}_o(\omega) &= \alpha_{+1}(\omega)\hat{a}_i(\omega) + \beta_{+1}(\omega)\hat{b}_i(\omega) + \hat{L}_{+1}(\omega), \\ \hat{b}_o(\omega) &= \alpha_{-1}(\omega)\hat{b}_i(\omega) + \beta_{-1}(\omega)\hat{a}_i(\omega) + \hat{L}_{-1}(\omega), \end{aligned} \tag{5.6}$$

where $\hat{L}_{+1}$ and $\hat{L}_{-1}$ are the Langevin operators accounting for the losses in the scattering process (see section 2.3) [78, 80, 81], and α_{+1}, α_{-1}, β_{+1}, and β_{-1} are the helicity-splitting coefficients that are fully described in the next subsection.

5.3.1 Helicity-splitting coefficients

Equation (5.6) describes the scattering of quantum states of light, but the α_{+1}, α_{-1}, β_{+1}, and β_{-1} coefficients can be calculated from the classical response of the system as obtained from Maxwell's equations because Maxwell's equations determine how the electromagnetic modes get transformed, both in the classical and quantum regimes [64, 196]. Thus, to obtain the helicity-splitting coefficients, we consider a classical scattering problem where incident light beam with $m = 0$ is scattered by the nanostructure. The scattered light is separated by its helicity contributions, and each helicity contribution is detected separately. For example, in this chapter, we consider that the detection is done by coupling each helicity contribution of the scattered field to a single-mode fiber connected to a detector.

In particular, we consider two classical input beams with a helicity of either $\Lambda = +1$ or $\Lambda = -1$ and total angular momentum $m = 0$. The electric fields for these input beams are represented by $\boldsymbol{E}^i_{+1}$ and $\boldsymbol{E}^i_{-1}$, respectively. We then calculate the scattered fields, $\boldsymbol{E}^{\text{sca}}_{+1}$ ($\boldsymbol{E}^{\text{sca}}_{-1}$), when the nanostructure is illuminated by the input beam $\boldsymbol{E}^i_{+1}$ ($\boldsymbol{E}^i_{-1}$). The helicity-splitting coefficients are determined by projecting the scattered field into two classical output beams, $\boldsymbol{E}^o_{+1}$ and $\boldsymbol{E}^o_{-1}$, which also have an angular momentum of $m = 0$ and a helicity of $\Lambda = +1$ and $\Lambda = -1$, respectively:

$$\begin{aligned}
\alpha_{+1}(\omega) &= \iint_{\mathcal{A}} d\mathcal{A}[\boldsymbol{E}^o_{+1}(\boldsymbol{r},\omega)]^* \cdot \boldsymbol{E}^{\text{sca}}_{+1}(\boldsymbol{r},\omega),\\
\alpha_{-1}(\omega) &= \iint_{\mathcal{A}} d\mathcal{A}[\boldsymbol{E}^o_{+1}(\boldsymbol{r},\omega)]^* \cdot \boldsymbol{E}^{\text{sca}}_{-1}(\boldsymbol{r},\omega),\\
\beta_{+1}(\omega) &= \iint_{\mathcal{A}} d\mathcal{A}[\boldsymbol{E}^o_{-1}(\boldsymbol{r},\omega)]^* \cdot \boldsymbol{E}^{\text{sca}}_{+1}(\boldsymbol{r},\omega),\\
\beta_{-1}(\omega) &= \iint_{\mathcal{A}} d\mathcal{A}[\boldsymbol{E}^o_{-1}(\boldsymbol{r},\omega)]^* \cdot \boldsymbol{E}^{\text{sca}}_{-1}(\boldsymbol{r},\omega).
\end{aligned} \tag{5.7}$$

This operation corresponds to calculating the coupling between the scattered fields and a single-mode fiber connected to the detector, and $\mathcal{A}$ is the area of the fiber.

In this chapter, we consider a simple detection scheme (discussed in section 5.4) where $\alpha_{+1}(\omega) = \alpha_{-1}(\omega) = \alpha(\omega)$ and $\beta_{+1}(\omega) = \beta_{-1}(\omega) = \beta(\omega)$. In this case, Eq. (5.6) simplifies to

$$\begin{aligned}
\hat{a}_o(\omega) &= \alpha(\omega)\hat{a}_i(\omega) + \beta(\omega)\hat{b}_i(\omega) + \hat{L}_{+1}(\omega),\\
\hat{b}_o(\omega) &= \alpha(\omega)\hat{b}_i(\omega) + \beta(\omega)\hat{a}_i(\omega) + \hat{L}_{-1}(\omega).
\end{aligned} \tag{5.8}$$

5.3.2 Output $|\Psi^o_+\rangle$ state

By considering the simplified transformation in Eq. (5.8) we can obtain a the output state $|\Psi^o_+\rangle$ from the projection of the input state, $|\Psi^i_+\rangle$, on all the two-photon

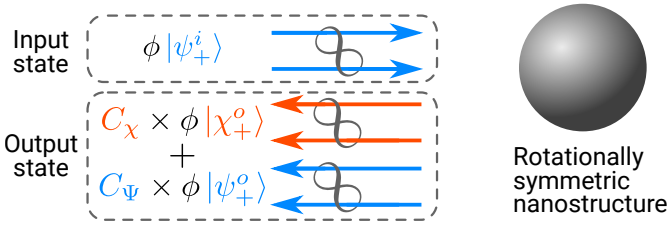

Figure 5.2: Scheme of the scattering process. The $|\Psi^i_+\rangle$ input state is scattered as a superposition of $|\psi^o_+\rangle$ and $|\chi^o_+\rangle$ with amplitudes given by $C_\psi\phi$ and $C_\chi\phi$, respectively

states of the output basis:

$$
\begin{aligned}
|\Psi^o_+\rangle = \Big[& |\psi^o_+(\omega_3,\omega_4)\rangle \langle\psi^o_+(\omega_3,\omega_4)| + \\
& + |\psi^o_-(\omega_3,\omega_4)\rangle \langle\psi^o_-(\omega_3,\omega_4)| + |\chi^o_+(\omega_3,\omega_4)\rangle \langle\chi^o_+(\omega_3,\omega_4)| + \\
& + |\chi^o_-(\omega_3,\omega_4)\rangle \langle\chi^o_-(\omega_3,\omega_4)| \Big] \cdot \iint d\omega_1 d\omega_2 \phi(\omega_1,\omega_2)\, |\psi^i_+(\omega_1,\omega_2)\rangle\,. \qquad (5.9)
\end{aligned}
$$

To evaluate Eq. (5.9), we first substitute the expressions of the $\hat{a}_o(\omega)$ and $\hat{b}_o(\omega)$ operators in Eq. (5.8) into the expressions of $\langle\psi^o_+(\omega_1,\omega_2)|$, $\langle\psi^o_-(\omega_1,\omega_2)|$, $\langle\chi^o_+(\omega_1,\omega_2)|$, and $\langle\chi^o_-(\omega_1,\omega_2)|$ in Eqs. (5.2a) and (5.2b), *i.e.*, we express the output basis bra states in terms of the input operators. Then we perform the projection of each output bra state onto the $|\psi^i_+(\omega_1,\omega_2)\rangle$ state. After some algebraic manipulation, Eq. (5.9) becomes:

$$
|\Psi^o_+\rangle = \iint d\omega_1 d\omega_2 \phi(\omega_1,\omega_2) \left[C_\psi(\omega_1,\omega_2)\, |\psi^o_+(\omega_1,\omega_2)\rangle + C_\chi(\omega_1,\omega_2)\, |\chi^o_+(\omega_1,\omega_2)\rangle \right], \qquad (5.10)
$$

with $C_\psi(\omega_1,\omega_2)$ and $C_\chi(\omega_1,\omega_2)$ defined as:

$$
C_\psi(\omega_1,\omega_2) = \alpha(\omega_1)\alpha(\omega_2) + \beta(\omega_1)\beta(\omega_2), \qquad (5.11a)
$$

$$
C_\chi(\omega_1,\omega_2) = \alpha(\omega_1)\beta(\omega_2) + \beta(\omega_1)\alpha(\omega_2). \qquad (5.11b)
$$

Equation (5.10) shows that, in general, the output state is a superposition of two different entangled photon modes, $|\psi^o_+(\omega_1,\omega_2)\rangle$ and $|\chi^o_+(\omega_1,\omega_2)\rangle$. Each output mode has a different amplitude, $C_\psi(\omega_1,\omega_2)\phi(\omega_1,\omega_2)$ for $|\psi^o_+(\omega_1,\omega_2)\rangle$ and $C_\chi(\omega_1,\omega_2)\phi(\omega_1,\omega_2)$ for $|\chi^o_+(\omega_1,\omega_2)\rangle$, as we show in the scheme of figure 5.2. The $C_\psi(\omega_1,\omega_2)$ and $C_\chi(\omega_1,\omega_2)$ coefficients in Eqs. (5.11a) and (5.11b) may have a strong frequency dependence due to rapid spectral changes of the α and β coefficients, greatly affecting the purity of the output state. To illustrate the formalism, we artificially set $\beta(\omega) = 0.2$ and $\alpha(\omega) = \omega_L\gamma/[2(\omega_L^2 - \omega^2 + i\gamma\omega)]$ a Lorentzian function that mimics the resonant behavior of a nanostructure. Figure

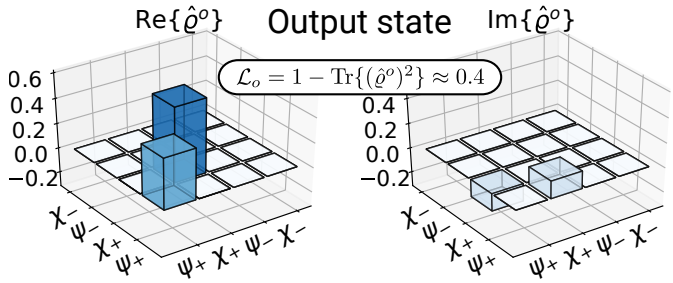

Figure 5.3: Real (left) and imaginary (right) components of $\hat{\varrho}^o$, the post-selected density matrix of the output state $|\Psi_+^o\rangle$ that results from the scattering of the incident input state $|\Psi_+^i\rangle$ in Fig. 5.1. For the calculation, we chose that the helicity splitting coefficient $\beta(\omega) = 0.2$, and $\alpha(\omega)$ is a Lorentzian function with $\omega_L = 17.5 \times 10^{14}$ rad/s and $\gamma = 1$ THz. $\mathcal{L}_o \approx 0.4 > 0$ indicates that the output state is not pure

5.3 shows the output density matrix $\hat{\varrho}^o$ calculated using Eqs. (5.5) and (5.10)-(5.11b), for these α and β helicity-splitting coefficients. The $\hat{\varrho}^o$ obtained for the output state represents a partially coherent superposition of $|\psi_+^o(\omega_1, \omega_2)\rangle$ and $|\chi_+^o(\omega_1, \omega_2)\rangle$ (as indicated by Eq. (5.10)). The purity of this state is $\mathcal{L}_o \approx 0.4 > 0$ (*i.e.*, the output state is mixed). Thus, this simple example demonstrates that the purity of the incident quantum state can be lost in the interaction with a nanostructure.

Origin of the loss of purity under the quasi–monochromatic approximation

To identify the origin of this loss of purity, we consider that the input two-photon spectral function, $\phi(\omega_1, \omega_2)$ is quasi-monochromatic (*i.e.,* its spectral variance σ is significantly smaller than the central frequency of the pulse, ω_{in}). Under this approximation, we first expand the α and β coefficients to first order around the central frequency of the two-photon spectral function ω_{in}:

$$\alpha(\omega) \approx A\left(1 + \frac{A'}{A}\Delta\omega\right), \tag{5.12}$$

$$\beta(\omega) \approx B\left(1 + \frac{B'}{B}\Delta\omega\right), \tag{5.13}$$

with $A = \alpha(\omega_{in})$, $B = \beta(\omega_{in})$, $A' = d\alpha(\omega)/d\omega|_{\omega_{in}}$, $B' = d\beta(\omega)/d\omega|_{\omega_{in}}$, and $\Delta\omega = \omega - \omega_{in}$.

Using Eqs. (5.12) and (5.13) we can write Eq. (5.11a) and (5.11b) as:

$$C_\psi(\omega_1, \omega_2) \approx (A^2 + B^2)[1 + (\Delta\omega_1 + \Delta\omega_2)(F_\psi + i\tau_\psi)], \tag{5.14}$$

$$C_\chi(\omega_1, \omega_2) \approx 2AB[1 + (\Delta\omega_1 + \Delta\omega_2)(F_\chi + i\tau_\chi)], \tag{5.15}$$

with

$$F_\psi = \frac{1}{|A|^4+|B|^4+2|A|^2|B|^2\cos(2\delta)}\left\{\left(\frac{|A|'}{|A|}|A|^4+\frac{|B|'}{|B|}|B|^4\right)+ |A|^2|B|^2\left[\cos(2\delta)\left(\frac{|A|'}{A}+\frac{|B|'}{B}\right)+\sin(2\delta)(\arg\{A\}'-\arg\{B\}')\right]\right\}, \tag{5.16}$$

$$\tau_\psi = \frac{1}{|A|^4+|B|^4+2|A|^2|B|^2\cos(2\delta)}\left\{\arg\{A\}'|A|^4+\arg\{B\}'|B|^4+ |A|^2|B|^2\left[\cos(2\delta)\left(\arg\{A\}'+\arg\{B\}'\right)+\sin(2\delta)\left(\frac{|B|'}{|B|}-\frac{|A|'}{|A|}\right)\right]\right\}, \tag{5.17}$$

$$F_\chi = \frac{1}{2}\left(\frac{|A|'}{|A|}+\frac{|B|'}{|B|}\right), \tag{5.18}$$

$$\tau_\chi = \frac{1}{2}\left(\arg\{A\}'+\arg\{B\}'\right). \tag{5.19}$$

In Eqs. (5.16)-(5.19) we have introduced $\arg\{A\}' = d\arg\{\alpha(\omega)\}/d\omega|_{\omega_{in}}$, $\arg\{B\}' = d\arg\{\beta(\omega)\}/d\omega|_{\omega_{in}}$, $\delta = \arg\{B\} - \arg\{A\}$, $|A|' = d|\alpha(\omega)|/d\omega|_{\omega_{in}}$, and $|B|' = d|\beta(\omega)|/d\omega|_{\omega_{in}}$. We further make the approximation $1 + x\Delta\omega \approx e^{x\Delta\omega}$ in Eqs. (5.14) and (5.15), which gives

$$C_\psi(\omega_1,\omega_2) \approx (A^2+B^2)\exp\left[(\Delta\omega_1+\Delta\omega_2)(F_\psi+i\tau_\psi)\right], \tag{5.20}$$

$$C_\chi(\omega_1,\omega_2) \approx 2AB\exp\left[(\Delta\omega_1+\Delta\omega_2)(F_\chi+i\tau_\chi)\right]. \tag{5.21}$$

Then, the $\phi(\omega_1,\omega_2)C_\psi(\omega_1,\omega_2)$ and $\phi(\omega_1,\omega_2)C_\chi(\omega_1,\omega_2)$ functions (Eq. (5.10)) result in:

$$\phi(\omega_1,\omega_2)C_\psi(\omega_1,\omega_2) \approx \approx A_\psi\exp\left[-\frac{[\omega_1-(\omega_{\text{in}}+\sigma^2F_\Psi)]^2}{2\sigma^2}+i\omega_1\tau_\psi\right]\exp\left[-\frac{[\omega_2-(\omega_{\text{in}}+\sigma^2F_\Psi)]^2}{2\sigma^2}+i\omega_2\tau_\psi\right], \tag{5.22}$$

$$\phi(\omega_1,\omega_2)C_\chi(\omega_1,\omega_2) \approx \approx A_\chi\exp\left[-\frac{[\omega_1-(\omega_{\text{in}}+\sigma^2F_\chi)]^2}{2\sigma^2}+i\omega_1\tau_\chi\right]\exp\left[-\frac{[\omega_2-(\omega_{\text{in}}+\sigma^2F_\chi)]^2}{2\sigma^2}+i\omega_2\tau_\chi\right]. \tag{5.23}$$

Note that A_Ψ, F_Ψ, τ_Ψ, A_χ, F_χ, and τ_χ depend only on the classical response of the system evaluated at the central frequency of the incident pulse, ω_{in}.

Equations (5.22) and (5.23) show that the output two-photon modes can be represented as two distinct two-photon pulses. Each two-photon pulse can be factorized as two Gaussian pulses, one for each photon. However, the pulses

associated with the $|\psi_+^o(\omega_1,\omega_2)\rangle$ and $|\chi_+^o(\omega_1,\omega_2)\rangle$ states have different properties. The pulse in Eq. (5.22) has an amplitude A_ψ, a common central frequency for both photons ($\omega_{\text{in}}+\sigma^2 F_\psi$), and a central time τ_ψ (identified from the $i\omega_1\tau_\psi$ and $i\omega_2\tau_\psi$ terms in Eq. (5.22)). Similarly, the pulse in Eq. (5.23) has an amplitude A_χ, a central frequency ($\omega_{\text{in}}+\sigma^2 F_\chi$), and a central time τ_χ. This implies that after the interaction with the nanostructure, the resulting quantum state is a superposition of two different quantum states with different time-frequency properties. As we show next, the loss of purity in the output state can be attributed to the time delay and frequency shift between the output pulses.

Analytical expression of the loss of purity

Using Eqs. (5.5), (5.10), (5.22), and (5.23) we obtain an analytical expression for the purity of the output state in the quasi-monochromatic approximation,

$$\mathcal{L}_o = \frac{2|A_\Psi|^2|A_\chi|^2 e^{\sigma^2(F_\chi^2+F_\Psi^2)}}{(|A_\Psi|^2 e^{2\sigma^2 F_\Psi^2}+|A_\chi|^2 e^{2\sigma^2 F_\chi^2})^2}[e^{\sigma^2\Delta F^2}-e^{-\sigma^2\Delta\tau^2}], \tag{5.24}$$

with $\Delta F = F_\Psi - F_\chi$ and $\Delta\tau = \tau_\Psi - \tau_\chi$. This equation indicates that the output state is pure under any of the following conditions:

- If $\sigma = 0$, corresponding to a purely monochromatic incident state. In this case, the output state is pure and consists of a superposition of two different states with amplitudes A_Ψ and A_χ (Eqs. (5.10)-(5.23)).
- If $\beta(\omega_{\text{in}}) = 0$, corresponding to the condition of helicity preservation [27]. In this case, the output state becomes a frequency superposition of only $|\psi_+^o(\omega_1,\omega_2)\rangle$ states.
- If $\alpha(\omega_{\text{in}}) = 0$, corresponding to the condition of total conversion of helicity [27]. In this case, the output state also becomes a frequency superposition of only $|\psi_+^o(\omega_1,\omega_2)\rangle$ states.
- If $\alpha(\omega_{\text{in}}) = \pm\beta(\omega_{\text{in}})$, corresponding to the situation where the incident light only excites either magnetic or electric modes of the nanostructure [27,29,197]. In this case, the output state is a superposition of output $|\psi_+^o(\omega_1,\omega_2)\rangle$ and $|\chi_+^o(\omega_1,\omega_2)\rangle$ states with the same amplitude, and the time delays and frequency shifts between the output pulses become zero ($\Delta\tau = 0$ and $\Delta F = 0$). This situation is discussed in more detail at the end of section 5.4.2.
- If $\alpha(\omega)$ and $\beta(\omega)$ are almost constant in a spectral range given by σ. From Eqs. (5.16)-(5.19) we find that this case leads to $\Delta F \approx 0$ and $\Delta\tau \approx 0$.

From the conditions above, we can expect a substantial loss of purity if an incident non-monochromatic pulse ($\sigma \neq 0$) excites both electric and magnetic resonances of the nanostructure (thus, $\alpha(\omega_{\text{in}}) \neq \pm\beta(\omega_{\text{in}}) \neq 0$), while $\alpha(\omega)$ and $\beta(\omega)$ change abruptly near the illumination frequency.

5.3.3 Other excitation states

So far, we considered the loss of purity when the incident state is $|\Psi_+^i\rangle$ (Eq. (5.3)). Next, we consider the other input states that are frequency suppositions of the rest of the elements of the basis. First we consider the state

$$|X_-^i\rangle = \iint d\omega_1 d\omega_2 \phi(\omega_1,\omega_2)\,|\chi_-^i(\omega_1,\omega_2)\rangle\,, \tag{5.25}$$

with $|\chi_-^i(\omega_1,\omega_2)\rangle = \frac{1}{2}[\hat{a}_i^\dagger(\omega_1)\hat{b}_i^\dagger(\omega_2) - \hat{b}_i^\dagger(\omega_1)\hat{a}_i^\dagger(\omega_2)]\,|0\rangle$ (Eq. (5.1b)).

In this chapter, we consider that the two-photon spectral amplitude is symmetric, *i.e.* it does not change under the permutation of the arguments $\phi(\omega_1,\omega_2) = \phi(\omega_2,\omega_1)$. On the other hand, the state $|\chi_-^i(\omega_1,\omega_2)\rangle$ is antisymmetric under permutation of the frequencies. Thus, the incident state, $|X_-^i\rangle$, becomes zero,

$$|X_-^i\rangle = \iint d\omega_1 d\omega_2 \phi(\omega_1,\omega_2)\frac{1}{2}[\hat{a}_i^\dagger(\omega_1)\hat{b}_i^\dagger(\omega_2) - \hat{b}_i^\dagger(\omega_1)\hat{a}_i^\dagger(\omega_2)]\,|0\rangle = 0, \tag{5.26}$$

which means that this state cannot be generated, and, hence, there is no output state for this case.

Next, we consider the state

$$|\Psi_-^i\rangle = \iint d\omega_1 d\omega_2 \phi(\omega_1,\omega_2)\,|\psi_-^i(\omega_1,\omega_2)\rangle\,, \tag{5.27}$$

with $|\psi_-^i(\omega_1,\omega_2)\rangle = \frac{1}{2}[\hat{a}_i^\dagger(\omega_1)\hat{a}_i^\dagger(\omega_2) - \hat{b}_i^\dagger(\omega_1)\hat{b}_i^\dagger(\omega_2)]\,|0\rangle$ (Eq. (5.1a)). To obtain the output state, we proceed in the same manner as in section 5.3.2 by using the transformation given in Eq. (5.8),

$$|\Psi_-^o\rangle = \iint d\omega_1 d\omega_2 \phi(\omega_1,\omega_2)\left\{[\alpha(\omega_1)\alpha(\omega_2) - \beta(\omega_1)\beta(\omega_2)]\,|\psi_-^o(\omega_1,\omega_2)\rangle + \right.$$
$$\left. + [\alpha(\omega_1)\beta(\omega_2) + \beta(\omega_1)\alpha(\omega_2)]\,|\chi_-^o(\omega_1,\omega_2)\rangle\right\}. \tag{5.28}$$

Due to the use of indistinguishable photons ($\phi(\omega_1,\omega_2) = \phi(\omega_2,\omega_1)$), $\iint d\omega_1 d\omega_2 \phi(\omega_1,\omega_2)[\alpha(\omega_1)\beta(\omega_2) + \beta(\omega_1)\alpha(\omega_2)]\,|\chi_-^o(\omega_1,\omega_2)\rangle = 0$ (similar to Eq. (5.26)), and the only contribution to $|\Psi_-^o\rangle$ are the $|\psi_-^o(\omega_1,\omega_2)\rangle$ states,

$$|\Psi_-^o\rangle = \iint d\omega_1 d\omega_2 \phi(\omega_1,\omega_2)[\alpha(\omega_1)\alpha(\omega_2) - \beta(\omega_1)\beta(\omega_2)]\,|\psi_-^o(\omega_1,\omega_2)\rangle\,. \tag{5.29}$$

Thus, the output detected density matrix of this state (Eq. (5.5)) has only one element and it is pure. This result could also have been expected from the mirror and cylindrical symmetries of this particular state and of the nanostructure, as discussed in references [20, 191].

Last, we consider the incident state

$$|X_+^i\rangle = \iint d\omega_1 d\omega_2 \phi(\omega_1,\omega_2)\,|\chi_+^i(\omega_1,\omega_2)\rangle\,, \tag{5.30}$$

with $|\chi_+^i(\omega_1,\omega_2)\rangle = \frac{1}{2}[\hat{a}_i^\dagger(\omega_1)\hat{b}_i^\dagger(\omega_2) + \hat{b}_i^\dagger(\omega_1)\hat{a}_i^\dagger(\omega_2)]\,|0\rangle$ (Eq. (5.1b)). Again, we proceed as in section 5.3.2 and obtain the output state,

$$\begin{aligned}|X_+^o\rangle = \iint d\omega_1 d\omega_2 \phi(\omega_1,\omega_2)\Big\{&[\alpha(\omega_1)\alpha(\omega_2)+\beta(\omega_1)\beta(\omega_2)]\,|\chi_+^o(\omega_1,\omega_2)\rangle + \\ &+[\alpha(\omega_1)\beta(\omega_2)+\beta(\omega_1)\alpha(\omega_2)]\,|\psi_+^o(\omega_1,\omega_2)\rangle\Big\} = \\ = \big[C_\psi(\omega_1,\omega_2)\,|\chi_+^o(\omega_1,\omega_2)\rangle &+ C_\chi(\omega_1,\omega_2)\,|\psi_+^o(\omega_1,\omega_2)\rangle\big]\,,\end{aligned} \tag{5.31}$$

which is the same result obtained for the output state $|\Psi_+^o\rangle$ (Eq. (5.10)) except that the coefficients $C_\psi(\omega_1,\omega_2)$ and $C_\chi(\omega_1,\omega_2)$ of the states $|\chi_+^o(\omega_1,\omega_2)\rangle$ and $|\psi_+^o(\omega_1,\omega_2)\rangle$ are interchanged. By applying Eq. (5.5) we arrive to a similar output post-selected density matrix to that of the $|\Psi_+^o\rangle$ state, but with interchanged elements, *i.e.*, the $\hat{\varrho}^o_{\psi_+,\psi_+}$, $\hat{\varrho}^o_{\chi_+,\chi_+}$, $\hat{\varrho}^o_{\psi_+,\chi_+}$, and $\hat{\varrho}^o_{\chi_+,\psi_+}$ density matrix elements of the output state $|\Psi_+^o\rangle$ are equal to the $\hat{\varrho}^o_{\chi_+,\chi_+}$, $\hat{\varrho}^o_{\psi_+,\psi_+}$, $\hat{\varrho}^o_{\chi_+,\psi_+}$, and $\hat{\varrho}^o_{\psi_+,\chi_+}$ elements of the output state $|X_+^o\rangle$, respectively. These changes do not affect the loss of purity, and thus, the output post-selected density matrix obtained for $|X_+^o\rangle$ has the same purity as the density matrix obtained for $|\Psi_+^o\rangle$.

5.4 Loss of purity due to the scattering by a silicon spherical nanoparticle

In this section we study the loss of purity of the quantum state $|\Psi_+^i\rangle$ (Eq. (5.3)) when scattered by a silicon spherical nanoparticle of radius $R = 250$ nm in vacuum (the permittivity of silicon is obtained from reference [48]). We chose this particular nanoparticle as a study case, since dielectric nanoparticles show substantially smaller intrinsic losses than their plasmonic counterparts, making them especially suitable for the manipulation of quantum states of light.

To analyze the loss of purity in this scenario we first obtain, in subsection 5.4.1, the helicity-splitting coefficients that define the quantum transformation (Eq. (5.8)) of the silicon spherical nanoparticle to states of light with a specific angular momentum and polarization. In subsection 5.4.2, we use these coefficients to calculate the output state of the interaction of an incident $|\Psi_+^i\rangle$ state with the nanoparticle, and we find that the output scattered state loses its quantum purity. We then proceed to analyze this loss of purity at the end of the same subsection.

5.4.1 Classical response: helicity-splitting coefficients

As we discuss in section 5.3, the helicity-splitting coefficients determining the transformation of quantum states can be obtained from classical calculations of

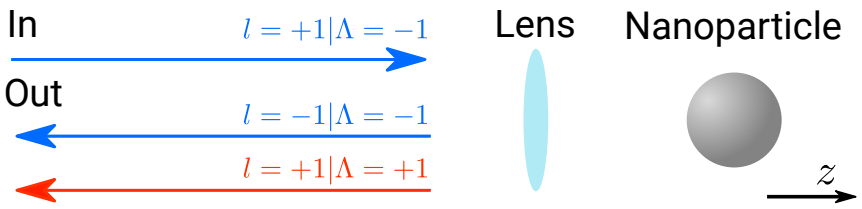

Figure 5.4: Scheme of the classical scattering by a silicon spherical nanoparticle. A Laguerre-Gauss beam with $m = 0$, $\Lambda = -1$ ($l = +1$), and width $w_0 = 0.5$ mm propagates along the positive z-axis towards a $R = 250$ nm silicon [48] spherical nanoparticle situated in a vacuum. The incident beam is focused on the center of the nanoparticle with a high numerical aperture lens ($NA = 0.9$) and focal length $f = 1$mm. The light backscattered by the nanoparticle is collimated with the same lens and separated into the two different helicities $\Lambda = +1$ and $\Lambda = -1$.

the fields scattered by the nanoparticle. In particular, here we obtain the fields scattered by the nanoparticle using Mie theory formalism as introduced in section 1.4.3. We consider incident illumination close to that in experimental configurations: a circularly right polarized Laguerre-Gauss LG_0^1 mode (Eq. (1.73)) with spatial width $w_0 = 0.5$ mm focused at the center of the nanoparticle by a high numerical aperture lens ($NA = 0.9$) with focal length $f = 1$ mm (see scheme in Fig. 5.4). The incident Laguerre-Gauss beam has a well-defined orbital angular momentum and spin, with $l = +1$ and $s = -1$, respectively. This is due to the paraxial nature of the beam, as discussed in subsection 1.4.1. Thus, this incident beam corresponds to $\boldsymbol{E}^i_{-1}$ in the notation introduced in Eq. (5.7), *i.e.*, the electric field for an incident beam with $m = 0$ and $\Lambda = -1$. Figure 5.5 (left panel) shows the spatial distribution of the phase and intensity of the input beam at the aperture of the lens for an incident monochromatic illumination of wavelength $\lambda = 1000$ nm.

The lens used to focus the incident beam also collects the backscattered light, corresponding to $\boldsymbol{E}^{\text{sca}}_{-1}$ in Eq. (5.7), *i.e.*, the fields scattered by the nanoparticle under $\boldsymbol{E}^i_{-1}$ illumination. Figure 5.5 (right panel) shows the spatial field distribution of $\boldsymbol{E}^{\text{sca}}_{-1}$ after being collimated by the lens and after being separated into its two helicity contributions, one with $\Lambda = +1$ and another with $\Lambda = -1$ (scheme in Fig. 5.4). Since the output collimated beams are paraxial, we can determine the spin and orbital angular momentum for each helicity contribution of $\boldsymbol{E}^{\text{sca}}_{-1}$. Specifically, we find that $s = -1$ and $l = +1$ for the $\Lambda = +1$ and $m = 0$ contribution, and $s = +1$ and $l = -1$ for the $\Lambda = -1$ and $m = 0$ contribution. Note that the spin and helicity have opposite signs for the backscattered field, as it propagates along the negative z-direction.

To obtain the helicity splitting coefficients, we use Eq. (5.7). In this equation the α_{-1} and β_{-1} coefficients are obtained by projecting $\boldsymbol{E}^{\text{sca}}_{-1}$ onto the output modes $\boldsymbol{E}^o_{+1}$ and $\boldsymbol{E}^o_{-1}$, corresponding to electromagnetic modes with $m = 0$ and $\Lambda = -1$, and $m = 0$, $\Lambda = +1$, respectively. Here we consider the simple situation where $\boldsymbol{E}^o_{+1}$ ($\boldsymbol{E}^o_{-1}$) correspond to a Laguerre-Gauss LG_0^1 (LG_0^{-1}), same as for the input beam, but in this case the output Laguerre-Gauss modes propagate towards the negative z-direction. Because the Laguerre-Gauss output modes are paraxial, we

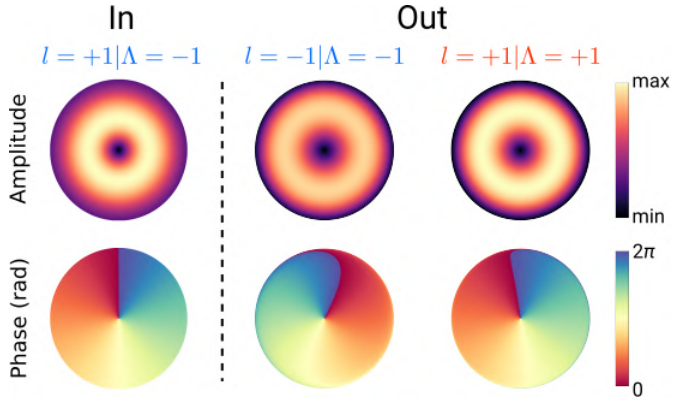

Figure 5.5: Spatial distribution of the amplitude (left column) and phase (right column) of the input and output electric fields for illumination wavelength $\lambda = 1000$ nm. The studied system consists of a silicon spherical nanoparticle of radius $R = 250$ nm illuminated by a focused $l = +1$, $m = 0$ Laguerre-Gauss beam as indicated in the caption of Fig. 5.4. The input and output fields are both plotted in the same plane of the aperture of the lens. The input electric field (first row) is normalized to its maximum value. The output beam (second and third row) is decomposed into the two different contributions with different helicities, as indicated in the figure. The amplitude of both output contributions is normalized to the maximum of the output field with helicity $\Lambda = +1$.

can assign the helicity directly to the spin and, thus, to circular polarization: the $\Lambda = +1$ beam has $s = -1$ corresponding to a circular right polarization vector $\boldsymbol{v}_-$ (Eq. (1.79)) and $\Lambda = -1$ has $s = +1$ corresponding to a circular left polarization vector $\boldsymbol{v}_+$ (Eq. (1.78)). Note that because these output fields propagate along the negative z-direction, the helicity and spin have opposite signs. Finally, using Eq. (5.7) we can directly obtain the helicity-splitting coefficients:

$$\alpha_{-1}(\omega) = \iint_{\mathcal{A}} d\mathcal{A}[LG_0^{-1}(\boldsymbol{r})\boldsymbol{v}_- e^{-i\omega t}]^* \cdot \boldsymbol{E}_{-1}^{\text{sca}},$$
$$\beta_{-1}(\omega) = \iint_{\mathcal{A}} d\mathcal{A}[LG_0^{+1}(\boldsymbol{r})\boldsymbol{v}_+ e^{-i\omega t}]^* \cdot \boldsymbol{E}_{-1}^{\text{sca}}. \tag{5.32}$$

The integrating area $\mathcal{A}$ in Eq. (5.32) corresponds to the surface of the aperture of the lens (same area of the fields shown in Fig. 5.5).

In a similar manner, we can calculate α_{+1} and β_{+1}, for the fields scattered by the nanoparticle when illuminated with $m = 0$, $\Lambda = +1$, Laguerre-Gauss mode LG_0^{-1}. We have verified that for this case, we obtain $\alpha_{+1} = \alpha_{-1} = \alpha$ and $\beta_{+1} = \beta_{-1} = \beta$, and thus, we can use the simple transformation introduced in Eq. (5.8).

We show in Fig. 5.6a-b the amplitude and phase spectra of α (blue line) and β (orange line), obtained by evaluating Eq. (5.32) for different wavelengths $\lambda \in [975, 1150]$ nm. Figure 5.6a shows that the spectra of the amplitudes $|\alpha(\omega)|$ (blue line) and $|\beta(\omega)|$ (orange line) exhibit two clear peaks: a relatively broad

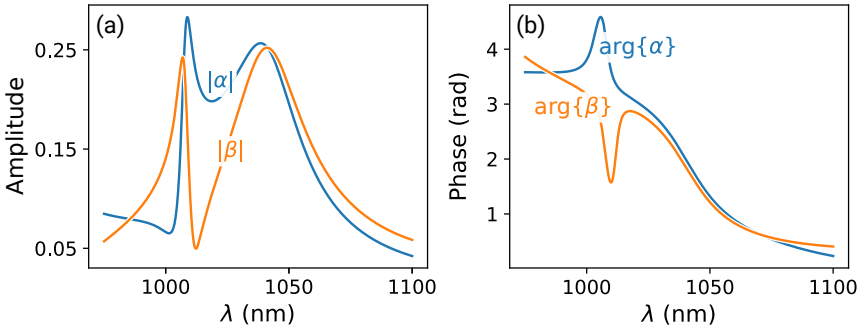

Figure 5.6: (a) Amplitude and (b) phase of the helicity-splitting coefficients α (blue line) and β (orange line) that are obtained from the classical scattering calculation, as a function of wavelength λ. The coefficients are obtained for a silicon spherical nanoparticle of radius $R = 250$ nm illuminated by a focused $l = +1$, $m = 0$ Laguerre-Gauss beam as indicated in the caption of Fig. 5.4.

maxima centered at $\lambda \approx 1040$ nm and a sharp peak centered at $\lambda \approx 1000$ nm. In the proximity of these two peaks the phase of the coefficients ($\arg\{\alpha(\omega)\}$ and $\arg\{\beta(\omega)\}$) varies rapidly, particularly near the sharp peak (Fig. 5.6b).

Analysis of the contributions of the differents resonances of the nanoparticle to the helicity-splitting coefficients

We next analyze the nature of the peaks of $|\alpha(\omega)|$ and $|\beta(\omega)|$ in Fig. 5.6a by using Mie theory. To that end, we show in Fig. 5.7 (black line) the classical scattering cross-section spectrum σ_{Sca} of the $R = 250$ nm silicon spherical nanoparticle under the illumination of the focused $l = +1$, $m = 0$ Laguerre-Gauss beam. σ_{sca} presents again two clear peaks, a broad one centered at $\lambda \approx 1040$ nm and a narrow peak centered at $\lambda \approx 1010$ nm. The spectral position of the maximum of these two peaks is very close to the maximum of the two peaks of the $|\alpha(\omega)|$ and $|\beta(\omega)|$ helicity-splitting coefficients (shown in Fig. 5.6a), which indicates that the peaks of the helicity-splitting coefficients are due to the excitation of the resonances of the nanoparticles. To analyze which resonances are excited at these spectral positions, we decompose σ_{sca} as a sum of the contributions of each multipole (see section 1.3.2) [67]:

$$\sigma_{\text{sca}} = \frac{2\pi}{k^2} \sum_{n=0}^{\infty} |C_n(\omega)|^2 \left(|a_n(\omega)|^2 + |b_n(\omega)|^2 \right), \tag{5.33}$$

where C_n is given by Eq. (1.95) and a_n and b_n (in Eqs. (1.62a) and (1.62b), respectively) are the scattering coefficients of the electric and magnetic multipoles, respectively.

In Fig. 5.7, we plot the two contributions given by the scattering coefficients a_2 (dashed blue line) and b_3 (dashed orange line) in Eq. (5.33). The broad peak

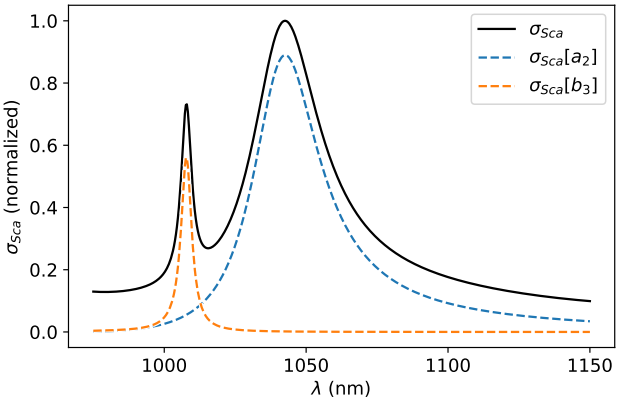

Figure 5.7: Different contributions to the cross section of the silicon [48] spherical nanoparticle of radius $R = 250$ nm studied in section 5.4. The nanoparticle is illuminated by a Laguerre-Gauss beam with $l = 1$, $s = -1$, and width $w_0 = 0.5$ mm that is focused at the center of the spherical nanoparticle by a lens of $NA = 0.9$ and $f = 1$ mm. The solid black line corresponds to the total scattering cross section of the system σ_{sca} and the dashed lines to the two main contributions to σ_{sca}, due to the electric quadrupolar ($\sigma_{\text{sca}}[a_2]$ proportional to $|a_2(\omega)|^2$ in Eq. (5.33), dashed blue line) and the magnetic octopolar ($\sigma_{\text{sca}}[b_3](\omega)$ proportional to $|b_3(\omega)|^2$ in Eq. (5.33), dashed orange line) modes of the nanoparticle.

centered at $\lambda \approx 1040$ nm is due to the term proportional to $|a_2|^2$ in Eq. (5.33), which indicates that this peak results from the excitation of an electric quadrupolar resonance in the nanoparticle [40]. The term proportional to $|b_3|^2$ is behind the narrow peak centered at $\lambda \approx 1010$ nm and corresponds to the excitation of an octopolar magnetic resonance [40].

5.4.2 Quantum response: Analysis of the purity of the scattered state

With the results of $\alpha(\omega)$ and $\beta(\omega)$ shown in Fig. 5.6a-b we can now calculate the post-selected output density matrix $\hat{\varrho}^o$ (using Eqs. (5.5)-(5.11b)) when the silicon spherical nanoparticle is illuminated by the focused entangled input state $|\Psi_+^i\rangle$. The input state in this case is a two-photon Gaussian pulse with a bandwidth of $\sigma = 3$ THz (the same bandwidth is considered in the results in this chapter). Figures 5.8a and b show the output post-selected density matrix, using illumination at central wavelength $\lambda_{\text{in}} = 1003$ nm (hitting one nanoparticle resonance) and $\lambda_{\text{in}} = 1025$ nm (in between nanoparticle resonances), respectively. This figure shows that the output scattered states are different depending on the wavelength of the illumination. This is due to changes in the helicity-splitting coefficients in this range of wavelengths. Furthermore, the output state is pure ($\mathcal{L}_o = 0$) when illuminated at $\lambda_{\text{in}} = 1025$ nm, but there is a loss of quantum purity ($\mathcal{L}_o \approx 0.5 > 0$) when illuminated at $\lambda_{\text{in}} = 1003$ nm, as indicated in the figure.

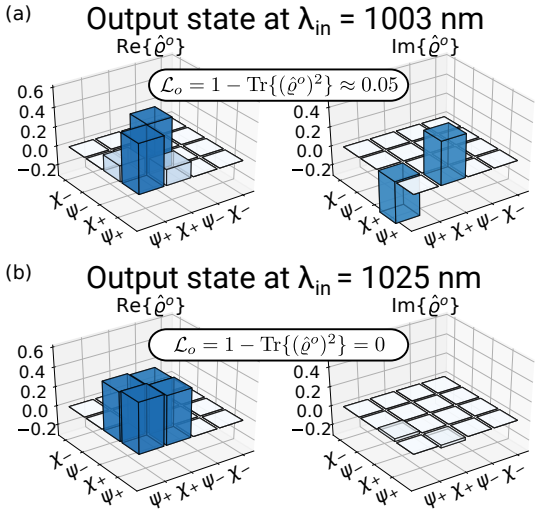

Figure 5.8: Real (left) and imaginary (right) components of $\hat{\varrho}^o$, the post-selected density matrix of the output state $|\Psi_+^o\rangle$ that results from the scattering of the incident input state $|\Psi_+^i\rangle$ in Fig. 5.1 with a silicon spherical nanoparticle of radius $R = 250$ nm (more details of the system in the caption of Fig. 5.4). Panels (a) and (b) correspond to $\hat{\varrho}^o$ calculated for an incident state pulsed at central wavelength $\lambda_{\mathrm{in}} = 1003$ nm and $\lambda = 1025$ nm respectively. We indicate the loss of purity $\mathcal{L}_o$ for each illumination, where $\mathcal{L}_o \approx 0.05 > 0$ in panel (a) indicates that the output state for $\lambda_{\mathrm{in}} = 1003$ nm is not pure, and $\mathcal{L}_o = 0$ in panel (b) indicates that the output state for $\lambda_{\mathrm{in}} = 1025$ nm is pure.

To further study the loss of quantum purity, we show in Fig. 5.9a (solid black line), $\mathcal{L}_o$, of the output state as a function of the central wavelength of the pulse $\lambda_{\mathrm{in}} = 2\pi c_0/\omega_{\mathrm{in}}$. We find two clear peaks situated at $\lambda_{\mathrm{in}} \approx 1003$ nm and $\lambda_{\mathrm{in}} = 1012$ nm where the purity loss becomes significant ($\mathcal{L}_o \sim 0.1$).

To understand the cause of the loss of purity, we examine the quasi-monochromatic approximation discussed in section 5.3.2. According to this approximation, the output state is a combination of two time-delayed and frequency-shifted states [198]. We show in Fig. 5.9b the spectral dependence of the time delays τ_Ψ (solid blue line) and τ_χ (solid red line), and in Fig. 5.9c we show the corresponding values of the frequency shifts $\sigma^2 F_\Psi$ and $\sigma^2 F_\chi$. The loss of purity can be calculated in the quasi-monochromatic approximation by using Eq. (5.24). Figure 5.9a (green dashed line) shows the result of this calculation. We observe that there is a very good agreement between the results obtained with the approximated expression (green dashed line) and the exact expression of the loss of purity (solid black line). Further, the quasi-monochromatic model provides a clear explanation for the results, as the loss of purity is highest when there is a greater difference in time delays and frequency shifts, as observed in the region of 1000 nm $\lesssim \lambda_{\mathrm{in}} \lesssim$ 1020 nm of Figs. 5.9a-c.

Following the equations of the frequency shift and time delays between the

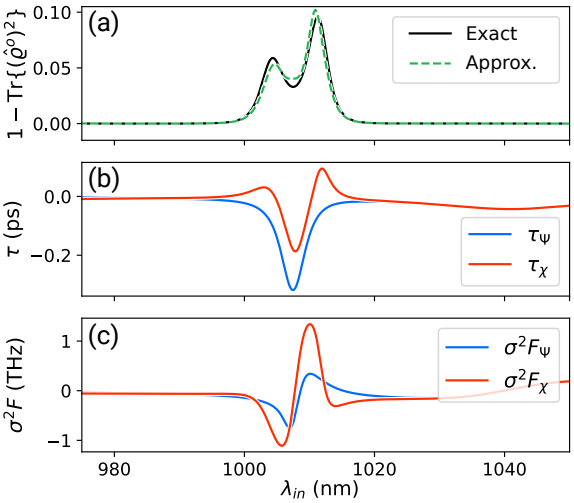

Figure 5.9: Analysis of the purity loss for a focused incident $|\Psi_+^i\rangle$ state interacting with a $R = 250$ nm silicon [48] spherical nanoparticle in vacuum. (a) Spectrum of the purity loss $1 - \mathrm{Tr}\{(\hat{\varrho}^o)^2\}$. The solid black line corresponds to the purity loss of the numerically calculated density matrix (Eq. (5.5)) of the output state (Eq. (5.10)) and the dashed green line to the result of the approximated Eq. (5.24). (b) Spectrum of the time delay of the two two-photon modes of the total output state according to Eqs. (5.17) and (5.19). The solid blue line corresponds to τ_Ψ and the solid red line to τ_χ. (c) Spectrum of the frequency-shift of the two two-photon modes of the total output state according to Eqs. (5.16) and (5.18). The solid blue line corresponds to $\sigma^2 F_\Psi$ and the solid red line to $\sigma^2 F_\chi$.

output pulse (Eq. (5.16)-(5.19)), we can note that the differences in frequency shifts and time delays maximize in the spectral region where the variations of $|\alpha(\omega)|-|\beta(\omega)|$ and $\arg\{\alpha(\omega)\}-\arg\{\beta(\omega)\}$ are pronounced within the spectral width of the incident pulse. Indeed, by inspecting the helicity-splitting coefficients in Figs. 5.6a-b we can observe that the spectral region where these differences between the helicity-splitting coefficients are largest corresponds to 1000 nm $\lesssim \lambda_{\mathrm{in}} \lesssim$ 1020 nm, where the loss of purity is maximized.

Influence of the magnetic and electric resonances on the loss of purity

In section 5.3.2 we discuss that an abrupt spectral variation of $(|\alpha(\omega)| - |\beta(\omega)|)$ and of $\arg\{\alpha(\omega)\} - \arg\{\beta(\omega)\}$ can cause the loss of purity of the output state. Interestingly, we can track down such fast spectral variation to the simultaneous excitation of both magnetic octopole and electric quadrupole resonances of the nanoparticle, clearly pointing out towards the influence of the optical resonances of the nanostructure in the loss of purity. In fact, we show next that the loss of purity only occurs when the nanoparticle supports both electric and magnetic resonances.

A nanoparticle that only supports magnetic resonances satisfies $a_n = 0$ for all n in Eqs. (1.97) and (1.98). In this case, a detailed analysis of the fields

scattered by the nanoparticle when illuminated by beams with well-defined angular momentum (section 1.4.3) leads to $\alpha(\omega) = -\beta(\omega)$ [27, 40, 67]. On the other hand, if a nanoparticle only supports electric resonances, then $b_n = 0$ for all n in Eqs. (1.97) and (1.98), and in this case we obtain $\alpha(\omega) = \beta(\omega)$. From the intuitive quasi-monochromatic picture introduced in section 5.3.2, $\alpha(\omega) = \pm\beta(\omega)$ constitute two special cases, both leading to $\tau_\psi = \tau_\chi$ and $F_\psi = F_\chi$ in Eqs. (5.16)-(5.19), *i.e.*, there is no time delay nor frequency shift between the output pulses, and thus, the loss of purity in Eq. (5.24) becomes zero.

Beyond the quasi-monochromatic approximation, we also obtain that the output state is always pure for $\alpha(\omega) = \pm\beta(\omega)$. Using Eqs. (5.10)-(5.11b), we obtain the output state in these cases,

$$|\Psi^o_+[\alpha = \pm\beta]\rangle = \iint d\omega_1 d\omega_2 \phi(\omega_1, \omega_2) \left[2\alpha(\omega_1)\alpha(\omega_2)\right] \left[|\psi^o_+(\omega_1, \omega_2)\rangle \pm |\chi^o_+(\omega_1, \omega_2)\rangle\right] \tag{5.34}$$

In this expression, $|\psi^o_+(\omega_1, \omega_2)\rangle$ and $|\chi^o_+(\omega_1, \omega_2)\rangle$ are multiplied by the same spectral function $\phi(\omega_1, \omega_2)[2\alpha(\omega_1)\alpha(\omega_2)]$. This shared weighting function causes the detected output state to be pure, as directly proved by inserting Eq. (5.34) in Eq. (5.5). We obtain an output detected density matrix with only four non-zero terms, $\hat{\varrho}^o_{\psi_+,\psi_+} = \hat{\varrho}^o_{\chi_+,\chi_+} = 1/2$, $\hat{\varrho}^o_{\psi_+,\chi_+} = \hat{\varrho}^o_{\chi_+,\psi_+} = \pm 1/2$, which is an idempotent matrix, (*i.e.*, $(\hat{\varrho}^o)^n = \hat{\varrho}^o$), corresponding to a pure state, $\mathrm{Tr}\{(\hat{\varrho}^o)^2\} = 1 \rightarrow \mathcal{L}_o = 0$. Thus, the loss of purity can be attributed to the simultaneous excitation of electric and magnetic resonances of the nanoparticle.

5.5 Conclusions

In summary, in this chapter we provide a framework to treat the quantum scattering of a two-photon state in modes of well-defined angular momentum and helicity interacting with a rotationally symmetric nanostructure. We find that the interaction of entangled photons with nanostructures can produce a loss of purity of the incident state, even when the nanostructure is smaller than the wavelength of the incident field. We apply our framework to analyze the loss of purity in a realistic scenario, a silicon spherical nanoparticle illuminated by a focused two-photon state generated by, for example, a SPDC process where the two photons are indistinguishable. Further, we developed a simple physical picture that explains the loss of quantum purity as a consequence of time delay and frequency shift between the two-photon modes of the output state. Importantly, these frequency shifts and time delays can be traced back to the spectral width of the incident pulsed states and the excitation of different optical resonances of the nanoparticle.

Our framework and findings can be extended to treat the scattering of quantum states by other nanostructures. This can be useful in either preventing the loss of purity in quantum information applications handled at the nanoscale or utilizing the loss of purity as a tool for characterizing the properties of the nanostructure.

CONCLUSIONS AND OUTLOOK

This thesis explores the scattering of classical and quantum states of light by nanostructures. Chapters 1 and 2 discuss the fundamentals of classical and quantum electrodynamics, which are essential for understanding how nanostructures and quantum emitters, such as molecules or quantum dots, respond to light. Chapters 3 and 4 concentrate on one of the core aspects of this thesis, the resonant interaction between a quantum emitter (QE) and a nanostructure under classical illumination. In chapter 3, we consider the extinction spectrum of a QE weakly coupled to a nanostructure, a situation that can be analyzed within a classical framework. In contrast, in chapter 4, we analyze the statistics of the light emitted by a QE-nanostructure in different conditions, including very strong interaction strength, which requires a quantum description of the response of the hybrid system. On the other hand, chapter 5 considers the possibility of illuminating the nanostructure with quantum states of light and explores the preservation or loss of purity in such a scattering process. The main results from chapters 3-5 and some potential directions for future research along three lines are summarized below:

- In chapter 3, we use classical electromagnetism to analyze the asymmetry on the Fano lineshape that appears in the extinction spectrum of a metallic nanostructure interacting weakly with a QE. In particular, we explain the origin of the asymmetry that arises when the plasmonic mode of the nanostructure is in resonance with the exciton of the QE. Such asymmetry is not expected in these resonant conditions, but it has been experimentally shown in recent work. We used numerical simulations, analytical expressions, and simple models to determine the causes of this asymmetry. We found that the asymmetry is mostly caused by two effects: (i) the phase acquired due to the propagation of the fields induced by the nanostructure on the QE and vice-versa, and (ii) the direct excitation of the QE by the incident field exciting the system together with the direct emission of the QE to the far-field. We also found that incorporating the radiative damping of the nanostructure is crucial to describe the aforementioned effects accurately. Neglecting this damping can render the models unreliable. On the other hand, our analysis reveals that the contribution of d-electrons of the nanostructure can also impact the asymmetry significantly, particularly for nanostructures that resonate at shorter wavelengths. Last, we find a relatively minor effect on the asymmetry by higher-order modes of the nanostructure. The validity of our

analysis is demonstrated for a single nanoparticle and a dimer nanostructure, indicating the wide-ranging applicability of our study.

- The analysis of the extinction cross-section conducted in chapter 3 is based on the classical electromagnetism framework, which is appropriate to address that situation because the pumping strength of the system and the interaction strength between the QE and the nanostructure were both weak. However, we go beyond these limits in chapter 4, to study quantum effects that we address by using a novel formulation of the quantum Rabi model (QRM). Specifically, we consider a system illuminated incoherently through the QE, and we analyze the changes in the intensity correlation of the emitted light through different pumping strengths and different regimes of interaction between the nanostructure and the QE, namely the so-called weak, strong, and ultra-strong coupling regimes. We find that the light emitted by the system can get strongly bunched in any coupling regime for sufficiently weak pumping due to the direct excitation from the ground state to an excited state that can decay by emitting two or more photons. The bunching in the weak coupling regime is particularly surprising because the Jaynes-Cummings model (JCM, a simplified description based on the rotating-wave approximation, expected to be valid in this coupling regime) predicts antibunched emission for any coupling regime and any illumination strength. Our results thus indicate that the intensity correlations can be a highly sensitive probe to reveal the differences between the JCM and QRM and can serve to identify the breakdown of the rotating wave approximation induced by the occupation number non-conserving terms in the QRM Hamiltonian.

- In chapters 3 and 4, we consider the response of nanophotonics systems illuminated by a classical beam. In contrast, in chapter 5, we consider the response of nanostructures illuminated by quantum states of light. We consider rotationally symmetric nanostructures and illumination states that encode information in the angular momentum properties of two entangled photons. We develop an analytical framework to calculate the output scattered state and find that the quantum purity of the incident state can be lost in the scattering process, which is highly detrimental for quantum information applications. We explain the origin of this loss of quantum purity within a simple physical picture that describes the output state as the superposition of two different pulses. The purity is lost when these two pulses are frequency-shifted or time-delayed, as occurs for a nanostructure that sustains narrow electric and magnetic resonances. The framework and analysis presented in this chapter thus allow for addressing the scattering of quantum light by nanostructures in quite general conditions and gives insights into the loss of quantum purity in nanophotonics.

The results in this thesis offer different possibilities for further studies in classical and quantum nanophotonics. For instance, the analysis of Fano asymmetry in the resonant systems discussed in chapter 3 indicates that the impact of high-order

modes of the nanostructure on the asymmetry is relatively small. However, this study considered an illumination by a plane wave and it would be interesting to investigate the Fano asymmetry when the QE-nanostructure system is excited by a point source, such as the tunneling electrons in a scanning tunneling microscope configuration. In this scenario, the point source is expected to efficiently excite highly-order modes of the nanostructure, thereby potentially increasing the impact of these modes in the asymmetry, as suggested by recent experiments.

The results of chapter 4 indicate that intensity correlations are a sensitive tool for observing phenomena caused by the occupation number non-conserving terms in the interaction Hamiltonian. However, the system considered here is relatively simple, and it would be interesting to explore the robustness of the results in more complex configurations, such as a nanostructure coupled to multiple QEs. Another interesting development would be to study the emission from a nanostructure-QE system when it is illuminated by a laser, which would require introducing a time-dependent term to the Hamiltonian.

Last, the framework introduced in chapter 5 to describe the scattering of quantum states of light can be used to analyze the response of more complex nanostructures as compared to spherical nanoparticles. For example, it would be interesting to study the loss of purity of two-photon states scattered by a nanohole in a gold sheet, as recent experiments found a relatively higher loss in this case. Further, the model can be refined to capture further complexities present in experimental configurations. For example, we consider a symmetric Gaussian pulse to represent the two-photon states generated by spontaneous-parametric-down-conversion (SPDC), however, recent experimental results have found that the photon pulse of a SPDC can present an asymmetric lineshape, which results in a loss of indistinguishability and could ultimately lead to a higher loss of quantum purity after interaction with the nanostructure. Additionally, we assume that the detectors are connected to output modes that have the same characteristics as the input modes (*i.e.* Laguerre-Gauss modes), which requires a complex detection setup. It would be worthwhile investigating other detection setups often used in experiments, such as detectors that couple to modes with a flat intensity profile.

Appendices

Appendix A

Derivation of the two contributions to the Fano asymmetry

In this appendix we separate the analytical expression of the total Fano asymmetry factor q (Eq. (3.35)) into the two contributions, q_{E} and q_{R}, that were introduced in Eq. (3.36) of chapter 3. This appendix builds upon the derivation in Section 3.3.1 and uses the same notation introduced there.

A.1 Derivation of q_{R}

As discussed in chapter 3, the q_{R} contribution corresponds to the asymmetry factor q that is obtained when the direct excitation of the QE by the incident plane wave and the direct emission of the QE to the far field are ignored. This premise changes two key elements of the derivation of the total asymmetry factor q shown in section 3.3. On the one hand, neglecting the direct emission of the QE is equivalent to neglecting the E_x^{E} contribution in Eq. (3.9), so that the forward-scattered electric field induced by the system on a point-like detector placed at $\boldsymbol{r}_{\mathrm{d}}$ is

$$E_{x,\mathrm{R}}^{\mathrm{FF}}(\boldsymbol{r}_{\mathrm{d}},\omega) = E_x^{\mathrm{A}}(\boldsymbol{r}_{\mathrm{d}},\omega) + E_x^{\mathrm{EA}}(\boldsymbol{r}_{\mathrm{d}},\omega), \tag{A.1}$$

where E_x^{A} and E_x^{EA} are still given by Eq. (3.10) and (3.15), respectively, and we have introduced the subindex R to differentiate the terms that are modified in this appendix. On the other hand, when the direct excitation of the QE by the incident plane wave of amplitude E_0 is ignored, the expression of the field $E_{x,\mathrm{R}}^{\mathrm{NF}}$ that excites the QE (Eq. (3.17)) changes to

$$E_{x,\mathrm{R}}^{\mathrm{NF}}(\boldsymbol{r}_{\mathrm{e}},\omega) = E_x^{\mathrm{AE}}(\boldsymbol{r}_{\mathrm{e}},\omega) + E_x^{\mathrm{EAE}}(\boldsymbol{r}_{\mathrm{e}},\omega), \tag{A.2}$$

with E_x^{AE} and E_x^{EAE} given by Eqs. (3.18) and (3.19), respectively.

Using Eqs. (3.18), (3.19), (3.21), and (A.2) we can write $E_{x,\mathrm{R}}^{\mathrm{FF}}$ in Eq. (A.1) as

$$E^{\mathrm{FF}}_{x,\mathrm{R}}(\boldsymbol{r}_\mathrm{d},\omega) = \left[K^{\mathrm{FF}}(\boldsymbol{r}_\mathrm{d},\omega) + S^{\mathrm{FF}}_{x,x}(\boldsymbol{r}_\mathrm{d},\omega)\frac{A_\mathrm{e}K(\boldsymbol{r}_\mathrm{e},\omega)}{\omega_0'(\omega)^2-\omega^2-i\gamma'(\omega)\omega}\right]E_0. \tag{A.3}$$

We obtain the extinction cross-section of the coupled QE-nanoantenna by inserting Eq. (A.3) into (3.8):

$$\sigma_{\mathrm{ext},\ \mathrm{R}}(\omega) = \frac{4\pi}{k^2}\mathrm{Re}\left\{(-ikz_\mathrm{d})e^{-ikz_\mathrm{d}}\left[K^{\mathrm{FF}}(\boldsymbol{r}_\mathrm{d},\omega) + S^{\mathrm{FF}}_{x,x}(\boldsymbol{r}_\mathrm{d},\omega)\frac{A_\mathrm{e}K(\boldsymbol{r}_\mathrm{e},\omega)}{\omega_0'(\omega)^2-\omega^2-i\gamma'(\omega)\omega}\right]\right\}. \tag{A.4}$$

Following the same procedure as in the derivation of the total asymmetry factor $q$in section 3.3.1, and expressing the normalized extinction cross section as a Fano lineshape

$$\frac{\sigma^{(R)}_{\mathrm{ext}}(\omega)}{\sigma^{(0)}_{\mathrm{ext}}} \approx \frac{[\Omega+q_\mathrm{R}]^2+B_\mathrm{R}^2}{\Omega^2+1}, \tag{A.5}$$

where $\Omega = ({\omega_0'}^2-\omega^2)/(\omega\gamma')$, $\omega_0' = \omega_0+\Delta\omega$, $\gamma' = (P_\mathrm{F}+1)\gamma+\gamma_\mathrm{NR}$, and $\sigma^{(0)}_{\mathrm{ext}}$, $\Delta\omega$, and P_F expressed in Eqs. (3.6), (3.7), (3.31a), (3.31b), and (3.31c), respectively.

The zero-dip parameter B_R and the asymmetry factor q_R in Eq. (A.5) are given by

$$B_\mathrm{R} = 1-q_\mathrm{R}^2 - \frac{1}{\frac{k_0^2}{4\pi}\sigma^{(0)}_{\mathrm{ext}}}\frac{A_\mathrm{e}}{\gamma'\omega_0}\mathrm{Im}\left\{(-ik_0z_\mathrm{d})e^{-ik_0z_\mathrm{d}}S^{\mathrm{FF}}_{x,x}(\boldsymbol{r}_\mathrm{d},\omega_0)K(\boldsymbol{r}_\mathrm{e},\omega_0)\right\}, \tag{A.6}$$

$$q_\mathrm{R} = \frac{A_\mathrm{e}}{2\sigma^{(0)}_{\mathrm{ext}}\gamma' c_0\varepsilon_0}\mathrm{Re}\{K(\boldsymbol{r}_\mathrm{e},\omega_0)\}\mathrm{Im}\{K(\boldsymbol{r}_\mathrm{e},\omega_0)\}. \tag{A.7}$$

To obtain Eq. (A.7) we have simplified the expressions of the far-field Green's functions $G^{\mathrm{FF}}_{0_{x,x}}$ and $G^{\mathrm{FF}}_{x,x}$ according to Eqs. (3.14) and (3.34), respectively. The expression of q_R in Eq. (A.7) is the same as the expression of q_R in Eq. (3.36).

A.2 Derivation of q_E

The q_E contribution to the Fano asymmetry factor q describes the additional asymmetry introduced by the direct excitation of the QE by the incident plane wave and by the direct emission of the QE to the far field. Thus, it can be directly obtained by subtracting the contribution q_R in Eq. (A.7) to the total asymmetry factor q given in Eq. (3.35):

$$q_\mathrm{E} = q - q_\mathrm{R} = \frac{A_\mathrm{e}}{\sigma^{(0)}_{\mathrm{ext}}\gamma' c_0\varepsilon_0}\mathrm{Im}\{K(\boldsymbol{r}_\mathrm{e},\omega_0)\}, \tag{A.8}$$

which corresponds to Eq. (3.36).

Furthermore, we show in the following that q_{E} can be separated into two additive contributions q_{E1} and q_{E2} ($q_{\mathrm{E}} = q_{\mathrm{E1}} + q_{\mathrm{E2}}$) that are obtained by introducing separately the direct excitation and the direct emission of the QE, respectively. We also find that both contributions are equal ($q_{\mathrm{E1}} = q_{\mathrm{E2}}$).

To derive q_{E1}, we proceed as in the derivation of q_{R} (subsection A.1) except that we include the direct excitation of the QE but not the direct emission of the QE. Thus, the field that excites the QE corresponds to E_x^{NF} in Eq. (3.17), and the field that the QE generates in the far field corresponds to $E_{x,\mathrm{R}}^{\mathrm{FF}}$ in Eq. (A.1). We then apply the optical theorem in Eq. (3.8) and obtain the extinction cross-section

$$\sigma_{\mathrm{ext,\ E1}}(\omega) = \frac{4\pi}{k^2}\mathrm{Re}\left\{(-ikz_{\mathrm{d}})e^{-ikz_{\mathrm{d}}}\left[K^{\mathrm{FF}}(\boldsymbol{r}_{\mathrm{d}},\omega) + S_{x,x}^{\mathrm{FF}}(\boldsymbol{r}_{\mathrm{d}},\omega)\frac{A_{\mathrm{e}}(K(\boldsymbol{r}_{\mathrm{e}},\omega)+1)}{\omega_0'(\omega)^2 - \omega^2 - i\gamma'(\omega)\omega}\right]\right\}, \tag{A.9}$$

where the "E1" subindex indicates that these expressions are only used to obtain the q_{E1} factor. If we proceed as in section 3.3.1 we can express the normalized extinction cross section in Eq. (A.9) as a Fano lineshape (Eq. (3.30)), with the zero-dip parameter B_{E1} and the asymmetry factor Q_{E1} given by

$$B_{\mathrm{E1}} = 1 - Q_{\mathrm{E1}}^2 - \frac{1}{\frac{k_0^2}{4\pi}\sigma_{\mathrm{ext}}^{(0)}}\frac{A_{\mathrm{e}}}{\gamma'\omega_0}\mathrm{Im}\left\{(-ik_0z_{\mathrm{d}})e^{-ik_0z_{\mathrm{d}}}S_{x,x}^{\mathrm{FF}}(\boldsymbol{r}_{\mathrm{d}},\omega_0)(K(\boldsymbol{r}_{\mathrm{e}},\omega_0)+1)\right\}, \tag{A.10}$$

$$Q_{\mathrm{E1}} = \frac{A_{\mathrm{e}}}{\sigma_{\mathrm{ext}}^{(0)}\gamma' c_0\varepsilon_0}\left(\frac{1}{2}\mathrm{Im}\{K(\boldsymbol{r}_{\mathrm{e}},\omega_0)\} + \mathrm{Re}\{K(\boldsymbol{r}_{\mathrm{e}},\omega_0)\}\mathrm{Im}\{K(\boldsymbol{r}_{\mathrm{e}},\omega_0)\}\right), \tag{A.11}$$

where we have simplified the expression of Q_{E1} using Eqs. (3.34) and (3.14). The contribution q_{E1} can be obtained subtracting the contribution of q_{R} from Eq. (A.11),

$$q_{\mathrm{E1}} = Q_{\mathrm{E1}} - q_{\mathrm{R}} = \frac{1}{2}\frac{A_{\mathrm{e}}}{2\sigma_{\mathrm{ext}}^{(0)}\gamma' c_0\varepsilon_0}\mathrm{Im}\{K(\boldsymbol{r}_{\mathrm{e}},\omega_0)\}. \tag{A.12}$$

Comparing Eq. (A.8) with Eq. (A.12) we can directly observe that $q_{\mathrm{E1}} = q_{\mathrm{E}}/2$.

Next we derive the analytical expression of the q_{E2} contribution by ignoring the direct excitation of the QE, but considering its direct emission. The procedure to obtain q_{E2} is again the same as for the derivation of q, but the emission to the far field corresponds to E_x^{FF} in Eq. (3.9), and the field that excites the QE corresponds to $E_{x,\mathrm{R}}^{\mathrm{NF}}$ in Eq. (A.2). The corresponding extinction cross section is

$$\sigma_{\text{ext, E2}}(\omega) = \frac{4\pi}{k^2}\text{Re}\Bigg\{(-ikz_\text{d})e^{-ikz_\text{d}}\Big[K^\text{FF}(\boldsymbol{r}_\text{d},\omega)+ \\ (G_0^\text{FF}{}_{x,x}(\boldsymbol{r}_\text{d},\omega) + S^\text{FF}_{x,x}(\boldsymbol{r}_\text{d},\omega))\frac{A_\text{e}K(\boldsymbol{r}_\text{e},\omega)}{\omega_0'(\omega)^2-\omega^2-i\gamma'(\omega)\omega}\Big]\Bigg\}, \tag{A.13}$$

The Fano lineshape is obtained dividing $\sigma_{\text{ext, E2}}$ by $\sigma^{(0)}_\text{ext}$ (see Eq. (3.30)), and it is characterized by the following zero-dip parameter B_E2 and asymmetry factor Q_E2,

$$B_\text{E2} = 1 - Q^2_\text{E2} - \frac{1}{\frac{k_0^2}{4\pi}\sigma^{(0)}_\text{ext}}\frac{A_\text{e}}{\gamma'\omega_0}\text{Im}\left\{(-ik_0z_\text{d})e^{-ik_0z_\text{d}}S^\text{FF}_{x,x}(\boldsymbol{r}_\text{d},\omega_0)(K(\boldsymbol{r}_\text{e},\omega_0)+1)\right\}, \tag{A.14}$$

$$Q_\text{E2} = \frac{A_\text{e}}{2\sigma^{(0)}_\text{ext}\gamma' c_0\varepsilon_0}\left(\frac{1}{2}\text{Im}\{K(\boldsymbol{r}_\text{e},\omega_0)\} + \text{Re}\{K(\boldsymbol{r}_\text{e},\omega_0)\}\text{Im}\{K(\boldsymbol{r}_\text{e},\omega_0)\}\right). \tag{A.15}$$

$Q_\text{E2} = q_\text{E2} + q_\text{R}$, and thus by using Eqs. (A.7) and (A.15) we obtain

$$q_\text{E2} = \frac{1}{2}\frac{A_\text{e}}{2\sigma^{(0)}_\text{ext}\gamma' c_0\varepsilon_0}\text{Im}\{K(\boldsymbol{r}_\text{e},\omega_0)\}, \tag{A.16}$$

which is equal to q_E1 in Eq. (A.12).

Appendix B

Relationship between the field enhancement and the Purcell Factor

In this section we derive Eq. (3.38), which relates the near-field enhancement factor K and the enhanced decay rate γ' of the QE in the presence of a nanoantenna.

As introduced in Eqs. (3.17) and (3.18), the presence of a nanoantenna enhances the electric field at the position of the QE, $\boldsymbol{r}_e$, under plane wave illumination by a factor $(K(\boldsymbol{r}_e, \omega_0)+1)$, where ω_0 is the frequency of the incident plane wave. On the other hand, the QE emits directly to the far field with a spontaneous decay rate γ_0, or via the nanoantenna with a decay rate $P_F \times \gamma_0$, where P_F is the Purcell Factor (we consider that the intrinsic non-radiative losses of the QE are $\gamma_{NR} = 0$). Thus, the total decay rate of the QE in the presence of the nanoantenna is $\gamma' = (P_F+1)\gamma_0$. To derive the relationship between K and P_F we first consider the definition of the radiative yield η_R [134],

$$\eta_R = \frac{\gamma_R}{\gamma'} \ , \tag{B.1}$$

where γ_R is the rate of the radiative emission of the QE towards the far field in the presence of the nanoantenna. γ_R is defined considering the emission in all directions, and it can be related to the rate of radiative emission in a particular direction $\gamma_R(\theta_s, \phi_s)$ (where θ_s and ϕ_s are the standard spherical coordinates azimuthal and polar angles, respectively) by introducing the directivity factor $D_R(\theta_s, \phi_s)$ [42, 130] (see also section 1.2.2),

$$\frac{\gamma_R(\theta_s, \phi_s)}{\gamma_R} = \frac{D_R(\theta_s, \phi_s)}{4\pi}, \tag{B.2}$$

which is a function widely used in antenna theory [42].

Likewise, we can relate the rate of spontaneous emission of the QE in the absence of the antenna in all directions (γ_0) and in a particular direction ($\gamma_0(\theta_s, \phi_s)$) by

$$\frac{\gamma_0(\theta_s,\phi_s)}{\gamma_0} = \frac{D_0(\theta_s,\phi_s)}{4\pi}. \tag{B.3}$$

In particular, for the forward direction $\theta_s = 0$ and $\phi_s = 0$ considered in section 3.3.1:

$$\frac{\gamma_R}{\gamma_0} = \frac{\gamma_R(0,0)}{\gamma_0(0,0)} \underbrace{\frac{D_0(0,0)}{D_R(0,0)}}_{1/\mathcal{D}}, \tag{B.4}$$

where we introduce the parameter $\mathcal{D} = D_R(0,0)/D_0(0,0)$ that appears in Eqs. (3.38) and (3.39). In the systems that we consider, the direct emission of the QE and the emission of the nanoantenna has very similar radiation patterns corresponding to that of an electric dipole oriented along the x-axis (with a possible small distortion in the presence of the nanoantenna). Thus, $D_R(\phi_s = 0, \theta_s = 0) \approx D_0(\phi_s = 0, \theta_s = 0) = 3/2$ [42] and $\mathcal{D} \approx 1$.

Next we focus on the ratio $\gamma_R(0,0)/\gamma_0(0,0)$. $\gamma_0(0,0)$ scales with the squared modulus (intensity) of the electric field E_x^E radiated by the QE in the forward direction (at a $\boldsymbol{r}_d$ point) in the absence of the nanoantenna, *i.e.* $\gamma_0(0,0) \propto |E_x^E(\boldsymbol{r}_d,\omega)|^2$. In a similar manner, $\gamma_R(0,0) \propto |E_x^{E\text{-}Tot}(\boldsymbol{r}_d,\omega)|^2$, where $E^{E\text{-}Tot}$ is the electric field radiated by the QE in the forward direction in the presence of the nanoantenna. Thus,

$$\frac{\gamma_R(0,0)}{\gamma_0(0,0)} = \frac{|E_x^E(\boldsymbol{r}_d,\omega)|^2}{|E_x^{E\text{-}Tot}(\boldsymbol{r}_d,\omega)|^2}. \tag{B.5}$$

Using Eqs. (3.11) and (3.13) we write E_x^E and $E_x^{E\text{-}Tot}$ as proportional to the Green's functions $G_{x,x}^{FF}$ and ${G_0^{FF}}_{x,x}$ that models the emission of the QE in the presence or in the absence of the nanoantenna, respectively, and obtain

$$\frac{\gamma_R(0,0)}{\gamma_0(0,0)} = \frac{|{G^{FF}}_{x,x}(\boldsymbol{r}_d,\boldsymbol{r}_e,\omega)|^2}{|{G_0^{FF}}_{x,x}(\boldsymbol{r}_d,\boldsymbol{r}_e,\omega)|^2}. \tag{B.6}$$

Further, we relate the near-field enhancement factor K to $G_{x,x}^{FF}$ using the reciprocity theorem [140–142] (Eq. (3.34)) and obtain,

$$\frac{\gamma_R}{\gamma_0}\mathcal{D} = \frac{\gamma_R(0,0)}{\gamma_0(0,0)} = \frac{|{G^{FF}}_{x,x}(\boldsymbol{r}_d,\boldsymbol{r}_e,\omega)|^2}{|{G_0^{FF}}_{x,x}(\boldsymbol{r}_d,\boldsymbol{r}_e,\omega)|^2} = |K(\boldsymbol{r}_e,\omega)+1|^2. \tag{B.7}$$

As in the discussion of Eq. (3.34) we have considered in Eq. (B.7) that the emission in the forward and backward direction are identical in our system. Using Eqs. (B.1), (B.7), and $\gamma' = (P_F+1)\gamma_0$ we finally obtain:

$$\eta_R = \frac{\gamma_0}{\gamma'}\mathcal{D}|K(\boldsymbol{r}_e,\omega)+1|^2 = \frac{\mathcal{D}|K(\boldsymbol{r}_e,\omega)+1|^2}{P_F+1}, \tag{B.8}$$

which corresponds to Eq. (3.38).

Appendix C

Details of the classical electromagnetic calculations of the optical response of a dimer nanostructure under different illuminations

According to section 3.3.1, the calculation of the extinction cross-section spectrum, as well as the evaluation of the parameters quantifying the Fano feature of a QE–nanoantenna system can be related to the response of the nanoantenna when it is illuminated by a plane wave and by an electric point-like dipole. According

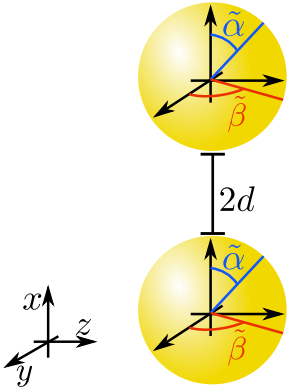

Figure C.1: Scheme of the dimer nanostructure studied in section 3.5 showing the angles of discretization in *MNPBEM17*. $\tilde{\alpha}$ is the inclination angle with respect to the x- axis, and $\tilde{\beta}$ is the angle of projection on the yz-plane between the y- and the z-axis.

to Eqs. (3.31a)-(3.31e), we need to obtain the extinction cross-section spectrum of the bare nanoantenna $\sigma_{\text{ext}}^{(0)}$, the field-enhancement factor K (Eq. (3.18)), the (x,x)-component of the Green's function that describes the emission of the QE towards the detector in the presence of the nanoantenna $G_{x,x}^{\text{FF}}$ (Eq. (3.11)), and the (x,x)-component of the Green's function that describes the self-interaction of the QE $S_{x,x}^{\text{NF}}$ (Eq. (3.19)). We note that $S_{x,x}^{\text{NF}}$ allows for obtaining, for example, the enhanced decay rate of the QE in the presence of the nanoantenna γ' (Eq. (3.21)) and the Lamb shift $\Delta\omega$ (Eq. (3.21)).

In section 3.5, we analyze the Fano spectra present in the extinction cross-section of a QE situated in the junction of two gold spherical nanoparticles. We use the *MNPBEM17* Matlab's package [153–155] to calculate the optical response under plane wave or dipolar illumination of the dimer nanostructure, and obtain all of the necessary parameters mentioned above. We have found that in order to converge our simulations, it is enough to discretize each nanoparticle with 125 and 35 elements obtained from an equidistant distribution of the $\tilde{\alpha}$ and $\tilde{\beta}$ angles, respectively (see definition of these angles in Fig. C.1).

List of publications

Publications related to this thesis:

1. **Á. Nodar**, T. Neuman, Y. Zhang, J. Aizpurua, and R. Esteban: "On the Fano asymmetry in zero-detuned exciton-plasmon systems", Accepted at Optics Express (2023).
https://doi.org/10.1364/OE.477200

2. **Á. Nodar**, R. Esteban, U. Muniain, M. J. Steel, J. Aizpurua, and M. K. Schmidt: "Identifying unbound strong bunching and the breakdown of the Rotating Wave Approximation in the quantum Rabi model", ArXiv preprint, arXiv:2211.13249 (2022).
https://arxiv.org/abs/2211.13249

3. **Á. Nodar**, R. Esteban, C. Maciel-Escudero, J. Lasa-Alonso, J. Aizpurua, and G. Molina-Terriza: "Preservation and destruction of the purity of two-photon states in the interaction with a nanoscatterer", ArXiv preprint, arXiv:2211.14244 (2022).
https://arxiv.org/abs/2211.14244

Other publications:

1. J. Lasa-Alonso, D. R. Abujetas, **Á. Nodar**, J. A. Dionne, J. J. Saenz, G. Moline-Terriza, J. Aizpurua, and A. García-Etxarri: "Surface-Enhanced Circular Dichroism Spectroscopy on Periodic Dual Nanostructures", ACS Photonics **7**, 2978-2986 (2020).
https://doi.org/10.1021/acsphotonics.0c00611

2. F. Madzharova, **Á. Nodar**, V. Zivanović, M. R. S. Huang, C. T. Koch, R. Esteban, J. Aizpurua, and J. Kneipp: "Gold- and Silver-Coated Barium Titanate Nanocomposites as Probes for Two-Photon Multimodal Microspectroscopy", Advanced Functional Materials **29**, 1904289 (2019).
https://doi.org/10.1002/adfm.201904289

Bibliography

[1] J. C. Maxwell. VIII. A dynamical theory of the electromagnetic field. *Philosophical transactions of the Royal Society of London*, (155):459–512, 1865.

[2] G. Mie. Beiträge zur Optik trüber Medien, speziell kolloidaler Metallösungen. *Annalen der physik*, 330(3):377–445, 1908.

[3] M. Pelton, J. Aizpurua, and G. Bryant. Metal-nanoparticle plasmonics. *Laser & Photonics Reviews*, 2(3):136–159, 2008.

[4] L. Novotny and S. J. Stranick. Near-field optical microscopy and spectroscopy with pointed probes. *Annu. Rev. Phys. Chem.*, 57:303–331, 2006.

[5] Y. Yu, T.-H. Xiao, Y. Wu, W. Li, Q.-G. Zeng, L. Long, and Z.-Y. Li. Roadmap for single-molecule surface-enhanced Raman spectroscopy. *Advanced Photonics*, 2(1):014002, 2020.

[6] B. Yang, G. Chen, A. Ghafoor, Y. Zhang, Y. Zhang, Y. Zhang, Y. Luo, J. Yang, V. Sandoghdar, J. Aizpurua, *et al.* Sub-nanometre resolution in single-molecule photoluminescence imaging. *Nature Photonics*, 14(11):693–699, 2020.

[7] A. Rosławska, T. Neuman, B. Doppagne, A. G. Borisov, M. Romeo, F. Scheurer, J. Aizpurua, and G. Schull. Mapping lamb, stark, and Purcell effects at a chromophore-picocavity junction with hyper-resolved fluorescence microscopy. *Physical Review X*, 12(1):011012, 2022.

[8] Y. Zhang, Q.-S. Meng, L. Zhang, Y. Luo, Y.-J. Yu, B. Yang, Y. Zhang, R. Esteban, J. Aizpurua, Y. Luo, J.-L. Yang, Z.-C. Dong, and J. Hou. Sub-nanometre control of the coherent interaction between a single molecule and a plasmonic nanocavity. *Nature Communications*, 8:15225, 2017.

[9] A. R. Rastinehad, H. Anastos, E. Wajswol, J. S. Winoker, J. P. Sfakianos, S. K. Doppalapudi, M. R. Carrick, C. J. Knauer, B. Taouli, S. C. Lewis, *et al.* Gold nanoshell-localized photothermal ablation of prostate tumors in a clinical pilot device study. *Proceedings of the National Academy of Sciences*, 116(37):18590–18596, 2019.

[10] X. Huang, P. K. Jain, I. H. El-Sayed, and M. A. El-Sayed. Plasmonic photothermal therapy (PPTT) using gold nanoparticles. *Lasers in medical science*, 23:217–228, 2008.

[11] J. G. Smith, J. A. Faucheaux, and P. K. Jain. Plasmon resonances for solar energy harvesting: a mechanistic outlook. *Nano Today*, 10(1):67–80, 2015.

[12] M. Dhiman. Plasmonic nanocatalysis for solar energy harvesting and sustainable chemistry. *Journal of Materials Chemistry A*, 8(20):10074–10095, 2020.

[13] M. S. Tame, K. McEnery, Ş. Özdemir, J. Lee, S. A. Maier, and M. Kim. Quantum plasmonics. *Nature Physics*, 9(6):329–340, 2013.

[14] Z. Jacob and V. M. Shalaev. Plasmonics goes quantum. *Science*, 334(6055):463–464, 2011.

[15] S. S. R. Oemrawsingh, X. Ma, D. Voigt, A. Aiello, E. R. Eliel, G. W. 't Hooft, and J. P. Woerdman. Experimental Demonstration of Fractional Orbital Angular Momentum Entanglement of Two Photons. *Physical Review Letters*, 95:240501, 2005.

[16] S. Franke-Arnold, L. Allen, and M. Padgett. Advances in optical angular momentum. *Laser & Photonics Reviews*, 2(4):299–313, 2008.

[17] G. Molina-Terriza, A. Vaziri, J. Řeháček, Z. Hradil, and A. Zeilinger. Triggered qutrits for quantum communication protocols. *Physical Review Letters*, 92(16):167903, 2004.

[18] G. Molina-Terriza, J. P. Torres, and L. Torner. Twisted photons. *Nature Physics*, 3(5):305–310, 2007.

[19] Y. Tang and A. E. Cohen. Optical chirality and its interaction with matter. *Physical Review Letters*, 104(16):163901, 2010.

[20] J. Lasa-Alonso, M. Molezuelas-Ferreras, J. M. Varga, A. García-Etxarri, G. Giedke, and G. Molina-Terriza. Symmetry-protection of multiphoton states of light. *New Journal of Physics*, 22(12):123010, 2020.

[21] H. J. Carmichael. *Statistical methods in quantum optics 1: Master equations and Fokker-Planck equations*. Springer Science & Business Media, 1999.

[22] A. F. Kockum, M. Sandberg, M. R. Vissers, J. Gao, G. Johansson, and D. P. Pappas. Detailed modelling of the susceptibility of a thermally populated, strongly driven circuit-QED system. *Journal of Physics B: Atomic, Molecular and Optical Physics*, 46(22):224014, 2013.

[23] S. A. Maier. Effective mode volume of nanoscale plasmon cavities. *Optical and Quantum Electronics*, 38(1):257–267, 2006.

[24] S. Huang, T. Ming, Y. Lin, X. Ling, Q. Ruan, T. Palacios, J. Wang, M. Dresselhaus, and J. Kong. Ultrasmall Mode Volumes in Plasmonic Cavities of Nanoparticle-On-Mirror Structures. *Small*, 12(37):5190–5199, 2016.

[25] G.-C. Li, Q. Zhang, S. A. Maier, and D. Lei. Plasmonic particle-on-film nanocavities: a versatile platform for plasmon-enhanced spectroscopy and photochemistry. *Nanophotonics*, 7(12):1865–1889, 2018.

[26] F. Benz, R. Chikkaraddy, A. Salmon, H. Ohadi, B. de Nijs, J. Mertens, C. Carnegie, R. W. Bowman, and J. J. Baumberg. SERS of Individual Nanoparticles on a Mirror: Size Does Matter, but so Does Shape. *The Journal of Physical Chemistry Letters*, 7(12):2264–2269, 2016.

[27] J. Olmos-Trigo, C. Sanz-Fernández, D. R. Abujetas, J. Lasa-Alonso, N. de Sousa, A. García-Etxarri, J. A. Sánchez-Gil, G. Molina-Terriza, and J. J. Sáenz. Kerker conditions upon lossless, absorption, and optical gain regimes. *Physical Review Letters*, 125(7):073205, 2020.

[28] J. Lasa-Alonso, D. R. Abujetas, Á. Nodar, J. A. Dionne, J. J. Sáenz, G. Molina-Terriza, J. Aizpurua, and A. García-Etxarri. Surface-enhanced circular dichroism spectroscopy on periodic dual nanostructures. *Acs Photonics*, 7(11):2978–2986, 2020.

[29] X. Zambrana-Puyalto, I. Fernandez-Corbaton, M. Juan, X. Vidal, and G. Molina-Terriza. Duality symmetry and Kerker conditions. *Optics Letters*, 38(11):1857–1859, 2013.

[30] A. Babaze, R. Esteban, J. Aizpurua, and A. G. Borisov. Second-Harmonic Generation from a Quantum Emitter Coupled to a Metallic Nanoantenna. *ACS Photonics*, 7(3):701–713, 2020.

[31] J. Butet, P.-F. Brevet, and O. J. F. Martin. Optical Second Harmonic Generation in Plasmonic Nanostructures: From Fundamental Principles to Advanced Applications. *ACS Nano*, 9(11):10545–10562, 2015.

[32] M. R. Singh. Enhancement of the second-harmonic generation in a quantum dot–metallic nanoparticle hybrid system. *Nanotechnology*, 24(12):125701, 2013.

[33] B. J. Hunt. Oliver Heaviside. *Phys. Today*, 65(11):48, 2012.

[34] H. Benisty, J.-J. Greffet, and P. Lalanne. *Introduction to Nanophotonics*. Oxford University Press, 2022.

[35] L. Novotny and B. Hecht. *Principles of nano-optics*. Cambridge university press, 2012.

[36] J. D. Jackson. *Classical electrodynamics*. Wiley NY, 1999.

[37] H. Weber and G. Riemann. *Die partiellen differential-gleichungen der mathematischen physik nach Riemann's Vorlesungen: bd. Hülfsmittel aus der theorie der linearen differentialgleichungen. Wärmeleitung. Elasticitätstheorie. Elektrische schwingungen. Hydrodynamik.* F. Vieweg und Sohn, 1901.

[38] L. Silberstein. Elektromagnetische grundgleichungen in bivektorieller behandlung. *Annalen der Physik*, 327(3):579–586, 1907.

[39] L. Silberstein. Nachtrag zur Abhandlung über Elektromagnetische Grundgleichungen in bivektorieller Behandlung. *Annalen der Physik*, 329(14):783–784, 1907.

[40] C. Bohren and D. Huffman. *Absorption and Scattering of Light by Small Particles.* Wiley, 1983.

[41] P. B. Johnson and R. W. Christy. Optical Constants of the Noble Metals. *Physical Review B*, 6:4370–4379, 1972.

[42] C. Balanis. *Antenna Theory: Analysis and Design.* Wiley, 2015.

[43] J. H. Poynting. XV. On the transfer of energy in the electromagnetic field. *Philosophical Transactions of the Royal Society of London*, (175):343–361, 1884.

[44] R. Carminati and J. C. Schotland. *Principles of Scattering and Transport of Light.* Cambridge University Press, 2021.

[45] H. C. Van de Hulst. *Light scattering by small particles.* Courier Corporation, 1981.

[46] J. A. Stratton. *Electromagnetic theory.* John Wiley & Sons, 2007.

[47] D. Schebarchov, B. Auguié, and E. C. Le Ru. Simple accurate approximations for the optical properties of metallic nanospheres and nanoshells. *Phys. Chem. Chem. Phys.*, 15:4233–4242, 2013.

[48] E. D. Palik. *Handbook of optical constants of solids.* Academic press, 1998.

[49] A. Krasnok, M. Caldarola, N. Bonod, and A. Alú. Spectroscopy and Biosensing with Optically Resonant Dielectric Nanostructures. *Advanced Optical Materials*, 6(5):1701094, 2018.

[50] I. Staude and J. Schilling. Metamaterial-inspired silicon nanophotonics. *Nature Photonics*, 11(5):274–284, 2017.

[51] M. Caldarola, P. Albella, E. Cortés, M. Rahmani, T. Roschuk, G. Grinblat, R. F. Oulton, A. V. Bragas, and S. A. Maier. Non-plasmonic nanoantennas for surface enhanced spectroscopies with ultra-low heat conversion. *Nature Communications*, 6(1):1–8, 2015.

[52] K. Koshelev and Y. Kivshar. Dielectric resonant metaphotonics. *Acs Photonics*, 8(1):102–112, 2020.

[53] A. García-Etxarri, R. Gómez-Medina, L. S. Froufe-Pérez, C. López, L. Chantada, F. Scheffold, J. Aizpurua, M. Nieto-Vesperinas, and J. J. Sáenz. Strong magnetic response of submicron silicon particles in the infrared. *Optics Express*, 19(6):4815–4826, 2011.

[54] S. Sanders, W. J. Kort-Kamp, D. A. Dalvit, and A. Manjavacas. Nanoscale transfer of angular momentum mediated by the Casimir torque. *Communications Physics*, 2(1):1–7, 2019.

[55] I. Fernandez-Corbaton, X. Zambrana-Puyalto, and G. Molina-Terriza. Helicity and angular momentum: A symmetry-based framework for the study of light-matter interactions. *Physical Review A*, 86(4):042103, 2012.

[56] M. D. Schwartz. *Quantum field theory and the standard model*. Cambridge University Press, 2014.

[57] R. A. Beth. Mechanical detection and measurement of the angular momentum of light. *Physical Review*, 50(2):115, 1936.

[58] J. P. Torres and L. Torner. *Twisted photons: applications of light with orbital angular momentum*. John Wiley & Sons, 2011.

[59] C. T. Schmiegelow, J. Schulz, H. Kaufmann, T. Ruster, U. G. Poschinger, and F. Schmidt-Kaler. Transfer of optical orbital angular momentum to a bound electron. *Nature Communications*, 7(1):1–6, 2016.

[60] H. He, M. Friese, N. Heckenberg, and H. Rubinsztein-Dunlop. Direct observation of transfer of angular momentum to absorptive particles from a laser beam with a phase singularity. *Physical Review Letters*, 75(5):826, 1995.

[61] F. Pampaloni and J. Enderlein. Gaussian, hermite-gaussian, and laguerre-gaussian beams: A primer. *arXiv preprint physics/0410021*, 2004.

[62] A. E. Siegman. *Lasers*. University science books, 1986.

[63] D. J. Griffiths. *Introduction to electrodynamics*. Pearson, 2013.

[64] I. Białynicki-Birula. On the wave function of the photon. *Acta Physica Polonica A*, 86(1):97–116, 1994.

[65] N. Tischler, X. Zambrana-Puyalto, and G. Molina-Terriza. The role of angular momentum in the construction of electromagnetic multipolar fields. *European journal of physics*, 33(5):1099, 2012.

[66] M. E. Rose. *Elementary theory of angular momentum*. Courier Corporation, 1995.

[67] X. Zambrana-Puyalto, X. Vidal, and G. Molina-Terriza. Excitation of single multipolar modes with engineered cylindrically symmetric fields. *Optics Express*, 20(22):24536–24544, 2012.

[68] E. Wigner. *Group theory: and its application to the quantum mechanics of atomic spectra*. Elsevier, 2012.

[69] R. J. Glauber. One hundred years of light quanta. *Nobel Lecture*, 8, 2005.

[70] C. Gerry and P. Knight. *Introductory quantum optics*. Cambridge university press, 2005.

[71] A. Muthukrishnan, M. O. Scully, and M. S. Zubairy. The Concept of the Photon—Revisited. *Optics & Photonics News*, 14:59–80, 2003.

[72] H.-P. Breuer and F. Petruccione. *The theory of open quantum systems*. Oxford University Press, 2002.

[73] D. Manzano. A short introduction to the Lindblad master equation. *Aip Advances*, 10(2):025106, 2020.

[74] C. Cohen-Tannoudji, B. Diu, and F. Laloe. *Quantum Mechanics, Volume 1*. John Wiley & Sons, Ltd, 1986.

[75] R. A. Campos, B. E. Saleh, and M. C. Teich. Quantum-mechanical lossless beam splitter: SU (2) symmetry and photon statistics. *Physical Review A*, 40(3):1371, 1989.

[76] G. R. Fowles. *Introduction to modern optics*. Courier Corporation, 1989.

[77] R. Loudon. *The quantum theory of light*. Oxford, 2000.

[78] S. M. Barnett, J. Jeffers, A. Gatti, and R. Loudon. Quantum optics of lossy beam splitters. *Physical Review A*, 57(3):2134, 1998.

[79] N. Tischler, C. Rockstuhl, and K. Słowik. Quantum optical realization of arbitrary linear transformations allowing for loss and gain. *Physical Review X*, 8(2):021017, 2018.

[80] R. Matloob, R. Loudon, S. M. Barnett, and J. Jeffers. Electromagnetic field quantization in absorbing dielectrics. *Physical Review A*, 52(6):4823, 1995.

[81] R. Matloob and R. Loudon. Electromagnetic field quantization in absorbing dielectrics. II. *Physical Review A*, 53(6):4567, 1996.

[82] R. Hanbury Brown and R. Q. Twiss. Correlation between photons in two coherent beams of light. *Nature*, 177(4497):27–29, 1956.

[83] C. S. Muñoz. *Generation of non classical states of light*. PhD thesis, Universidad Autónoma de Madrid, 2016.

[84] O. Di Stefano, A. Settineri, V. Macrì, L. Garziano, R. Stassi, S. Savasta, and F. Nori. Resolution of gauge ambiguities in ultrastrong-coupling cavity quantum electrodynamics. *Nature Physics*, 15(8):803–808, 2019.

[85] W. Salmon, C. Gustin, A. Settineri, O. Di Stefano, D. Zueco, S. Savasta, F. Nori, and S. Hughes. Gauge-independent emission spectra and quantum correlations in the ultrastrong coupling regime of open system cavity-QED. *Nanophotonics*, 11(8):1573–1590, 2022.

[86] A. Settineri, V. Macrí, A. Ridolfo, O. Di Stefano, A. F. Kockum, F. Nori, and S. Savasta. Dissipation and thermal noise in hybrid quantum systems in the ultrastrong-coupling regime. *Physical Review A*, 98(5):053834, 2018.

[87] A. Settineri, O. Di Stefano, D. Zueco, S. Hughes, S. Savasta, and F. Nori. Gauge freedom, quantum measurements, and time-dependent interactions in cavity QED. *Physical Review Research*, 3(2):023079, 2021.

[88] M. Babiker and R. Loudon. Derivation of the Power-Zienau-Woolley Hamiltonian in quantum electrodynamics by gauge transformation. *Proceedings of the Royal Society of London A*, 385(1789):439–460, 1983.

[89] S. Hughes, M. Richter, and A. Knorr. Quantized pseudomodes for plasmonic cavity QED. *Optics letters*, 43(8):1834–1837, 2018.

[90] E. Waks and D. Sridharan. Cavity QED treatment of interactions between a metal nanoparticle and a dipole emitter. *Physical Review A*, 82(4):043845, 2010.

[91] P. Lodahl, S. Mahmoodian, and S. Stobbe. Interfacing single photons and single quantum dots with photonic nanostructures. *Reviews of Modern Physics*, 87(2):347, 2015.

[92] C. Cohen-Tannoudji, J. Dupont-Roc, and G. Grynberg. *Photons and Atoms: Introduction to Quantum Electrodynamics*. John Wiley & Sons, 1997.

[93] G. Colas des Francs, S. Derom, R. Vincent, A. Bouhelier, and A. Dereux. Mie plasmons: modes volumes, quality factors, and coupling strengths (purcell factor) to a dipolar emitter. *International Journal of Optics*, 2012, 2012.

[94] P. T. Kristensen and S. Hughes. Modes and mode volumes of leaky optical cavities and plasmonic nanoresonators. *ACS Photonics*, 1(1):2–10, 2014.

[95] E. M. Purcell. Spontaneous Emission Probabilities at Radio Frequencies,. *Physical Review*, 69:681, 1946.

[96] K. Joulain, R. Carminati, J.-P. Mulet, and J.-J. Greffet. Definition and measurement of the local density of electromagnetic states close to an interface. *Physical Review B*, 68:245405, 2003.

[97] D. De Bernardis, P. Pilar, T. Jaako, S. De Liberato, and P. Rabl. Breakdown of gauge invariance in ultrastrong-coupling cavity QED. *Physical Review A*, 98(5):053819, 2018.

[98] P. Heimann. Reviews: The Born-Einstein Letters. Correspondence between Albert Einstein and Max and Hedwig Born from 1916 to 1955 with commentaries by Max Born. *European Studies Review*, 3(2):198–199, 1973.

[99] C. Francis. *Light after dark II: the large and the small.* Troubador Publishing Ltd, 2016.

[100] W. Sulis. Locality is dead! Long live locality! *Frontiers in Physics*, 8:360, 2020.

[101] A. F. Starace. Length and velocity formulas in approximate oscillator-strength calculations. *Physical Review A*, 3(4):1242, 1971.

[102] R. Girlanda, A. Quattropani, and P. Schwendimann. Two-photon transitions to exciton states in semiconductors. Application to CuCl. *Physical Review B*, 24(4):2009, 1981.

[103] S. Ismail-Beigi, E. K. Chang, and S. G. Louie. Coupling of nonlocal potentials to electromagnetic fields. *Physical Review Letters*, 87(8):087402, 2001.

[104] S. Savasta and R. Girlanda. The particle-photon interaction in systems described by model Hamiltonians in second quantization. *Solid state communications*, 96(7):517–522, 1995.

[105] J. Larson and M. T. Tavis. Special issue on Jaynes–Cummings physics. *J. Phys. B: At. Mol. Opt. Phys*, 46:220201, 2013.

[106] C. A. Brasil, F. F. Fanchini, and R. d. J. Napolitano. A simple derivation of the Lindblad equation. *Revista Brasileira de Ensino de Física*, 35:01–09, 2013.

[107] A. G. Redfield. On the theory of relaxation processes. *IBM Journal of Research and Development*, 1(1):19–31, 1957.

[108] X. Wu, S. K. Gray, and M. Pelton. Quantum-dot-induced transparency in a nanoscale plasmonic resonator. *Optics Express*, 18(23):23633–23645, 2010.

[109] G. M. Akselrod, C. Argyropoulos, T. B. Hoang, C. Ciracì, C. Fang, J. Huang, D. R. Smith, and M. H. Mikkelsen. Probing the mechanisms of large Purcell enhancement in plasmonic nanoantennas. *Nature Photonics*, 8(11):835–840, 2014.

[110] A. F. Koenderink. Single-Photon Nanoantennas. *ACS Photonics*, 4(4):710–722, 2017.

[111] L. Novotny and N. Van Hulst. Antennas for light. *Nature Photonics*, 5(2):83–90, 2011.

[112] T. Neuman, C. Huck, J. Vogt, F. Neubrech, R. Hillenbrand, J. Aizpurua, and A. Pucci. Importance of Plasmonic Scattering for an Optimal Enhancement of Vibrational Absorption in SEIRA with Linear Metallic Antennas. *The Journal of Physical Chemistry C*, 119(47):26652–26662, 2015.

[113] F. Neubrech, A. Pucci, T. W. Cornelius, S. Karim, A. García-Etxarri, and J. Aizpurua. Resonant Plasmonic and Vibrational Coupling in a Tailored Nanoantenna for Infrared Detection. *Physical Review Letters*, 101:157403, 2008.

[114] I. Abid, W. Chen, J. Yuan, S. Najmaei, E. C. Peñafiel, R. Péchou, N. Large, J. Lou, and A. Mlayah. Surface enhanced resonant Raman scattering in hybrid MoSe2@Au nanostructures. *Optics Express*, 26(22):29411–29423, 2018.

[115] R. D. Artuso and G. W. Bryant. Optical Response of Strongly Coupled Quantum Dot-Metal Nanoparticle Systems: Double Peaked Fano Structure and Bistability. *Nano Letters*, 8(7):2106–2111, 2008.

[116] D. O. Sigle, S. Kasera, L. O. Herrmann, A. Palma, B. de Nijs, F. Benz, S. Mahajan, J. J. Baumberg, and O. A. Scherman. Observing single molecules complexing with cucurbit [7] uril through nanogap surface-enhanced Raman spectroscopy. *The journal of physical chemistry letters*, 7(4):704–710, 2016.

[117] A. B. Zrimsek, N. Chiang, M. Mattei, S. Zaleski, M. O. McAnally, C. T. Chapman, A.-I. Henry, G. C. Schatz, and R. P. Van Duyne. Single-molecule chemistry with surface-and tip-enhanced Raman spectroscopy. *Chemical reviews*, 117(11):7583–7613, 2017.

[118] A. E. Miroshnichenko, S. Flach, and Y. S. Kivshar. Fano resonances in nanoscale structures. *Rev. Mod. Phys.*, 82:2257–2298, 2010.

[119] B. Gallinet. *Fano Resonances in Plasmonic Nanostructures Fundamentals, Numerical Modeling and Applications*. PhD thesis, École Polytechnique Fédérale De Lausanne, Lausanne, 2012.

[120] M. F. Limonov, M. V. Rybin, A. N. Poddubny, and Y. S. Kivshar. Fano resonances in photonics. *Nature Photonics*, 11(9):543–554, 2017.

[121] M. Autore, L. Mester, M. Goikoetxea, and R. Hillenbrand. Substrate matters: surface-polariton enhanced infrared nanospectroscopy of molecular vibrations. *Nano letters*, 19(11):8066–8073, 2019.

[122] A. Lovera, B. Gallinet, P. Nordlander, and O. J. Martin. Mechanisms of Fano Resonances in Coupled Plasmonic Systems. *ACS Nano*, 7(5):4527–4536, 2013.

[123] J. Kundu, F. Le, P. Nordlander, and N. J. Halas. Surface enhanced infrared absorption (SEIRA) spectroscopy on nanoshell aggregate substrates. *Chemical Physics Letters*, 452(1):115–119, 2008.

[124] T. Hartsfield, W.-S. Chang, S.-C. Yang, T. Ma, J. Shi, L. Sun, G. Shvets, S. Link, and X. Li. Single quantum dot controls a plasmonic cavity's scattering and anisotropy. *Proceedings of the National Academy of Sciences*, 112(40):12288–12292, 2015.

[125] M. Pelton, S. D. Storm, and H. Leng. Strong coupling of emitters to single plasmonic nanoparticles: exciton-induced transparency and Rabi splitting. *Nanoscale*, 11(31):14540–14552, 2019.

[126] E. Kamenetskii, A. Sadreev, and A. Miroshnichenko. *Fano Resonances in Optics and Microwaves Physics and Applications*. Springer International Publishing, 2018.

[127] R. Ruppin. Decay of an excited molecule near a small metal sphere. *The Journal of Chemical Physics*, 76(4):1681–1684, 1982.

[128] W. E. Lamb and R. C. Retherford. Fine Structure of the Hydrogen Atom by a Microwave Method. *Physical Review*, 72:241–243, 1947.

[129] M. V. Rybin, S. F. Mingaleev, M. F. Limonov, and Y. S. Kivshar. Purcell effect and Lamb shift as interference phenomena. *Scientific Reports*, 6(1):20599, 2016.

[130] R. Esteban, T. V. Teperik, and J. J. Greffet. Optical Patch Antennas for Single Photon Emission Using Surface Plasmon Resonances. *Physical Review Letters*, 104:026802, 2010.

[131] D. J. Heinzen and M. S. Feld. Vacuum Radiative Level Shift and Spontaneous-Emission Linewidth of an Atom in an Optical Resonator. *Physical Review Letters*, 59:2623–2626, 1987.

[132] J. M. Wylie and J. E. Sipe. Quantum electrodynamics near an interface. II. *Physical Review A*, 32:2030–2043, 1985.

[133] H. Walther, B. T. H. Varcoe, B.-G. Englert, and T. Becker. Cavity quantum electrodynamics. *Reports on Progress in Physics*, 69(5):1325–1382, 2006.

[134] P. Anger, P. Bharadwaj, and L. Novotny. Enhancement and Quenching of Single-Molecule Fluorescence. *Physical Review Letters*, 96:113002, 2006.

[135] B. Gurlek, V. Sandoghdar, and D. Martín-Cano. Manipulation of Quenching in Nanoantenna–Emitter Systems Enabled by External Detuned Cavities: A Path to Enhance Strong-Coupling. *ACS Photonics*, 5(2):456–461, 2018.

[136] D. C. Marinica, H. Lourenço-Martins, J. Aizpurua, and A. G. Borisov. Plexciton Quenching by Resonant Electron Transfer from Quantum Emitter to Metallic Nanoantenna. *Nano Letters*, 13(12):5972–5978, 2013.

[137] R. Carminati, J.-J. Greffet, C. Henkel, and J. Vigoureux. Radiative and non-radiative decay of a single molecule close to a metallic nanoparticle. *Optics Communications*, 261(2):368–375, 2006.

[138] R. Esteban, J. Aizpurua, and G. W. Bryant. Strong coupling of single emitters interacting with phononic infrared antennae. *New Journal of Physics*, 16(1):013052, 2014.

[139] P. Törmä and W. L. Barnes. Strong coupling between surface plasmon polaritons and emitters: a review. *Reports on Progress in Physics*, 78(1):013901, 2014.

[140] R. Carminati, M. Nieto-Vesperinas, and J.-J. Greffet. Reciprocity of evanescent electromagnetic waves. *J. Opt. Soc. Am. A*, 15(3):706–712, 1998.

[141] P. Bharadwaj, B. Deutsch, and L. Novotny. Optical Antennas. *Adv. Opt. Photon.*, 1(3):438–483, 2009.

[142] R. Esteban, M. Laroche, and J.-J. Greffet. Influence of metallic nanoparticles on upconversion processes. *Journal of Applied Physics*, 105(3):033107, 2009.

[143] E. C. Le Ru, W. R. C. Somerville, and B. Auguié. Radiative correction in approximate treatments of electromagnetic scattering by point and body scatterers. *Physical Review A*, 87:012504, 2013.

[144] J. Zuloaga and P. Nordlander. On the Energy Shift between Near-Field and Far-Field Peak Intensities in Localized Plasmon Systems. *Nano Letters*, 11(3):1280–1283, 2011.

[145] J. Chen, P. Albella, Z. Pirzadeh, P. Alonso-González, F. Huth, S. Bonetti, V. Bonanni, J. Åkerman, J. Nogués, P. Vavassori, A. Dmitriev, J. Aizpurua, and R. Hillenbrand. Plasmonic Nickel Nanoantennas. *Small*, 7(16):2341–2347, 2011.

[146] J. J. Baumberg, J. Aizpurua, M. H. Mikkelsen, and D. R. Smith. Extreme nanophotonics from ultrathin metallic gaps. *Nature Materials*, 18(7):668–678, 2019.

[147] F. Benz, C. Tserkezis, L. O. Herrmann, B. de Nijs, A. Sanders, D. O. Sigle, L. Pukenas, S. D. Evans, J. Aizpurua, and J. J. Baumberg. Nanooptics of Molecular-Shunted Plasmonic Nanojunctions. *Nano Letters*, 15(1):669–674, 2015.

[148] I. Romero, J. Aizpurua, G. W. Bryant, and F. J. G. de Abajo. Plasmons in nearly touching metallic nanoparticles: singular response in the limit of touching dimers. *Optics Express*, 14(21):9988–9999, 2006.

[149] L. Mao, Z. Li, B. Wu, and H. Xu. Effects of quantum tunneling in metal nanogap on surface-enhanced Raman scattering. *Applied Physics Letters*, 94(24):243102, 2009.

[150] J. Zuloaga, E. Prodan, and P. Nordlander. Quantum Description of the Plasmon Resonances of a Nanoparticle Dimer. *Nano Letters*, 9(2):887–891, 2009.

[151] C. Lumdee, B. Yun, and P. G. Kik. Gap-Plasmon Enhanced Gold Nanoparticle Photoluminescence. *ACS Photonics*, 1(11):1224–1230, 2014.

[152] R. T. Hill, J. J. Mock, A. Hucknall, S. D. Wolter, N. M. Jokerst, D. R. Smith, and A. Chilkoti. Plasmon Ruler with Angstrom Length Resolution. *ACS Nano*, 6(10):9237–9246, 2012.

[153] U. Hohenester and A. Trügler. MNPBEM - A Matlab toolbox for the simulation of plasmonic nanoparticles. *Computer Physics Communications*, 183(2):370–381, 2012.

[154] U. Hohenester. Simulating electron energy loss spectroscopy with the MNPBEM toolbox. *Computer Physics Communications*, 185(3):1177–1187, 2014.

[155] J. Waxenegger, A. Trügler, and U. Hohenester. Plasmonics simulations with the MNPBEM toolbox: Consideration of substrates and layer structures. *Computer Physics Communications*, 193:138–150, 2015.

[156] M. Kuisma, B. Rousseaux, K. M. Czajkowski, T. P. Rossi, T. Shegai, P. Erhart, and T. J. Antosiewicz. Ultrastrong Coupling of a Single Molecule to a Plasmonic Nanocavity: A First-Principles Study. *ACS Photonics*, 9(3):1065–1077, 2022.

[157] R. Chikkaraddy, B. de Nijs, F. Benz, S. J. Barrow, O. A. Scherman, E. Rosta, A. Demetriadou, P. Fox, O. Hess, and J. J. Baumberg. Single-molecule strong coupling at room temperature in plasmonic nanocavities. *Nature*, 535(7610):127–130, 2016.

[158] H. Groß, J. M. Hamm, T. Tufarelli, O. Hess, and B. Hecht. Near-field strong coupling of single quantum dots. *Science Advances*, 4(3):4906, 2018.

[159] O. Bitton and G. Haran. Plasmonic Cavities and Individual Quantum Emitters in the Strong Coupling Limit. *Accounts of Chemical Research*, 55(12):1659–1668, 2022.

[160] S. N. Gupta, O. Bitton, T. Neuman, R. Esteban, L. Chuntonov, J. Aizpurua, and G. Haran. Complex plasmon-exciton dynamics revealed through quantum dot light emission in a nanocavity. *Nature Communications*, 12(1):1–9, 2021.

[161] M. O. Scully and M. S. Zubairy. *Quantum Optics*. Cambridge University Press, 1997.

[162] S. Haroche. Nobel Lecture: Controlling photons in a box and exploring the quantum to classical boundary. *Reviews of Modern Physics*, 85(3):1083, 2013.

[163] R. Thompson, G. Rempe, and H. Kimble. Observation of normal-mode splitting for an atom in an optical cavity. *Physical Review Lett.*, 68(8):1132, 1992.

[164] G. Rempe, H. Walther, and N. Klein. Observation of quantum collapse and revival in a one-atom maser. *Physical Review Lett.*, 58(4):353, 1987.

[165] A. F. Kockum, A. Miranowicz, S. De Liberato, S. Savasta, and F. Nori. Ultrastrong coupling between light and matter. *Nat. Rev. Phys.*, 1(1):19–40, 2019.

[166] P. Forn-Díaz, L. Lamata, E. Rico, J. Kono, and E. Solano. Ultrastrong coupling regimes of light-matter interaction. *Rev. Mod. Phys.*, 91:025005, 2019.

[167] R. Hanbury Brown, R. Jennison, and M. D. Gupta. Apparent angular sizes of discrete radio sources: Observations at Jodrell bank, manchester. *Nature*, 170(4338):1061–1063, 1952.

[168] R. Hanbury Brown and R. Q. Twiss. The Question of Correlation between Photons in Coherent Light Rays. *Nature*, 178(4548):1447–1448, 1956.

[169] H. J. Kimble, M. Dagenais, and L. Mandel. Photon Antibunching in Resonance Fluorescence. *Physical Review Lett.*, 39(11):691–695, 1977.

[170] E. Zubizarreta Casalengua, J. C. López Carreño, F. P. Laussy, and E. d. Valle. Conventional and Unconventional Photon Statistics. *Laser & Photonics Reviews*, 14(6):1900279, 2020.

[171] A. Ridolfo, S. Savasta, and M. J. Hartmann. Nonclassical radiation from thermal cavities in the ultrastrong coupling regime. *Physical Review Lett.*, 110(16):163601, 2013.

[172] X.-M. Chen, Z.-K. Chen, H.-X. Che, and C. Wang. Nonclassical photon statistics and photon squeezing in the dissipative mixed quantum Rabi model. *J. Phys. B.: At. Mol. Phys.*, 55(11):115502, 2022.

[173] S. Kéna-Cohen, S. A. Maier, and D. D. C. Bradley. Ultrastrongly Coupled Exciton–Polaritons in Metal-Clad Organic Semiconductor Microcavities. *Adv. Opt. Mater.*, 1(11):827–833, 2013.

[174] D. Melnikau, R. Esteban, D. Savateeva, A. Sánchez-Iglesias, M. Grzelczak, M. K. Schmidt, L. M. Liz-Marzán, J. Aizpurua, and Y. P. Rakovich. Rabi splitting in photoluminescence spectra of hybrid systems of gold nanorods and J-aggregates. *J. Phys. Chem. Lett.*, 7(2):354–362, 2016.

[175] S. Gambino, M. Mazzeo, A. Genco, O. Di Stefano, S. Savasta, S. Patane, D. Ballarini, F. Mangione, G. Lerario, D. Sanvitto, *et al.* Exploring light–matter interaction phenomena under ultrastrong coupling regime. *ACS Photonics*, 1(10), 2014.

[176] H.-S. Wei, C.-C. Jaing, Y.-T. Chen, C.-C. Lin, C.-W. Cheng, C.-H. Chan, C.-C. Lee, and J.-F. Chang. Adjustable exciton-photon coupling with giant Rabi-splitting using layer-by-layer J-aggregate thin films in all-metal mirror microcavities. *Optics Express*, 21(18):21365–21373, 2013.

[177] J. Johansson, P. Nation, and F. Nori. QuTiP: An open-source Python framework for the dynamics of open quantum systems. *Computer Physics Communications*, 183(8):1760–1772, 2012.

[178] J. Johansson, P. Nation, and F. Nori. QuTiP 2: A Python framework for the dynamics of open quantum systems. *Computer Physics Communications*, 184(4):1234–1240, 2013.

[179] E. Del Valle, F. P. Laussy, and C. Tejedor. Luminescence spectra of quantum dots in microcavities. II. Fermions. *Physical Review B*, 79(23):235326, 2009.

[180] O. J. Farías, V. D'Ambrosio, C. Taballione, F. Bisesto, S. Slussarenko, L. Aolita, L. Marrucci, S. P. Walborn, and F. Sciarrino. Resilience of hybrid optical angular momentum qubits to turbulence. *Scientific Reports*, 5(1):1–5, 2015.

[181] A. H. Ibrahim, F. S. Roux, M. McLaren, T. Konrad, and A. Forbes. Orbital-angular-momentum entanglement in turbulence. *Physical Review A*, 88(1):012312, 2013.

[182] M. Krenn, R. Fickler, M. Fink, J. Handsteiner, M. Malik, T. Scheidl, R. Ursin, and A. Zeilinger. Communication with spatially modulated light through turbulent air across Vienna. *New Journal of Physics*, 16(11):113028, 2014.

[183] T. D. Ladd, F. Jelezko, R. Laflamme, Y. Nakamura, C. Monroe, and J. L. O'Brien. Quantum computers. *Nature*, 464(7285):45–53, 2010.

[184] M. A. Nielsen and I. Chuang. *Quantum computation and quantum information*. Cambridge University Press, 2011.

[185] L. Thévenaz, I. Dicaire, and S. Chin. Enhancing the light-matter interaction using slow light: towards the concept of dense light. In *Advances in Slow and Fast Light V*, 8273:193–200. SPIE, 2012.

[186] E. Rodriguez, T. Bonazzi, H. Dely, M. Mastrangelo, K. Pantzas, G. Beaudoin, I. Sagnes, A. Vasanelli, Y. Todorov, and C. Sirtori. Metamaterial engineering for optimized photon absorption in unipolar quantum devices. *Optics Express*, 30(12):20515–20531, 2022.

[187] L. Huang, A. Krasnok, A. Alú, Y. Yu, D. Neshev, and A. E. Miroshnichenko. Enhanced light–matter interaction in two-dimensional transition metal dichalcogenides. *Reports on Progress in Physics*, 85(4):046401, 2022.

[188] J. Kern, A. Trügler, I. Niehues, J. Ewering, R. Schmidt, R. Schneider, S. Najmaei, A. George, J. Zhang, J. Lou, *et al.* Nanoantenna-enhanced light–matter interaction in atomically thin WS2. *Acs Photonics*, 2(9):1260–1265, 2015.

[189] L. Xu, M. Rahmani, Y. Ma, D. A. Smirnova, K. Z. Kamali, F. Deng, Y. K. Chiang, L. Huang, H. Zhang, S. Gould, *et al.* Enhanced light–matter interactions in dielectric nanostructures via machine-learning approach. *Advanced Photonics*, 2(2):026003, 2020.

[190] F. Benz, M. K. Schmidt, A. Dreismann, R. Chikkaraddy, Y. Zhang, A. Demetriadou, C. Carnegie, H. Ohadi, B. De Nijs, R. Esteban, *et al.* Single-molecule optomechanics in "picocavities". *Science*, 354(6313):726–729, 2016.

[191] A. Büse, M. L. Juan, N. Tischler, V. D'Ambrosio, F. Sciarrino, L. Marrucci, and G. Molina-Terriza. Symmetry protection of photonic entanglement in the interaction with a single nanoaperture. *Physical Review Letters*, 121(17):173901, 2018.

[192] B. Vest, M.-C. Dheur, É. Devaux, A. Baron, E. Rousseau, J.-P. Hugonin, J.-J. Greffet, G. Messin, and F. Marquier. Anti-coalescence of bosons on a lossy beam splitter. *Science*, 356(6345):1373–1376, 2017.

[193] J. M. Varga, J. Lasa-Alonso, M. Molezuelas-Ferreras, N. Tischler, and G. Molina-Terriza. Bandwidth control of the biphoton wavefunction exploiting spatio-temporal correlations. *Optics Communications*, 504:127461, 2022.

[194] N. Tischler, A. Büse, L. G. Helt, M. L. Juan, N. Piro, J. Ghosh, M. J. Steel, and G. Molina-Terriza. Measurement and shaping of biphoton spectral wave functions. *Physical Review Letters*, 115(19):193602, 2015.

[195] J. B. Altepeter, E. R. Jeffrey, and P. G. Kwiat. Photonic state tomography. *Advances in Atomic, Molecular, and Optical Physics*, 52:105–159, 2005.

[196] J. C. Schotland, A. Cazé, and T. B. Norris. Scattering of entangled two-photon states. *Optics Letters*, 41(3):444–447, 2016.

[197] J. Lasa-Alonso, J. Olmos-Trigo, A. García-Etxarri, and G. Molina-Terriza. Correlations between helicity and optical losses within general electromagnetic scattering theory. *Mater. Adv.*, 3:4179–4185, 2022.

[198] R. Rangarajan, M. Goggin, and P. Kwiat. Optimizing type-I polarization-entangled photons. *Optics Express*, 17(21):18920–18933, 2009.